Geodätisch-geophysikalische Arbeiten in der Schweiz

(Fortsetzung der Publikationsreihe
«Astronomisch-geodätische Arbeiten in der Schweiz»)

herausgegeben von der

Schweizerischen Geodätischen Kommission
(Organ der Akademie der Naturwissenschaften Schweiz)

Neunundsiebzigster Band
Volume 79

In-flight Quality Assessment and Data Processing for Airborne Laser Scanning

Philipp Schaer

2010

Adresse der Schweizerischen Geodätischen Kommission:

Institut für Geodäsie und Photogrammetrie
Eidg. Technische Hochschule Zürich
ETH Zürich
8093 Zürich
Switzerland

Internet: http://www.sgc.ethz.ch

ISBN 978-3-908440-23-9

Redaktion des 79. Bandes:
Dr. Ph. Schaer, Prof. Dr. A. Geiger
Druck: Print-Atelier ADAG, Zürich

VORWORT

Für Flächen ab einigen Hektaren ist luftgestütztes Laserscanning die präziseste und effektivste Technologie für die Erzeugung von hochauflösenden, digitalen Geländemodellen. Solche Modelle sind unabdingbar in vielen Bereichen, wie zum Beispiel Raum- und Städteplanung oder Kartierung von Naturgefahren. Zusätzlich zum eigentlichen Laser-Messinstrument hängt dieses Verfahren auch von zwei Navigationstechnologien (namentlich globale Satellitenpositionierung und Inertialnavigation) ab, welche nicht konzipiert sind um die hohen Genauigkeiten der Lasermessung (Zentimeter-Genauigkeit bei Distanzmessung und 10 Bogensekunden für die Orientierung) zu erreichen. Die in der Industrie verwendeten Prozesse zur Berechnung dieser Daten sind häufig langsam und umständlich und erlauben nur eine begrenzte Kontrolle der Datenqualität.

Die Dissertation von Philipp Schär überwindet diese Nachteile mit dem Design und der Implementierung neuer, innovativer Algorithmen welche parallel zur Datenakquisition ausgeführt werden können. Somit wird eine 3D-Kartographie in Echtzeit und eine umfassende Qualitätskontrolle noch während dem Messflug möglich. Dieser optimierte Prozess ermöglicht die automatisierte Klassifizierung der in Echtzeit berechneten Punktwolke, sowie die Ableitung von digitalen Terrain- und Oberflächenmodellen durch Triangulation. Des Weiteren wird für jede Lasermessung die Präzision durch rigorose Fehlerfortpflanzung berechnet. In Verbindung mit Geländeneigungsanalysen, sowie Kenntnis der ursprünglichen Punktdichte kann somit für jeden Modellpunkt ein Qualitätsindikator berechnet werden. Diese Information wird während dem Flug laufend aktualisiert und kann dem Systemoperator als farblich kodierte Datenebene, zusammen mit dem Flugplan, präsentiert werden.

Die Implementierung dieser Methodologie erlaubt eine drastische Verkürzung der Produktionszeiten sowie eine Steigerung der Zuverlässigkeit und Wirtschaftlichkeit. Dies wird in der Dissertation mit mehreren realen Messflügen mit verschiedenen Szenarien aufgezeigt. Schlussendlich erlauben diese Algorithmen nicht nur eine Verbesserung der bereits bestehenden Prozesse, sondern sie eröffnen auch ganz neue Anwendungsgebiete, welche eine sehr kurze Reaktionszeit erfordern (so z.B. luftgestütztes Monitoring von Naturgefahren, Erstellung von Notfallplänen nach Naturkatastrophen, usw.).

Dr. Jan Skaloud, MER
Institut für Topometrie
EPF Lausanne

Prof. Dr. Alain Geiger
ETH Zürich
Präsident der SGK

PREFACE

Le scannage aéroporté est la méthode la plus précise et la plus efficace pour saisir des modèles altimétriques numériques de haute résolution. Ces modèles sont essentielles dans différents domaines tels que l'aménagement du territoire, la planification urbaine ou encore la cartographie des zones de dangers naturels. Cette approche se base sur deux technologies de navigation (c.à.d. le positionnement par satellites et la navigation inertielle) qui ne sont pas conçues a priori pour égaler les précisions élevées de la mesure laser proprement dite (précision centimétrique pour la mesure de distance et 10 arcs seconds pour l'orientation). De plus, les processus de traitement des données actuellement utilisés par l'industrie de cartographie civile sont souvent lents, incommodes et offrent peu de moyens de contrôle de la qualité des données.

La thèse de Philipp Schär surmonte ces inconvénients par le design et l'implémentation d'algorithmes innovants qui s'exécutent en parallèle à l'acquisition des données. Une cartographie 3D en temps réel, qui inclut le contrôle de qualité durant le vol devient alors possible. Ce processus hautement optimisé commence avec la classification automatique du nuage de points généré en temps réel, ainsi que la génération des modèles numériques de terrain et de surface par triangulation. Ensuite, la précision est estimée pour chaque mesure du laser par une propagation rigoureuse des erreurs. Cette information est combinée avec l'analyse de la pente du terrain et avec l'échantillonnage des points afin d'obtenir un indicateur de qualité pour chaque point du modèle numérique. Cette information est mise à jour directement en vol après le bouclement d'une ligne de vol et peut être présentée à l'operateur par le biais de couches géocodées et superposables sur le plan de vol.

L'implémentation d'une telle méthodologie réduit considérablement la durée de production tout en rendant les produits cartographiques plus fiables et plus économiques. La faisabilité est démontrée dans la thèse lors de divers missions de cartographie aérienne réalisées dans des conditions très diverses. Finalement, cette nouvelle méthodologie ne présente pas uniquement une amélioration des processus traditionnels, mais rend possible des nouveaux champs d'applications qui exigent un temps de réaction très court (par exemple : la surveillance aéroportée des sites de dangers naturels, la cartographie d'urgence lors de catastrophes naturels, etc.).

Dr. Jan Skaloud, MER
Laboratoire de Topométrie
EPF Lausanne

Prof. Dr. Alain Geiger
ETH Zürich
Président de la CGS

FOREWORD

The method of airborne laser scanning is the most accurate and most effective mean of obtaining high-resolution elevation models of the topographical surface from few hectares to thousands of hectares. These models are essential in various fields as land management, urban planning or supervision of natural hazards, to name a few. Apart the laser-scanner instrument itself, the mapping approach relies on two navigation technologies (namely the satellite positioning and inertial navigation) which were not conceived to match the scanner's cm-level ranging and 10 arc-seconds pointing accuracies. The conventional data processing chain as carried out by today's civilian mapping industry is known to be slow and cumbersome while it offers limited control of the resulting quality.

The dissertation of Philipp Schär overcomes such drawback through design and implementation of innovative algorithms that are executed parallel to data collection. This results in real-time 3D mapping, which quality is evaluated directly within the flight mission. Such highly optimized computation includes first the automated classification of the real-time generated laser-point cloud and its triangulation to digital surface and terrain models, respectively. Second, accuracy is estimated for each laser reflection by rigorous error propagation. This is combined with the analysis of terrain steepness and with the actual surface sampling density to yield quality measure for the obtained terrain model. This information is updated within the flight after each scan line and is presented to the operator as a color-coded layer drawn over the flight plan.

The implementation of such methodology considerably shortens the mapping cycle while making it more reliable and therefore economical. This is proven within the dissertation through many real mapping missions carried over surfaces of different types. Finally, this novel methodology not only improves the traditional approach of airborne laser scanning but opens the door to completely new applications requiring fast response time (e.g. airborne monitoring of natural hazards, natural disaster mapping, etc.).

Dr. Jan Skaloud, MER
Institute for Topometry
EPF Lausanne

Prof. Dr. Alain Geiger
ETH Zürich
President of SGC

Contents

List of Figures

List of Tables

Notations and Abbreviations

Conventions

- Vectors are represented by lower-case bold letters.
- A superscript in a vector indicates a particular frame in which the vector is represented.
- Matrices are represented by upper-case bold letters.
- Rotation matrices between coordinate systems have a subscript (original frame) and superscript (target frame) indicating the two coordinate systems (e.g. $\mathbf{R}_b^l$ indicates the rotation matrix from the b-frame to the l-frame.
- The elementary rotation matrices are defined such as

$$\mathbf{R}_1(\alpha_1) = \begin{bmatrix} 1 & 0 & 0 \\ 0 & \cos(\alpha_1) & \sin(\alpha_1) \\ 0 & -\sin(\alpha_1) & \cos(\alpha_1) \end{bmatrix}$$

$$\mathbf{R}_2(\alpha_2) = \begin{bmatrix} \cos(\alpha_2) & 0 & -\sin(\alpha_2) \\ 0 & 1 & 0 \\ \sin(\alpha_2) & 0 & \cos(\alpha_2) \end{bmatrix}$$

$$\mathbf{R}_3(\alpha_3) = \begin{bmatrix} \cos(\alpha_3) & \sin(\alpha_3) & 0 \\ -\sin(\alpha_3) & \cos(\alpha_3) & 0 \\ 0 & 0 & 1 \end{bmatrix}$$

- The elements of a matrix are contained within square brackets following the matrix and consist of the row and column number. For example $\mathbf{R}[2, 3]$ indicates the element at the intersection of row 2 and column 3.
- Georeferenced grids are represented with upper case italic letters. The elements in square brackets (e.g. $D[x, y]$) evaluate the value of the grid D at position x, y (in map coordinates).

Definition of standard deviation (STD)

$$\sigma = \sqrt{\frac{\sum_{i=1}^{n} (x_i^2 - \overline{x})^2}{n}}$$

Definition of Root Mean Square Error (RMSE) and Root Mean Square Difference (RMS)

$$RMS = \sqrt{\frac{\sum_{i=1}^{n} x_i^2}{n}}$$

Terminology

For QA/QC the definitions proposed by [7] are applied:

- Quality Assurance (QA) is the process of evaluating overall project performance on a regular basis to provide confidence that the project will satisfy the required quality standards.
- Quality Control (QC) is the process of monitoring specific project results to determine if they comply with relevant quality standards, and identifying means of eliminating causes of unsatisfactory performance.

For the context of this research, accuracy is the degree to which information matches true or accepted values. Accuracy is reported at a 1-sigma level. Accuracy is synonym to the RMSE if it is evaluated as difference between dataset coordinates and coordinate values from an independent source of higher accuracy.

Abbreviations

ABAS	Aircraft Based Augmentation System
AGNES	Swiss Automated GNSS Network
ALS	Airborne Laser Scanning
ANN	Artificial Neural Network
C/A	Coarse/Acquisition
COTS	Commercial off-the-shelf
CP-DGPS	Carrier-Phase Differential GPS
CPU	Central Processing Unit
CW	Continuous Wave
DEM	Digital Elevation Model
DG	Direct Georeferencing
DGPS	Differential GPS

DOP	Dilution of Precision
DSM	Digital Surface Model
DTM	Digital Terrain Model
ECEF	Earth-Centered-Earth-Fixed
EGNOS	European Geostationary Navigation Overlay Service
EKF	Extended Kalman Filter
EO	Exterior Orientation
FDE	Fault Detection and Exclusion
FDI	Fault Detection and Isolation
FMS	Flight Management System
FOV	Field of View
GBAS	Ground Based Augmentation System
GCP	Ground Control Point
GIS	Geographical Information System
GLONASS	Global Orbiting Navigation Satellite System
GNSS	Global Navigation Satellite System
GPRS	General Packet Radio Service
GPS	Global Positioning System
GSM	Global System for Mobile Communications
GUI	Graphical User Interface
ICP	Iterative Closest Point
IDW	Inverse Distance Weighting
IFOV	Instantaneous Field of View
IMU	Inertial Measurement Unit
INS	Inertial Navigation System
IO	Interior Orientation
KF	Kalman Filter
LiDAR	Light Detection and Ranging
LSM	Least Squares Matching
MEMS	Micro-Electro-Mechanical Systems
NaN	Not-a-Number
PC	Projection Center
PP	Post-Processing
PPP	Precise Point Positioning
PPS	Pulse-per-Second
PRF	Pulse Repetition Frequency/Rate
PRN	Pseudo-random Noise Code
QA/QC	Quality Assurance / Quality Control
RAIM	Receiver Autonomous Integrity Monitoring
RT	Real-Time

RTK	Real-Time Kinematics
SBAS	Satellite Based Augmentation System
SLF	Swiss Institute for Snow and Avalanche Research
SNR	Signal-to-Noise Ratio
SPP	Single Point Positioning
SPS	Standard Positioning Service
SW	Swath Width
TCP/IP	Transmission Control Protocol/Internet Protocol
TIN	Triangulated Irregular Network
TLS	Terrestrial Laser Scanner
TOF	Time of Flight
UERE	User equivalent Range Error
UMTS	Universal Mobile Telecommunications System
UWB	Ultra Wide Band
VRS	Virtual Reference Station
WAAS	Wide Area Augmentation System
ZTD	Tropospheric Zenith Total Delay

Chapter 1

Introduction

1.1 Context

During the last decade, Airborne Laser Scanning (ALS[1]) has become a well established and broadly employed technology in the mapping industry. The performance of the commercially available ALS systems is increasing at an astonishing pace, going hand in hand with the reduction in acquisition time and production cost. Surprisingly, the development of the accompanying data processing and system monitoring software has not followed the same evolution [131]. Although Direct Georeferencing (DG) can be considered as a well established industrial method, a number of open questions related to its reliability and integrity are remaining [149]. The reason for this is the tremendous complexity of the ALS technology that groups the latest in several research fields.

Currently, no ALS system providers can claim to control the complex chain of ALS from data acquisition, data georeferencing and system calibration to final mapping product generation. Instruments and methods are often connected upon without rigorous links or feedbacks among them. This leads to situations where users may encounter pitfalls due to undetected sensor behavior, varying data quality and consistency. Fig. 1.1 illustrates some examples of possible problems in ALS datasets: For instance, data gaps originated by poor ground reflectance (Fig. 1.1.A) or insufficient strip overlaps (Fig. 1.1.B) can only be seen once the point-cloud is available. Fig. 1.1.C shows another example where the bare-earth model in a forested area is of poor quality due to reduced laser beam penetration across the canopy. This results in few available ground points for surface modeling. Fig. 1.1.D depicts the influence of inhomogeneous navigation accuracy that causes problems in the georeferencing of the point-cloud visible as data discrepancies within strip overlaps.

In the classical ALS workflow, the trajectory computation (kinematic DGPS processing and GPS/INS integration) and point-cloud generation is performed in post-processing (PP). As a consequence, problems in data consistency and accuracy can only be detected after the

[1] Although ALS is used as type designation by a particular system manufacturer, in the context of this research ALS will be used as a general term for Airborne Laser Scanning (including GPS/INS), while the term LiDAR (Light Detection and Ranging) will be used for the scanner itself.

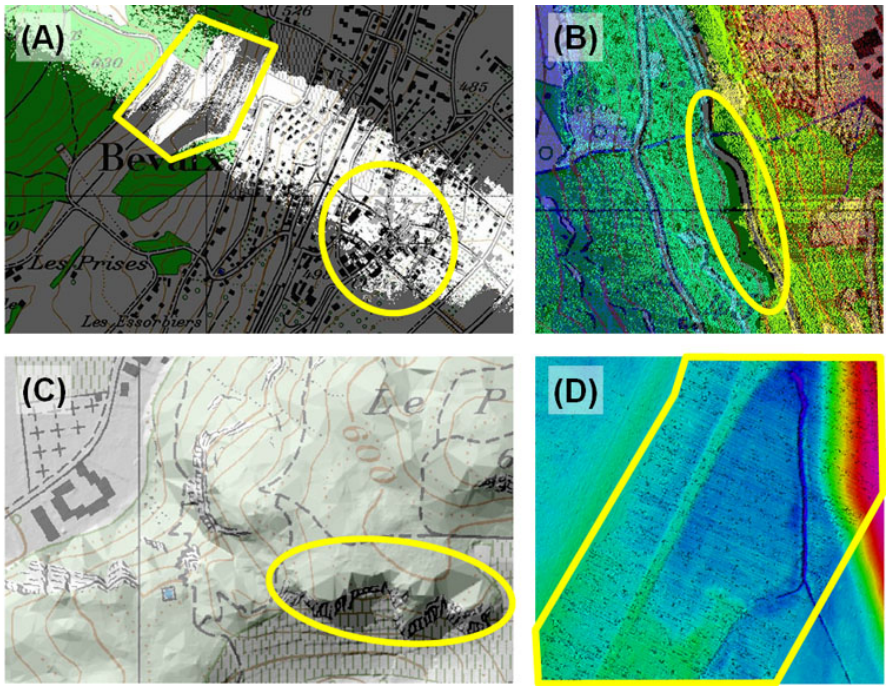

FIG. 1.1: Possible problems occurring in ALS data: (A) No laser signal returns due to poor reflectance, (B) Missing strip overlap, (C) Poor ground point density, (D) Poor navigation accuracy.

flight. The applied QA/QC (Quality Assurance/Quality Control) methods usually involve field collection of independent survey checkpoints [193]. This may result in situations where the quality control and problem mitigation takes an overwhelming part of the cost of the final mapping product. Furthermore, if the QC reveals that the data does not comply with the specifications and no ad-hoc mitigation is possible, the quality degradation either has to be accepted or the parts failing the quality requirements have to be re-acquired. This may lead to delays in data delivery and further increase in production cost (see FIG. 1.2.A).

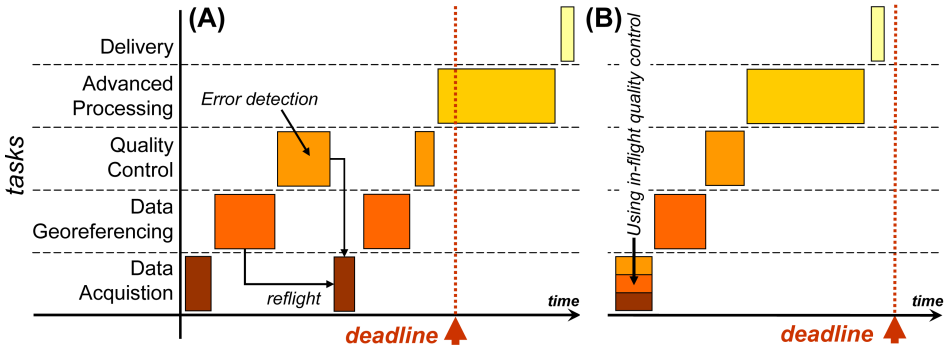

FIG. 1.2: Potential ALS mission workflow without (A) and with (B) in-flight QA/QC tool.

The capacity to perform parts of the ALS processing and QA/QC directly during data acquisition (in-flight) could substantially reduce the risk to encounter unwanted quality degradation in PP. Such tool would also have a positive economic impact for the mapping industry by reducing the effort for quality control and preventing situations that require

(partial) re-acquisition of data (see FIG. 1.2.B). This would translate into increased profit margin in conventional ALS mapping applications and could open a new field of mapping applications, where excellent data quality and a short hand-over time are crucial (e.g. risk management, natural hazards, security, etc.).

In 2005, the aforementioned motivations have prompted *BSF-Swissphoto AG*[2] and the *Geodetic Engineering Laboratory* (TOPO-EPFL[3]) to launch a project called IQUAL. This project aimed at developing a tool performing QA/QC of the recorded ALS data "on the fly" [81]. The project ended in February 2009 and was supported by the Swiss Innovation Promotion Agency (CTI/KTI) [75]. The research presented in this thesis is an integrated part of this project.

1.2 Research Objectives

The objectives of this research are threefold:

1. **Elaborate the theoretical concepts and methodologies needed for performing fast and automated QA/QC of ALS data.** This embraces the definition of a methodology to automatically assess the quality of laser measurements and to evaluate the point-cloud coverage and homogeneity. A further objective is to establish a concept to assess the accuracy of derived surface models.

2. **Implement the theoretical concepts in a fully functional in-flight QA/QC-tool embedded in an ALS system.** This requires merging data streams from different technologies (i.e. inertial navigation, GNSS positioning, laser measurements) in real-time (RT), developing its qualitative evaluation and presenting it to the system operator.

3. **Provide a thorough analysis of the system performance using data acquired under real operating conditions.** The objective is to demonstrate the usefulness of the provided QC information in-flight and to determine the achievable accuracies for ALS data processed in-flight. A particular attention is payed to the evaluations of benefits using real-time Kinematics (RTK) for improving the accuracy of the RT navigation, point-cloud generation and derivation of quality metrics.

1.3 Methodology

The development of RT algorithms is very critical as they need to be optimized for processing speed to handle the data at their original data rates. This requires special testing environments where the algorithms can be evaluated in PP (without speed constraints) and in "emulated RT". For this purpose a multi-level methodology has been designed, where each level depends on the results of the previous one but simultaneously allows feedbacks for adjustments at lower level.

[2]BSF-SWISSPHOTO AG, based in Regensdorf, is the largest private mapping company in Switzerland providing worldwide ALS mapping services

[3]Swiss Federal Institute of Technology, Lausanne

The different levels (from bright gray to dark gray) are depicted in Fig. 1.3. First, the theoretical concepts for in-flight quality monitoring are developed. This level mainly depends on the inherent characteristics of the involved technologies, that are Global Navigation Satellite Systems (GNSS) for absolute positioning, Inertial Measurement Units (IMU) for attitude determination and LiDAR (Light Detection and Ranging) for ranging. This is followed by the algorithmic implementation for evaluation in PP. Due to its simulation and programming simplicity, primarily the MATLAB-environment is employed in this step. The Proof-of-Concept (POC) can be carried out using recorded datasets. Once the algorithms are stable in PP, they can be adapted for RT use. At this stage, the implementation has to account for the hardware that is interfaced with the software application. For this implementation level, the C++ programming language is chosen.

To facilitate the code development and debugging, a "simulated RT" environment precedes the in-flight tests. For this purpose a special server application, called RFLOWS, has been developed. This application redistributes recorded datasets (raw GPS, IMU and LiDAR measurements) at RT data rates [151]. This step allows testing the behavior of the algorithms under RT conditions including mission specific characteristics (terrain, point density, etc.) without need to acquire new data. Finally, the tool is tested during flight operation, where the user-friendliness and the ergonomics of the graphical user interface (GUI) can be evaluated.

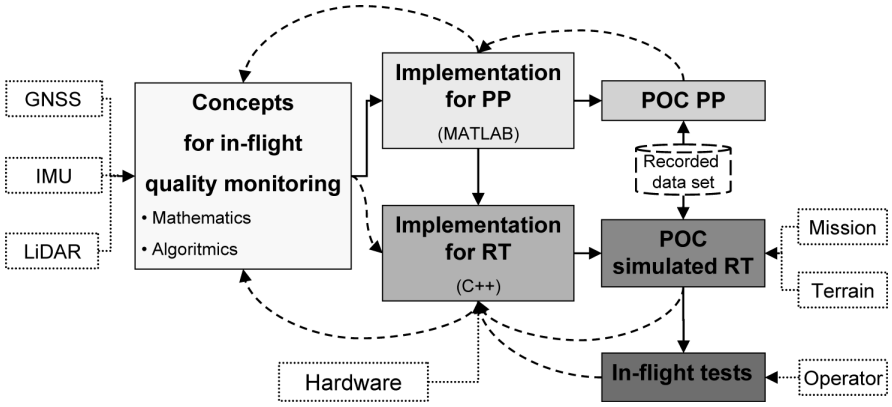

Fig. 1.3: Methodology for the development of the in-flight quality monitoring tool.

Implementation Platform

Embedding an in-flight QA/QC-tool in an ALS system requires in-depth knowledge about the system components and free access to all internal data flows. Yet, commercial system providers rarely grant access to detailed information (i.e. data exchange protocols, file formats, algorithms) of their systems to the customers. The commercial strategy is to sell the systems as black-boxes, where the interacting possibilities are reduced and the input and output interfaces are well defined.

The Geodetic Engineering Laboratory of the Swiss Federal Institute of Technology (TOPO-EPFL) lead the built up of an ALS system called **Scan2map**, that combines GPS, INS, LiDAR and a medium format digital camera, and where it controls all interfaces, internal

data streams and has full access to the source codes (more details in CHAP. 6.1). Thus, in the frame of this thesis, the Scan2map-system served as vector and testing platform for the presented research.

1.4 External Contributions

The development of a fully functional in-fight quality monitoring application is characterized by a high complexity both on the scientific and engineering level. To achieve the aforementioned objectives within the given time frame of a PhD thesis, the author could benefit of the punctual assistance of several persons. Although the author is the main contributor, the developments presented in this thesis are the result of a joint effort of several members of the Geodetic Engineering Laboratory (TOPO-EPFL). The most important external contributions are:

- The RT GPS Quality assessment tool (CHAP. 6.4)
- The RT GPS/INS integration engine (CHAP. 6.5)
- The RT point-cloud georeferencing engine (CHAP. 6.6)

Wherever external resources have been used for the development, their contribution will be clearly referenced and the main contributions of the author emphasized.

1.5 Thesis Outline

This thesis is structured in 7 chapters and can be roughly divided into 4 major blocks:

- **Review of ALS technology**: Chapter 2 delivers the background material related to ALS technology. The mathematical concept and the reference frames used for the process of DG of laser data are introduced. Additionally, the enabling technologies for ALS, namely laser range-finder technology, satellite positioning (GNSS) and integrated navigation technology (GNSS/INS) are presented in detail.
  Chapter 3 discusses the challenges related to the calibration of the ALS system and the ALS data (strip adjustment). Furthermore, the basic principles for point-cloud processing, such as spatial indexing, point-cloud classification and height model generation are presented.
- **Development of concepts for QA/QC of ALS data**: Chapter 4 is devoted to the concepts of quality assessment of a single ALS measurement. Particular focus is given to the development of a new method to assess the influence of the scanning geometry on the final accuracy. The validity of this method is discussed using both simulated and real datasets.
  In chapter 5, the quality concept is extended to surfaces. Methods to measure the data coverage, data sampling rate and the internal data accuracy are presented. Special attention is given to the construction of quality indicators for height models derived from ALS data.

- **Implementation into in-flight QA/QC-application**: Chapter 6 presents the available hardware infrastructure and discusses the implementation of the concepts introduced in the previous chapters into a fully functional in-flight quality monitoring tool. The adopted modular architecture for interfacing the involved hardware and software components together with the functional principles of the modules are presented in detail.

- **Performance analysis and conclusions**: Chapter 7 is dedicated to the analysis of the performance of the developed application. The accuracies of the different quantities computed by the tool are assessed by comparison with the post-processed solutions. Additional tests evaluate the computational performances (in terms of processing speed) of the tool and highlight strategies for improving the computational efficiency.
  Chapter 8 presents a summary of the main contributions of the author, conclusions and perspectives for future work. This is followed by bibliography and appendices.

Chapter 2

ALS Enabling Technologies

Before developing an in-flight ALS quality monitoring tool, it is beneficial to know the current industry standards for in-flight ALS processing and quality control. Furthermore, the constraints imposed by the enabling technologies on the process of DG should be understood. After a short overview of the in-flight QA/QC capabilities of today's ALS systems, this chapter presents the mathematical concepts and the reference frames used for DG of laser data. The necessary background material about the involved technologies, i.e. laser ranging, GNSS and IMU, is also provided in this chapter.

2.1 Airborne Laser Scanning

2.1.1 History of ALS Technology

Compared to photogrammetry, which has been deployed for airborne mapping and height model generation since the early 1920s [32], ALS is a fairly new technology. The development of ALS has been mainly driven by hardware evolution. Initially, it became possible by pulse lasers operating in the near infrared band, which gave clearly recordable return signals after being backscattered on the ground [2]. Its development goes back to the 1970s and 1980s, with an early NASA system and other attempts in USA and Canada. But the real breakthrough of the technology came only in the 1990s, when the carrier-phase differential kinematic GPS (CP-DGPS) became accurate enough to meet the requirements for DG. By the end of the 1990s, the technology was mature and had successfully established itself within the airborne mapping community, quickly spreading into various practical applications.
In the last decade, the development was marked by rapidly increasing pulse repetition rates (PRF) of LiDAR scanners and the emergence of so-called full-waveform lasers [96]. Most recent sensor developments lead to the ability of multi-pulse systems. Such systems have multiple laser signals in the air simultaneously [106, 124], thus greatly increasing the PRF for high flying heights. A detailed overview of currently available commercial-of-the-shelf (COTS) ALS systems and their technical specifications can be found in [83].

2.1.2 Current in-flight QA/QC Capabilities

The ALS community is predominantly hardware-driven, pushing the performance of their systems further (increasing PRF, max. flying height, etc.). The key-numbers of this evolution are well-documented. For the associated processing software, including the flight management system (FMS) and in-flight quality monitoring less effort has been made. Moreover, commercial ALS system providers are less eager to communicate the concepts behind their software. Hence, it is somehow difficult to obtain a "detailed picture" of what is currently implemented for in-flight quality monitoring in commercial ALS systems. The following survey (Tab. 2.1) is based on freely available information (mainly sales material) for some selected FMS provided by leading ALS manufacturers. Thus, it has no pretension to be complete or exhaustive. The selected FMS suites (with used sources) are :

(**A**) IGI CCNS4/AEROcontrol [46]

(**B**) Optech ALTM Orion/DASHmap [140]

(**C**) LEICA ALS50-II/60 FCMS [82]

(**D**) TopoSys FALCON [173]

(**E**) RIEGL RiACQUIRE [122]

	FMS				
In-flight computation/display options	**A**	**B**	**C**	**D**	**E**
RT Position	✓	✓	✓	✓	✓
RT Attitude	✓	✓	✓	✓	✓
Scanner swath display	×	✓	(✓)[a]	×	✓
Point-cloud georeferencing	×	×	×	(✓)[a]	✓[b]
Point-cloud density analysis	×	×	×	×	×
Trajectory quality monitoring	×	×	✓	✓[c]	×
Point-cloud quality monitoring	×	×	×	×	×

[a]Not clear from documentation, [b]Probably only swath borders, [c]Only based on GPS DOP-values

Tab. 2.1: Survey of in-flight QA/QC and data processing capacities of commercial FMS.

Tab. 2.1 illustrates that the display of RT information of position and attitude is a standard feature in the ALS industry. Also the display of the swath becomes a common feature of these tools. However, for some FMS it is not clear if the displayed swath represents the real swath (i.e. 2D projection of most left/right point in a scanning profile) or only a derived swath, where borders are drawn using the field of view of the laser, an average height over ground and the banking angle. Although RT GPS/INS integration is sometimes implemented (e.g. used for roll compensation or stabilization of gimbaled systems), no FMS presented in this survey implements in-flight point-cloud generation. Also the GPS/INS quality control provided by some FMS remains rudimentary. It is essentially based on simple thresholds on DOP values (GPS) and displaying the computed attitude angles without confidence levels.

2.1.3 Trends in ALS

At the beginning of the year 2009, Cary and Associates of Longmont (Colorado, USA) issued a detailed business analysis of the global ALS market [20]. Tab. 2.2 summarizes the top four wishes of ALS system users for the future development published in this report. The increase in point density, thus scanning rate, is placed as top answer of this survey. Responses two and three are in line with the objectives of this research, as the possibility to perform in-flight QA/QC has a direct influence on production time and thus production cost. In-flight point-cloud processing capabilities would also greatly help alleviating the post-processing and data analysis. The ever-growing clients requirements in terms of point accuracy and point density, coupled with tight hand-over schedules, should incite the ALS system providers to enhance their FMS by in-flight QC and processing tools, in order to allow ALS system users to gather data with maximum control and cost-effectiveness.

Percent	Top wishes 2009-2012
25%	Increasing point density
18%	Decreasing costs of data
14%	Easier and improved post-processing and analysis software
11%	Multi-sensor data / fusion

Tab. 2.2: Top four wishes of ALS service providers for developments in the ALS industry in the next three years (after [20]).

2.2 Direct Georeferencing: Basic Relations

According to [144], georeferencing can be defined as a process of obtaining knowledge about the origin of some event in space-time. Depending on the sensor type, this origin needs to be defined by a number of parameters such as time, position, attitude (orientation), and possibly also the velocity of the object of interest. When this information is obtained directly by measurements from sensors aboard the vehicle, the term Direct Georeferencing (DG) is used. In other words, DG comprises a long process that involves acquisition, synchronization, processing, integration and transformation of measured data from navigation (GPS/INS) and remote sensing instruments (such as scanners, digital cameras, radar, etc.).

2.2.1 Direct Georeferencing for ALS

Unlike airborne photogrammetry, where the georeferencing of the data (the images) can be established a-posteriori by means of ground control points (GCP), ALS is entirely depending on DG for sensor orientation and coordinate computation. Accordingly, every ALS consists of two main units:

1. **The navigation unit** embraces all the necessary sensors to compute position and attitude of the system. The so-called positioning sensors namely are a GPS-antenna and receiver and an inertial navigation system (INS) or unit (IMU).

2. **The laser unit** includes a laser range finder and a scanner as the remote sensing component. This segment can further be divided: The laser ranging unit includes a laser transmitter and receiver optics, the optical scanning mechanism reflects the laser beam across-track (see FIG. 2.1).

The end-product of an ALS system are geometric measures in terms of distance, position, attitude and coordinates. For each laser shot, the spatial vector from the laser platform to the point of reflection is established, thus providing the XYZ coordinates of the footprint. The final product after georeferencing is a so-called point-cloud.

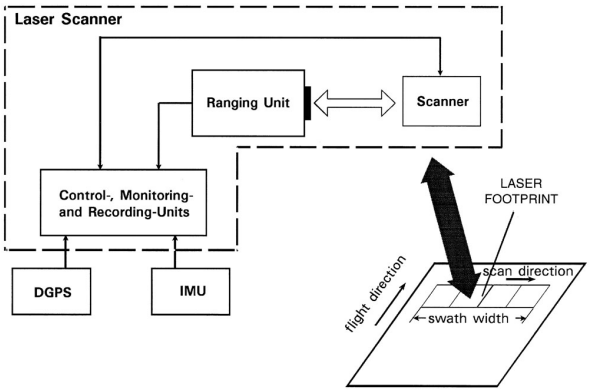

FIG. 2.1: Principal components of an ALS system (after [191]).

2.2.2 Used Reference Frames

As georeferencing of airborne laser data involves GPS and inertial measurements, computing final point-cloud coordinates in a desired mapping frame cannot be done without using a global reference frame and a series of intermediate frames. TAB. 2.3 and FIG. 2.2 provide an overview of the principal frames involved in ALS point computation. All the subsequent formulas involve the annotations listed in TAB. 2.3. The definitions follow the notations used in [85].

Sensor Frame (s)

Most airborne laser scanners are line scanners, providing a 2D-scan across a line. A target coordinate in the sensor frame can therefore be expressed in function of the encoder angle θ and the range measurement ρ. Assuming that the scanning plane $(y_s z_s)$ and the encoder angle θ are defined as in FIG. 2.2 (positive rotation around x_s), the relation can be described by EQN. 2.2.1.

$$\mathbf{x}^s = \rho \begin{pmatrix} 0 \\ \sin\theta \\ \cos\theta \end{pmatrix} \tag{2.2.1}$$

ID	Frame Name	Description
s	Sensor Frame	Frame of the laser sensor, defined by the principal axes of the scanner. The yz-plane defines the scanning plane.
b	Body Frame	Frame materialized by the triad of accelerometers with an INS.
l	Local Level Frame	Also called NED-Frame, this frame is tangent to the global earth ellipsoid (normally WGS84), with the orthogonal components **N**orth, **E**ast and **D**own.
e	ECEF Frame	Earth-centered Earth-fixed frame. The origin is the geocenter of the earth, the **X**-axis points towards the Greenwich meridian and the **Z**-axis is the mean direction of the earth rotation axis. The **Y**-axis is completed by the right-handed Cartesian system.
m	Mapping Frame	Cartesian Frame with **E**ast, **N**orth and **U**p component. The easiest implementation is the local tangent plane frame, but this frame can also be represented by a national projection.

TAB. 2.3: Overview of reference frames (adopted after [85]).

ECEF Frame (e)

The satellite orbits of the common GNSS-systems are referred to some Earth-Centered Earth-Fixed frame. The outcome of the trajectory computation is primarily provided in this frame. A geocentric ellipsoid is normally attached with the ECEF frame which together with some other geophysical parameters defines a world datum, such as WGS84 used for GPS measurements [135]. Coordinates in this frame can either be expressed as Geocentric coordinates (x^e,y^e,z^e), or as Geographical coordinates (latitude φ, longitude λ, ellipsoidal height h). The latter notation is often used to output the GPS/INS trajectory of the carrier. The transfer from geocentric to geographic coordinates can be performed as follows:

$$\mathbf{x}^e = \begin{bmatrix} x \\ y \\ z \end{bmatrix}^{\mathrm{e}} = \begin{pmatrix} (N+h)\cos\varphi\cos\lambda \\ (N+h)\cos\varphi\sin\lambda \\ (\frac{b^2}{a^2}N+h)\sin\varphi \end{pmatrix} \tag{2.2.2}$$

where a,b are semi-major and semi-minor axes of the ellipsoid and $N = \frac{a}{\sqrt{1-e^2\sin^2\varphi}}$ is the radius of curvature in the prime vertical. The transfer from geocentric to geographic coordinates can either be done by an approximate closed formula or by using an iterative approach. The respective formulas can be found in [33].

Local-level Frame (l)

This frame is generally used as reference for the orientation angles outputted from the GPS/INS processing. Its origin can be defined as the intersection of the local plumb line from the actual sensor position with the world ellipsoid. The x^l-axis points along the local meridian to the north , the y^l-axis points to the east and the z^l-axis is defined along the local plumb line. This frame may be called NED (for North−East−Down). The rotation matrix $\mathbf{R}_l^e$ for the coordinate transformation from the l- to the e-frame can be written as follows:

$$\mathbf{R}_{l_{NED}}^e = \begin{pmatrix} -\sin\varphi\cos\lambda & -\sin\lambda & -\cos\varphi\cos\lambda \\ -\sin\varphi\sin\lambda & \cos\lambda & -\cos\varphi\sin\lambda \\ \cos\varphi & 0 & -\sin\varphi \end{pmatrix} \tag{2.2.3}$$

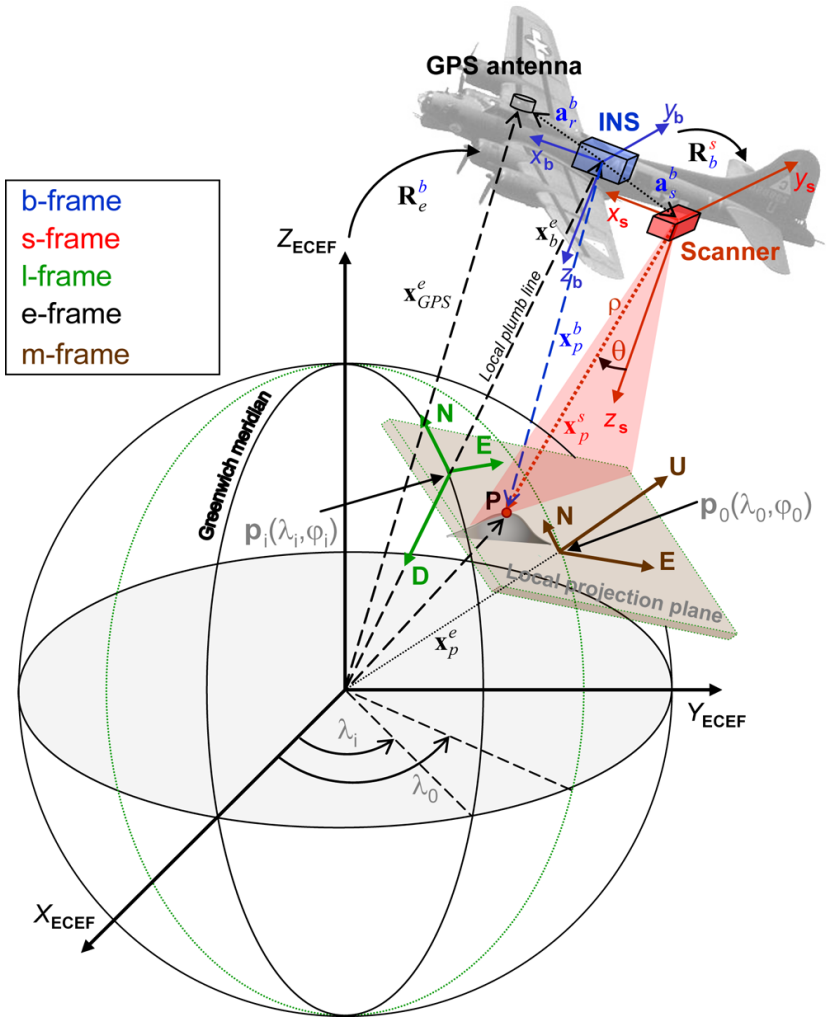

FIG. 2.2: ALS observation geometry and used frames.

Body Frame (b)

In most cases the body-frame is represented by the axes of the inertial navigation system. The origin of the b-frame is located at the navigation center of the INS. The axes are congruent with the axes spanned by the triad of accelerometers. Normally, the b-frame axis coincide with the principal axis of rotation of the carrier or can be rotated to them by some cardinal rotation. According to the aerospace norm ARINC 705, the axis and the rotations describing the 3D attitude are defined as follows. The x^b-axis is pointing forward along the fuselage, the y^b-axis points to the right and the z^b-axis points down. The associated rotation angles are called roll(r), pitch(p) and yaw(y) (see FIG. 2.3). Respecting the aerospace attitude definitions, the corresponding rotation matrix that relates the l-frame to the b-frame takes the following form:

$$\mathbf{R}^b_{l_{NED}} = \mathbf{R}_1(r)\mathbf{R}_2(p)\mathbf{R}_3(y) \tag{2.2.4}$$

where the composed rotation must be read from the right-hand side.

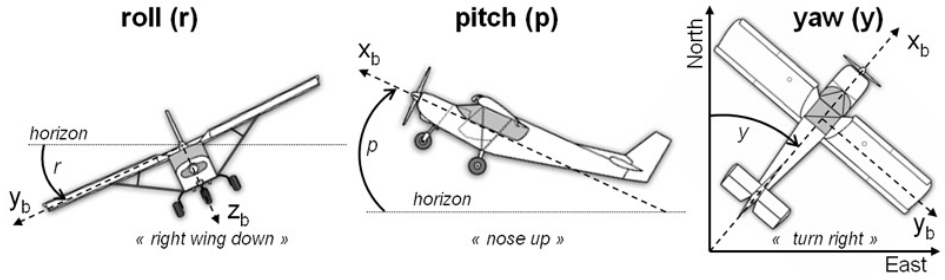

FIG. 2.3: Definition of navigation angles.

Mapping Frame (m)

This frame is employed as substitute for the datum in which the point-cloud should be delivered. The easiest implementation of such mapping frame is the Local Tangent Plane Frame: The origin is defined as an arbitrary position (φ_0, λ_0) on the ellipsoid, the x^m-axis is pointing to the east, the y^m-axis pointing north along the central meridian (λ_0) and the z^m-axis is pointing upwards along the ellipsoid normal at the plane origin. The rotation matrix $\mathbf{R}^e_{m_{ENU}}$ for coordinate transformation from the m-frame (as local tangent frame) to the e-frame is

$$\mathbf{R}^e_{m_{ENU}} = \begin{pmatrix} -\sin\lambda_0 & -\sin\varphi_0\cos\lambda_0 & \cos\lambda_0 \\ \cos\lambda_0 & -\sin\varphi_0\sin\lambda_0 & \cos\varphi_0\sin\lambda_0 \\ 0 & \cos\varphi_0 & \sin\varphi_0 \end{pmatrix} \tag{2.2.5}$$

The m-frame can also represent some other datum or projection or a national coordinate system.

2.2.3 ALS Observation Equation

FIG. 2.2 helps depicting the geometrical relations between the frames presented above. Let us first consider the relationship between the b- and s-frame. An arbitrary measurement on some point $\mathbf{p}$ by the sensor can be expressed in the b-frame as

$$\mathbf{x}^b_p = \mathbf{a}^b_s + \mathbf{R}^b_s(\omega, \phi, \kappa)\mathbf{x}^s_p \tag{2.2.6}$$

where $\mathbf{a}^b_s$ is the leverarm vector between the INS center and the firing center of the laser expressed in the b-frame, and $\mathbf{R}^b_s$ is the so-called boresight matrix parametrized by the three Euler angles ω, ϕ, κ. Their determination will be discussed in the section related to the system calibration (CHAP. 3.1). Following the previous relation, the laser measurement in the e-frame can be expressed as:

$$\mathbf{x}^e_p = \mathbf{x}^e_b + \mathbf{R}^e_b\left(\mathbf{a}^b_s + \mathbf{R}^b_s\mathbf{x}^s_p\right) \tag{2.2.7}$$

After rearranging and expanding EQN. 2.2.7 by EQN. 2.2.1 to EQN. 2.2.4, the ALS observation equation for an arbitrary laser point $\mathbf{x}_p$ expressed in the e-frame, in function of time varying measurements, denoted with (t), can be written as:

$$\mathbf{x}^e_p(t) = \mathbf{x}^e_b(t) + \mathbf{R}^e_l(t)\mathbf{R}^l_b(t)\mathbf{R}^b_s(\omega, \phi, \kappa)\left[\mathbf{a}^b_s + \rho(t)\begin{pmatrix} 0 \\ \sin\theta(t) \\ \cos\theta(t) \end{pmatrix}\right] \tag{2.2.8}$$

where

$\mathbf{R}_l^e(t)$	is the rotation matrix in function of the geographic position $(\varphi(t), \lambda(t))$ on the reference ellipsoid measured by GPS
$\mathbf{R}_b^l(t)$	is the so-called attitude matrix parametrized by the Euler angles $r(t), p(t), y(t)$ measured by GPS/INS
$\rho(t), \theta(t)$	are the range and the encoder angle measurement of the laser scanner

The GPS position can be attached to EQN. 2.2.8 by

$$\mathbf{x}_b^e(t) = \mathbf{R}_b^e(t)\mathbf{a}_{GPS}^b + \mathbf{x}_{GPS}^e(t) \tag{2.2.9}$$

where $\mathbf{a}_{GPS}^b$ is the leverarm of the INS navigation center to the GPS antenna center expressed in the b-frame, and $\mathbf{x}_{GPS}^e(t)$ is the vector of the GPS measure in the e-frame.

2.3 Laser Scanner Technology

2.3.1 Laser Ranging

The laser ranging unit contains the laser transmitter and the receiver. The two units are mounted so that the received laser path is the same as the transmitted path. This ensures that the system will detect the target the transmitter points to. The size of the laser footprint is a function of the flying height above ground and the divergence of beam. The divergence ϵ of the beam defines the instantaneous field of view (IFOV) of the sensor. For currently available systems on the market, the beam divergence (or IFOV) typically spans from 0.2 mrad to 3 mrad (e.g. [83]).

To obtain a range measurement from a laser, the transmission must be modulated. There exist two major ranging principles [191]:

- **Pulsed ranging or TOF (Time of Flight)**: The transmitter generates a rectangular pulse with widths from 4 to 15 ns. The time difference between the pulse leaving the transmitter and its detection by the receiver is proportional to the returned distance:

  $$t = 2\frac{D}{c} \tag{2.3.1}$$

  where t is the total elapsed time, D the range of the pulse and c the speed of light.

- **Continuous wave ranging (CW)**: This modulation type employs a transmitter to emit a sinusoidal continuous light wave at a given frequency. The phase difference of the received light wave is proportional to the travel time and thus to the range:

  $$t = \frac{\phi}{2\pi}T + nT \tag{2.3.2}$$

  where t is the total elapsed time, ϕ the phase difference of the returned wave, T the period of the modulated signal and n the number of full wavelengths included in the distance from the transmitter to the receiver.

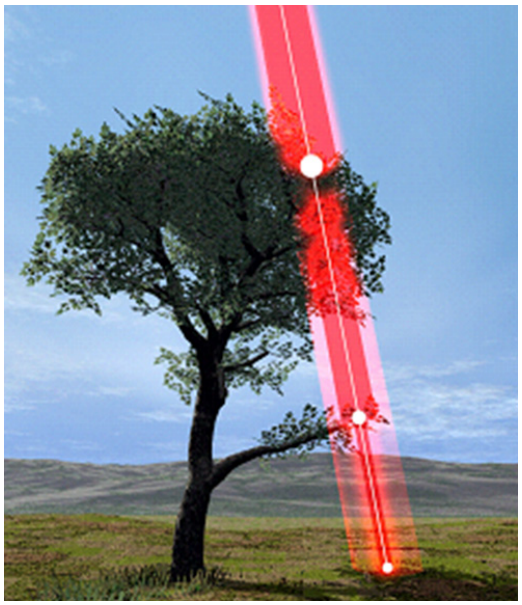

FIG. 2.4: Principle of multiple echos from a laser signal.

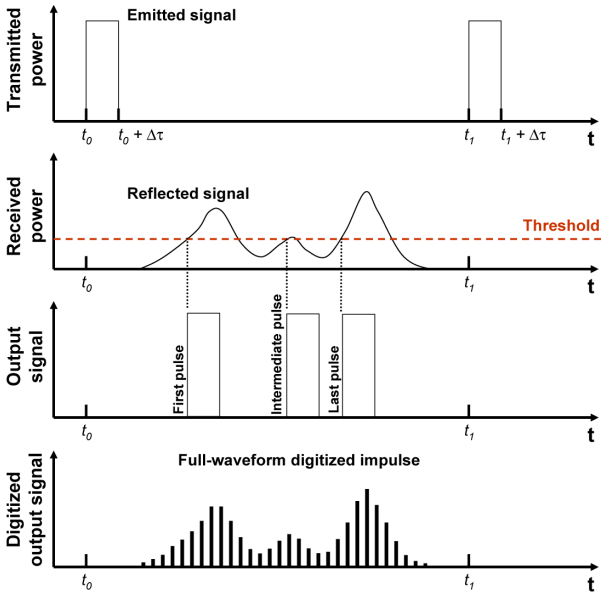

FIG. 2.5: Emitted and received impulse for discrete echo scanners and full-waveform scanners.

Today's ALS systems are almost solely based on pulsed ranging technology [111]. Currently, there are two different types of commercial ALS sensor systems available:

- **Discrete echo scanners** detect a representative trigger signal for an echo in RT using analog detectors. A discrete echo scanner can reflect multiple targets in its line of sight. This allows gathering ground points even through the canopy (see FIG. 2.4). The gaps between the leaves and branches permit parts of the pulse to penetrate further to the ground, while some energy is reflected immediately. Every reflection is detectable as a peak in the gathered return signal. Based on some threshold (see FIG. 2.5), the received input signal is discretized into single pulses. Today's commercial discrete echo systems can record up to 5 returns, whereas the minimum pulse separation has reached submeter level [54]. These returns can be labeled according to their returning position and number of returns: First (of many), last (of many), intermediate and only return [105].
- **Full-waveform scanners** digitize the entire analog echo waveform, i.e. the time-dependent variation of the received signal power, for each emitted laser pulse (see FIG. 2.5). Hence, they overcome the minimum pulse separation limitation of discrete echo scanners. Digitization is performed typically with an interval of 1 ns (corresponding to a discretization resolution of 15 cm). For most full-waveform systems, the determination of the individual echoes is performed in PP. However, a new generation of ALS systems performing full echo digitization and waveform analysis in-flight has recently emerged on the market [121].

2.3.2 Intensity Measure

Most commercial laser rangers operate between 900 and 1500 nm (near-infrared). The transmitted energy interacts with the target surface and permits the derivation of range and

reflectance measurements. The intensity[1] of the reflected near-infrared signal can be added as an additional attribute to the coordinates or can be used to form a grayscale orthoimage (see FIG. 2.6) of the measured area. The amount of backscattered energy depends on several factors:

- **Laser wavelength**: Varying the laser wavelength results in very different reflectance response diagrams. Lasers deploying long wavelength ($> 1500\,\text{nm}$) have very good reflectance responses on dark surfaces, whereas bright surfaces (i.e. glaciers, snow) reflect weakly [191]. On the other side, systems with shorter wavelength ($< 1000\,\text{nm}$) have poor reflectance on concrete and dark pavement and are less suitable for mapping in urban areas.
- **Reflectance of target material**: Objects with high reflectivity (or other words: high albedo) such as street mark paintings or cement contrast distinctly with objects of low reflectivity such as coal or soil (see FIG. 2.7).
- **Incidence angle of laser beam**: The backscattered signal from the target surface is a function of the integrated energy distribution across the whole footprint. Accordingly, the bigger the incidence angle, the larger the footprint and consequently the smaller the backscattered energy.
- **Atmospheric illumination and attenuation**: Laser scanners are active measurement devices as they illuminate the target by themselves. Therefore, every external illumination, such as sun light or reflectance from clouds, is considered as noise. Additionally, light propagation in the troposphere is affected by both, scattering and absorption characteristics of the atmospheric medium [186], thus reducing the beam energy proportional to the range. Accordingly, the intensity measure is heavily subject to the actual range, the atmospheric and meteorological conditions (air humidity, cloud cover, day time, etc.).

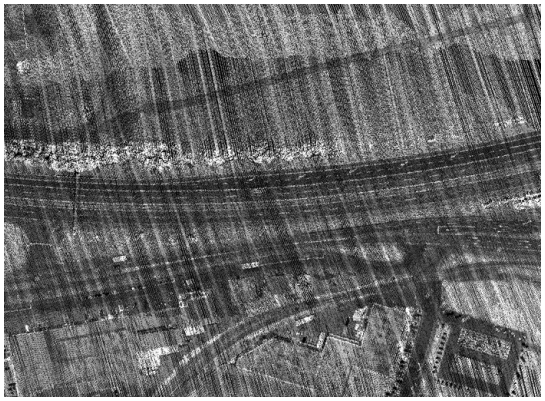

FIG. 2.6: Point-cloud colored by non-normalized intensity values.

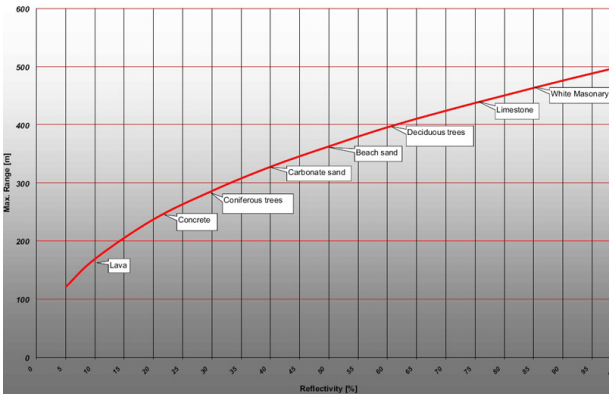

FIG. 2.7: Reflectivity for different surfaces for a laser operating at 905 nm (after [119]).

FIG. 2.6 illustrates the large intensity disparities that can occur for points measured on a same surface but gathered in different strips (thus different ambient lighting conditions and

[1]Term used in the ALS industry for the amplitude of the reflected signal

incidence angles). As the single intensity measure is influenced by so many parameters that vary in time and space, a normalization of the intensity values is crucial, should the intensity data be applicable e.g. as attribute for ALS point-cloud filtering, segmentation or feature extraction. This issue has been addressed by many authors [52, 60, 76], however, an easy and robust intensity normalization procedure is not yet available.

2.3.3 Scanning Patterns

Airborne scanners must be moved across a surface to complete a scan. This is generally achieved with rotating mirrors or other means to deflect the laser beam to provide across-track scanning, while the motion of the platform provides along-track scanning. The total across-track scanning angle defines the swath width or field of view (FOV). The swath width SW can be computed in function of the flying height H and the FOV ϕ_{max}:

$$SW = 2H \tan \frac{\phi_{max}}{2} \tag{2.3.3}$$

Today's commercial systems typically have FOV's around 60 degrees [83], although systems with FOV's up to 80 degrees are available [120]. There exist several scanning techniques employed in current ALS systems (see Fig. 2.8):

- **Constant velocity-rotating polygon mirror**: This type of scanner produces measurements that appear as parallel lines on the ground. The mirror is rotated in one direction by a motor and the angle is measured either directly from the motor or from an angular encoder mounted to the mirror.
- **Oscillating mirror**: With this technique the mirror is rotated back and forth. This has the effect of creating a "Z" or "zigzag" line of points on the ground.
- **Nutating mirror**: Rather than moving a mirror to project the laser onto the ground, a small nutating mirror is used to direct a laser into a linear fiber-optical array. The array transmits the pulse at a fixed angle onto the ground.
- **Elliptical scanner**: This system employs two mirrors to move the laser along an elliptical path around the aircraft [100].

The advantages and drawbacks of the different scan patterns are summarized in Tab. 2.4.

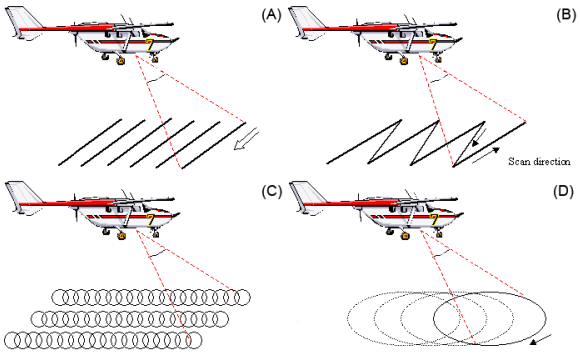

FIG. 2.8: Different scanning patterns: (A) Line scanner, (B) Oscillating mirror, (C) Nutating mirror, (D) Elliptical mirror (after [100]).

Scan Pattern	**Advantages/Drawbacks**
Line scanner	✓ Does not induce any systematic errors in the observation due to mirror acceleration/deformation. ✓ Regularly spaced sampling along and cross-track can be achieved. ✕ For a certain amount of time during each rotation, the mirror is not pointing at the ground and no observations can be taken. ✕ FOV is fixed and cannot be adapted. ✕ Are usually limited to lower flying heights (height above ground $< 1000\,\mathrm{m}$).
Oscillating mirror	✓ Mirror is always pointing towards the ground guaranteeing continuous data collection. ✓ FOV and scan rate can be controlled. ✓ It is possible to compensate for aircraft motion (roll compensation). ✓ Can be used for long ranges ($> 3\,\mathrm{km}$). ✕ Changing velocity and acceleration of the mirror cause torsion between the mirror and the angular encoder. ✕ Measured points are not equally spaced. The point density increases at the edge of the scan field where the mirror slows down, and decreases at nadir.
Nutating mirror	✓ With fewer and smaller moving parts, the scan rate can be greatly increased. ✓ Sufficient scan rate to guarantee overlap in the along-track position. ✕ FOV is mostly much smaller than for a rotating mirror. ✕ The across-track spacing is fixed.
Elliptical scanner	✓ Ground is often measured twice from different perspectives, thus allowing areas that were occluded on the first pass to be scanned. ✕ Increased complexity for system calibration due to two mirrors.

TAB. 2.4: Comparison of different scanning patterns.

2.4 Positioning Technology

2.4.1 GNSS Systems

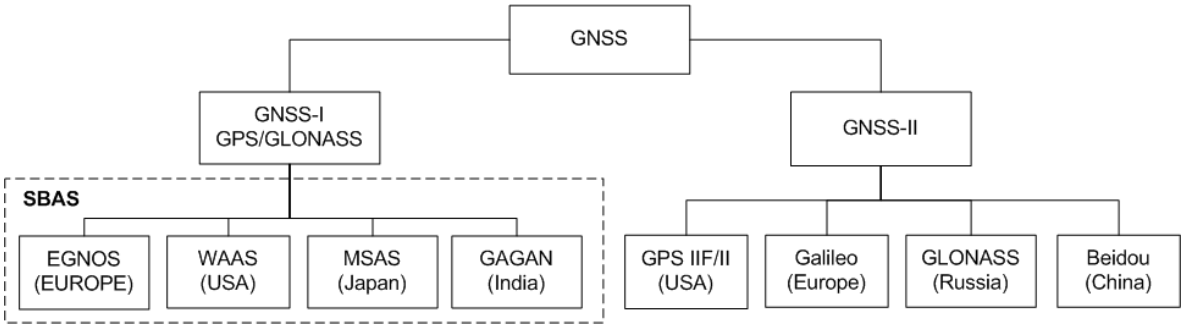

FIG. 2.9: Overview of Global Navigation Satellite Systems.

In general terms, a GNSS (Global Navigation Satellite System) estimates the absolute location of static and dynamic objects on earth, air and space using precise timing and geometric triangulation based on orbiting satellites [88]. GNSS systems can be characterized by a non-stop availability, providing accurate three-dimensional positioning for everyone equipped with the appropriate radio reception and processing equipment. At the present state, there a two world-wide functioning GNSS systems in operation:

- **Global Positioning System (GPS)**: The system was developed by the U.S. Department of Defense (DoD). The first satellite was launched in 1978 and the system was declared fully operational in 1995. The system can be divided into three segments: The user segment consists of the antenna and a receiver including a processor to compute the navigation solutions and to monitor the time shifts. The space segment is currently composed of 24 satellites, arranged in 6 very precise orbits each at an altitude of 20'200 km. The satellites send information to the receiver of their position with respect to the center of the earth, together with the time signal. The ground segment consists of several monitoring stations, where every satellite passes at least twice a day. These stations are equipped to calculate satellite positions with high precision and to uplink the corrected information to them.

- **Global Orbiting Navigation Satellite System (GLONASS)**: Its concept is similar to the GPS, albeit it employs different signal modulation and processing techniques. In 2008, GLONASS had 18 satellites in constellation, however some of them where in maintenance and therefore not available for the users. Although GLONASS in its present state cannot be used as a standalone positing system, most geodetic GPS receivers are able to receive GLONASS signals, hereby increasing the number of satellites. This is particularly beneficial for surveys in demanding topography [57].

The first generation satellite position systems (GNSS-I) are mainly controlled by military authorities. They are completed by four civil Satellite Based Augmentation Systems (SBAS) (see CHAP. 2.4.4) to improve the accuracy and integrity of the existing GNSS (see FIG. 2.9):

- The European Geostationary Navigation Overlay Service (EGNOS) with a core coverage area over Europe and the northern Africa
- The American Wide Area Augmentation System (WAAS) covering North-America
- The Japanese Multi Functional Transport Satellites (MTSAT) Satellite - Based Augmentation System (MSAS)
- The Indian GPS /GLONASS And Geo-Stationary Augmented Navigation (GAGAN)

The next decade will be marked by the appearance of a new generation of GNSS, called GNSS-II (see Fig. 2.9). Although the second generation systems are not yet (or only partly) operational, their arrival will have a huge impact on the RT positioning accuracy and reliability. GNSS-II will see the emergence of the first GNSS totally under control of a civil authority (GALILEO) and new carrier frequencies (e.g. L5 in GPS Block IIF) will improve the accuracy and availability of GPS positioning services for all users. A detailed overview of the GNSS-II systems can be found in [188].

2.4.2 GPS Signal

Every satellite within the GPS framework produces a fundamental frequency ($f_0 = 10.23\,\text{MHz}$), precisely timed by embarked high precision atomic clocks. Coherently derived from f_0 are (currently) two signals, the L1 and the L2 carrier waves generated by multiplying the fundamental frequency. These dual-frequencies are crucial for eliminating the major source of error due to signal propagation, i.e. the ionospheric refraction [53]. L1 and L2 are modulated by pseudo-random noise codes (PRN). The pseudo-ranges that are derived from the measured travel times between satellite and receiver use PRN that are modulated on L1 and L2, respectively. The C/A-code (coarse/acquisition-code) is modulated on L1 and is available for civilians, giving access to the Standard Positioning Service (SPS), whereas the P-Code (precise-code) is reserved for U.S. military and other authorized users. In addition to the PRN codes, a data message is modulated onto L1/L2, transmitting status information, satellite clock bias and satellite ephemeris data.

2.4.3 GPS Positioning Modes

Based on the requirement of the project in terms of accuracy, data disposability (RT or delayed) and the available equipment, GPS can furnish different positioning modes with different performances. Fig. 2.10 depicts the most important positioning techniques applied in the ALS context:

- **Single Point Positioning (SPP)** (② in Fig. 2.10) is based on phase-smoothed code measurements and is the most frequently used technology for RT positioning. Provided that SBAS corrections are available, this approach can deliver accuracies of a level of 1 to 4 m [14, 109, 187]. However, SBAS is not available worldwide and the reception of the correction signal emitted by the geostationary satellite (placed at the equator) can be difficult for regions in higher latitudes. In this case the **Standard Positioning Service (SPS)** (① in Fig. 2.10) has to be used that provides an accuracy of about 4 to 5 m [104].

- The availability of precise GPS satellite orbit and clock products (near-RT broadcasting of precise GPS ephemeris data) has led to the development of a novel positioning methodology known as the **Precise Point Positioning (PPP)** (③ in FIG. 2.10). This technique can achieve decimetric position accuracy [126, 139] when continuous signal tracking is possible and is available world-wide without need of any augmentation system.
- If at least five common satellites per epoch are available, **dual-frequency carrier-phase measurements** can be used to perform differential GPS (CP-DGPS). If applied in PP, no communication link has to be established, as the reference and rover data are processed as one. PP algorithms feature ambiguities recovery through forward/backward processing. Additional trajectory smoothing techniques, atmospheric modeling and clock bias estimation pull down the accuracy to a centimeter level for **kinematic processing** (⑤ in FIG. 2.10). For **static processing** (⑥ in FIG. 2.10), when respecting some considerations about baseline length and observation time, sub-millimeter accuracy can be achieved [87, 113].
- RT differential applications, such as **RT Kinematics (RTK)** (④ in FIG. 2.10) require a continuous data exchange between reference and rover, as the differential corrections are transmitted via some communication link. RTK is based on CP-DGPS, solving the ambiguities on-the-fly (see CHAP. 2.4.4). If the ambiguities are fixed correctly, sub-decimeter to centimeter accuracy can be achieved.

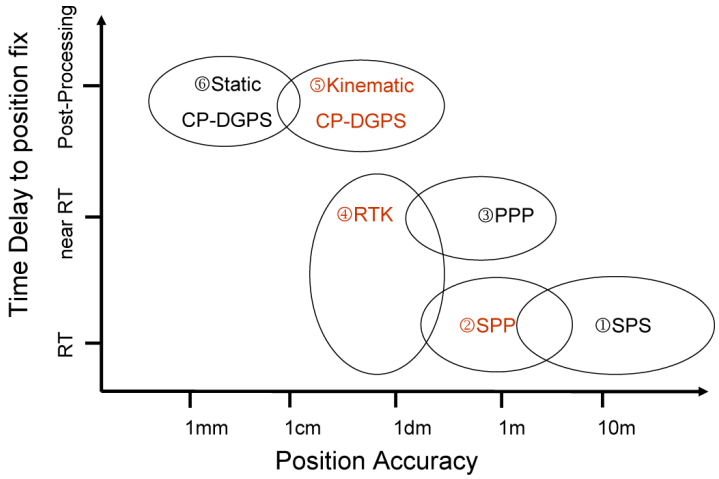

FIG. 2.10: Overview of GPS positioning methods with respect to their accuracy and time delay to position fix. Methods of particular interest within the ALS context are marked red.

2.4.4 GPS Quality Monitoring Techniques

In the ALS context, the position of the carrier is usually determined using dual-frequency GPS receivers and post-processed by CP-DGPS. This has the major drawback that during data collection, no information about the data quality can be provided. This implies that possible occurrences of local signal distortions or erroneous sensor behavior affecting both the GPS code and phase measurements remain undiscovered and become apparent only during

the PP step [130]. As a consequence, point-cloud accuracy degradation due to undetected GPS quality problems have either to be accepted or parts on the mission have to be re-flown, which rises the production costs.
To avoid such situations, the collected GPS data should either be processed in RT to solve the ambiguities on-the-fly or analyzed in RT in order to predict the likelihood of fixing the differential carrier-phase ambiguities in PP. The different methods and technologies to perform GPS quality monitoring, applicable in the ALS context, are presented in this section.

Observable based Indicators

The basic observations of GPS are the ephemeris informations, code pseudo-ranges, carrier-phases and Doppler measurements. Combinations of these can be used to construct RT quality measures for the positioning accuracy:

- **Satellite geometry**: Using the broadcast ephemeris of all satellites and the present rover location the current constellation and their associated dilution of precision (DOP) values can be computed. Together with the accuracy of a single pseudo-range measurement, expressed by the User Equivalent Range Error σ_{UERE}, the DOP parameters can serve to estimate theoretical horizontal and vertical position accuracies. Detailed information about the computation of DOP values and the associated accuracy measures can be found in [135]. Their applicability for the prediction of the fixability of ambiguities in PP is limited, as these indicators do not consider any signal disturbance on the carrier phases. Nevertheless, a good satellite geometry is a prerequisite for ambiguity validation.

- **Signal-to-noise ratio (SNR)**: The relevance of the SNR and satellite elevation as quality indicators for GPS observations has been emphasized by many authors (e.g. [42, 79]). The relationship between SNR or Carrier-to-Noise density ratio (C/N0) and multipath, which is a major problem in precise GPS positioning, is well known. Accordingly, the SNR value can be directly deployed as a quality measure of the individual GPS phase values [50].

- **Cycle slip detection**: The use of carrier-phase measurements implies the resolution of the ambiguities. If a loss of lock of the signal occurs simultaneously on several satellites, the ambiguity resolution has to be started again. Cycle slips are very frequent in the context of airborne mapping and can occur in cases where tracking is interrupted by shadowing, weak satellite signal (low SNR), rapid change in dynamics or due to atmospheric effects. As a consequence adjacent carrier-phase observations jump by one or more cycles and the integer ambiguity parameter has to be re-estimated. To identify cycle slips, the velocity trend method, as proposed by [195], can be used:

$$\Delta_t N_i = \Delta_t \Phi_i - \int_{t_{i-1}}^{t_i} D_i dt + \epsilon \tag{2.4.1}$$

  where the ambiguity time difference ($\Delta_t N_i$) can be computed as the temporal difference between the phase ($\Delta_t \Phi_i$) and Doppler observations (D_i).

- **Phase tracking loop output analysis**: Situations where the phase tracking loop is not able to maintain the lock are important to detect. L2 is generally more affected by loss of lock, because of the lower transmitting power on L2 and absence of the C/A code on this frequency.
- **Interference detection**: GPS receivers are vulnerable to Radio-Frequency (RF) interference. The latter can result in degraded navigation accuracy or complete loss of signal tracking [62]. RF interference detection is of particular interest in the airborne mapping context since avionic equipments, rotor rotation and cellular phones constitute potential interference sources that degrade satellite signals. RF interferences have effects on code correlation and loop filtering functions by reducing the C/N0 of all the GPS signals. In other words, they have the same effect as signal blockage, foliage attenuation, ionospheric scintillation and multipath, which are all factors that reduce the effective C/N0 of the GPS signals. Accordingly, C/N0 values can be used to detect possible interferences.

GPS Augmentation Systems

Within civil aviation much effort has been undertaken to develop techniques providing integrity information for airborne use of GPS. Augmentation systems enable the improvement of the RT GPS positioning (i.e. accuracy, integrity, continuity and reliability) through integration of additional information. Several systems exist and are usually classified based on how the GNSS sensor receives this additional information [165]:

- **Ground Based Augmentation System (GBAS)**: GBAS are local Differential GPS systems (DGPS) transmitting differential corrections to the users. The corrections are computed using accurately surveyed ground stations. After the processing, the corrections are directly sent to the users by radio transmitters operating in the Very High Frequency (VHF) or Ultra High Frequency (UHF) bands. Other GBAS approaches are based on ground-based pseudo-satellites (pseudolites) that send GPS signals. By combining them with a classical DGPS reference station, the number of signals can be increased, adding at the same time precision and integrity check capabilities.
- **Aircraft Based Augmentation System (ABAS)**: One functional principle of ABAS is to compute the integrity information using Receiver Autonomous Integrity Monitoring (RAIM) functions. RAIM is a user-based integrity enhancement technique based on redundant code observations. If more than 5 satellites are available, RAIM allows detecting anomalies and removal of faulty satellites from the navigation solution, the so-called Fault Detection and Isolation (FDI). RAIM also provides precious information about the state/quality of the constellation that can be used for GPS quality prediction. More details about RAIM algorithms can be found in [180].
- **Satellite Based Augmentation System (SBAS)**: SBAS are systems that support wide-area or regional augmentation through the use of additional satellite-broadcast messages. Due to the size of the covered area, SBAS systems must send differential corrections based on spatial and temporal modeling. Similarly to the GBAS, the corrections and the integrity information are computed by ground based stations and then

sent via geostationary satellites to the users. The user specific corrections are computed by interpolation functions.

Real-time Kinematics (RTK)

RTK-GPS positioning offers the possibility to provide on one side RT information on the ability to resolve the ambiguities, on the other side a high-accuracy navigation solution usable for DG of the laser point-cloud. The base receiver measurements and coordinates are formatted and transmitted via a communication link to the rover receiver. This enables the operator to be aware of the quality of the RT GPS position through three basic status:

- **Fixed position**: The RTK engine is capable of resolving correctly the ambiguities on the baseline. The expected position accuracy is below decimeter level and the data can be used further for DG of the ALS data.
- **Float position**: Due to poor GPS constellation, cycle slips or long baseline, the estimated ambiguities on the baseline cannot be fixed. Compared to the fixed status a accuracy deterioration has to be expected. Such data does not meet the requirements for high accuracy ALS applications.
- **Standalone position**: The rover cannot communicate with the base and no differential GPS computation can be carried out. The computed position equals to that of a standalone receiver solution.

RTK Communication Link. The nature of communication link (see Tab. 2.5) dictates the maximal distance from the rover to the base station(s) as well as the amount of data that can be transmitted. For classical RTK applications (stake-out, stop-and-go), often radio transmission is used. In the ALS context however, the range of operation becomes quickly limited by the transmission power (legally) possible.
The limiting factor for GSM is the low data-rate of about 9.6 kps; this corresponds to 5 Hz of dual-frequency measurements from one reference station [152]. Additionally, GSM is a bi-directional point-to-point communication on a reserved channel. This complicates the transmission of GPS corrections to several receivers. [148] also mentions the problems related to cell registration and hand-over, that might be problematic for fast moving carriers, such as aircrafts.
GPRS (General Packet Radio Service) is available on almost all GSM networks and allows much higher data throughput rates. The more recent UMTS technology can handle even larger data rates. However, the transmission is handled in "bursts" of packets resulting in varying latency [157], therefore UMTS is less suitable for RTK than GPRS. The major drawback of these mobile phone network based technologies are the high communication costs and the reduced spatial availability of these services, as mobile network coverage quickly decreases in rural or inhabited areas.
The principle advantage of satellite communication based on Low Earth Orbiting (LEO) satellites is their spatial availability, but the cost and power consumption of SatCom modems is approximately ten times higher than for GPRS modems.

	Radio	GSM	GPRS	UMTS	SatCom
Proprietary	+	+/-	+	-	+/-
Data rate	+	-	+	+	-
Availability	+	-	-	-	+
Range	-	+	+	+	+
Cost	+	-	-	-	-

TAB. 2.5: Appropriateness of communication links for transmission of GPS corrections and integrity informations in the ALS context.

RTK Networks. The last decade has seen the emergence of permanent GPS networks that broadcast RT corrections via GPRS (e.g [47]). Many of these networks incorporate the Virtual Reference Station (VRS) approach, where the corrections are interpolated from the three closest permanent stations to generate a virtual base close to the rover [118]. FIG. 2.11 depicts the general architecture of the Swiss Automated GNSS Network (AGNES), that was used for several tests within this thesis (see CHAP. 7.1.2). The spatial availability and quality of these permanent networks is growing quickly, thus enabling RTK for helicopter-based ALS missions, at least in central European milieu [129].

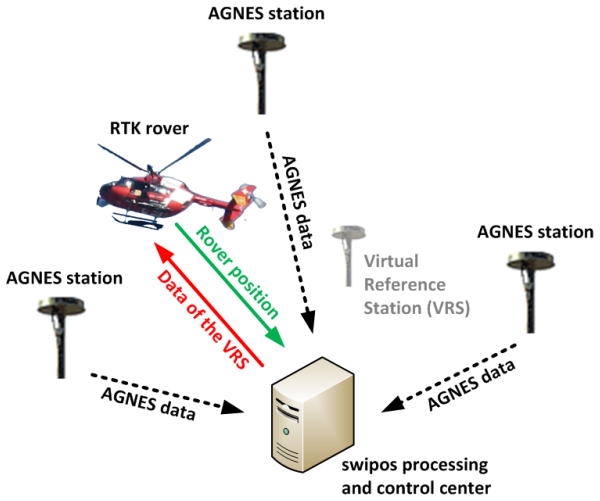

FIG. 2.11: Architecture of AGNES RTK network using VRS.

2.5 Integrated Navigation Technology

This section introduces the concepts of inertial navigation, the used inertial sensors and the GPS/INS coupling techniques to provide a final trajectory including position and attitude, inalienable for georeferencing the scanner measurements.

2.5.1 Inertial Measurement Units

Inertial measurement units (IMU) are normally made up of three orthogonally mounted accelerometers and gyroscopes, each of them measuring the specific force and the angular

rate, respectively, in one orthogonal direction. In the context of DG, their primary role is in the determination of orientation and the improvement of the position in higher frequencies of the motion.

Sensor Accuracy

The spectrum of different inertial technologies, costs and achievable accuracies is very large. In order to classify inertial systems they are normally divided into three main categories (see TAB. 2.6) based on the position error accumulated after 1 hour (expressed in nautical miles/hour) of standalone dead-reckoning [45]:

- **Navigation grade**: Navigation-grade instruments accumulate a position error of about 1 nmi/h. These systems could be used for standalone inertial navigation over several minutes.
- **Tactical grade**: Instruments in this category may accumulate as much as 10 to 20 nmi/h. The performances are good enough to perform unaided dead-reckoning up to one minute. Due to their relative low cost paired with the capability to bridge GPS outages, these instruments are the most frequently used in the context of INS/GPS navigation for airborne mapping.
- **MEMS**: Instruments of this category cannot be used for standalone navigation, as the accumulation error exceeds already several nautical miles after one minute. In combination with other sensors and regular position update, GPS/MEMS integration can provide sub-decimeter position accuracies and sub-degree orientation accuracies (e.g. [188]). However, these accuracies are yet not good enough to be used for DG of ALS data, but due to their low cost and increasing accuracy, this may become an interesting alternative for mobile mapping within a near future [44, 134, 163].

Grade	MEMS	Tactical	Navigation
Gyro drift [deg/hr]	> 100	0.1 - 10	0.005 - 0.01
Accelerometer bias [m/s^2]	0.05 - 0.5	$2 - 5 \cdot 10^{-3}$	$5 \cdot 10^{-5}$
Price (€)	> 100	> 40'000	> 100'000

TAB. 2.6: Sensor accuracy and price for MEMS, tactical and navigation grade IMU's (after [188]).

Strapdown Technology

During decades, inertial sensors were mounted on stabilized (or gimbaled) platforms, thus mechanically isolated from the rotational motion of the carrier. The advances in digital processing made it possible to avoid gimbaled mounts: Nowadays, the inertial sensors are rigidly mounted (strapped down) to its casing, hereby decreasing the complexity and cost of INS while increasing the dynamic range of motion that can be tracked. The resulting systems are much cheaper and smaller (less mechanical parts) and excel with higher reliability, however penalized by an increased computational complexity and higher INS data rates [167]. Such strapdown systems opened the field for building light weight and compact ALS systems, that can be embarked on a helicopter without particular infrastructure [179].

2.5.2 GPS/INS Integration

Complementarity

GPS/INS integration can be seen as a self-calibration technique for the gyros and a high-frequency interpolator/smoother of the GPS position. The positioning accuracy of a mid-grade IMU operated in an unaided mode degrades very quickly due to time-dependent systematic error behavior. Therefore, even the good quality tactical-grade IMU's cannot be used as standalone systems for DG applications. However, within a short period of time, during which the error growth is still limited, standalone inertial navigation can deliver relative positioning accuracy of CP-DGPS level. As it can be seen in TAB. 2.7, GPS and INS have a very different but complementary behavior. Their error spectrum is partially uncorrelated, making them to ideal synergistic partners [146]. The GPS data allows confining the effects of the systematic errors in inertial data, while the INS data is capable of bridging the GPS outages (i.e. due to signal blockage, jamming or spoofing) and smoothing the short-term fluctuations (e.g. due cycle slips, constellation change, etc.) of the GPS position accuracy. The integrated trajectory therefore represents the most optimal solution in terms of position and attitude accuracy and can be outputted at data rates reflecting the whole spectrum of aircraft motion.

INS	CP-DGPS	GPS/INS
✓ Self contained and independent system	✕ Dependent on satellite reception	Needs periodic satellite reception for initialization and calibration of IMU errors
✓ Signal continuity	✕ Signal reception could be interrupted	Continuous solution
✓ High short-time/relative accuracy for position and velocity	✓ High long-time/absolute accuracy for position and velocity	High accuracy for position and velocity
✓ High short-time/relative accuracy for attitude	✕ No attitude information available[a]	Precise attitude determination
✕ Sensor errors grow with time	✓ Almost time-independent error behavior	Uniform accuracy over time
✕ Influenced by gravity field	✓ Insensitive to local gravity anomalies	Gravity anomalies are leveled out

[a] Attitude could be computed using an array of GPS antennas

TAB. 2.7: Complementarity of GPS and INS

Integration Schemes

The most common integration approach is the so-called **loosely coupled integration** (see FIG. 2.12). The raw IMU measurements (specific force $\mathbf{f}_b$ and angular rates ω_{ib}^b) are integrated (also called strapdown mechanization) to yield position and attitude ($\mathbf{r}_{INS}, \theta_{INS}$) at the IMU output rate (normally 100 to 400 Hz). The position and velocity data ($\mathbf{r}_{GPS}, \mathbf{v}_{GPS}$) gathered by GPS is processed independently, yielding a sequence of positions and velocities at a certain frequency (normally 1 to 2 Hz). This data is subsequently feed as updates within an Extended Kalman Filter (EKF) to derive differences in velocity and position ($\Delta\mathbf{r}, \Delta\mathbf{v}$).

These updates are used to estimate the elements of the filter state vector, containing on one side the error states related to the trajectory (i.e. position $\delta\mathbf{r}$, velocity $\delta\mathbf{v}$ and orientation $\delta\theta$) and on the other side those related to the inertial sensors themselves (i.e. gyro drifts $\delta\mathbf{b}_g$, accelerometers bias $\delta\mathbf{b}_a$).

Another approach is the **tightly coupled integration**, where the GPS raw measurements (normally double-differenced ambiguities and Doppler measurements) and the inertial data are feed into a common filter. In this case, GPS measurements can be used in the filter to correct the INS errors even if the number of visible satellites is not sufficient to compute an independent GPS position (below 4). Accordingly, this integration scheme is advantageous for environments with reduced GPS signal receptions (e.g. urban canyons), and is commonly used for terrestrial mobile mapping systems (e.g. [44]). A good comparison of the performances of the two presented integration schemes can be found in [192].

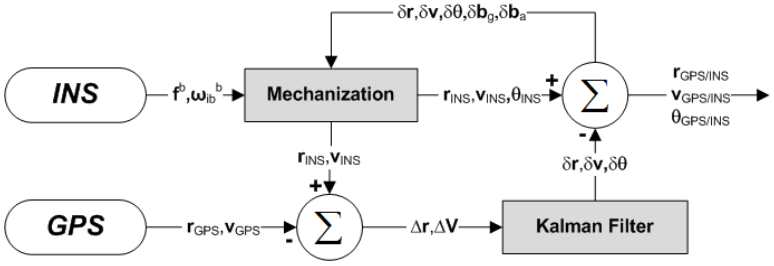

FIG. 2.12: Example for loosely coupled EFK integration scheme.

2.5.3 IMU Alignment

The alignment process determines the initial orientation of the IMU. It precedes every survey mission and is generally done in two stages [144]:

- **Coarse alignment:** For static coarse alignment the approximate attitude parameters are estimated using the raw sensor output assuming that nothing but the Earth rotation and the gravity are measured (so-called accelerometer leveling and gyro-compassing). Dynamic coarse alignment is using GPS position and velocity data within parts of a flight with constant heading and speed (thus minimal kinematic acceleration), to deduce the yaw angle. Roll and pitch are estimated based on the inertial data.
- **Fine alignment**: The information of the coarse alignment is refined using a Kalman filter with the misalignment states and external observations (e.g. GPS position/velocity) as updates.

Static IMU alignment is somehow problematic for inertial systems with poor accuracy (i.e. low-cost IMU's), because the level of the gyro drift risks to mask completely the needed signal from the Earth rotation ($15°/h$). Generally, to better separate the inertial errors and specially the heading uncertainty, it is advised to proceed dynamic maneuvers (e.g. step curves in figure-eight pattern) within the flight alignment. This enables to observe the misalignment uncertainties through the velocity errors and to estimate the errors in all channels by using a filter with DGPS velocity and position updates [145].

2.5.4 GPS/INS Quality Monitoring

Inertial systems are integrated with GPS to bound the rapid accumulation of systematic inertial errors. The integrated system can bridge gaps in the GPS observations and smooth its short-term quality fluctuations. However, depending on the flight dynamics (such as strong vibrations or long near-static phases) and on the abundance of GPS gaps, the accuracy of trajectory estimated by GPS/INS integration will not be sufficient. One may also encounter a measurement failure or degradation of one of the components of the IMU (gyros or accelerometers). As there is no sensor redundancy within the IMU, a wrong measurement on one of these sensors may result in situations where the trajectory cannot be computed anymore. Moreover, also classical GPS/INS integration provides little redundancy and cannot be considered as a good method for Fault Detection and Exclusion (FDE) due to the following reasons [148]: Firstly, GPS and inertial sensors do not sense the motion dynamics in the same spectral band. Second, the integration is normally performed using a Kalman-Filter that is designed to trust the inertial sensor more than the GPS in case of an unpredicted disagreement. There exist, however, several theoretical approaches to overcome these problems:

- **Sensor redundancy**: A redundant IMU is composed of more than three accelerometers and gyros. Thus, it becomes possible to combine the inertial observations to generate new "synthetic" measurements, or to modify the mechanization equations to account for the observation redundancy. Although very popular for increasing system reliability in avionics [98], the method is novel in the context of DG [23, 48, 189] and not yet exploited in commercial systems.
- **Fault detection via Kalman Filter (KF)**: The chosen architecture of a KF not only has an impact on the optimal parameter estimation but also on the capability for FDE. Organizing the integration through decentralized and federated filtering, where every sensor or subsystem has its own KF, allows fault detection by comparing the outputs of these different sub-KF (e.g. [25, 95]).
- **Artificial Neural Networks**: In the recent years Artificial Neural Networks (ANN) have been used for the GPS/INS modeling and fault detection. ANN are trained directly with the data and extract the essential characteristics without implicitly knowing the underlying physical mathematical model. The disadvantage of this concept is the dependency of representative training data for different motion scenarios and that any deviation of these trained scenarios may trigger an alarm that could be considered as a fault [103].

Mainly due to economic reasons, these INS quality monitoring principles have not yet found their way into commercial ALS systems. However, the rapid evolution of inexpensive MEMS sensors (close to tactical-grade accuracy) may remove such constraints. This will enable the development of redundant DG systems capable of detecting faults in the inertial data.

Chapter 3

ALS System Calibration and Point-cloud Processing

ALS data is prone to be affected by systematic errors that often originate from inaccurate and incomplete system calibration. This chapter discusses the most important system calibration steps together with their impact on the final data accuracy. In the following, the basic principles for point-cloud processing, such as strip adjustment, point-cloud classification and digital elevation model generation are presented.

3.1 System Calibration

The accuracy of a final ALS point-cloud is the sum of all accumulated errors throughout the entire processing chain of DG. Achieving the highest accuracy requires therefore that all components of an ALS system are correctly calibrated (see Tab. 3.1). One can distinguish three main types of calibration:

- **Sensor Calibration**: Each individual sensor of an ALS system must be calibrated. For example, the scanning device itself is subject to internal error sources, such as the range-finder error, the encoder angle error, encoder latency or scanner torsion. In general, these parameters are calibrated by the manufacturer and are supposed to be stable in time. A detailed overview of these internal scanning errors can be found in [65, 100]. Also some elements of the INS have to be pre-calibrated. Depending on the IMU-type, this may represent axis non-orthogonalities or major parts of the scale factors and bias errors. The residual errors are time-variant and their values have to be re-estimated after every flight via the state vector modeling and the Kalman filter.
- **System Mount Calibration**: The involved sensors in an ALS system cannot physically all have the same origin and same alignment. These spatial and orientation offsets must be calibrated after every new installation of the system or its components. They should, however, remain stable within one configuration. The determination of these quantities will be discussed in the following sections. Also in this category falls the time synchronization of the involved sensors. The data of the individual sensors can only be

merged if they are time-tagged in a common time frame (often GPS time). In most cases the synchronization scale is governed by a regular pulse-per-second (PPS) signal emitted by one of the sensors (normally GPS), while the time offset is communicated with a message (i.e. NMEA/ZDA) over serial or other interface (e.g. [26, 160, 174]).

- **Strip adjustment**: Even if the system is perfectly calibrated, differences between overlapping sections of data (strip overlaps) may occur due to undetected or uncompensated systematic effects in trajectory determination. Strip adjustment procedures will be discussed in detail in Chap. 3.2.

Calibration	Time Dependency	Calibration Frequency	Calibration Mode
Scanner	Stable	At assembly or at the first mount	Laboratory or within test flight
INS	Random within bounds	At assembly and for every mission	In-flight calibration
GPS/Scanner/INS leverarm	Stable within the same installation	At new system mount	Pre-flight calibration (lab and/or field)
Scanner/INS boresight	Stable within the same installation	At new system mount	In-flight calibration
Strip differences	Time-variant	For every mission	In post-processing

Tab. 3.1: Overview of different calibrations involved in ALS.

3.1.1 Boresight Calibration

The most critical part in ALS system calibration is the angular misalignment (or boresight) between the scanner (s-frame) and the INS system (b-frame). Besides some cardinal rotation, also known as the mounting matrix ($\mathbf{T}_s^b$), these angular displacements should be small ($< 1°$). Hence, the boresight matrix $\mathbf{R}_s^b$ can be modeled as a skew-symmetric matrix with the remaining misalignments in roll(e_x), pitch(e_y) and yaw(e_z):

$$\mathbf{R}_s^b = \begin{pmatrix} 1 & -e_z & e_y \\ e_z & 1 & -e_x \\ -e_y & e_x & 1 \end{pmatrix} \mathbf{T_s^b} \tag{3.1.1}$$

The influence of the misalignment in roll, pitch and yaw is illustrated in Fig. 3.1. The misalignment between the laser and the IMU causes each laser observation to be registered with an incorrect attitude. A roll error causes a slant range to be incorrectly registered. The resulting elevation differences increase with the scan angle. The pitch error results in a tilted range to be recorded as nadir. As the slant range is normally longer, the entire strip tends to be pushed down. The yaw error induces a skewing in each scan line, namely in the horizontal coordinates.

The impact of these errors is only visible in overlapping ALS data. When profiling across areas with elevation gradients (such as tilted roofs), some inconsistencies between different strips can be revealed. Fig. 3.2 shows a cross-section of a building covered by 8 flightlines,

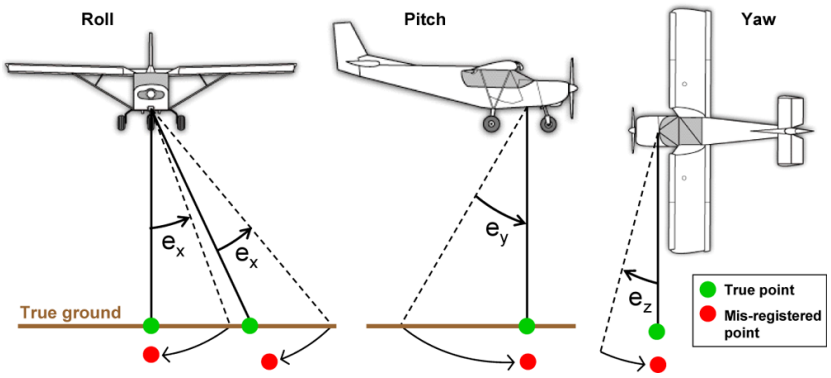

FIG. 3.1: Point registration errors due to boresight misalignment (adapted after [101]).

flown in a cloverleaf pattern at different flying heights. The discrepancies due to roll errors (FIG. 3.2.A) are clearly visible on the inclined and horizontal planes. The errors due to pitch (FIG. 3.2.B) are not apparent in horizontal planes; however, they have an opposite effect on inclined planes, where the displacement can be depicted. The influence of the heading error (FIG. 3.2.C) is much harder to assess within a profile, as the influence is only noticeable at the outer bounds of the swath.

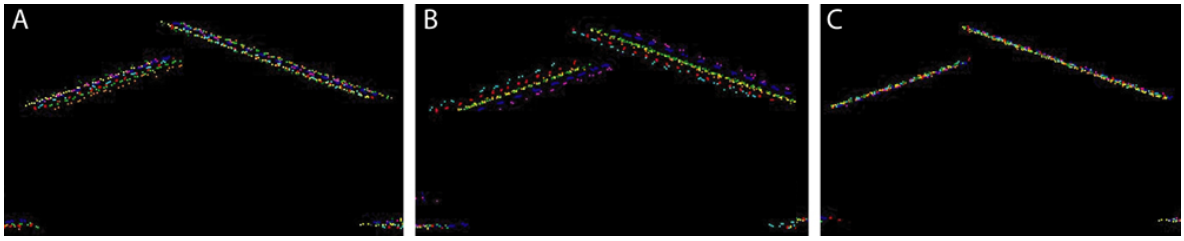

FIG. 3.2: Visibility of boresight angles on a cross-section plotted separately for roll (A), pitch (B) and yaw (C) for 8 different strips with different flying heights and directions.

Unlike photogrammetry, ALS boresight errors affect each laser observation individually and can therefore not be removed by applying e.g. a simple affine transformation to an entire strip. The differences must be modeled by observing the induced errors in the position of some control points or on common features (e.g. surfaces).
The adopted approaches for boresight calibration are manifold: [132] proposes a calibration method based on physical boundaries or cross-sections, that has found its way into ALS industry (e.g. [105]). [18] presents a method based on slope gradients, this method is implemented in one of the most popular software packages for ALS data handling [162]. However, these calibration procedures based on slope information, although very popular, are recognized as being sub-optimal since they need human interaction, are non-rigorous and provide no statistical quality assurance measures [154]. Additionally, they are not able to properly recover the misalignment in yaw.
More rigorous calibration procedures have emerged in the last few years, modeling the systematic errors directly in the measurement domain [35, 37, 39]. The so-called LIBOR approach is a rigorous method for estimating the boresight angles and the range-finder offset [154]. The technique is based on expressing the system calibration parameters within the

DG equation separately for each target point, and conditioning a group of points to lie on a common surface (normally a plane). The plane parameters are estimated together with the calibration parameters in a combined adjustment model that makes use of GPS/INS-derived position and orientation as well as the range and encoder angle measures.
Based on the LIBOR-algorithm, [156] presents a methodology that directly identifies points belonging to a same plane and finds class-correspondences among the flightlines (see Fig. 3.3). These point clusters are directly fed into the LIBOR-algorithm, yielding a fully automated procedure for boresight calibration with accuracies at 1/1000°-level.

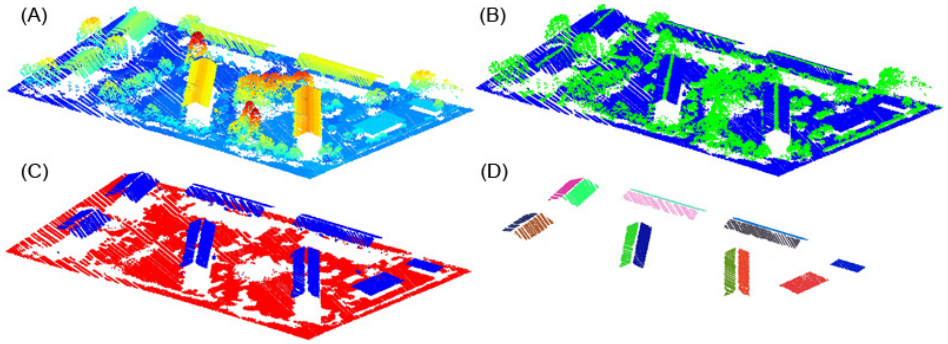

Fig. 3.3: Automated plane detection for LIBOR boresight estimation: (A) Raw point-cloud, (B) Classification of vegetation points, (C) Classification of ground points and roof detection, (D) Roof groups clustering.

3.1.2 Leverarm Calibration

In a standard ALS system two leverarms have to be determined. First, the eccentricity between the center of the IMU and the scanner origin (denoted $\mathbf{a}_s^b$) has to be estimated. This displacement is normally very small, as the IMU and the laser scanner are mounted very close to each other. Moreover, they may be hidden in one black-box (see Fig. 3.4). Hence, this leverarm is normally evaluated by the manufacturer. Secondly, the leverarm between the GPS antenna and the IMU navigation center (denoted as $\mathbf{a}_{GPS}^b$) needs to be determined by the system user. Depending on the installation, the eccentricity can be important ($>$ 1 m). Hence, an accurate determination of the GPS/INS leverarm is important for the overall system accuracy.

The influence of the leverarm can be properly modeled and thus theoretically calibrated within the EKF. However, due to correlations with other parameters, such approach cannot match the accuracy of a determination by independent means [155]. The most reliable and accurate way to observe this leverarm is tachometry (i.e. total station), assumed that the GPS phase center and the IMU navigation center are identifiable and visible. Spatial offset calibration is rather complicated when the respective sensor centers are not or badly visible, or, like in the case of an airplane, the GPS antenna is placed on the fuselage while the scanner/IMU are placed inside the plane. Additionally, the GPS/INS leverarm has to be correctly expressed in the b-frame, which implies that the relative orientation of the IMU with respect to local frame, in which the leverarm needs to be surveyed, is known.
Fig. 3.4 demonstrates a possible solution to overcome these problems by joint GPS and

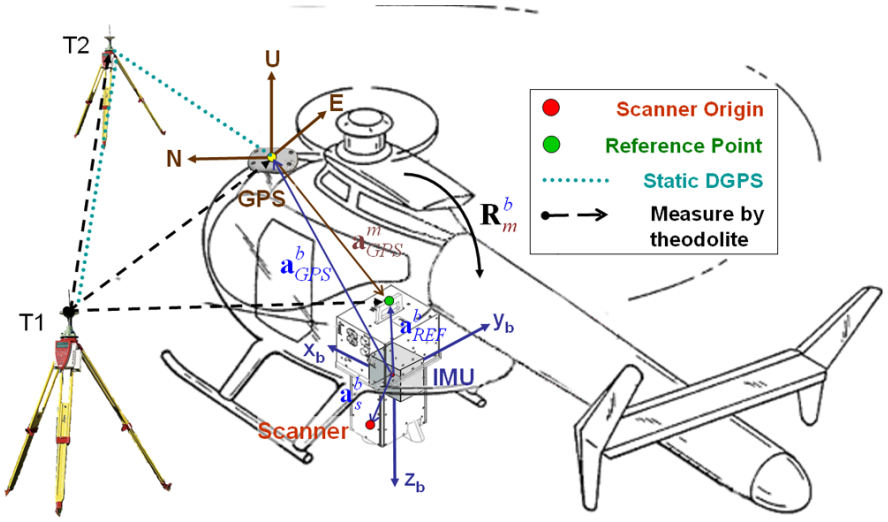

FIG. 3.4: Possible procedure for GPS/INS leverarm calibration.

tachometric observations. A common local frame is established by two total stations (T1 and T2), that are placed such as from at least one of them the defined reference point on the sensor head can be seen directly (eccentricity $\mathbf{a}^b_{REF}$ defined by the manufacturer, because the IMU navigation origin is generally not visible from the outside). Subsequently, this reference point is surveyed by tachometry in the mapping frame defined by T1 and T2. The relative coordinates of the GPS antenna phase center between T1 and T2 are obtained by static CP-DGPS. This defines the rotation between the arbitrary mapping frame and the local-level frame ($\mathbf{R}^l_m$). The rotation matrix $\mathbf{R}^b_l$ between the IMU body-frame and the local-level frame can be recovered either after some static alignment phase or, even better, after landing, when the INS is well aligned dynamically. Subtracting the coordinates for the reference point and the GPS antenna (both expressed in a local m-frame) yields $\mathbf{a}^m_{GPS}$, so the GPS/INS leverarm can be computed as follows:

$$\mathbf{a}^b_{GPS} = \mathbf{a}^b_{REF} - \mathbf{R}^b_l \mathbf{R}^l_m \mathbf{a}^m_{GPS} \tag{3.1.2}$$

The outcome of such calibration procedure normally delivers sub-centimeter accuracy for the eccentricity vector, what is fair in the context of ALS.

3.2 Strip Adjustment

Even after ALS system calibration, differences in strip overlaps can still occur [37]. This either originates from residual calibration errors inducing systematic effects (e.g. bad determination of yaw angle in boresight) or from dynamically changing effects (i.e. non-sufficient IMU alignment, changing GPS accuracy within a flight). If these offsets cannot be modeled and recovered correctly, a seamless and homogeneous dataset cannot be achieved (see e.g. FIG. 3.5). This leads to height models affected by e.g. sudden jumps (steps) along strip borders [117].
Due to the different origins the correct modeling and recovery of the strip discrepancies is far

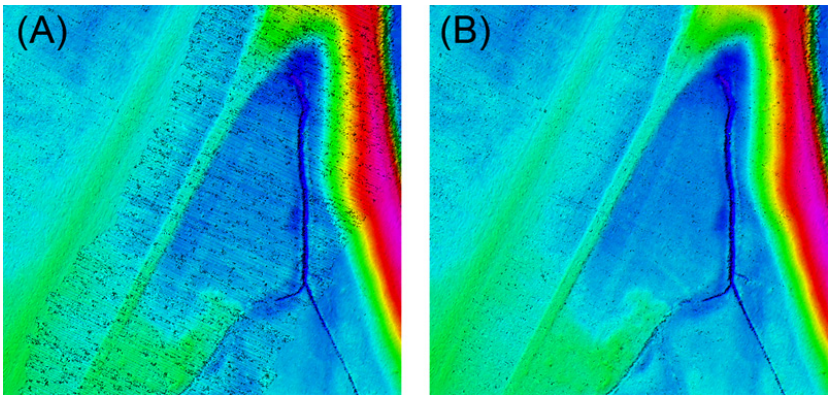

FIG. 3.5: Hillshaded DSM TIN: (A) No strip adjustment, (B) With strip adjustment.

from a trivial task. Based on the type of input data, current strip adjustment methods can be divided into two main approaches:

- **Data-driven calibration**: First generation strip adjustment algorithms are one-dimensional adjustment procedures, as they consider only shifts in height [61, 70, 181]. Their implementation is generally based on reference features (control or tie objects) in flat horizontal surfaces, where the height offsets are noticeable, well defined, and easy to measure. However, planimetric offsets in the data may not be entirely compensated. To recover full 3D displacements, other methods are based on surface least square matching (LSM). The LSM is either applied using a TIN surface [93] or a regular raster [18, 73, 194]. [16] proposes a method based on the comparison of each laser strip with a photogrammetrically derived DSM, and on the modeling of the discrepancies between these two datasets.

- **System-driven calibration**: [35, 36] propose a model to eliminate the systematic errors by constraining the laser points to a surface. The error recovery model is based on modeling the system errors and their effect on the georeferencing of the laser point. A similar approach is presented by [154] where the laser points are conditioned to lie on a common planar surface patch without need to know the true surface position and orientation. However, system driven solutions have a major drawback as they require system observations (i.e. trajectory, range, encoder angle) as an input. Often these observations are not available to the end-user. To overcome this problem, [117] presents a strip adjustment method that models the discrepancies by strip-wise 3D shift, roll and affine yaw parameters without requiring GPS/INS-trajectory data.

Despite the large number of different strip adjustment procedures, several processing steps are common to the majority of these procedures:

- **Selection of strip overlap**: Finding areas with data from several flightlines is rather trivial. However, the process to automatically identify zones suitable for strip adjustment, such as zones with clearly distinguishable surface patches that vary in orientation and slope (see FIG. 3.6), remains very challenging.

- **Determination of discrepancies based on selected features**: Based on the feature type (point, line, surface) used for the strip matching, the translations (1D or 3D, for some methods also rotations) can be computed.
- **Application of the corrections to the data**: For data-driven methods, the corrections are applied directly to the point-cloud, typically by applying a 3D similarity transformation, whereas for system-driven methods the translations can be feed back into a refined sensor model used to reprocess the entire point-cloud.

An exhaustive overview of common strip adjustment procedures and their application can be found in [136].

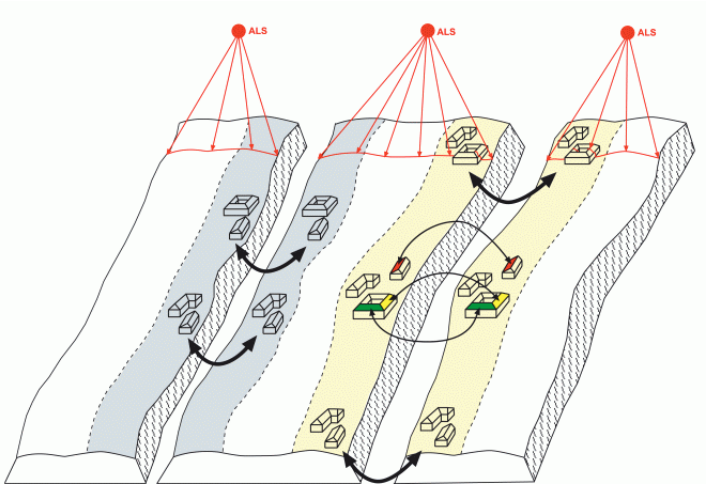

FIG. 3.6: Principle of strip adjustment (after [182]).

3.3 ALS Point-cloud Data Processing

3.3.1 Spatial Data Indexing

With the rapidly increasing size of the point-clouds, efficient data mining, querying and processing have almost become unfeasible without pre-ordering the unorganized raw point datasets along a spatial dimension (spatial indexing). It is always possible to perform any query by a "brute-force" process, e.g. computing the distances between the query point and each of the other data points. Such operations result in high computation time that are growing quadratically with data size ($O(n^2)$). A possibility to increase the query speed is to use tree structures to index the data, as for example the kd-tree originally proposed by [13]. At each node of the tree, the data space is split with a hyperplane along one of the basic dimensions (see FIG. 3.7). This procedure allows reducing the computation and query time to ($O(n \log n)$). The computation time can even be reduced further [97]: Instead of finding e.g. the exact k-nearest neighbors, the ϵ-k-nearest neighbors suffice. This so-called approximate nearest neighbor search was first introduced by [6]. This algorithm was implemented in an open-source C++ library called ANN [102], which has been used as tool for spatial indexing and querying of laser data throughout all developments presented in this thesis.

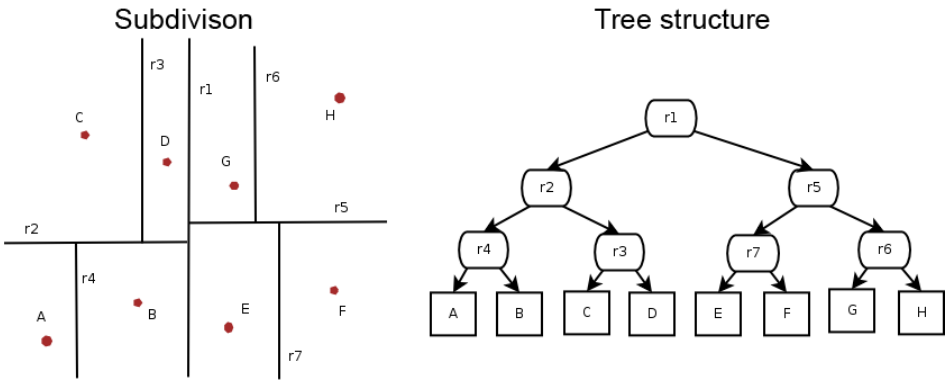

FIG. 3.7: Example of building up a kd-tree in 2D.

3.3.2 Co-registration

The co-registration of different point-clouds is a very common task in TLS/ALS point-cloud processing. Most of the time the Iterative Closest Point Algorithm (ICP), first presented by [15], is used for this purpose. The ICP algorithm uses distance metrics (such as closest point) between two datasets to be co-registered. For example, a 3D rigid body transformation could be applied between the corresponding data to determine translations and rotations iteratively. To support computing efficiency, a kd-tree structure is used for finding closest points. The target function of the ICP algorithm can be expressed in a general form as:

$$\min_{(\mathbf{R},\mathbf{T})} \sum_{i} \|M_i - (\mathbf{R}D_i + \mathbf{T})\|^2 \tag{3.3.1}$$

where i refers to the corresponding (closest) points of the datasets M (model) and D (data), $\mathbf{R}_{3\times3}$ is a rotation matrix and $\mathbf{T}_{3\times1}$ is the translation vector. The main advantages of the ICP when dealing with ALS point-cloud co-registration are:

- No need for point-to-point correspondence: Point-clouds to be co-registered may be very different in sampling rate and scan pattern. As long as the local geometry is well represented in both datasets, ICP is invariant to such differences.
- Robust performance for surfaces with moderate complexity and high data overlap.
- Can be parametrized to search either only for translations (planimetry, altimetry, 3D), only rotations or all together.

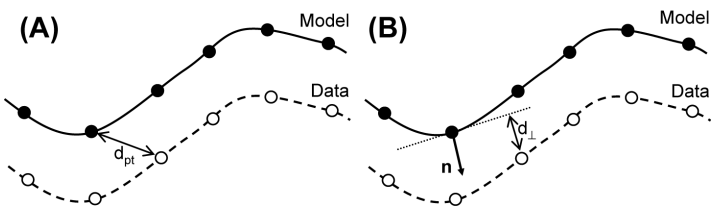

FIG. 3.8: Difference in distance metrics formulation: (A) Closest point, (B) Normal shooting.

However, searching for the best correspondence by minimizing the sum of the square distances metric sometimes leads to problems in convergence speed, accuracy and reliability of the resulting transform. To mitigate these problems, [21] proposes to replace the distance metric by a distance measured along the surface normal vector (so-called normal shooting). The normal vector is defined by locally approximating a tangent plane to the model surface (see FIG. 3.8).

3.3.3 Point-cloud Geometry Analysis

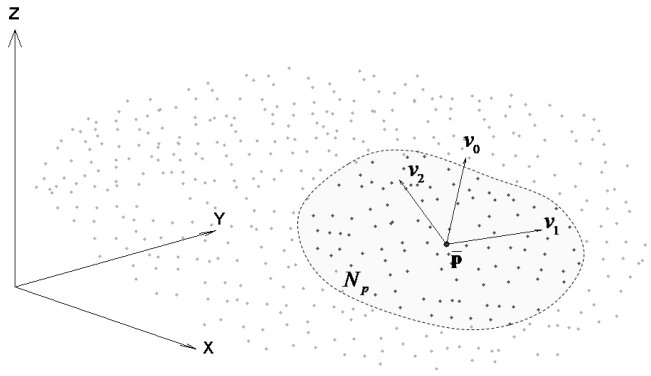

FIG. 3.9: Neighborhood N_p of k-points and the computed principal directions.

Geometric primitives, such as the surface normal vector, curvature or change of curvature are very interesting parameters for raw point-cloud interpretation and classification. As shown in [108] and [10], Principal Component Analysis (PCA) of the covariance matrix of a local neighborhood can be used to estimate local surface properties. Based on a kd-tree and approximate nearest neighbor search, finding of the k-nearest neighbors can be carried out very fast. The covariance matrix $\mathbf{C}_{[3\times3]}$ for a sample point $\mathbf{p}$ can be computed using the coordinates of the neighbor points:

$$\mathbf{C} = \begin{bmatrix} \mathbf{p}_{i_1} - \bar{\mathbf{p}} \\ \vdots \\ \mathbf{p}_{i_k} - \bar{\mathbf{p}} \end{bmatrix}^T \begin{bmatrix} \mathbf{p}_{i_1} - \bar{\mathbf{p}} \\ \vdots \\ \mathbf{p}_{i_k} - \bar{\mathbf{p}} \end{bmatrix}, i_j \in N_p \tag{3.3.2}$$

where $\bar{\mathbf{p}}$ is the centroid of the neighborhood N_p including k-points (see FIG. 3.9). The covariance matrix can be decomposed into its principal components by eigenvector decomposition:

$$\mathbf{C} \cdot \mathbf{v}_l = \lambda_l \cdot \mathbf{v}_l, l \in \{0, 1, 2\} \tag{3.3.3}$$

where $\mathbf{C}$ is symmetric and semi-definite. Therefore, its eigenvalues ($\lambda_0 < \lambda_1 < \lambda_2$) are real ($\geq 0$) and the corresponding eigenvectors ($\mathbf{v}_0, \mathbf{v}_1, \mathbf{v}_2$) form the orthogonal frame corresponding to the principal components (directions/orientations) of the point set defined by N_p (see FIG. 3.9). The eigenvalues λ_l measure the variation of the points $\mathbf{p}_i, i \in N_p$, along the direction of the corresponding eigenvectors. They describe the variance in each principal direction. Ac-

cordingly, the eigenvector $\mathbf{v}_0$ corresponding to the smallest variance (thus smallest eigenvalue λ_0) approximates the local terrain normal at point $\mathbf{p}_i$:

$$\mathbf{n}_{p_i} = \begin{pmatrix} n_x \\ n_y \\ n_z \end{pmatrix} = \frac{\mathbf{v}_0}{\|\mathbf{v}_0\|} \tag{3.3.4}$$

If the point-cloud coordinates are expressed in a local mapping frame (with y-axis towards north), slope S and aspect A (orientation towards north) can be derived using the local normal components (see also FIG. 3.10):

$$S_{p_i} = \operatorname{atan}\left(\frac{\sqrt{n_x^2 + n_y^2}}{n_z}\right), S \in [0, \pi/2] \tag{3.3.5}$$

$$A_{p_i} = \operatorname{atan2}\left(\frac{n_x}{n_y}\right), A \in [0, 2\pi] \tag{3.3.6}$$

If a neighborhood is a planar region, the variance in the normal direction is low, while for a surface that is not planar the variance in the normal direction is high. This property can be used to construct an easy metric to estimate the surface variation (or change in geometric curvature) $M_{cc}(\mathbf{p}_i)$ of point $\mathbf{p}_i$:

$$M_{cc}(\mathbf{p}_i) = \frac{\lambda_0}{\lambda_0 + \lambda_1 + \lambda_2}, 0 \leq \lambda_0 \leq \lambda_1 \leq \lambda_2 \tag{3.3.7}$$

This metric is very easy to interpret: If $M_{cc}(\mathbf{p}_i) = 0$, the selected points are perfectly planar, if $M_{cc}(\mathbf{p}_i) = 1/3$, the points are completely isotropically distributed. λ_1 and λ_2 describe the variation of the sampling distribution in the tangent plane and can thus be used e.g. to estimate the local anisotropy. However, the surface variation (as presented in EQN. 3.3.7) cannot be considered as an intrinsic feature for a point-sampled surface, as it depends of the number of points and the radius of the used neighborhood around $\mathbf{p}_i$ [12]. In [11] another expression to compute the change in geometric curvature can be found using the mean dot product of the normal vectors of $\mathbf{p}_i$ and its neighborhood:

$$M_{cc}(\mathbf{p}_i) = \frac{1}{k} \sum_{j=1}^{k} \left| \mathbf{n}_{p_i} \cdot \mathbf{n}_{neighbor(j,p_i)} \right| \tag{3.3.8}$$

where $\mathbf{n}_{p_i}$ and $\mathbf{n}_{neighbor(j,p_i)}$ are the normal vectors of $\mathbf{p}_i$ and its $j-$th neighborhood point, respectively, and k is the number of neighborhood points. The advantage of EQN. 3.3.8 is that the value is normalized by the size of the neighborhood and bounded between 0 and 1. A similar expression allows the computation of the geometric curvature $M_{curv}(\mathbf{p}_i)$ for a given point:

$$M_{curv}(\mathbf{p}_i) = \frac{1}{k} \sum_{j=1}^{k} \left\| \mathbf{n}_{p_i} - \mathbf{n}_{neighbor(j,p_i)} \right\| \tag{3.3.9}$$

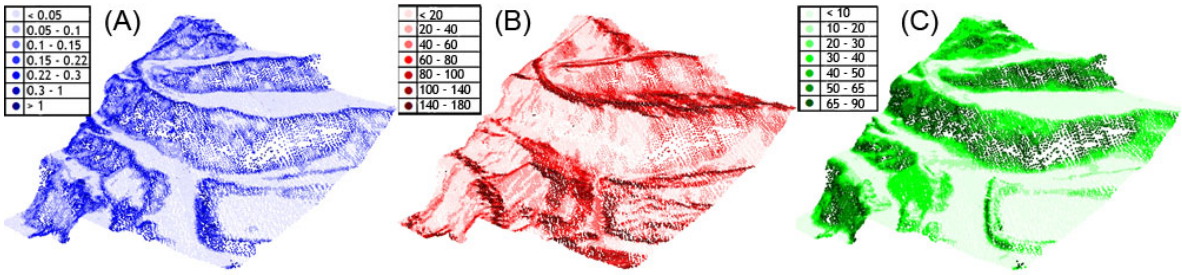

FIG. 3.10: Color-coded point-cloud by PCA-derived geometric quantities: (A) Curvature (-), (B) Aspect (°), (C) Slope (°).

3.3.4 Point-cloud Filtering and Classification

As ALS is a non-selective mapping method, the acquired data consists of a point-cloud that includes all kind of objects (e.g. vegetation, buildings, wires, etc.) that have been in the line of sight of the laser beam. Without the semantic information about the nature of each laser point, the derivation of value-added products, like Digital Terrain Models, is not possible. Accordingly, prior to any further processing, the point-cloud must be classified into different categories (see FIG. 3.11).

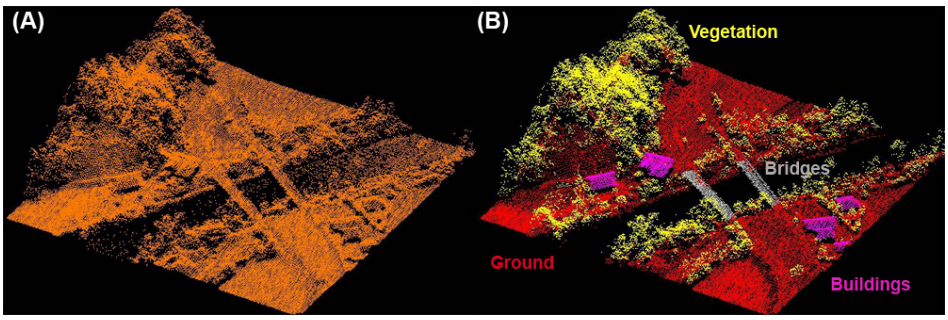

FIG. 3.11: (A) Raw point-cloud, (B) Point-cloud classified in ground-, bridge-, vegetation- and building-points.

The most common classification separates the laser points into bare-ground and non-ground objects (e.g. trees, buildings, wires). According to [99], current ground classification algorithms can be grouped into three major categories:

- **Directional filtering**: These filtering algorithms operate on gridded elevation values derived by interpolation of the raw point-cloud. The used interpolation techniques are manifold and include fitting a linear function [107], surface functions [72], morphology functions [67] or a local mean or minimum value [114]. [141] and [185] propose a slope-based filtering technique, that works by pushing up vertically a structuring element. [99] proposes a multi-directional ground filtering algorithm to incorporate a two-dimensional neighborhood in the directional scanning.
- **Neighborhood-based algorithms**: The filtering is directly performed in the point-cloud domain. [29] estimates the ground surface by employing active shape models by means of energy minimization. Axelsson [8] proposes a progressive TIN densification

method, where based on some initial points (local minimas) a TIN is computed. Further points are iteratively added to the TIN based on some geometrical constraints (see Fig. 3.12). Compared to more recent developments, Axelsson's method is reported to be still one of the most efficient ground classification algorithms [99, 142]. This method is also implemented in point-cloud processing software TerraSolid [161].

- **Surface-based filters**: These filters, also designated as robust interpolation filters, initially assume that all points belong to the ground and removal of non-ground points is carried out by stochastic behavior analysis of the terrain (e.g. [71]).

A detailed overview and comparison of different ground filtering algorithms can be found in [99, 142, 197].

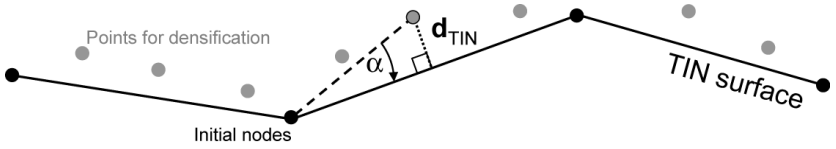

Fig. 3.12: Ground filtering using Axelsson's method: To be added as a terrain point, the angle α between the point and its projection on the TIN vertex and the normal distance d_{TIN} of the point to the vertex plan must be smaller than a certain threshold.

3.4 Digital Elevation Models

Digital Elevation Models (DEM) are discrete representations of a physical surface (terrain). For the reconstruction of a DEM from unorganized point-clouds generally two methods are applied:

- **Triangulated structure**: The surface is modeled as a triangulated surface based on irregular base points that may be completed with vector/breakline information.
- **Raster structure**: The surface is represented as a two-dimensional discrete matrix of data heights.

3.4.1 Triangulation

A triangulation converts the given set of points into a consistent polygonal model (mesh). The surface is discretized by dividing it into many small elements of geometrical primitives (e.g. triangles). Triangulation can be performed in 2D or in 3D, according to the geometry of the input data. For the 2D triangulation, the most popular construction method is the Delaunay triangulation. The Delaunay criterion ensures that no vertex lies within the interior of any of the circumcircles of the triangles in the network.
For DEM generation, mostly a 2.5D triangulation is applied, where the triangulation is performed in 2D and the z-value for each node is attached using an unique elevation function $z = f(x, y)$ for each point. The generated height surface is commonly called TIN (Triangulated Irregular Network).

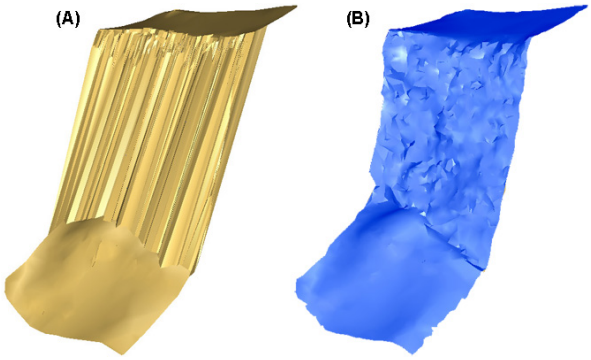

FIG. 3.13: Isometric view of a vertical rock face scanned by ALS modeled by triangulation: (A) 2.5D triangulation, (B) 3D triangulation.

Due to the implicit projection onto the x, y-plane, TIN's may lead to misinterpretation and mis-modeling of many 3D objects, such as buildings, bridges or vertical rock faces and overhangs (see FIG. 3.13). Although very popular in the computer vision and TLS community, rigorous 3D triangulation has not really gained ground in the ALS community. The reasons for this are manifold:

- 3D Triangulation algorithms are very complex and thus too slow to handle the large datasets gathered by modern ALS.
- Most software applications used in the mapping and GIS community deal only with 2.5D data (TIN and Raster), where a 2D coordinate can have only one unique height value.
- Absence of industry standards defining 3D model structures and data formats.
- Classical geo-products, such as DTM/DSM (as raster data) or contour lines derived from ALS point-cloud data cannot be interpreted correctly using real 3D data (e.g. crossing contour lines in pendent terrain do not make sense on a map).

However, real 3D modeling finds gradually its way also into the ALS community, especially for visualization and geomorphological analysis [17] and cultural heritage documentation [77].

3.4.2 Elevation Raster

The storage of irregular-spaced point-cloud data and its associated TIN requires large storage place, as every single coordinate has to be stored independently. A solution to overcome this problem is the generation of even-spaced elevation grids, where the x, y-coordinates can be described by an array and only the z-value has to be stored individually.

Digital Terrain Model (DTM)

DTM's are generated using the bare-earth (or ground) points, determined by the ground classification process (see CHAP. 3.3.4). To generate an even-spaced DTM raster, the surface

can first be modeled by a TIN generated with a 2.5D triangulation (see Fig. 3.14). The DTM heights are subsequently derived by linear interpolation on the TIN facet. There exist other interpolation techniques for DTM generation that do not require an intermediate triangulated surfaces, such as nearest neighbor Inverse Distance Weighting (IDW), kriging and spline interpolation methods [28]. However, the ground point coverage often suffers of reduced point density in forested areas or has data gaps, due to the non-ground point removal (e.g. buildings). Triangulation efficiently closes these gaps prior the interpolation, where the maximal size of gaps to be "closed" by triangulation can be parametrized by the facet edge length.

Digital Surface Model (DSM)

The term DSM is reserved for representations of the terrain including all surface features (buildings, vegetation, etc.). For the interpolation of DSM's, data gaps are less likely to occur. If the initial point-cloud density is close to the output raster size, assigning the elevation of the nearest point is a very fast and accurate method for DSM generation.

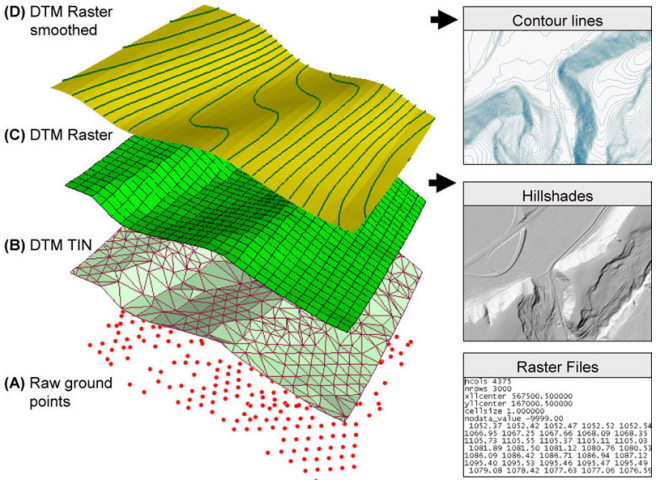

Fig. 3.14: Typical ALS product generation chain out of irregular spaced point-cloud data: (A) Raw ground points, (B) Generation of TIN by 2.5D Delaunay triangulation, (C) Interpolation of DTM grid, (D) Smoothing and derivation of contour lines.

3.4.3 DEM Analysis

Once a gridded surface model is generated, it can be used for a wide-spread of different raster based analysis. Using the principle of image convolution (operator $\star$), a large variety of filters (also called linear operators) can be applied for smoothing (e.g. Fig. 3.14.D) or filtering. Commonly used filters in DEM processing are the directional gradient filters:

$$f_x = \begin{bmatrix} -1 & 0 & 1 \\ -2 & 0 & 2 \\ -1 & 0 & 1 \end{bmatrix}, f_y = \begin{bmatrix} -1 & -2 & -1 \\ 0 & 0 & 0 \\ 1 & 2 & 1 \end{bmatrix} \tag{3.4.1}$$

Applying such or similar filters to height models, different derivate rasters can be computed (see also Fig. 3.15):

- **Slope raster**: Computing the slope value at column c and row r of a height model DEM can be performed as follows:

$$S[r,c] = \operatorname{atan}\left(R_x[r,c]^2 + R_y[r,c]^2\right) \tag{3.4.2}$$

where R_x is the height gradient grid in x-direction ($DEM \star f_x$) and R_y the height gradient grid in y-direction ($DEM \star f_y$), both obtained by convolution with the respective filters.

- **Aspect raster**: The aspect raster A can also be computed as a combination of the directional gradient grids:

$$A[r,c] = \operatorname{atan2}\left(\frac{R_y[r,c]}{-R_x[r,c]}\right) \tag{3.4.3}$$

- **Hillshade raster**: Hillshading corresponds to a hypothetical illumination of a surface with a chosen position for the artificial light source at an elevation angle ele and azimuth angle azi. The illumination values for each cell are computed in relation to its neighbors. This process greatly enhances the visualization of a height model for analysis or graphical display (see e.g. Fig. 3.15.D). Using the aspect and slope-grid for a given DEM, the hillshade grid can be computed by the following formula [31]:

$$\begin{aligned} H[r,c] = 255\,[&\cos(90^\circ - ele)\cos(S[r,c]) + \\ &\sin(90^\circ - ele)\sin(S[r,c])\cos(azi - 90^\circ - A[r,c])] \end{aligned} \tag{3.4.4}$$

where the resulting hillshade values are bounded between 0 and 255.

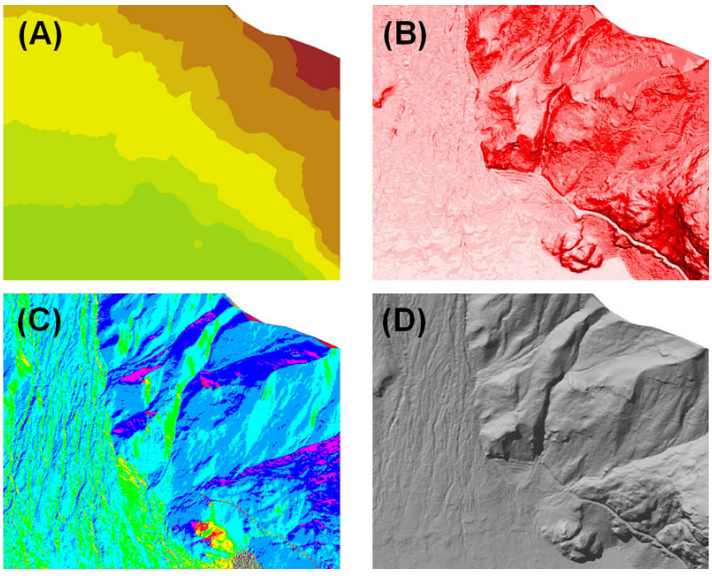

Fig. 3.15: Filtering of raster height model (DEM): (A) DTM color-coded by elevation, (B) DTM slope grid, (C) DTM aspect grid, (D) DTM hillshade.

Chapter 4

Point-cloud Quality Assessment

The previous chapters have introduced the different technologies and the mathematical concepts needed in ALS. This section first describes and quantifies the different error sources contributing to the accuracy of a single laser point coordinate. Second, the theoretical concepts to assess the accuracy are presented. A novel approach is proposed that yields a final quality indicator reflecting not only the georeferencing quality but also the scanning geometry. Finally, based on simulated and real datasets, the validity of the developed methods is assessed and the possibilities to use such quality indicators for advanced point-cloud processing are investigated.

4.1 Overview of ALS Error Sources

The total ALS error budget can be divided into three major segments (see Fig. 4.1):

1. **Navigation errors**: This includes the errors influenced by the GPS and the IMU and their impact on the obtained position and attitude uncertainties used for the georeferencing of the laser data. These errors are time-dependent and can vary within a mission.
2. **System errors**: These errors are related to the laser itself (scan angle encoders, range finder) and the incertitudes within the system assembly (e.g. boresight, leverarm). They are normally stable during a mission, or even during several missions, when the system mount remains unchanged.
3. **Scanning geometry errors**: This includes the influence of the incidence angle and the laser beamwidth on the obtained range. These errors are mainly scan-pattern and topography/target-dependent and their magnitude can vary quickly spatially and temporally.

4.2 ALS Navigation Errors

4.2.1 Trajectory Positioning Errors

The accuracy of the kinematic GPS/INS position is primarly influenced by two factors:

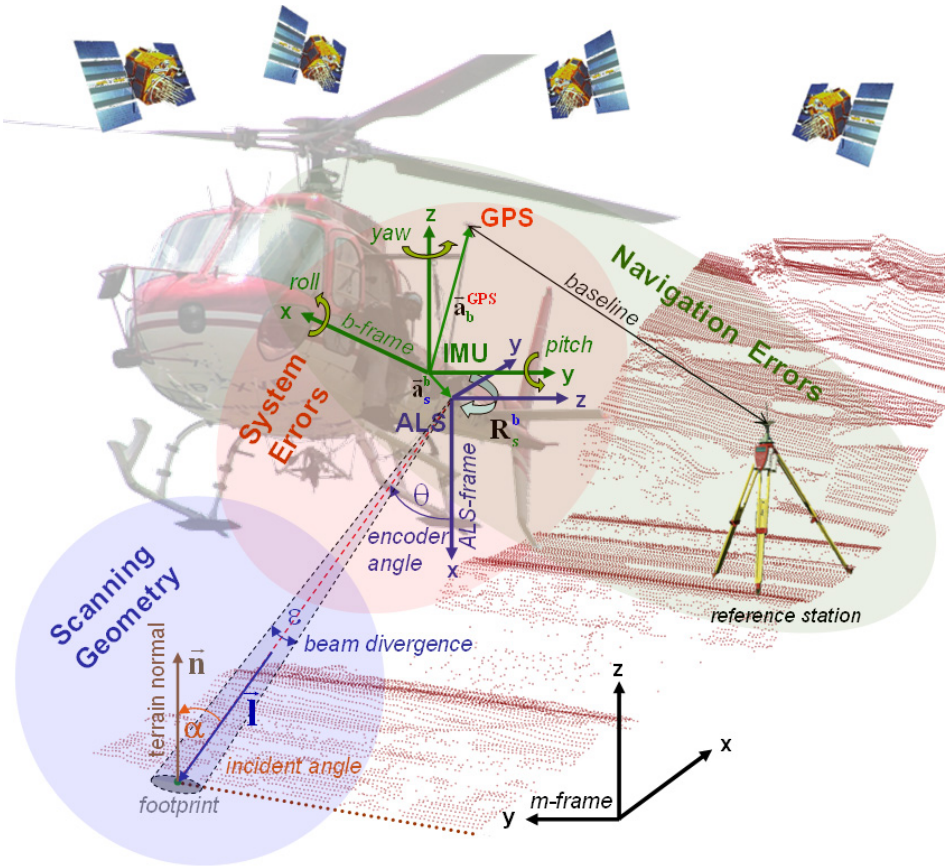

FIG. 4.1: Main components influencing the total error budget of ALS.

- **GPS satellite configuration and signal observability**: The number of visible satellites is governed by the satellite constellation and the obstructions either caused by the topography (skyplot) or by the carrier itself (i.e. antenna masking by wings for banking airplanes). Other important factors, such as baseline length, relative height difference and number of available baselines are depending on the ground infrastructure. Apart from physical obstructions, the signal observability can be degraded by signal blocking through jamming or interferences. As explained in CHAP. 2.5, the ability of an inertial system to bridge GPS outages for a certain time without substantial loss off accuracy largely depends on the quality of the IMU. For a tactical-grade IMU (mostly used in ALS systems) this time span does not exceed 15 sec, while for navigation-grade instruments this interval can be as long as 1 to 2 min [144].

- **Accuracy of observables**: The GPS processing is based on the differential carrier-phase (CP-DGPS) measurements. If the ambiguities can be resolved correctly, the residual errors on the baseline vector are relatively small for baselines up to 25 km and acceptable up to 100 km. TAB. 4.1 shows that for baselines shorter than 10 km, a relative accuracy of about 10-20 ppm (i.e. 1-2 cm) can be considered as the upper accuracy limit for a favorable satellite constellation. However, if the ambiguities cannot be resolved correctly, the accuracy degrades to a typical level of 100 ppm [144]. In order to keep the GPS error below decimeter-level it is therefore generally recommended not to exceed a

baseline length of 25 km [1, 3].
In airborne surveys the rover altitudes (on the carrier) may be very different from the reference altitudes (on ground). Hence, it is important to consider the relative height biases introduced by unmodeled tropospheric zenith total delay (ZTD). If the real temperature and pressure profiles differ from those assumed by the differential atmosphere correction model, these biases can be very important. According to [137], for height differences of several hundreds of meters, as typically the case in ALS surveys, the relative ZTD can be up to 0.05 - 0.3 m even if the horizontal baseline is small. A detailed report on the GPS error in function of baseline length and height difference can be found in [68].

	Troposhere	**Ionosphere**	**Multipath**	**Noise**	**Orbits**
Error [m]	$10^{-2} - 10^{-3}$	$10^{-2} - 10^{-3}$	10^{-2}	10^{-3}	10^{-2}

TAB. 4.1: Residual effects in CP-DGPS for baseline length < 10 km (after [166]).

4.2.2 Trajectory Orientation Errors

In contrary to the position, attitude determination by GPS/INS largely depends on the INS quality. The orientation errors budget has to be considered separately per axis, due to its dependency on dynamics. Generally, a better accuracy can be expected in roll and pitch determination (as compared to yaw) due to their correlation with the gravitational acceleration [143]. The error in yaw is only observable indirectly through the horizontal velocity error. This error cannot be de-correlated from other inertial errors, unless maneuvers inducing planimetric accelerations and direction changes (such as banking turns) occur.
The quality of the IMU alignment also has a significant impact on the residual orientation errors. Usually, the GPS/INS filter keeps on refining the initial alignment throughout the flight (refer to CHAP. 2.5.3: dynamic alignment). Flight dynamics enable to de-correlate the misalignment errors from the other error sources and thus strengthen the orientation accuracy. This means that the orientation accuracies, even with constant GPS quality, evolve during a mission in function of the abundance and the nature of flight maneuvers (see e.g. FIG. 4.13). A summary of potential orientation accuracies for today's most popular inertial sensors used within ALS can be found in TAB. 4.2.

	Navigation grade (∼0.01 deg/h)		**Tactical grade (∼0.1-3 deg/h)**	
Time	r/p(°)	y(°)	r/p(°)	y(°)
1 sec	0.0008-0.0014	0.008-0.002	0.001-0.02	0.001-0.05
1-3 min	0.0014-0.003	0.004-0.005	0.005-0.04	0.008-0.1
longer time	same as over 1 - 3 min but maneuver-dependent			

TAB. 4.2: Inertial attitude determination performance of GPS/INS depending on GPS outage time and INS quality (after [148]).

4.3 ALS System Errors

4.3.1 Range-finder and Scanner Errors

The modeling and calibration of the ranging errors is complex and the needed parameters depend on the internal laser design. [65] proposes a simplified relation to model the encoder angle errors related to the scanning mechanism:

$$\Delta\theta(t) = \Delta\theta_0 + \theta(t) \cdot s_\theta \tag{4.3.1}$$

where $\Delta\theta_0$ is a zero-offset bias and s_θ the scale factor. The latter is of special importance for oscillating mirrors, where the mirror is highly accelerated or decelerated at the swath border, thus inducing torsion effects that cause mis-registration of the observed distance.

The ranging accuracy mainly depends on the time-of-flight measurement. For pulsed ranging systems the absolute accuracy is settled around a few centimeters, whereas continuous wave systems can reach sub-centimeter ranging accuracy. Atmospheric effects are also known to contribute systematic and random sources of error into a laser range observation. The size of these errors is directly proportional to the length of the range (scale-dependent part s_r expressed in *ppm*). Accordingly, the total range error $\sigma_\rho(r)$ in function of the range r takes the following form:

$$\sigma_\rho(r) = \sigma_\rho + 10^{-6} \cdot s_r \cdot r \tag{4.3.2}$$

However, ALS system providers not always publish the range error according to this rule. Most modern ALS systems allow changing the PRF (thus amount of energy per pulse). This has a direct impact on the ranging accuracy. Manufacturers often prefer to state ranging accuracies in function of different flying heights and different PRF (e.g. [176]).
Tab. 4.3 presents a compilation of values for angular and range measurement accuracies for a representative selection of ALS sensors.

Sensor Type	**Range Error**	**Angular Resolution**	**Beam divergence**	**Angular Uncertainty**	**Total Angular Error**
	[m]	[°]	[mrad]	[°]	[°]
LMS Q-240	0.02+20 ppm	0.005	2.7	0.0387	0.0390
LMS Q-560	0.02[a]	0.001	0.5	0.0072	0.0073
Falcon III	0.02[a]	0.002	0.7	0.01	0.0102
ALTM Gemini	0.02[a]	0.001	0.15-0.3	0.0022	0.0024
ALS-50-II/60	0.02[a]	0.001	0.15	0.0022	0.0024

[a]No scale-dependent part published in official documentation

Tab. 4.3: Ranging and angular accuracy (at 1σ) specifications (adopted after [43]).

4.3.2 Calibration errors

As shown in Chap. 3.1.2, the GPS leverarm ($\mathbf{a}^b_{GPS}$) can be determined by tacheometric means with centimeter to sub-centimeter accuracy. As leverarms propagate one-to-one in to the

overall coordinate error, their impact is of minor importance. The accuracy of the boresight ($\mathbf{R}_s^b$) is more critical, as the impact of the boresight uncertainty on the target accuracy is growing with the range. According to [43], the accuracy of manual adjustment procedures for boresight angles is normally no better than the intrinsic accuracy of the IMU employed for attitude measurement. However, boresight determination based on surface conditioning by least squares adjustment, such as LIBOR (presented in CHAP. 3.1.1), can deliver boresight accuracies below the average attitude noise level.

4.4 Assessment of ALS Target Accuracy

The projection of the aforementioned individual error sources by the georeferencing formula (see EQN. 2.2.8) yields the accuracy of the target. This theoretical target accuracy can be computed by variance propagation. The error model for the propagation proposed in this research involves 14 error states:

- **6 navigation errors**: Namely the errors of the absolute positioning ($\sigma_X, \sigma_Y, \sigma_Z$) and the orientation ($\sigma_r, \sigma_p, \sigma_y$) as estimated by the GPS/INS-integration filter. These errors can rapidly change in time either due to a change in GPS constellation and/or variable flight dynamics.

- **6 system calibration errors**: Here, the residual errors in the boresight angles ($\sigma_{e_x}, \sigma_{e_y}, \sigma_{e_z}$) and in the leverarm ($\sigma_{a_x}, \sigma_{a_y}, \sigma_{a_z}$) are considered. These components should vary only with a change in system installation.

- **2 internal ALS errors**: The internal ALS error sources are restricted to random errors in distance and encoder angles only. This reduction is applied because most ALS manufacturers specify their expected accuracy in terms of these two main error components and do not specify the individual factors that contribute to the overall error. The final model considers a range-finder error (σ_ρ), having a constant and a scale-dependent part (ppm), and the error of the encoder angle (σ_θ). These errors are supposed to be intrinsic to every ALS system and are assumed to have a constant magnitude.

According to these 14 error states and assuming the scanning plane ($x_s z_s$) the georeferencing model EQN. 2.2.8 can be re-written such as:

$$\begin{bmatrix} x \\ y \\ z \end{bmatrix}^{\mathrm{m}} = \begin{bmatrix} X \\ Y \\ Z \end{bmatrix}^{\mathrm{m}} + \mathbf{R}_{\mathbf{b}}^{\mathbf{m}} \left[\mathbf{R}_{\mathbf{s}}^{\mathbf{b}} \rho \begin{pmatrix} sin\theta \\ 0 \\ cos\theta \end{pmatrix} + \begin{bmatrix} a_x \\ a_y \\ a_z \end{bmatrix}^{\mathrm{b}} \right] \tag{4.4.1}$$

where

$\mathbf{R}^{\mathbf{m}}_{\mathbf{b}}(r,p,y)$	is the attitude matrix from the IMU body frame to the mapping frame parametrized by roll, pitch and yaw
$\mathbf{R}^{\mathbf{b}}_{\mathbf{s}}(e_x,e_y,e_z)$	is the boresight matrix describing the angular offsets between the scanner frame and the body frame
ρ,θ	are the range and encoder angle measurements, respectively, of the laser scanner
$[a_x,a_y,a_z]_T$	is the leverarm from the IMU center to the GPS antenna expressed in the b-frame

Propagating the random errors through the functional model of the laser georeferencing equation given by Eqn. 4.4.1 yields a 3×3 point covariance matrix:

$$\mathbf{C}_{xyz} = \begin{bmatrix} \sigma_x^2 & \sigma_{xy} & \sigma_{xz} \\ \sigma_{xy} & \sigma_y^2 & \sigma_{yz} \\ \sigma_{xz} & \sigma_{yz} & \sigma_z^2 \end{bmatrix} = \mathbf{F}\mathbf{C}_{ll}\mathbf{F}^T \tag{4.4.2}$$

The stochastic model $\mathbf{C}_{ll}$ of all observations is given by

$$\underset{14\times14}{\mathbf{C}_{ll}} = diag\left[\begin{array}{ccc|ccc|ccc|ccc|c|c} \sigma_x^2 & \sigma_y^2 & \sigma_z^2 & \sigma_r^2 & \sigma_p^2 & \sigma_y^2 & \sigma_{a_x}^2 & \sigma_{a_y}^2 & \sigma_{a_z}^2 & \sigma_{e_x}^2 & \sigma_{e_y}^2 & \sigma_{e_z}^2 & \sigma_\rho^2(r) & \sigma_\theta^2 \end{array}\right] \tag{4.4.3}$$

where the range-dependent variance $\sigma_\rho^2(r)$ is computed using Eqn. 4.3.2 and the simplifying assumption is made that all individual error sources are uncorrelated.
The linear functional model (matrix $\mathbf{F}$) is normally obtained by expanding the georeferencing equation into a Taylor series and truncating after the first term [43, 78]. In order to speed up the computations, this research proposes to construct the functional model by analytical derivation of Eqn. 4.4.1. Thereby, $\mathbf{F}$ takes the form of:

$$\underset{3\times14}{\mathbf{F}} = [\mathbf{F}_{pos}|\mathbf{F}_{att}|\mathbf{F}_{leverarm}|\mathbf{F}_{boresight}|\mathbf{F}_{range}|\mathbf{F}_{encoder}] \tag{4.4.4}$$

The detailed formulation and the derivation for the sub-matrices of Eqn. 4.4.4 can be found in Appendix A.

Once $\mathbf{C}_{xyz}$ is computed, the covariance matrix can be decomposed into a horizontal and vertical ALS navigation error component for every laser point:

$$\sigma_{xy}^{nav} = \sqrt{\mathbf{C}_{xyz}(1,1) + \mathbf{C}_{xyz}(2,2)} \tag{4.4.5}$$

$$\sigma_{z}^{nav} = \sqrt{\mathbf{C}_{xyz}(3,3)} \tag{4.4.6}$$

where the superscript *nav* indicates the origin (system and navigation errors) of the error.

4.5 Assessment of Scanning Geometry

Conventional ALS error analysis considers the errors as described in Chap. 4.2 and Chap. 4.3. In such analyses, the accuracy of the range measurement is considered more or less constant. Let us consider the situation presented in Fig. 4.2. The laser points of this dataset, even if gathered with constant navigation and range measurement accuracy, have a large variation in their accuracy across the swath. The points inside the overlap area between strip A and B are likely to have better quality when gathered within strip B (measurements that are almost perpendicular to the terrain) than within strip A, where the range measurements are affected by unfavorable geometry.

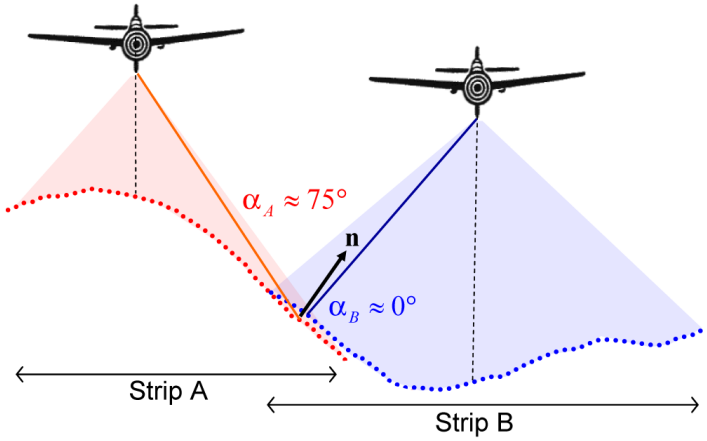

Fig. 4.2: Adjacent strips with changing geometry.

The impact of the incidence angle and the beamwidth on the total ALS error budget is acknowledged by many authors [4, 34, 43, 55, 71]. However, its modeling and evaluation has only found its way into the TLS community (e.g. [58, 86, 164]), where the measurement environment is easier to control than in the context of ALS (i.e. static scanner location and orientation, known surface properties, relatively short ranges, etc.).
Assessing the scanning geometry for airborne scans requires a-priori knowledge of the terrain slope and aspect. Recent developments using the signal of full-waveform laser systems have shown that certain surface attributes (e.g. slope, terrain cover) can be directly extracted by signal processing (e.g. [60, 115]). These computations are yet very time consuming as they require the full return signal for every range to be analyzed. For this reason, fast or near RT geometry analyses are not possible. Furthermore, full-waveform capacity remains limited to a relatively small number of systems on the market. In this research a more general approach is proposed that is suitable for every type of laser system (incl. single pulsed systems). The novel approach, first presented in [128], is fast enough for in-flight processing and will be explained in the sequel.

4.5.1 Laser Beam Power Distribution

One of the intrinsic properties of a laser scanner that strongly influences both the point-cloud resolution and the positional uncertainty is the laser beamwidth. The apparent location

of the range observation is along the centerline of the emitted beam. However, the real point location cannot be predicted since it could lie anywhere within the projected beam footprint. A good demonstration of this uncertainty is presented in [84]. There, the estimate of uncertainty assumes a uniform level of laser power across the entire beamwidth diameter and a circular footprint resulting in an angular uncertainty (at 1σ) of one-quarter of the beamwidth. However, an uniform power distribution within the footprint is typically not the case. Depending on the laser system, the spatial energy distribution of a pulse may appear in different shapes.

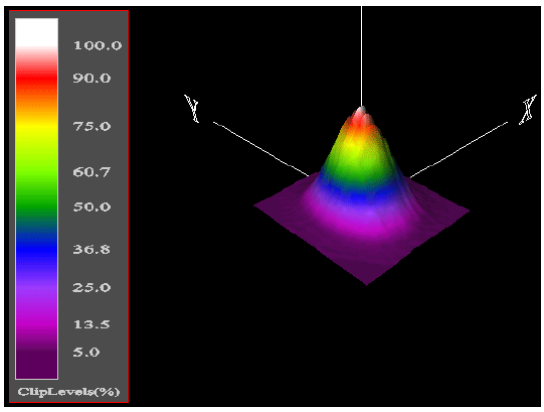

FIG. 4.3: Relative power distribution of an OPTECH ALTM LiDAR system (after [43]).

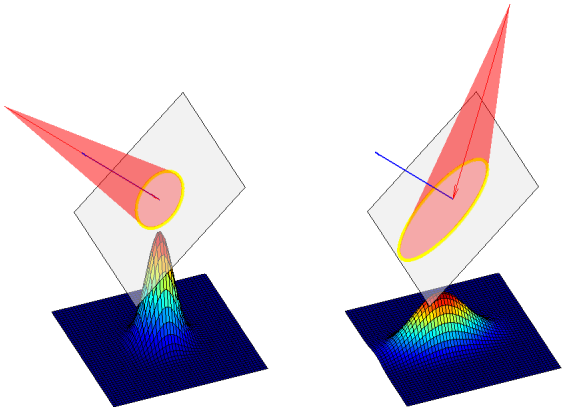

FIG. 4.4: Influence of incidence angle on relative power distribution: left: α=0°, right: α=60°.

FIG. 4.3 shows a typical power distribution of an outgoing laser pulse for the Optech ALTM LiDAR system. The power across the pulse is not uniform and can be approximated by a bivariate Gaussian distribution, where 100% of the energy lays within the footprint. Defining the footprint diameter to be $\pm 3\sigma$ (99.7% quantile), the angular uncertainty along one axis (at the 1σ level) can be approximated by one sixth of the footprint diameter. Based on this model, the influence of the changing incidence angle on the spatial energy distribution can be simulated (see FIG. 4.4). The backscattered signal from the target surface will be a function of the integrated energy distribution across the whole footprint. The amplitude and the centre of the signal power distribution are further modulated by the incidence angle, defined as the relative alignment between the beam direction and the normal of the reflecting surface.

4.5.2 3D Footprint Computation

The first prerequisite for the footprint computation is the (at least approximate) knowledge of the terrain normal. As shown in CHAP. 3.3.3, this can be performed by means of eigenvalue decomposition of the covariance matrix obtained from neighboring points. The other crucial information is the knowledge of the laser beam origin needed to compute the laser beam direction. These two quantities provide the missing link to the subsequent computation of the 3D footprint as a function of the beam divergence and estimated incident angle. Knowing the

terrain normal $\mathbf{n}$ (using EQN. 3.3.4), and the laser direction $\mathbf{l}$, the incidence angle α can be computed by

$$\alpha = \operatorname{acos}\left(\frac{\mathbf{l} \bullet \mathbf{n}}{|\mathbf{l}|\,|\mathbf{n}|}\right) \tag{4.5.1}$$

The laser footprint is modeled as an ellipse formed by the intersection between a cone having origin $\mathbf{O}$, direction $\mathbf{l}$ and beam divergence ϵ and the local tangent plane with normal $\mathbf{n}$ (see FIG. 4.5). As demonstrated in [19], the intersection of a cone with a plane can be computed using cone canonicals. The detailed mathematic development to compute a 3D footprint based on the aforementioned parameters can be found in Appendix B.

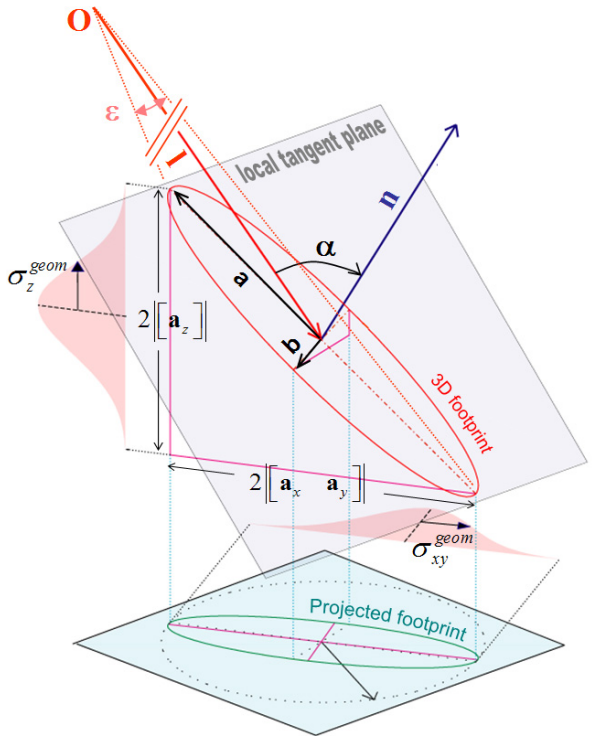

FIG. 4.5: Decomposition of the 3D footprint into its vertical and horizontal error components.

Once the main axis of the footprint (major half-axis a and minor half-axis b) are known in 3D, the footprint can be decomposed into its maximal horizontal and vertical extension (see FIG. 4.5). Taking into account the assumption of bivariate Gaussian power distribution within the footprint, the approximate positioning uncertainty in the horizontal and vertical component due to the scanning geometry can be expressed by

$$\sigma_{xy}^{geom} = \frac{1}{3} \cdot \max\left\langle \left|\begin{bmatrix} \mathbf{a}_x \\ \mathbf{a}_y \end{bmatrix}\right|, \left|\begin{bmatrix} \mathbf{b}_x \\ \mathbf{b}_y \end{bmatrix}\right| \right\rangle \tag{4.5.2}$$

and

$$\sigma_z^{geom} = \frac{1}{3} \cdot \max\left\langle |[\mathbf{a}_z]|, |[\mathbf{b}_z]| \right\rangle \tag{4.5.3}$$

4.6 Single Point Quality Indicator

Once all components contributing to the ALS error budget are assessed, this information can be applied to construct one unique quality attribute for each laser measurement. This "q-indicator" is constructed as accumulation of random errors coming from the error propagation of laser georeferencing equation (Eqn. 4.4.2) and the scanning geometry analysis (Eqn. 4.5.2 and Eqn. 4.5.3):

$$q_i = \sqrt{trace\left(\mathbf{C}_{xyz_i}\right) + \sigma_{xy_i}^{geom^2} + \sigma_{z_i}^{geom^2}} \tag{4.6.1}$$

4.6.1 Removal of non-ground Points

The assessment of the scanning geometry depends on the correct estimation of the local terrain normal. Applying the covariance method, this estimation is only reliable when the neighborhood of points approximately forms a planar surface. Laser points lying e.g. on vegetation have no clear geometric structure, hence the derived normal is geometrically not interpretable. As a consequence, prior to the computation of the incidence angle, the point-cloud has to be segmented into ground and non-ground points. In general, points on the ground or on buildings can be characterized by low curvature values (surface can often be approximated by a plane), whilst scanning points within vegetation and on roof edges generate high curvature values. These properties allow pre-classifying the laser points using a boolean test on the geometric curvature value $M_{cc}(\mathbf{p}_i)$ (Eqn. 3.3.9) with a given threshold *tol*:

$$\text{ground\_point}(\mathbf{p}_i) = \begin{cases} \text{TRUE if } M_{cc}(\mathbf{p}_i) < \text{tol} \\ \text{FALSE if } M_{cc}(\mathbf{p}_i) \geq \text{tol} \end{cases} \tag{4.6.2}$$

In general, the selection of the appropriate threshold depends on the size of the neighborhood k and the characteristics of the dataset (point density and topography). Further information about the appropriate choice of the neighborhood size can be found in [9].

4.6.2 Workflow for Q-indicator Computation

Fig. 4.6 and Fig. 4.7 summarize the workflow for the computation of the q-indicator. First, the error propagation is carried out using the navigation data and their accuracy estimates. Second, the point-cloud is generated in an arbitrary mapping system, followed by spatial indexing (see Chap. 3.3.1). After the computation of the local normal vector and curvature, the dataset is pre-filtered using Eqn. 4.6.2 (see Fig. 4.6.A), removing all points above a certain curvature threshold. The next step performs the scanning geometry analysis, using the estimated local terrain normal (Fig. 4.6.B), the laser direction and the beam divergence to compute the 3D footprint for the remaining laser points (Fig. 4.6.C). Finally, the effects of the scanning geometry are combined with the previously estimated covariances to construct one unique quality indicator using Eqn. 4.6.1. Thus, every laser point receives a separate q-indicator value (Fig. 4.6.D) that not only reflects the quality of georeferencing but also the scanning geometry.

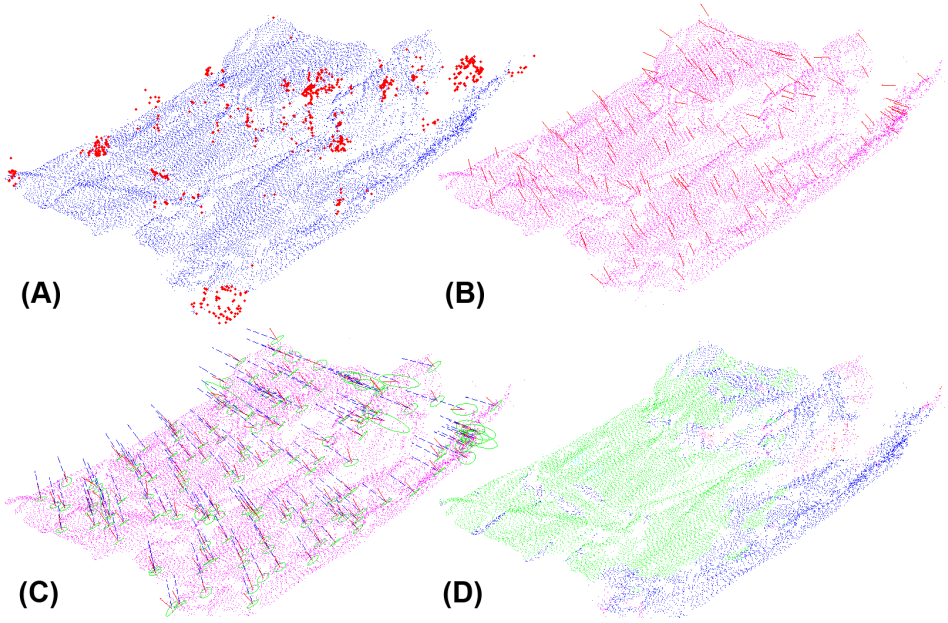

FIG. 4.6: Steps for q-indicator computation: (A) Pre-classification by threshold on local curvature, (B) Computation of local normal, (C) Computation of incident angle and 3D footprint, (D) Computation of final q-indicator.

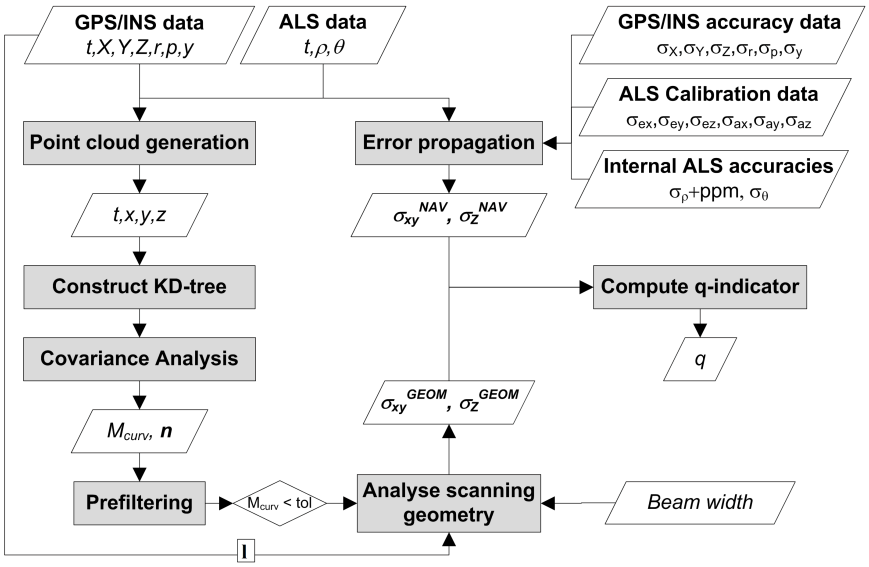

FIG. 4.7: Generalized workflow for the computation of the q-indicator.

4.7 Error Budget Evaluation

Based on theoretical scenarios as well as on real datasets, this section investigates the contribution of the aforementioned error components on the total point-cloud error budget.

4.7.1 Theoretical Analysis

The analysis presented in this section focuses on the error behavior of a standard long-range ALS system in function of the flying height, the scan angle and the scanning geometry. Three scenarios have been established for this purpose:

1. Nadir scan on a perfectly plane surface (Fig. 4.8)
2. Nadir scan on a tilted surface with a slope of 30° (Fig. 4.9)
3. Tilted scan (with roll = 30°) towards surface with a slope of 30° (Fig. 4.11)

For all three scenarios the previously presented quality indicators ($\sigma_{xy}^{nav}, \sigma_{z}^{nav}, \sigma_{xy}^{geom}, \sigma_{z}^{geom}, q_i$) have been computed for flying heights from 500 up to 2000 m and a theoretical FOV of 50° ($\theta = \pm 25°$). For the a-priori system and navigation accuracies the values published by [43] have been retained. These values are representative for a standard long-range ALS system with narrow beam setting. Rigorously performed system calibration and good GPS/INS data quality during the flight is assumed.

System calibration parameters	
Boresight	$\sigma_{e_x} = \sigma_{e_y} = 0.001°, \sigma_{e_z} = 0.004°$
Leverarm	$\sigma_{a_x} = \sigma_{a_y} = \sigma_{a_z} = 0.01\,\text{m}$
Intrinsic ALS parameters	
Range-finder	$\sigma_\rho = 0.04 + 15\,\text{ppm}$
Encoder angle	$\sigma_\theta = 0.00018°$
Beam divergence	$\epsilon = 0.3\,\text{mrad}$
Assumed navigation accuracies	
Position	$\sigma_X = \sigma_Y = 0.04\,\text{m}, \sigma_Z = 0.06\,\text{m}$
Attitude	$\sigma_r = \sigma_p = 0.005°, \sigma_y = 0.008°$

Tab. 4.4: A-priori system and navigation accuracies for theoretical error analysis.

Scenario 1

The plots in Fig. 4.8 show that the vertical component of the navigation error (σ_z^{nav}) is almost exclusively driven by the vertical accuracy of the used position, thus the GPS ($\sigma_Z = 0.06\,\text{m}$). For the horizontal accuracy (σ_{xy}^{nav}), the uncertainty in attitude has a larger impact, as the change in orientation is proportionally related (by distance) to a change in horizontal coordinates. Accordingly, for σ_{xy}^{nav}, the error growth is almost linear with the flying height. The plot also reveals the quality degradation towards the swath boundaries. On one side this is caused by the increased range at the swath border (thus increasing range-finder error due to the range-dependent part of σ_ρ), on the other side, due to increased angular uncertainty. The lower two sub-plots show the impact of the scanning geometry on the horizontal and vertical accuracy. For σ_{xy}^{geom}, the lower-left plot depicts the growth of the error with the scan angle. This can be explained by the increased footprint, that evolves as function of the range and the incidence angle: The shape of the footprint changes from a perfect circle at nadir (perpendicular incidence angle $\alpha = 0°$) to an ellipse enlarged by the deteriorating incidence

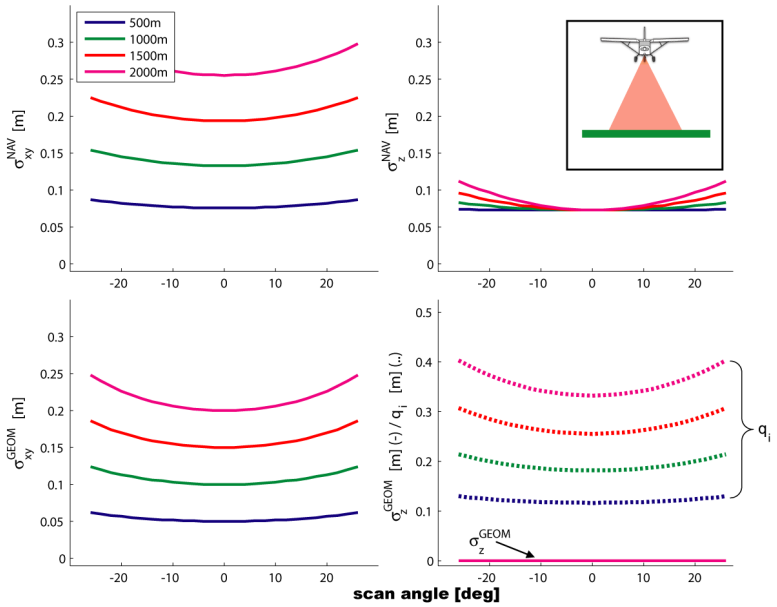

FIG. 4.8: Scenario 1: Horizontal and planimetric target accuracies in function of scan angle and flying height (assumptions: nadir scan on flat terrain).

angle (in this case $\alpha = \theta$) and increased range (in this case: $range = h/\cos(\theta)$). As the vertical projection of the footprint is always zero on a flat surface, σ_z^{geom} (solid line) remains 0 throughout the swath. The dotted line in the lower-right plot represents the overall quality indicator q_i. This value is primarily governed by σ_{xy}^{nav} and σ_{xy}^{geom}. The influence of the footprint on the total uncertainty increases with the height to reach more than 60% in flying heights above 1500 m.

Scenario 2

In the second scenario (FIG. 4.9), the impact of the tilted scanning surface on the error distribution can be depicted immediately. The quality degradation is not anymore symmetric around the nadir scan ($\theta = 0°$), but distorted towards the swath border with longer ranges. This distortion increases with the flying height, as the range discrepancies between the right swath border ($\theta = 25°, range \approx 1.5 \times h$) and the left swath border ($\theta = -25°, range \approx 0.87 \times h$) are scaled by the flying height. The effect of these large range differences and the change in scanning geometry ($\theta = 25° \rightarrow \alpha = 55°, \theta = -25° \rightarrow \alpha = 5°$) can also be seen in the geometric horizontal accuracy plot. Here the accuracy degradation is scaled by a factor 4 between the swath extremities for a flying height of 2000 m. In a tilted terrain, as the case in this scenario, the footprint size also influences the vertical accuracy, albeit their total contribution is of minor importance compared to the horizontal dilution of precision. The q-indicator plot (dotted lines in lower-right plot) highlights the unbalanced accuracy numbers within a same scan, as the points gathered at the left swath border are almost 3 times as accurate as those gathered at the right boarder. This example demonstrates clearly the uneven quality distribution within a dataset due to changes in scanning geometry.

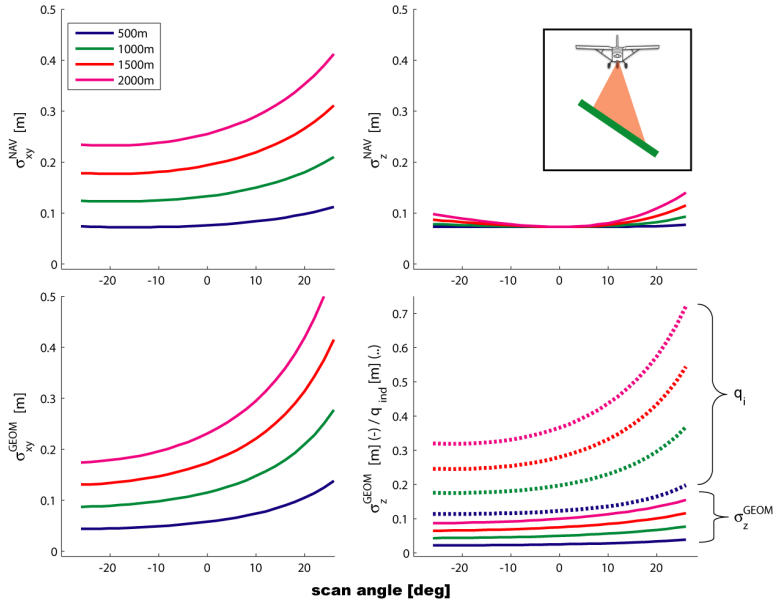

FIG. 4.9: Scenario 2: Horizontal and planimetric target accuracies in function of scan angle and flying height (assumptions: nadir scan on tilted terrain).

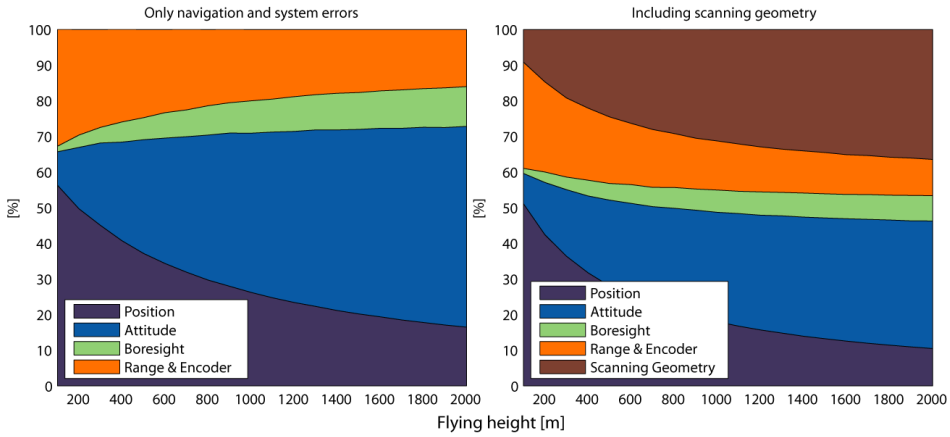

FIG. 4.10: Scenario 2: Repartition of total ALS error budget in function of flying height (assumptions: nadir scan on tilted terrain with slope of 30°).

FIG. 4.10 shows the relative repartition of errors for this scenario in function of the flying height, assuming a scan in the middle of the profile. The left sub-plot indicates the distribution (in percent) of error sources without considering the scanning geometry: For short ranges, the main part of the error comes from the position uncertainty, whereas for long ranges the attitude uncertainty covers the major part of the total error budget.
The right sub-plot reveals the important impact of the scanning geometry on the total error, especially for long ranges, where it stands for almost on third of the total error budget. If the beam divergence would be larger (e.g. short-range scanners have up to 3 mrad beam divergence), the contribution of the scanning geometry to the total error budget would even be larger.

Scenario 3

The third scenario depicts a practical solution to mitigate the impact of the scanning geometry on the point accuracy. In this case, the scanner is tilted towards the slope, hence reproducing a scanning geometry similar to scenario 1 and reducing the incidence angles considerably. The error behavior is again very similar to the first scenario, where the error is the smallest in the middle of the profile and the quality degrades towards the outer bounds of the swath. Compared to scenario 2, Fig. 4.11 shows that the accuracy is homogeneous throughout the scanning profile and up to 50% better for points at the outer bounds of the swath for higher flying altitudes.

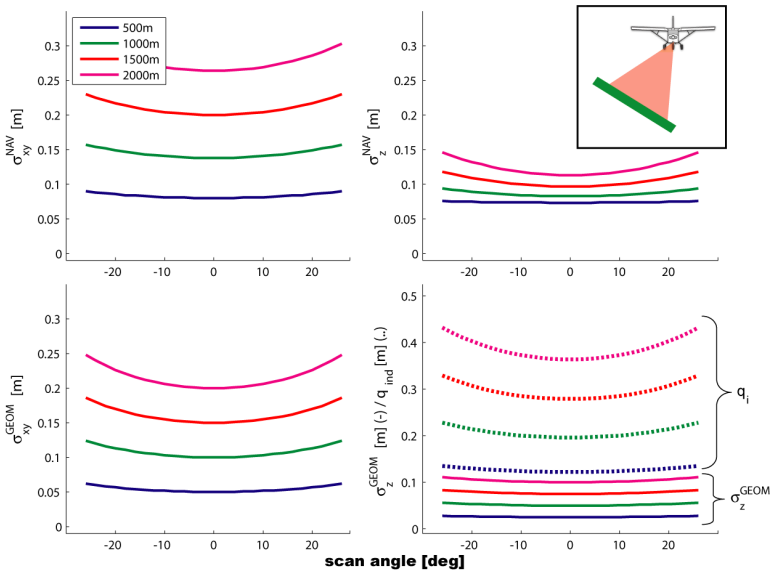

Fig. 4.11: Scenario 3: Horizontal and planimetric target accuracies in function of scan angle and flying height (assumptions: scan with roll = 30° on tilted terrain).

4.7.2 Error Budget for long-range ALS system

System and Flight Setup

The proposed approach was tested on a dataset collected in June 2006 near Gurtnellen (Canton Uri, Switzerland) using the Optech ALTM 3100 laser scanner mounted in nadir configuration on a helicopter. The flight was carried out with narrow beam setting (beam divergence = 0.3 mrad), a scan rate of 71 kHz and a mean flying height over ground of 1000 m. The dataset is characterized by very steep slopes (up to 90°) and large elevation differences (up to 1000 m) within the same strip. The flight planning was unfavorable, as the flight direction was parallel to the slope contour (see Fig. 4.12). These characteristics are ideal to reveal quality variations due to changing scanning geometry.

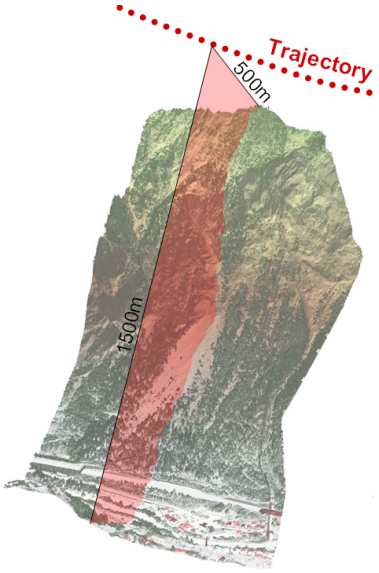

FIG. 4.12: Setup for Gurtnellen flight.

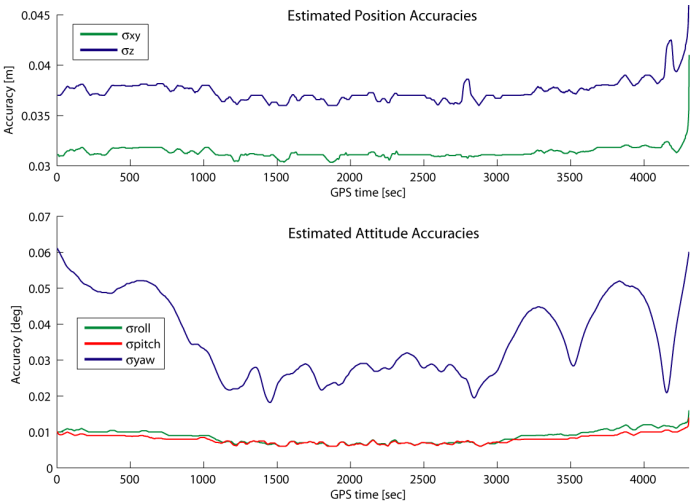

FIG. 4.13: Estimated navigation accuracies (RMSE) after GPS/INS integration for Gurtnellen dataset.

Results

The GPS/INS data was processed using the PosProc software package from Applanix. FIG. 4.13 shows the results of the navigation accuracy estimates after smoothing. The leverarm calibration was carried out by tachometric measurements and the boresight was determined by the LiBOR algorithm (see CHAP. 3.1.1). The intrinsic ALS error parameters were provided by the system manufacturer as published in [78].

System calibration parameters	
Boresight	$\sigma_{e_x} = \sigma_{e_y} = 0.0002°, \sigma_{e_z} = 0.003°$
Leverarm	$\sigma_{a_x} = \sigma_{a_y} = \sigma_{a_z} = 0.01$ m
Intrinsic ALS parameters	
Range-finder	$\sigma_\rho = 0.09 + 0$ ppm
Encoder angle	$\sigma_\theta = 0.00018°$
Beam divergence	$\epsilon = 0.3$ mrad

TAB. 4.5: A-priori system and calibration accuracies for error analysis with ALTM3100 system valid for the Gurtnellen dataset.

FIG. 4.14 illustrates the distribution of errors modeled by the error propagation as described in CHAP. 4.4. The range (FIG. 4.14.a) in nadir is about 1000 m, while at the extremities of the swath it oscillates from about 500 m (upper part) to 1500 m (lower part) respectively. It can be observed that the horizontal accuracy (FIG. 4.14.b) is mainly governed by the absolute value of the range. The vertical accuracy (FIG. 4.14.c) however, is also strongly influenced by the encoder angle. As predicted in the theoretical analysis of the previous section, the best vertical accuracy is achieved in the nadir. Generally, it can be stated that the point uncertainty increases with increasing range and encoder angle. It is also worth mentioning

that the accuracy variations follow a very homogeneous pattern with no sudden changes.

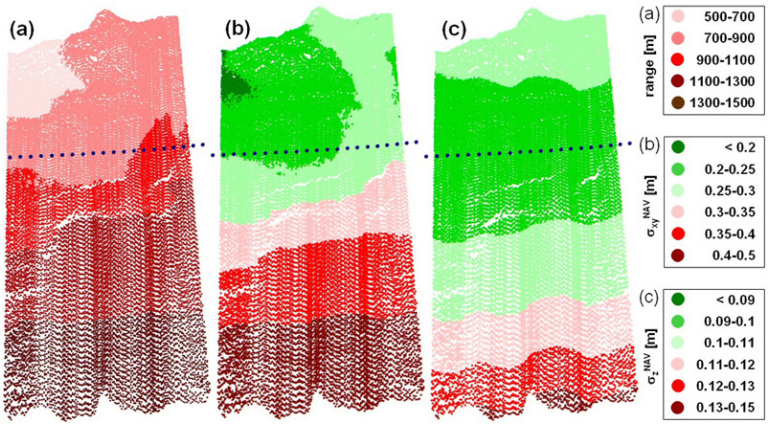

FIG. 4.14: Estimated point accuracies by error propagation (without scanning geometry analysis) for extract of Gurtnellen dataset: (a) ALS range length, (b) Estimated horizontal accuracy (σ_{xy}^{nav}), (c) Estimated vertical accuracy (σ_z^{nav}). The blue dots represent the projected helicopter positions.

The situation changes considerably when the effect of the incidence angle on the target accuracy is considered. FIG. 4.15 demonstrates the results of the scanning geometry analysis (as described in CHAP. 4.5). Unlike the navigation accuracy estimates (FIG. 4.14), the error distribution becomes inhomogeneous. The scanning geometry directly depends on the terrain topography, therefore abrupt changes in the scanning quality can occur. The dataset is characterized by a large variation in the incident angles (FIG. 4.14.a), especially in the middle part where slopes up to 90° occur. Correspondingly, a strong vertical accuracy degradation in this region has to be expected. The plot of the vertical accuracy (FIG. 4.14.c) affirms this assumption. The horizontal accuracy (FIG. 4.14.b) has a slightly different behavior. Here, the absolute range value is the predominant factor, as the horizontal footprint size is proportional to the distance of the laser head to the ground point. Hence, the quality degradation is larger towards the lower part of the slope.

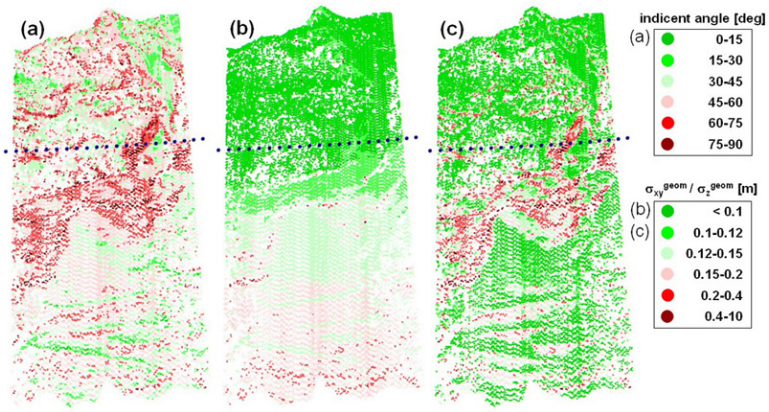

FIG. 4.15: Impact of scanning geometry on the target accuracy for Gurtnellen dataset: (a) Laser incident angles, (b) Horizontal geometric accuracy (σ_{xy}^{geom}), (c) Vertical geometric accuracy (σ_z^{geom}). The non-ground points have been previously removed.

4.7.3 Error Budget for short-range ALS System

Test Setup

Another evaluation was performed using a dataset flown in April 2007 near Sion (Canton Valais, Switzerland) using the Scan2map-system (see CHAP. 6.1). In comparison to the long-range system deployed in the previous test, this system has a 10 times larger beam divergence (Scan2map: ϵ =3 mrad, ALTM 3100 (narrow beam setting): ϵ =0.3 mrad).
To clearly assess the impact of the scanning geometry, a particular test setup has been chosen (see FIG. 4.16). Two strips covering the same area with different scanning geometries were acquired. For this purpose, two flightlines were flown in parallel to a strongly sloped mountain ridge (40 to 45°). Strip 1 (red) was flown in a nadir configuration ($roll \approx 0°$), resulting in poor intersection geometry in the lower (sloped) part of strip, whereas the second strip (green) was flown tilting the laser scanner towards the slope ($roll \approx 20°$), thus improving the intersection angle (analog to scenario 2 in CHAP. 4.7.1).
For independent ground control, 60 GCP's (blue dots in FIG. 4.16 and FIG. 4.17) were surveyed by RTK ($\sigma_{xyz} \approx 0.02$ m) in the strip overlap area. These measurements were used to compute punctual height differences to the height models formed by the points belonging to strip 1 and 2, respectively.

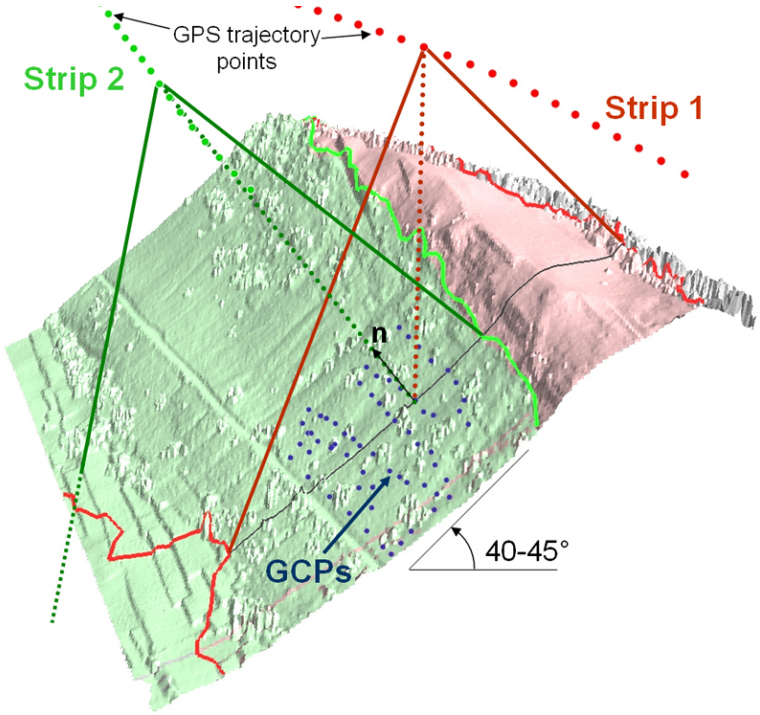

FIG. 4.16: Setup of test flight near Sion for q-indicator validation.

Results

The results of the comparison between the strip-wise height models and the GCP's are listed in TAB. 4.6. As expected, the data of strip 2 fits better to the GCP's than strip 1. Both strips

are affected by a bias (10 cm and 5 cm respectively). However, due to the strong slope, it is impossible to evaluate whether these biases originate from a horizontal or vertical error in the ALS data.
The position and navigation accuracy remained nearly constant throughout the two flightlines ($\sigma_{xyz} \approx 0.1\,m, \sigma_{r,p} \approx 0.005°, \sigma_p \approx 0.01°$). Additionally, the flightlines were planned and executed such as the mean ranges ($\overline{\rho} \approx 200\,m$) were nearly identical for both strips. Accordingly, the estimated contributions of the navigation errors ($\sigma_{xy}^{nav}, \sigma_z^{nav}$) were almost identical for both lines (see TAB. 4.6). The observed differences in point-cloud accuracy between data gathered in strip 1 or 2 should essentially come from the different scanning geometries (strip 1: $\overline{\alpha} \approx 50°$, strip 2: $\overline{\alpha} \approx 14°$). This is confirmed by the estimated quality indicator (strip 1: $\overline{q}_i = 0.3\,m$, strip 2: $\overline{q}_i = 0.26\,m$), whereas the horizontal channel (σ_z^{nav}) has the most significant contribution.

Strip	Comparison ALS data - GCP's				Computed quality indicators: Navigation		Scanning geometry			
	$\overline{\Delta Z}$ [m]	$\lvert\Delta Z_{max}\rvert$ [m]	$RMS_{\Delta Z}$ [m]	$\sigma_{\Delta Z}$ [m]	$\overline{\sigma}_{xy}^{nav}$ [m]	$\overline{\sigma}_z^{nav}$ [m]	$\overline{\alpha}$ [deg]	$\overline{\sigma}_{xy}^{geom}$ [m]	$\overline{\sigma}_z^{geom}$ [m]	$\overline{q}_i$ [m]
1	-0.10	0.29	0.12	0.07	0.07	0.06	50.6	0.10	0.27	0.30
2	-0.05	0.23	0.08	0.06	0.07	0.07	14.1	0.12	0.21	0.26

TAB. 4.6: Strip-wise height differences with GCP's and computed quality indicators.

FIG. 4.17 reveals the non-homogeneity of the quality distribution in the case of a poor intersection geometry (strip 1). While the q_i-values in the upper part of the strip and on the flat road segment are below 0.25 m (clear green colored), the points gathered near the declivity just above the road suffer of strongly reduced accuracy (dark red colored). This effect can also be seen in the profile $\overline{AB}$ plotted in FIG. 4.17. For strip 2, the quality distribution is more homogeneous, with a highly increased accuracy (as compared to strip 1) in the strongly sloped lower part.

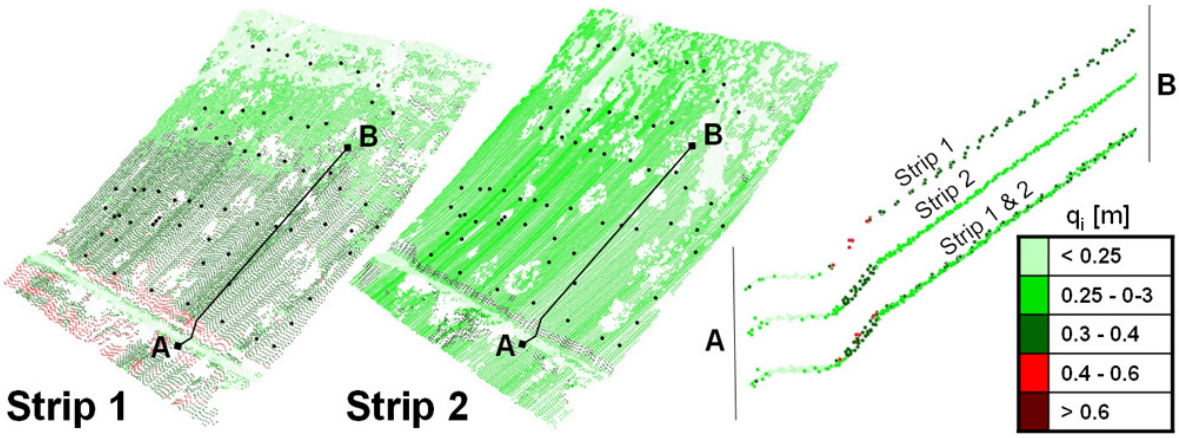

FIG. 4.17: Extracts and cross-profiles of strips color-coded by q-indicator.

Overall, this practical example highlights the substantial influence of the scanning geometry on the final target accuracy. If the accuracy estimation procedure should provide truthful point-cloud quality information, analyzing the scanning geometry is crucial. Additionally, if a dataset with homogeneous data quality should be achieved, this aspect should be considered and the flight planning and scanner configuration adopted accordingly.

4.8 Use of Quality Indicators in Point-cloud Processing

The profiles plotted in Fig. 4.17 illustrate a typical situation where a point-cloud consists of points that originate from different flightlines, thus having different accuracies. Computing the q-indicator of each individual point allows discriminating between "good quality" and "poor quality" points. This offers new possibilities to develop coherent QA/QC procedures and to increase the efficiency and quality in point-cloud processing and DSM/DTM generation.

4.8.1 Metadata Generation

With ALS becoming a well-established technology, the clients start demanding good documentation about the data origin, quality and processing history. [90] e.g. states that nowadays the compilation of metadata must be considered as an integral part of the ALS production workflow.
The capability to document the expected quality quickly and automatically by explicitly demonstrating the compliance (or lack of it) with the project specifications, represents a valuable asset when delivering comprehensive quality reports to the client [128]. Fig. 4.18 depicts some possibilities how to employ the quality indicators to produce such quality metadata. The shown quality maps were computed for a scan line acquired over a steep terrain by a nadir scan. They were generated by linear interpolation of the point-wise quality indicators (A: σ_{xy}^{nav}, B: σ_{z}^{nav}, C: q_i) to a regular raster map.

4.8.2 Strip Adjustment

Strip adjustment algorithms are based on the analysis of discrepancies in strip overlap. The methods to perform the subsequent derivation of correction values are manifold (see Chap. 3.2). However, all these methods consider that all used points, at least within the same strip, have the same quality. As previously shown, this assumption is not correct. Especially points situated at the outer border of the flightlines, typically where overlap analysis usually occurs, often have degraded accuracy, most notably in inclined terrain. The use of the q-indicator to weight points when solving for strip adjustment parameters will most certainly lead to improved accuracy and reliability of the results. This may enhance the quality of the derived strip correction values.

4.8.3 Ground Classification and DTM Generation

Most of todays ground classification algorithms show a high affinity towards low points, regardless of their origin and quality [128]. Using the q-indicator could increase the robustness

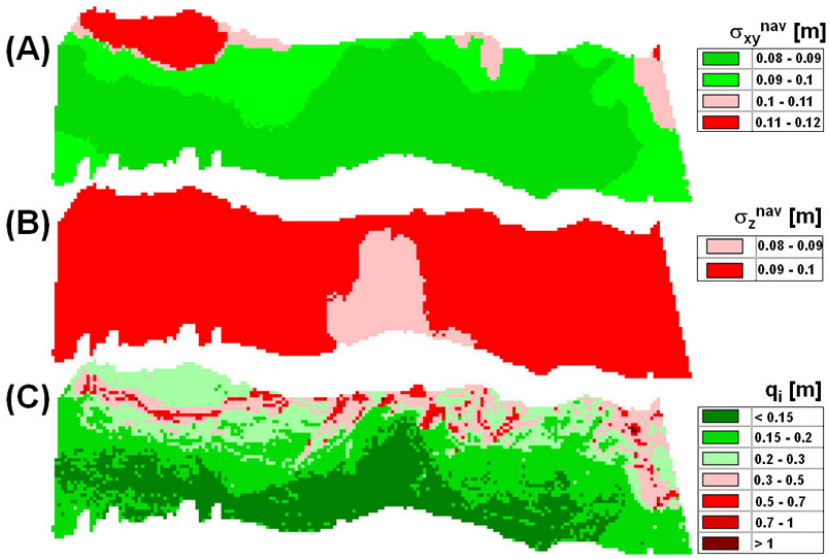

FIG. 4.18: Quality maps derived from nadir scan on sloped terrain: (A) Horizontal navigation accuracy map, (B) Vertical navigation accuracy map, (C) 3D quality (q_i) map.

of automated ground classification by considering only good quality points for the first iteration and adding points of lower quality subsequently.
To reach a DTM/DSM of high quality, sometimes visual inspection and manual editing is still necessary, particularly for data representing complex topography (e.g. mountain ridges, strongly sloped terrain, dense urban environment) [91]. Here, critical areas are examined visually and improved by reclassifying groups of points based on subjective decisions. Introducing q-indicators as an additional basis for deciding which points to prefer in manual classification (e.g. ground/non-ground) can help the operator to make more objective decisions, overall improving the quality of the end product.
For the gridding process, such indicator could also be used to increase the accuracy of the interpolation, by e.g. applying a weighting scheme to the node points [123]. More practical examples of the applicability of point-wise q-indicators within DTM generation and quality description will be presented in CHAP. 5.3.3.

Chapter 5

Surface Quality Assessment

In the previous chapter different ways to assess the accuracy of a single laser point have been discussed. In the ALS context however, laser measurements are rarely used as single values. A laser point-cloud is rather considered as a discretized representation of a continuous surface. The transfer from a single point measurement to a continuous surface model calls for new QA/QC-concepts, such as the analysis of the data coverage, point density and model accuracy. Accordingly, this chapter discusses surface-related quality indicators that describe the quality of the final geo-products derived from ALS raw data.

5.1 Data Coverage Analysis

5.1.1 Factors influencing the Point Density

Together with the point accuracy, the raw point-cloud density (normally expressed in $points/m^2$) is a key parameter. This parameter is often specified by the clients requirements and directly influences the main ALS mission settings (see Fig. 5.1):

- Flying height over ground
- Field of view (FOV)
- Ground speed of carrier
- Pulse repetition rate or line rate
- Scan pattern (often explicitly defined by the hardware)
- Strip overlap

The flying height together with the FOV directly influences the swath of a flightline. Together with the pulse repetition rate (PRF) and the scan pattern these parameters condition the across-track point spacing. For the along-track point spacing the ground speed is the most critical component. Within certain bounds, most modern ALS systems allow modifying the

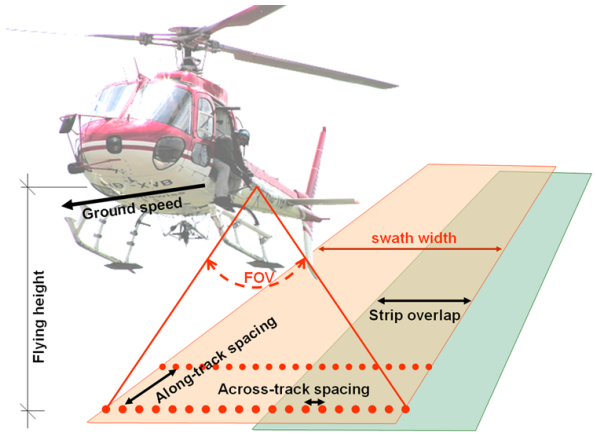

FIG. 5.1: Main parameters defining data coverage and point density for a line scanner system.

FOV and the PRF, whereas the scanning pattern is given by the functional principle of the laser (see CHAP. 2.3.3). The speed of the carrier is bound by the avionic characteristics of the carrier and the operation mode, whilst the flying height is limited by the power of the laser diode versus the terrain type (reflectivity). The strip overlap can be influenced by the flight planning. In function of the accuracy and point density to be achieved for a particular mission, these parameters have to be optimized under the constraint of economic efficiency (synonym to minimal flying time). For most missions, especially if a raster height model should be delivered, there is also an economic interest to achieve an even distribution of the raw point-cloud (across-track = along-track). This adds a further constraint to the flight planning.
Often the clients requirements also prescribe a certain ground point density to be achieved. In order to meet these specifications e.g. in forested areas, the abundance of foliage (thus selection of appropriate survey season) and the laser ground penetration rate (influenced by beamwidth, scan pattern and PRF) have to be considered.

5.1.2 2D Point Density

In most cases the point density is expressed as a 2D-function and represented as a 2D density raster map (see FIG. 5.2.B). In other words, the laser points are first projected into 2D, then a raster with a certain cell-size c is spanned over the covered area by the raw point-cloud. Thirdly, for every cell, the number n of projected laser points contained in one cell are counted. Finally, this count is normalized by the surface of the cell to obtain a 2D density value for a given resolution c:

$$\underset{[c\times c]}{\rho^{2D}} = n/c^2 \quad [points/m^2] \tag{5.1.1}$$

Such 2D density maps are straightforward to interpret and are therefore often employed as metadata to monitor the QA/QC process accompanying the height model production process (e.g. [5, 196]).

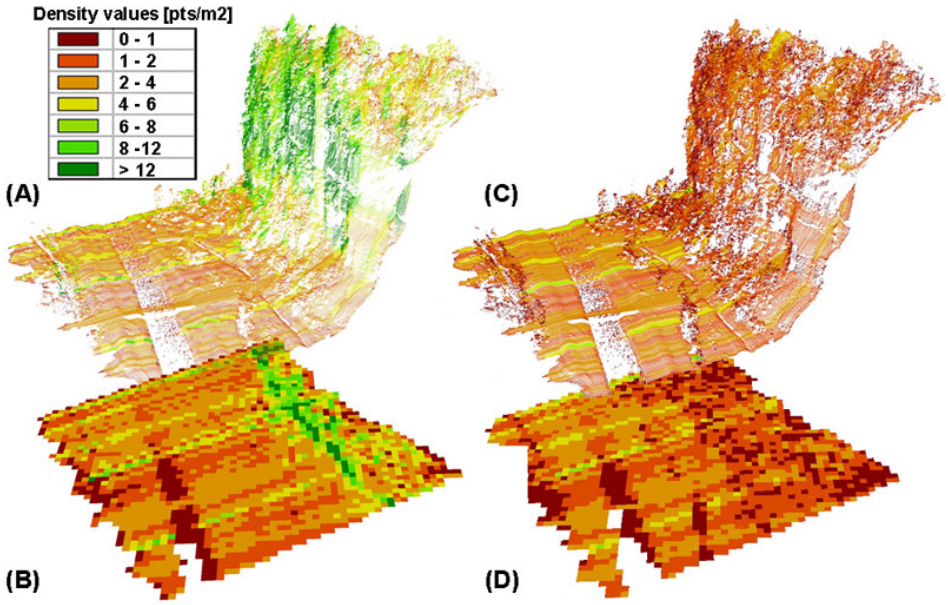

FIG. 5.2: Point density computation in 2D (left part) and 3D (right part) for a cell-size of 5 m. (A) Raw laser point-cloud color-coded by 2D density, (B) 2D density grid (C) Raw point-cloud color-coded by 3D-density, (D) Raster with projected 3D-density.

5.1.3 3D Point Density

Depending on the terrain and the scan characteristics the 2D point density concept is not always appropriate. In the case of a strongly tilted terrain or forested areas (including the canopy) the 2D projection of the points leads to an over-estimation of the surface-based point density. The illustration in FIG. 5.2.B depicts such a situation: Although the sloped part of the terrain has been scanned with equivalent point density than the flat part, the 2D density map indicates 3 to 4 times higher density values (green colored areas) in the tilted areas than in the flat areas.
One way to overcome this problem is the computation of a rigorous 3D point density, where the points are not projected for counting but their density is considered in a certain volume. The 3D density (ρ^{3D}) can be computed searching the kd-tree of a 3D dataset P_n for the number of neighboring points around a query point within a certain circular region [125]. Subsequently the count is normalized by the considered surface or volume. Using such approach, the point density of vertically scanned features can be represented either by coloring directly the point-cloud by the $\rho^{3D}-$value (FIG. 5.2.C) or by projecting this value into a raster map (see FIG. 5.2.D).

5.1.4 Data Extent and Gap Analysis

Depending on the scanning pattern, the reproduction of the data extent (perimeter of ground surface covered with laser data) can be evaluated by two methods:

1. Direct derivation through connection of swath-border points to form polylines representing the right and left swath border in each scan-line: This method is easy to implement

for scanning patterns where the end of a scanning profile can either be determined by an increased time jump between two subsequent measures (e.g. for line scanners) or by extracting the measures corresponding to maximum/minimum encoder-angle readout (e.g. for oscillating mirror). However, this procedure cannot be applied for other scanning principles such as nutating and elliptical mirrors, because the border points are not identifiable only based on laser observations.

2. Indirect computation by vectorizing the borders of the density map (see FIG. 5.3): This method works independently of the scanning principle. However, RT delivery of scan-border information is not possible, as the computation can only be started once a strip-wise density raster is produced.

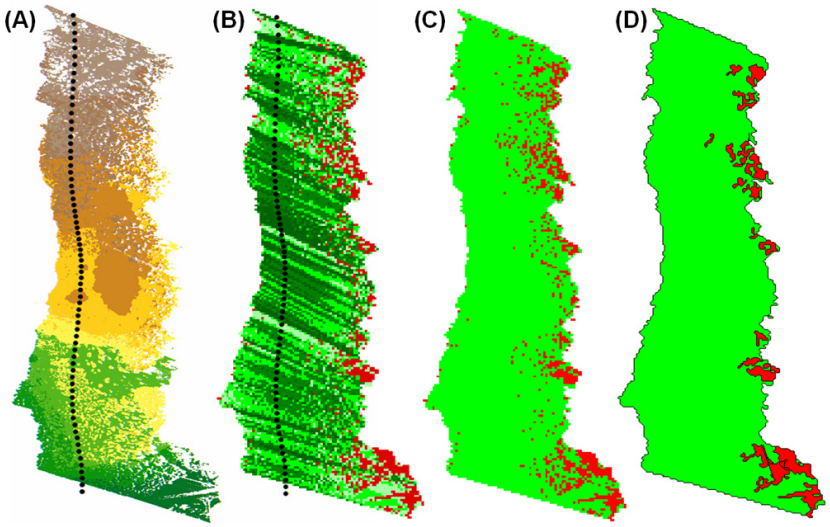

FIG. 5.3: Derivation of extent and data gaps: (A) Raw point-cloud color-coded by elevation, (B) Derived 2D density map, (C) Density map classified in cells above given density threshold (green) and below (red), (D) Vectorized extent and gaps. The black dots in (A) and (B) refer to the carrier positions.

The derivation of data gaps requires some previous density analysis. In the ALS context, a data gap is defined as a zone within the data extent that either has not been scanned at all (e.g. dark surface giving no laser return or missing strip overlap) or in which the point density falls below a certain threshold. As shown in FIG. 5.3, such gaps can be derived directly from the density map by classification and aggregation of gap zones in the raster domain (FIG. 5.3.C). In the latter, these zones can be vectorized for better transmission of information (FIG. 5.3.D). The implemented strategy for extent and gap detection is presented in detail in CHAP. 6.7.5.

5.2 Internal Data Accuracy

The occurrence of ALS strip overlaps introduces a certain data redundancy, because an area is scanned twice or more at different times and settings (range, incidence angle, etc.). As discussed in CHAP. 3.2, the observed discrepancies in strip overlaps can be compensated (to

a certain extent) by a strip adjustment. Yet, the observed discrepancies also present a good opportunity for estimating the internal accuracy of an ALS point-cloud. If the ALS system is correctly calibrated and the navigation solution is reliable, these discrepancies should lay within the predicted measurement accuracy. If the differences are larger and/or follow some systematic trends, they provide evidence for some unresolved problems in the chain of georeferencing (e.g. wrong calibration values or trajectory solution of poor quality). This section presents possible methods to estimate the internal point-cloud accuracy within strip overlaps. For this purpose, three scenarios have been established:

(A) Flight with correctly calibrated system and good quality trajectory data ($\sigma_{xyz} < 0.1\,m, \sigma_{att} < 0.01°$).

(B) Flight with error in boresight calibration ($\delta_{roll} = 0.1°$).

(C) Flight with poor trajectory quality (float ambiguities) in parts of the flight.

5.2.1 Strip Difference Map

The easiest way to monitor discrepancies between strips is to subtract the height grids (either DSM or DTM) derived from the adjunct flightlines. This produces a so-called strip difference map (e.g. [116]). Such representation can reveal if the occurring height differences are randomly distributed (within the system measurement noise), or are subject to systematic effects.

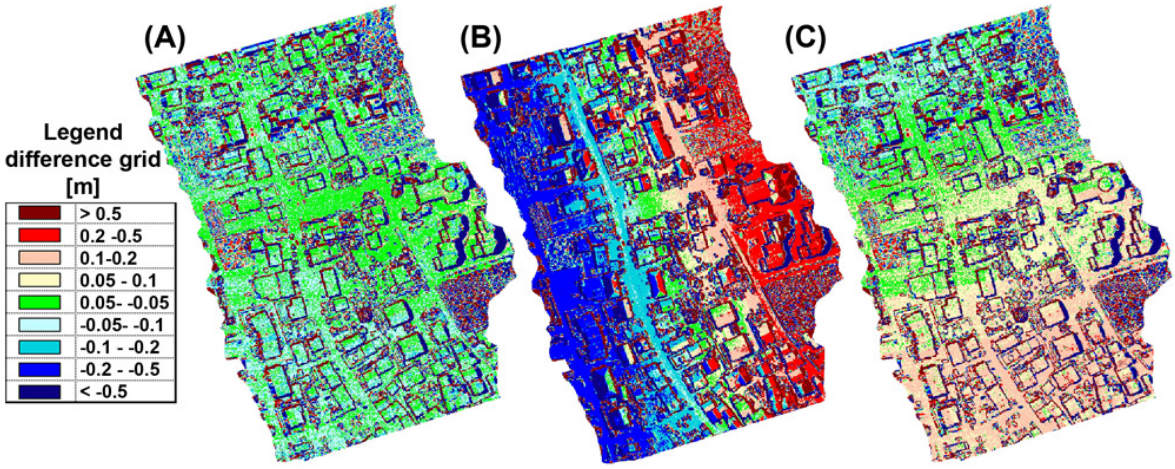

FIG. 5.4: Strip difference maps for different scenarios: (A) Calibration and trajectory ok, (B) Error in boresight ($\delta_{roll} = 0.1°$), (C) Error in trajectory (wrong ambiguity fix in one of the strips).

FIG. 5.4 depicts the difference maps for the aforementioned scenarios. The two adjacent strips were flown in opposite direction. For scenario A no systematic shifts can be seen. Except on the building borders, the height differences are mainly within the system accuracy (±5 cm in this case). For scenario B, the strip difference map depicts a systematic behavior as the differences change from positive to negative values across track. This is a clear indicator for a problem in the roll orientation, either provoked by wrong boresight calibration or poor trajectory orientation. The case for scenario C is different, as the differences do not follow

a homogeneous pattern. The sudden increase in height difference is a strong indicator that the trajectory in one of the strips suffers of severe quality degradation, e.g. due to wrong ambiguity resolution. The utility of such strip difference maps for in-flight quality monitoring will be discussed in CHAP. 6.7.10.

5.2.2 Translation and Rotation Detection by ICP

Planar shifts and/or rotations between strips cannot be evaluated with height difference maps. The full recovery of 6D strip differences is only possible with surface matching techniques, such as least-square matching (LSM) or ICP (see CHAP. 3.3.2). Rather than processing the complete strip overlap at once, matching techniques are often applied in distinct sample zones. TAB. 5.1 shows the strip differences (translations and rotations) computed by ICP for the three scenarios. The data and model points were extracted from two sample zones within the overlap (see FIG. 5.6 for zone location):

- For scenario A, the results depict 3D strip translations in the order of magnitude of $\Delta_{xyz} = 0.1\,\text{m}$ for both sample zones. This reflects the achievable accuracy for post-processed GPS trajectory.
- For scenario B, the translations are also very small, but the detected discrepancies in orientation (especially roll and yaw) are significant ($|\Delta_{roll}| \approx 0.2°$), delivering evidence for a problem in attitude determination.
- For scenario C, the discrepancies detected in zone 1 are within the expected accuracy, whereas zone 2 indicates a mis-match in height between the strips ($\Delta z = 0.17\,m$).

Besides the possibility to detect rotational discrepancies, scenario C reveals another essential advantage of the ICP compared to the strip difference map. Strip differences are not stringently constant (e.g. [94]). Hence, they cannot be described as a set of constant shifts for one overlap. ICP can model locally changing differences, as the method can be applied at many distinctive sample zones within a strip overlap.

Scenario	Sample zone											
	1						2					
	Δx	Δy	Δz	Δr	Δp	Δy	Δx	Δy	Δz	Δr	Δp	Δy
	[m]	[m]	[m]	[deg]	[deg]	[deg]	[m]	[m]	[m]	[deg]	[deg]	[deg]
A	-0.06	-0.03	0.02	-0.06	0.03	-0.1	-0.08	-0.03	0.01	0.02	0.02	-0.01
B	-0.01	0.02	-0.01	**-0.24**	0.08	**-0.25**	0.01	0.01	-0.01	**-0.17**	0.09	**-0.22**
C	-0.05	-0.1	0.02	-0.06	0.02	-0.11	0.04	-0.1	**0.17**	-0.02	0.02	-0.13

TAB. 5.1: Estimation of strip discrepancies using ICP for scenarios shown in FIG. 5.4 and samples zones defined in FIG. 5.6.

Influence of Geometry on Discrepancies Recovery

One problem of the ICP is the stability of the solution. As presented in Chap. 3.3.2, ICP is based on a local search algorithm to recover correspondence between two points by minimizing the square sum of distances between possible corresponding points. Certain surface geometries lead to a minimizing transform that is not unique. Let us e.g. consider two point-clouds of perfectly horizontal planar surfaces to be matched: Once matched, there are still three remaining degrees of freedom: translation in the xy-direction and rotation around the z-axis. There exist other geometrical features that can not constrain the 6 degrees of freedom (as shown in Fig. 5.5). [41] proposes a concept for a stability measure based on covariance analysis of the model points $\mathbf{p}_i$ and the normal $\mathbf{n}_i$ at point $\mathbf{p}_i$ for a dataset to be matched:

$$\underset{[6\times6]}{\mathbf{C}_p} = \begin{bmatrix} \underset{[3\times3]}{\mathbf{C}_t} & \ddots \\ \ddots & \underset{[3\times3]}{\mathbf{C}_r} \end{bmatrix} = \mathbf{F}\mathbf{F}^{\mathrm{T}}, \text{where } \mathbf{F} = \begin{bmatrix} \mathbf{p}_1 \times \mathbf{n}_1 & \dots & \mathbf{p}_k \times \mathbf{n}_k \\ \mathbf{n}_1 & \dots & \mathbf{n}_k \end{bmatrix} \tag{5.2.1}$$

where $\mathbf{C}_p$ is the covariance matrix expressing the torque ($\mathbf{p}_i \times \mathbf{n}_i$) and force ($\mathbf{n}_i$) components contributed by each point. This matrix can further be used to analyze whether the dataset has any unconstrained transformations by examining the eigenvalues ($\lambda_1 \leq \ldots \leq \lambda_6$) and the eigenvectors ($\mathbf{x}_1, \ldots, \mathbf{x}_6$) of the covariance matrix. Each of these eigenvectors corresponds to a general "screw" motion that can be interpreted as a rotation and a translation along this axis. An eigenvalue λ_k that is very small compared to λ_6 corresponds to a sliding direction. This property can be applied to construct a stability index

$$c_s = \lambda_1/\lambda_6 \tag{5.2.2}$$

that can be used to analyze if the selected dataset is prone to constrain sufficiently the rotations and translations to be correctly recovered by ICP. [112] proposes a adaptation of the method by splitting the matrix $\mathbf{C}_p$ into two sub-matrices $\mathbf{C}_t$ (only components related to translations) and $\mathbf{C}_r$ (components related to rotations) and proceeding the eigenvalue decomposition independently. Analog to Eqn. 5.2.2, different stability indexes for the translations and rotations can be constructed:

$$c_{ts} = \lambda_{ct1}/\lambda_{ct3},\ c_{rs} = \lambda_{cr1}/\lambda_{cr3} \tag{5.2.3}$$

This is of interest if e.g. only translations between datasets have to be detected, accordingly c_{ts} enables to measure the stability of the translation detection separately.

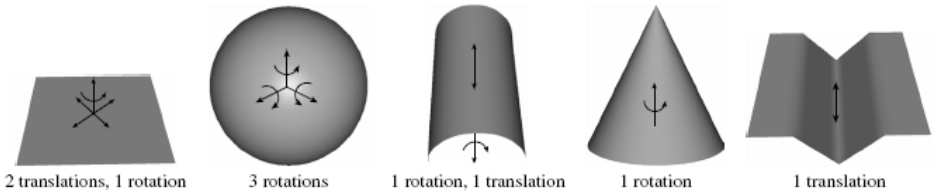

Fig. 5.5: Some examples of shapes unable to constrain 6D motion (after [41]).

Strategy for Strip Discrepancies Detection

TAB. 5.2 presents the computed stability indexes for the sample areas indicated in FIG. 5.6. The stability indexes for zones 1 and 2 (several buildings) are much higher than for zone 3 (flat area with no building or terrain relief). This reflects the difference in geometrical information of the data points fed into the ICP algorithm. Accordingly, the general strategy to estimate strip discrepancies can be described as follows:

1. Automatically select sample zones in strip overlaps and compute geometrical stability indexes (c_{ts}, c_{rs}) for each zone.
2. Based on some dynamically adapted threshold, remove sample zones that do not satisfy a given stability criteria ($c_{ts} < threshold\_c_{ts}$, $c_{rs} < threshold\_c_{rs}$).
3. Indicate areas where detected strip discrepancies are inconsistent with predicted point-cloud accuracy.

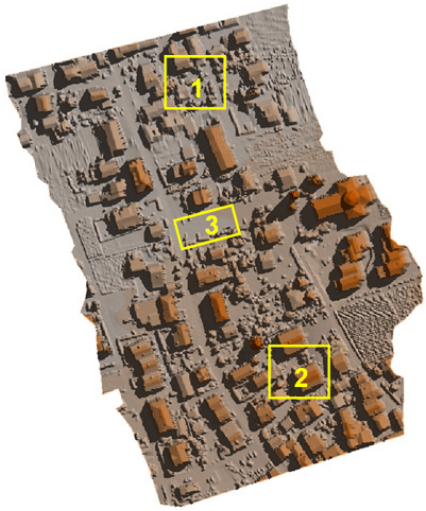

FIG. 5.6: Sample zones within strip overlap for computation of strip differences by ICP

Sample zones	Stability indexes		
	c_s	c_{ts}	c_{rs}
1	0.0679	0.1625	0.0787
2	0.0734	0.1878	0.0813
3	0.0002	0.0102	0.0002

TAB. 5.2: ICP stability index for 3 different sample zones in strip overlap.

5.3 Height Model Data Accuracy

5.3.1 Factors influencing DTM Accuracy

For the generation of DTM's from ALS data, the required processing steps, the associated error sources and the possibilities to estimate these errors can be summarized as follows (see FIG. 5.7):

- **Georeferencing of point-cloud**: The laser data and the trajectory are merged to obtain a point-cloud in a desired datum. The accuracy of the individual point can be assessed by single point error propagation (as discussed in CHAP. 4), whilst the raw point density can be measured by a density map (see CHAP. 5.1.1).

- **Ground classification**: The density of the remaining ground points after classification has a very strong impact on the final DTM quality [89]. For example [56] emphasizes the impact of vegetation on DTM accuracy, as dense canopy strongly degrades the ground penetration capacity of the laser beam. Therefore, independently of the applied classification algorithm, the density and spatial distribution of the ground points mainly depend on the topography and land cover of the scanned area. Another important factor is the correctness of the classified points. For instance, if only a single laser point situated on a tree is wrongly classified as ground point, this may (depending on the applied interpolation method) influence the resulting DTM heights over a large area. Ideally, the correctness of the classification should be measured by some sort of confidence factor r_i for each laser point scaling the individual point variance. However, this remains a very challenging task, as actually no algorithm is capable of correctly classifying all points and deliver additional confidence information. Hence, the correctness of the ground classification has to be controlled by visual inspection of the resulting surface [128].

- **Interpolation**: In the final step of DTM processing the individual points are connected to a continuous surface function describing the height for each location within the perimeter. To correctly assess the influence of each laser point on the interpolated surface, the interpolation should ideally be accompanied by some point-to-surface error propagation process. This process should consider on one side the input variance of the node points and on the other side, the output sampling rate, determining if the newly computed surface values are interpolated (over-sampling of surface) or extrapolated (sub-sampling of surface).

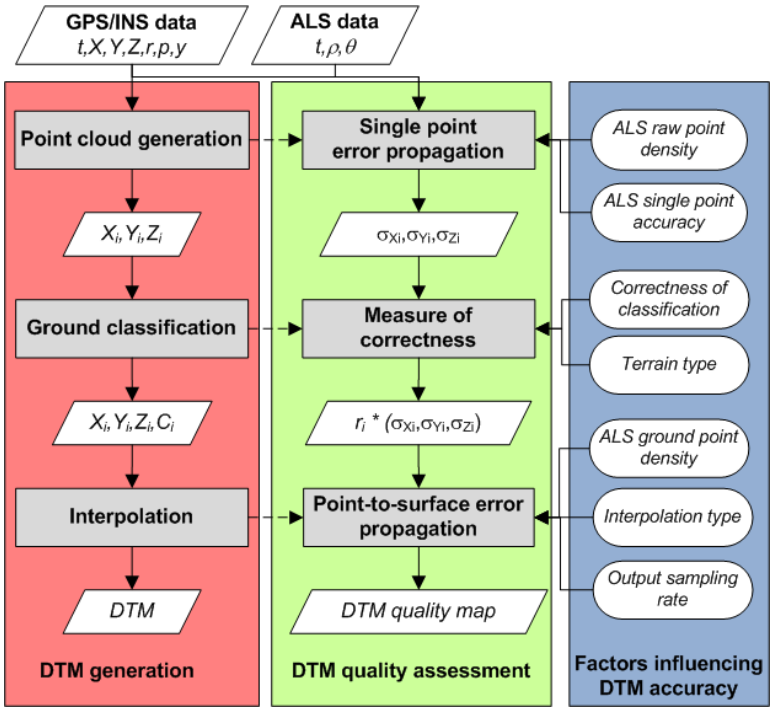

FIG. 5.7: General workflow for DTM production from ALS data and possible steps for QA/QC.

5.3.2 Empirical DTM Quality Assessment

As illustrated in Fig. 5.8, height accuracy assessment for DTM's is generally limited to the collection of punctual independent measurements (GCP's) gathered within the survey area. Subsequently, these are compared to the model heights at the given location (e.g. [51, 56]). This method has a major drawback as the estimated vertical accuracies cannot be generalized and only hold for areas that are covered by GCP's. Moreover, GCP's are often gathered on reference surfaces, where the point density is high, having low declivity and hard land cover (such as parking lots, sports field, etc.). Correspondingly, the issued height accuracies often over-estimate the model precision for parts of the DTM having other characteristics. Hence, the ASPRS guidelines for reporting vertical LiDAR accuracy [38] recommend to evaluate only the "fundamental" vertical accuracy in open, flat terrain and to specify additional relaxed vertical accuracies for different land cover classes (i.e. open terrain, tall weeds and crops, forested areas, urban areas, etc.).

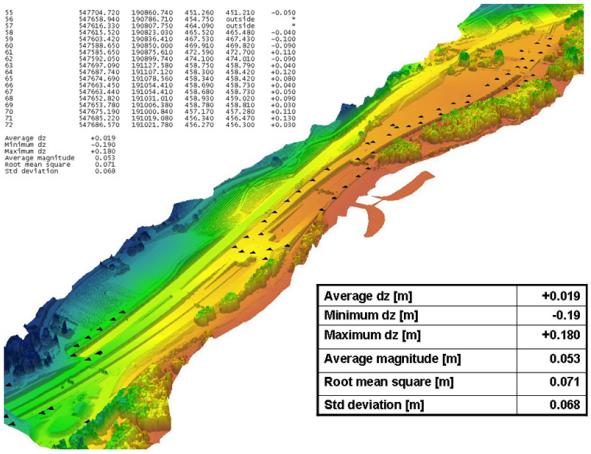

Fig. 5.8: Example for DTM quality control by GCP (marked as ▲) measurements.

There exist several methods to improve the general applicability of GCP derived height accuracies. The so-called Koppe formula for example allows expressing the height accuracy σ_H in function of the height measuring accuracy σ_Z, the planimetric measuring accuracy σ_G and the terrain slope α:

$$\sigma_H = \sigma_Z + \sigma_G \tan \alpha \tag{5.3.1}$$

[63] proposes an extension of Eqn. 5.3.1, where the DTM accuracy is computed considering the slope and the initial point density:

$$\sigma_H = \frac{a}{\sqrt{n}} + b \tan \alpha \tag{5.3.2}$$

where n is the point density in $points/m^2$ and (a, b) are terrain-dependent constant coefficients. However, the drawback of this methods remains its general applicability, as the model coefficients have to be determined empirically using large datasets with well known reference heights. In general, these values are not transmissible one-to-one across datasets of different type and accuracy.

Horizontal Error Assessment

Although horizontal errors in ALS data can be several times larger than height errors [184], recommendations regarding horizontal accuracy reporting have less been investigated [123]. This is mainly rooted in the fact that laser points do not carry semantic information and often the point density is too coarse for precisely locating distinct surface features [38]. Lately, several methods to assess the horizontal accuracy have been developed: For instance [133] proposes the so-called back-projection, where features in imagery are compared with their counterparts in the point-cloud. Methods without need of photogrammetric data are reported in [24], deploying signalized targets identifiable in the laser intensity image or in [49], using surface matching techniques.

5.3.3 Automated DTM Quality Assessment

The standard approach to perform DTM quality assessment remains highly correlated to the site conditions (such as slope, undergrowth, vegetation cover) and the mission parameters (such as flying height, employed equipment, etc.). There is also a consensus in the ALS community that there should be a differentiation in DTM quality analysis between precision, absolute and relative accuracy and reliability. Hence, a quality measure should also give an answer to questions such as how dense the data is, or how the accuracy is distributed. One way to respond to these questions are the generation of data distribution maps, such as the density map (see Chap. 5.1.2), depicting the amount of discretization of the terrain surface, or the distance map, indicating the distance to the nearest data point for each pixel center (e.g. [64]). This section proposes a novel procedure that enables the generation of a DTM quality map encapsulating all these factors assuming that the following two conditions are hold:

- The accuracy $(\sigma_x, \sigma_y, \sigma_z)$ of each ground point involved in DTM generation is known.
- The DTM is represented as a regular raster where the height values are calculated by projecting the cell center coordinates on the corresponding facet of the TIN which nodes are the irregular sampled ground points as depicted in Fig. 5.9.

Computation of DTM Quality Map

Let us consider the plane equation for a facet (with nodes **a**,**b**,**c**) of a TIN (Fig. 5.9):

$$ax + by + cz + d = 0, \text{where } \mathbf{n} = \begin{pmatrix} a \\ b \\ c \end{pmatrix} = \begin{pmatrix} n_x \\ n_y \\ n_z \end{pmatrix} \tag{5.3.3}$$

is the normal vector of the facet that can be computed by

$$\mathbf{n} = (\mathbf{c} - \mathbf{a}) \times (\mathbf{b} - \mathbf{a}) \tag{5.3.4}$$

By inserting Eqn. 5.3.3 into Eqn. 5.3.4 and introducing the node coordinates of point **a**, the height value Z_i for a given 2D coordinate (X_i, Y_i) can be directly computed by

$$Z_i = d - aX_i - bY_i \tag{5.3.5}$$

where

$$a = \frac{n_x}{n_z} = \frac{(y_c - y_a)(z_b - z_a) - (z_c - z_a)(y_b - y_a)}{(x_c - x_a)(y_b - y_a) - (y_c - y_a)(x_b - x_a)}$$
$$b = \frac{n_y}{n_z} = \frac{(z_c - z_a)(x_b - x_a) - (x_c - x_a)(z_b - z_a)}{(x_c - x_a)(y_b - y_a) - (y_c - y_a)(x_b - x_a)}$$
$$d = ax_a + by_a + z_a$$

Applying the law of error propagation to Eqn. 5.3.5, the direct estimate of the height accuracy of Z_i can be formulated such as:

$$\sigma^2_{Z_i} = \mathbf{F}\mathbf{C}_{ll}\mathbf{F}^{\mathrm{T}}. \tag{5.3.6}$$

where Matrix $\mathbf{F}$ can be constructed as the partial derivatives of Eqn. 5.3.4 and the node coordinates:

$$\mathbf{F} = \begin{bmatrix} \frac{\partial Z_i}{\partial x_a} & \frac{\partial Z_i}{\partial y_a} & \frac{\partial Z_i}{\partial z_a} & \frac{\partial Z_i}{\partial x_b} & \frac{\partial Z_i}{\partial y_b} & \frac{\partial Z_i}{\partial z_b} & \frac{\partial Z_i}{\partial x_c} & \frac{\partial Z_i}{\partial y_c} & \frac{\partial Z_i}{\partial z_c} \end{bmatrix} \tag{5.3.7}$$

The stochastic model $\mathbf{Q}_{ll}$ is constructed using the variance information for each node:

$$\underset{9\times 9}{\mathbf{C}_{ll}} = diag\left[\ \sigma^2_{x_a} \quad \sigma^2_{y_a} \quad \sigma^2_{z_a} \mid \sigma^2_{x_b} \quad \sigma^2_{y_b} \quad \sigma^2_{z_b} \mid \sigma^2_{x_c} \quad \sigma^2_{y_c} \quad \sigma^2_{z_c}\ \right] \tag{5.3.8}$$

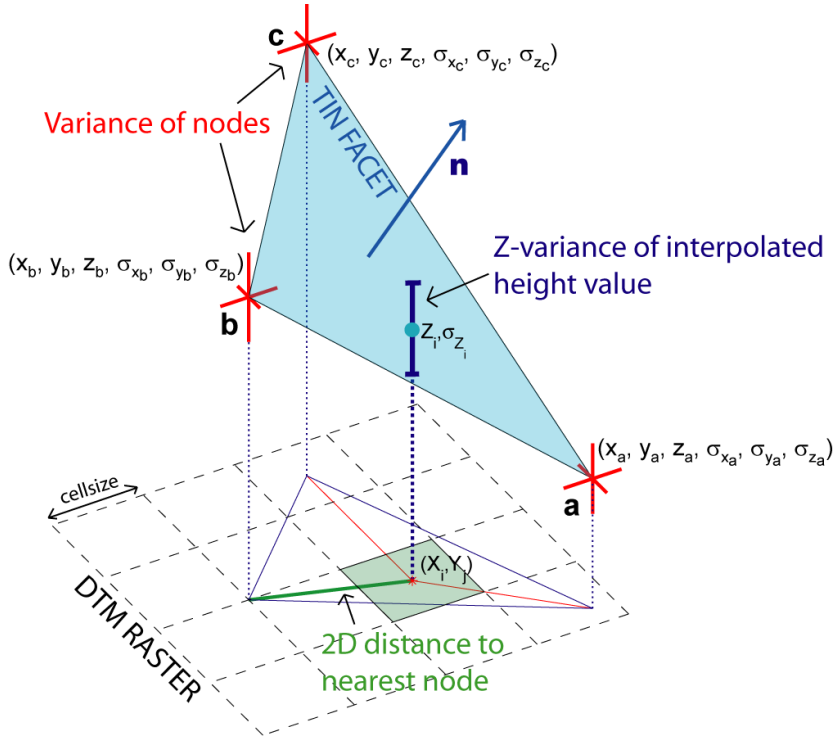

Fig. 5.9: Propagation of individual point errors to DTM height by TIN interpolation.

Depending on the raster cell-size (c), it can be determined whether the newly computed height value is based on a interpolation or extrapolation process. The Nyquist-Shannon sampling theorem [138] states that if a function $x(t)$ contains no frequencies higher than f, it can be completely reconstructed by points spaced $1/2f$ apart. Adopting this theorem to DTM generation, it can be deduced that a original sampling of half cell-size is needed to correctly describe the terrain features of the given output frequency (in our case c). Accordingly, if a pixel center coordinate is closer than $c/2$ to the initial node, the new value can be assumed as correctly interpolated. Hence, the terrain features at the output sampling rate are correctly represented. If the distance is larger than $c/2$, the height is supposed to be extrapolated. To incorporate this interpolation/extrapolation process into the DTM quality analysis, the 2D distance (d_{min}) of the pixel center coordinate to the nearest node (see Fig. 5.9) is applied to scale the computed height accuracies by the factor s to produce a height reliability index r_z:

$$r_z = \sqrt{s \cdot \sigma_{Z_i}^2} \begin{cases} s = \frac{d_{min}}{c} + 0.5, & \text{if } d_{min} \leq \frac{c}{2} \\ s = 2\frac{d_{min}}{c}, & \text{if } d_{min} > \frac{c}{2} \end{cases} \tag{5.3.9}$$

Finally, this index can be computed for every grid cell of the DTM and can be represented as a raster, serving as DTM quality map.

Application Example

Fig. 5.10.D shows such a quality map computed for an ALS point-cloud where the distribution of automatically classified ground points (see Fig. 5.10.A) is very disparate and contains important data gaps, i.e. due to dense vegetation and water cover. The triangulation process is closing these data gaps (see Fig. 5.10.B). In these areas, the derived DTM values (Fig. 5.10.C) are distant from the initial node points. They cannot be considered as trustful as they are the result of an extrapolation process. Due to the scaling of the height variance ($\sigma_{Z_i}^2$) yielding the height reliability index r_z (see Eqn. 5.3.9), the final quality map reflects the reliability deterioration for such areas (see e.g. water surface in upper part of DTM). The visual

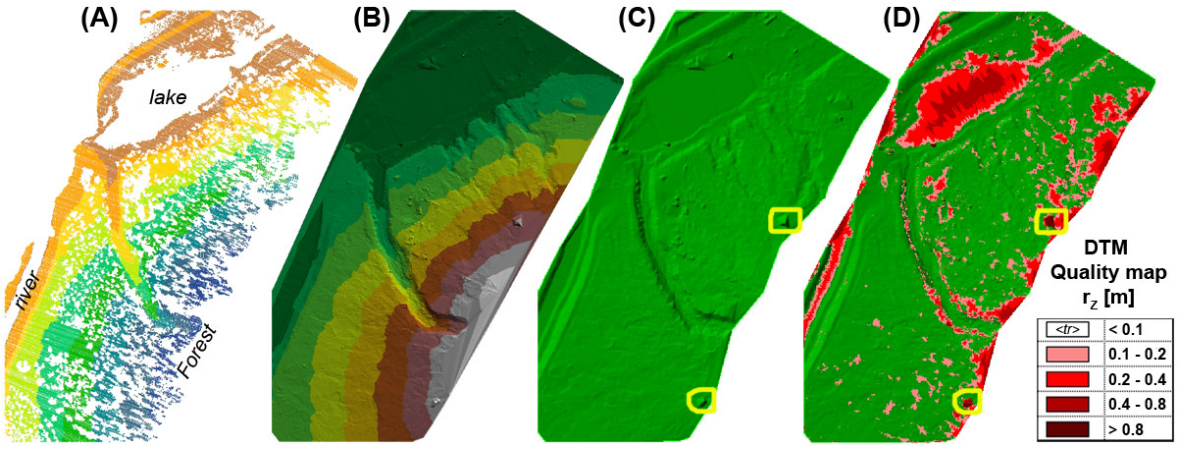

Fig. 5.10: (A) Automatically classified ground points color-coded by elevation, (B) DTM-TIN, (C) DTM raster interpolated from TIN, (D) DTM quality map superposed on DTM color-coded by index r_z (cells with $r_z < 0.1$ are transparent).

inspection of the hillshaded DTM (Fig. 5.10.C) allows identifying several wrongly classified points that can be seen as single peaks in pyramidal form (marked yellow in figure). As the slope of these incorrect TIN facets is normally much steeper than the slope of its neighbors, the resulting height variance (using Eqn. 5.3.6) is much larger. This enables highlighting such areas of incorrectly classified points, as they appear as zones with decreased height accuracy (dark red).

Applicability of DTM Quality Map

Similar to the concept discussed in Chap. 4.8.1, these quality maps can be employed as quality metadata associated to the DTM. These quality maps indicate areas where the height values are reliable and areas where they should be considered with precaution. DTM quality maps also represent a valuable asset to estimate the accuracy of DTM derived quantities (i.e slope, aspect). The availability of such cell-wise quality indicator allows constructing weighting schemes for DTM's generated by merging data of different sources and accuracies (e.g. [190]). Additionally, applying the laws of error propagation, the height accuracies of the merged rasters can be estimated. The applicability of such concept for in-flight processing will be discussed in Chap. 6.7.10.

Chapter 6

Implementation

Chapters 2 to 5 have presented the scientific background of the ALS technology and the different concepts to perform ALS data quality assessment. This chapter focuses on the challenges to incorporate such concepts in a fully functional in-flight quality monitoring tool. The implementation of such a tool together with its integration into an existing ALS system will be described in detail.

6.1 Handheld Airborne Mapping System

EPFL possesses a short-range laser system called Scan2map. This system was used as platform to implement the in-flight QC concepts presented in this thesis. The following section provides a short overview about the history of this system and the employed hardware components.

6.1.1 History of Scan2map

The development of an airborne mapping system, called **HELIMAP®**, started in 1998 at the Swiss Federal Institute of Technology (EPFL) as a response to the requirements of SLF Davos in mapping avalanches and snow transport [59, 177]. The most attention was payed on high resolution and accuracy ($10 - 15\,\text{cm}$), low cost and system portability (such as independence from a carrier [158]). The sensor block was designed to be light and small enough to be handheld by an operator. At the beginning, the system was based on handheld analog photogrammetry operated from the side of a helicopter. The system then progressively integrated GPS positioning, GPS/INS georeferencing, a high resolution CCD camera and finally a laser scanner unit. In 2005, a commercial spin-off company was founded [178] that exploits the system commercially for all kinds of large-scale airborne mapping projects.
Under the new name **Scan2map**, the Geodetic Engineering Laboratory (EPFL-TOPO) has continued its developments. Currently, the Scan2map-system integrates the latest in sensor technology and in sensor orientation and calibration. The system operates in missions related to natural hazard management and corridor mapping while serving the academia as a unique research tool. When needed, its data are exploited by universities, mapping-agencies, administrations and rescue services (e.g. [92, 159]).

6.1.2 Concept

The system concept adopts a modular design with off-the-shelf sensors and modern communication links to facilitate upgrades or hardware replacements. Its basic architecture allows the combination of different sensors (LiDAR, digital camera, IMU and GPS) without requiring a dedicated carrier for its utilization. Its structure and the "handheld" or "hook-on" mounting (see FIG. 6.1) is unique world-wide and represents number of advantages that can summarized as follows [159]:

- Lightweight carbon-aluminum structure that combines GPS/INS/LiDAR with a high resolution digital camera to a common compact sensor block (40x40x25 cm/12 kg). The block can be handheld or suspended on the side of a helicopter.
- Optimal setup for large-scale/small-area airborne surveying in demanding topography.
- Very little installation time (< 30 min) is required, thus allowing fast deployment on a short notice. Due to the sensor structure, boresight and GPS leverarm are not needed to be re-calibrated for different installations.
- Oblique and nadir surveying can be performed within the same flight. As shown in FIG. 6.2, the usual accuracy degradation due to the high incidence angle on steep surfaces is eliminated by turning the sensor head towards the slope, simulating a scanning geometry comparable to flat terrain (see also CHAP. 4.7.1 Scenario 3). This is achieved either manually (handheld installation) or during the setup (suspended installation).
- The scanner and the digital camera have a similar FOV of 60° and 56°, respectively. The flying parameters (height and speed) can be kept optimal for both devices.

FIG. 6.1: Scan2map-system suspended on the winch of a helicopter.

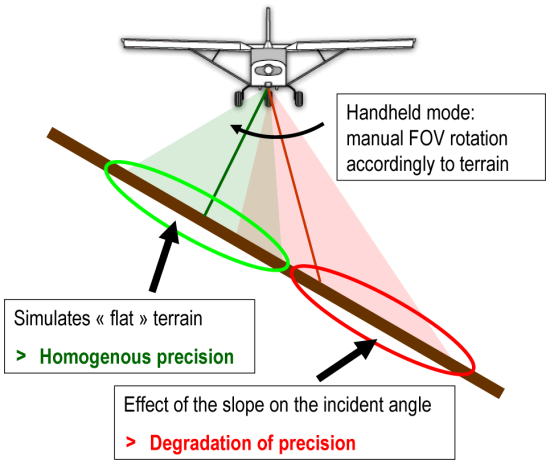

FIG. 6.2: Manual rotation of scanner towards slope to improve scanning geometry.

6.1.3 Hardware System Architecture

As illustrated in Fig. 6.3, the Scan2map-system can be divided into three main segments that intercommunicate via a common high-speed Ethernet assuring fast data exchange between the segments and the devices within:

- **Sensor Head:** The sensor head consists of navigation and remote-sensing devices, all rigidly joined by a carbon-aluminum structure. Besides the sensors, the structure also contains anchorage points for safety cables and suspension as well as handles for manual steering (see also Fig. 6.1). A button for manual image triggering is connected to one handle together with a switch for accepting automatic trigger from a PC. The automated triggering is based on RT analysis of the navigation data and optionally also the scanner data.
  The scanner (Fig. 6.3.A) is a short-range 2D scanner (RIEGL LMS-Q240-60i). Its FOV is 60° and the instrument has a maximum range of 450 m at 80% reflectance [119]. The rotating-mirror mechanism provides linear, unidirectional and parallel scan lines with a programmable rate up to 80 scans/s (10 kHz). The beam divergence is 3 mrad. Contrary to most today's airborne scanners, this instrument adapts a shorter laser wavelength of 900 nm that assures favorable reflection also on fresh snow.
  The digital camera (Fig. 6.3.B) is a Hasselblad H2 with focal length of 35 mm. Attached to the lens is the digital back Imacon Xpress 132C. The hosted CCD chip has 5448×4080 pixels (22 Mpix) with 9 μm pixel size. The shutter aperture generates a pulse that is interfaced via X-sync bus of the H2 camera to the event marker input of the GPS receiver.
  The sensor head also incorporates a tactical-grade IMU (Fig. 6.3.C) (Litton LN200/A1) and a GPS-L1L2/GLONASS airborne antenna (Fig. 6.3.D). The antenna is mounted on a carbon pole that can change its orientation with respect to scanner/camera plane from 15° to 90° according to the mapping requirements.

- **Data Rack:** The sensor head is connected via cables to the data rack, a solid cube placed inside the helicopter that assures instrument power supply, command, data synchronization and data storage. The LOG-PC (Panasonic Toughbook CF-19) is charged with the data acquisition and logging of the raw GPS, IMU and scanner measurements. The scanner data is directly transmitted using the Ethernet and logged on the LOG-PC. The GPS dual-frequency data passes through the GPS receiver and is sent to the NAV-PC for logging. The IMU is connected to the Ethernet via a specially designed interface [160, 183] that synchronizes the incoming inertial data in the GPS time frame and transmits them to the LOG-PC. The camera events are time-stamped by the dual-frequency GPS receiver, and this information is further processed by the LOG-PC. The taken images are stored on an external image bank that allows taking up to 850 pictures at full resolution. Finally, an uninterrupted power supply ensures seamless switching between helicopter and 24 VDC battery power.

- **Controlling and Guidance:** This segment consists of the NAV-PC (Panasonic Toughbook CF-19) connected through Ethernet to the data rack. The pilot screen (8 inch XClear TFT-screen) for pilot guidance is connected with a VGA cable to the NAV-PC. The NAV-PC is dedicated to mission and system control, pilot guidance, ALS data pro-

cessing and quality analysis. The functional principle of the different software modules involved in these processes will be explained in detail in the following sections.

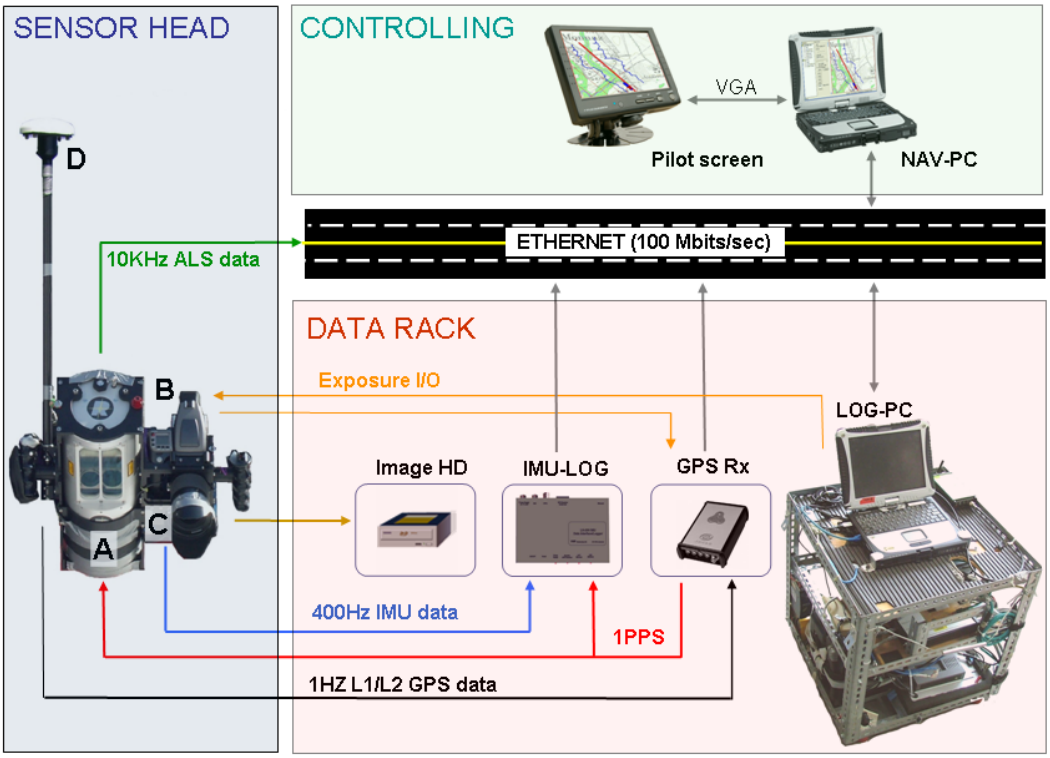

FIG. 6.3: General architecture of the Scan2map-system.

6.2 Flight Preparation

6.2.1 Flight-plan

Although not directly linked to the in-flight quality assessment, the flight-plan preparation is a crucial step in order to obtain the required mapping quality and its elaboration is worthwhile to be elucidated. The previously discussed particularities of the Scan2map-system also have a strong impact on the flight-plan establishment. The flexibility in gaze direction (due to the handheld mode) as compared to classical ALS systems (i.e. fixed installation of the laser head on a plane), involves more accurate flight-planning where the virtual swath for a given flight-line should be computed. For this purpose a flight-planning module (called MissionPlanner hereafter) has been developed (see FIG. 6.4). The main features of the MissionPlanner are [127]:

- Interactive drawing of flightlines where the obliquity (roll-angle) and height system (absolute height, constant height over ground, height over ground at starting point) can be specified.

- Computation of a virtual swath based on scanner characteristics (FOV, max. range), flightline characteristics (height and obliquity) and a coarse DTM of the area.
- Point-cloud accuracy prediction based on the scanning geometry (reconstructed using the virtual laser direction and the DTM) and a-priori assumptions about the navigation, range-finder and calibration accuracies.
- Computation of virtual data coverage maps to control whether the planned lines result in sufficient strip overlaps.
- Survey time estimation based on planned lines and the assumed flying speed on a flightline and during transfer.
- Export of trajectory to Almanac-module (see next section) for GPS constellation analysis.
- Export of flight-plan in xml-format to flight management system HELIPOS (see Chap. 6.8).

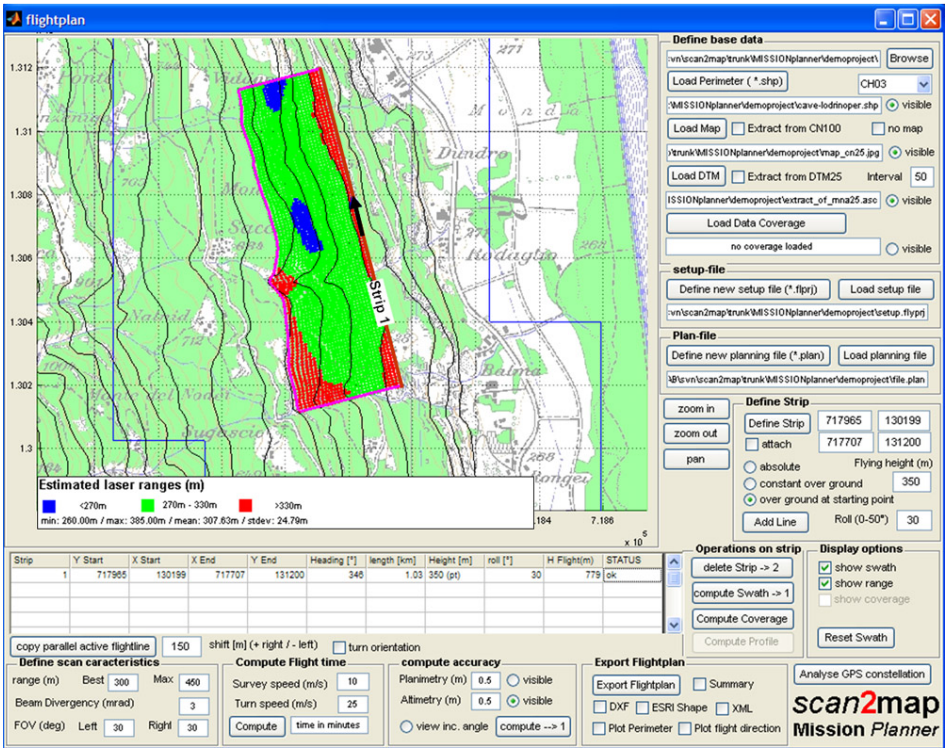

Fig. 6.4: GUI of MissionPlanner: Example of range estimation for one flightline with 30° obliquity.

6.2.2 Analysis of GPS Constellation

For mapping missions at low altitudes and in demanding topography, partial GPS satellite masking by the relief is very frequent and can lead to situations where a good navigation solution cannot be guaranteed (e.g. [110]). As the GPS constellation changes constantly, the

impact of terrain masking is not only dependent on the position and its associated horizon (also called skyplot), but also on the time when the mission is flown during the day. The modeling of the GPS constellation implemented in the Almanac-module considers these additional constraints. It computes satellite visibility maps for given 3D waypoints at a given time and deduces GPS constellation characteristics (such as DOP values, min. number of visible satellites) for each waypoint independently (see FIG. 6.5). To determine the most optimal flying time, the tool also features an algorithm, that searches for the most optimal starting-time: For every starting-time, the waypoint with the worst GPS characteristics (high DOP values, low number of visible satellites) is stored and compared to the worst-case for the other starting-times. This finally yields a plot of the evolution of the GPS quality throughout the day for a given flight (see FIG. 6.6).

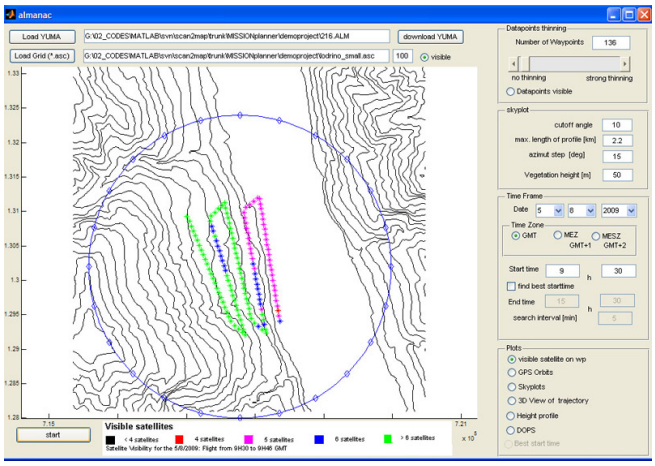

FIG. 6.5: Almanac module analyzing GPS constellation for a given flight-plan.

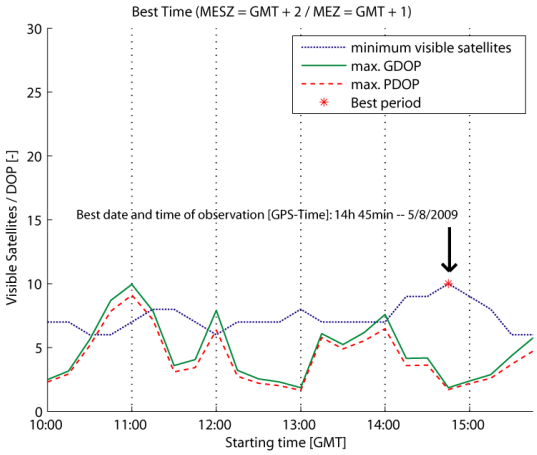

FIG. 6.6: Plot to indicate best flight time based on flight-plan and given time window.

6.3 In-flight Quality Assessment Tool (IQUAL)

As mentioned in the introductory chapter, the presented in-flight quality assessment tool (called **IQUAL** hereafter) was developed as an integrated effort at the EPFL-TOPO laboratory. The external contributions will be referenced wherever applicable. This section provides a general overview of the IQUAL architecture and functionalities. The different modules will be presented in more detail in the sequel.

6.3.1 General Strategy

As shown in CHAP. 6.1, the Scan2map-system is based on a modular design on the hardware level, with the Ethernet as a backbone for interfacing the individual elements. This modular design approach has also been adopted on the software level to allow scalable distribution of tasks across a network of computers. The setup and implementation of the different software modules for data acquisition, synchronization and processing was guided by the following principles [130]:

- **Independence of system functionalities**: The vital functionalities, such as raw data logging, synchronization and pilot guidance, must be independent from the extended functionalities (RT point-cloud processing and quality analysis) in order to avoid any disturbance with the needed functionalities for a successful data acquisition.
- **Performance scalability**: The second goal promises handling different scanning rates by means of separating modules individually (or in groups) across different computational platforms.
- **Centralized monitoring and control**: Despite the fact that the acquisition and processing is split on different modules, the information and the control of the individual functionalities must be communicated to one central interface.

6.3.2 Communication

The fundamental prerequisite for achieving the goals mentioned in the previous section is a fast communication across all hardware and software components. The Ethernet with TCP/IP protocol has been chosen for this purpose. In the particular case of the Scan2map-system, the Ethernet communication is already built-in in the scanner and IMU modules [160], while the GPS receiver needed to be interfaced to the network. The timing scale is governed by a 1 PPS signal sent by the GPS receiver and the timing offset is communicated between the modules via Ethernet. Based on the client-server architecture developed by [169], the different modules can send (as server) and receive (as client) data packages through socket ports whose corresponding IP addresses and port numbers can be freely chosen. Accordingly, the modules can be placed either on one computer or distributed on several computers connected to a network, where each module can be addressed by the corresponding IP-address of the computer and the associated ports.

6.3.3 Software Modules

Fig. 6.7 depicts the software modules and interconnections involved in IQUAL. The modules can be divided into three categories:

1. **Data logging**: All hardware devices have a proprietary data logging software module. These modules can run on different processors if needed. Each module is responsible for storing the raw data and for passing them together with a status message to the connected clients. The logging modules are:
   - ALS DataLogger [147]
   - IMU DataLogger [183]
   - GPS DataLogger [170]
2. **Data processing**: The modules dedicated to in-flight data processing connect to the data acquisition modules by Ethernet to gather the necessary input data. These modules are:
   - **GPSQUAL**: RT GPS quality analysis tool [165]

- **GIINAV**: The RT strapdown inertial navigation and GPS/INS integration engine [168]
- **LIEOS**: RT laser point-cloud georeferencing engine [150]
- **LIAN**: The **LI**DAR data **AN**alysis module

3. **Guidance and Controlling**: The control module **HELIPOS** runs as a separate instance (usually on a different processor) and connects to all data acquisition and processing modules in order to monitor their performance by means of status messages. HELIPOS is also in charge of the pilot guidance.

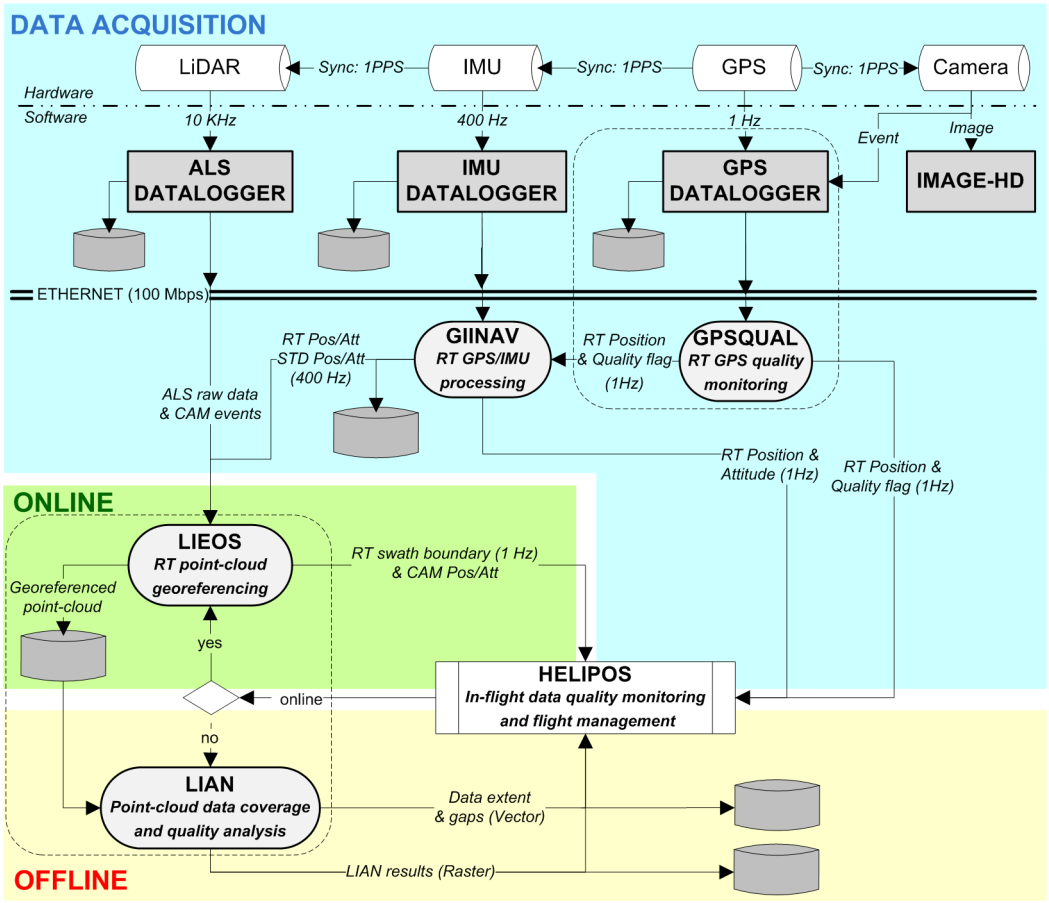

FIG. 6.7: IQUAL: Software architecture and inter-modular communication.

6.3.4 Inter-modular Communication

The data streams presented in FIG. 6.7 can be divided into three phases [131]:

1. **Data acquisition**: As soon as the system is started, the raw measurements are transmitted through proprietary devices to the data loggers and stored on disk. From the receiver the timestamps for each image event are communicated to the GPS data logger. The latter transmits the raw GPS measurements to the GPSQUAL-module that

performs a RT quality check. From there, the actual position (including a GPS quality flag) is transmitted to HELIPOS for displaying and to GIINAV for GPS/INS integration. GIINAV receives the GPS position and velocity solution as well as IMU measurements to compute RT attitude and position estimates and their respective variances. The resulting trajectory information is transmitted at the original IMU output rate (400 Hz) to the LIEOS module. GIINAV also broadcasts trajectory information (position and attitude) at 1 Hz to HELIPOS for display and system control purposes.

2. **Online**: LIEOS generates the point-cloud by merging the trajectory with the laser measurements broadcast by the ALS data logger (see Chap. 6.6). In addition, the point-cloud coordinates and all information needed for the error propagation is saved to a file. The RT swath boundaries are directly sent to HELIPOS for displaying (see Chap. 6.8).

3. **Offline**: LIEOS stops the georeferencing and the computed point-cloud of the previous flightline is loaded to LIAN (see Chap. 6.7). The strip is analyzed as one block and the outcome is sent to HELIPOS for displaying in form of vector and raster data (see Chap. 6.8).

Splitting of Online and Offline Phase

The distinction between the online and offline phase is made by the system operator. By pressing the on/offline button on the HELIPOS-GUI (see Fig. 6.24), the operator communicates to LIEOS, whether the system is online, thus activating the georeferencing of the point-cloud, or offline (e.g transfer flight, turn over from one flightline to the other), where no laser data will be used.
The reasons for implementing this control mechanism are manifold: The temporal splitting of the two main tasks (i.e. the RT georeferencing vs. strip-wise data analysis) allows keeping the CPU requirements at reasonable level. Performing both tasks in parallel would significantly increase the computational burden and could threaten the RT monitoring capacity. Additionally, by pressing the on/offline button in the HELIPOS application, the operator ensures that the computationally demanding analyses (such as the error propagation) are carried out only over the areas of interest.

6.4 GPS Quality Analysis Module (GPSQUAL)

The main task of GPSQUAL is to broadcast a quality flag for every GPS position that should reflect the likelihood of fixing the differential carrier-phase ambiguities in PP (see Fig. 6.8). The availability of technologies enabling RT resolution of the ambiguities (such as RTK) cannot be guaranteed for every survey mission. Hence, the tool must be capable of evaluating the likelihood for ambiguity resolution based on the raw GPS observations only. For this purpose GPSQUAL integrates a selection of the quality check approaches presented in Chap. 2.4.4 into a single algorithm. The algorithm adopts a “best from available” strategy [165], where the used checking mechanism is selected and adapted automatically in function of the collected raw data and the availability of additional information. To increase the computational efficiency, GPSQUAL is directly implemented as an embedded thread within the GPS Datalogger.

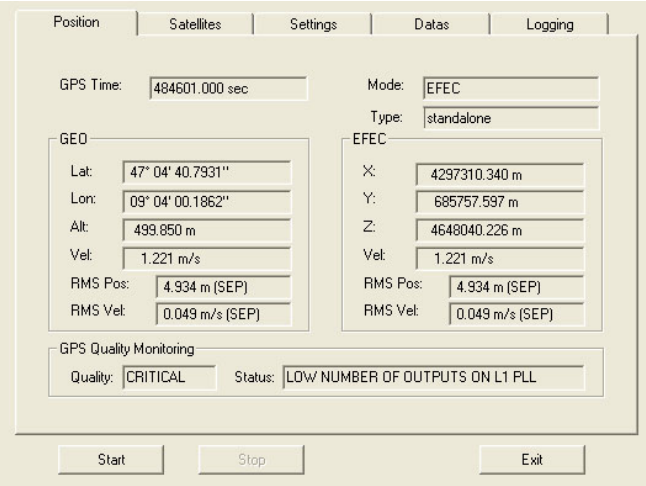

FIG. 6.8: GPS DataLogger GUI: Display of GPS position and quality flag issued by GPSQUAL.

6.4.1 Quality Indicators

GPSQUAL employs the following indicators (in order of their availability) to perform the GPS signal quality evaluation and to predict the likelihood to fix the ambiguity in PP:

- Analysis of the GPS constellation
- Carrier-phase tracking loop output analysis
- Cycle slip detection
- Receiver Autonomous Integrity Monitoring (RAIM)
- RTK

Method	GPS constellation	Phase tracking loop	Cycle slip detection	RAIM	RTK
Availability	always	always	always	Rx dependent	locally
Reliability of information	very high	high	high	very high	high
Accuracy of ambiguity fix prediction	fair	good	good	fair	very good
Technical feasibility	very good	very good	very good	very good	fair
External costs	none	none	none	Rx dependent	high

TAB. 6.1: Comparison of different GPS quality indicators used in GPSQUAL.

Except RTK and RAIM, all indicators depend on raw GPS observations only. The applicability of the proposed strategy is therefore independent of the used GPS positioning mode. Nevertheless, the usability for predicting the ambiguity resolvability remains only indicative. The best prediction can be achieved by solving the ambiguities directly on-the-fly using RTK. TAB. 6.1 summarizes the respective strengths and weaknesses of the individual indicators in function of availability, prediction accuracy and external costs. More details about the different quality indicators implemented in GPSQUAL can be found in [165].

6.4.2 Quality Flags

The final quality attribute computed by GPSQUAL can have three levels (Fig. 6.9):

- **Good**: The ambiguities should be fixed in PP without problem or are already **fixed** in the RTK operation. The expected 3D position accuracy should be below 0.1 m.
- **Critical**: It is most likely that the ambiguities can only be resolved partially or with low reliability. This equals to a **float** status under RTK. The GPS position accuracy is expected to be between 0.1 and 0.5 m.
- **Bad**: No ambiguity fix possible (**standalone** mode in RTK), the expected accuracy equals the float ambiguities or carrier-phase smoothed code solution (expected positioning accuracy > 0.5 m).

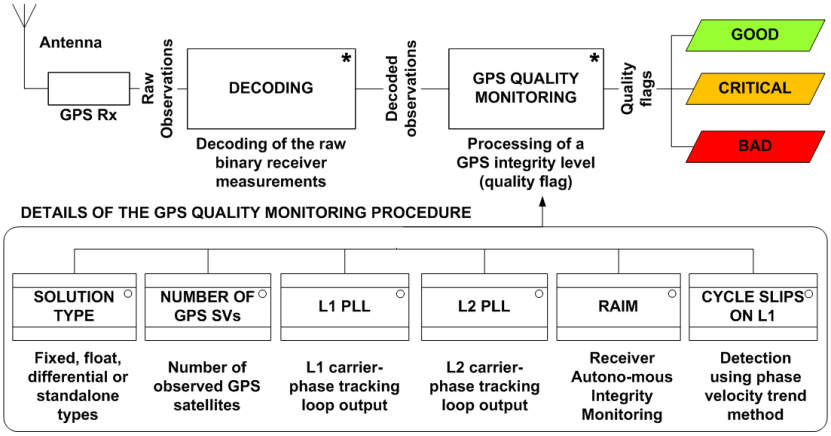

Fig. 6.9: Workflow for quality flag generation within GPSQUAL.

The use of such quality flags is twofold: Firstly, the quality flag associated to each GPS position is immediately presented to the system operator as color-coded quality marks (see Chap. 6.8). Secondly, for the purpose of ALS point-cloud quality analysis, the outputted position covariance of the GPS/INS integrated solution can be adopted to anticipate the achievable accuracy in PP. This yields more realistic position accuracy estimates which are subsequently used as input values for the strip-wise error propagation (see Chap. 6.7.9).

6.5 RT GPS/INS Integration Engine (GIINAV)

6.5.1 Integration Strategy

The navigation module GIINAV consists of a RT strapdown inertial navigator combined with an Extended Kalman Filter (EKF) for GPS/INS integration based on the work presented in [168, 171, 172]. The integration scheme follows a loosely-coupled approach, i.e. GPS position and velocity measurements are used to update the EKF state vector which is composed of a total of 22 elements, including the nine basic navigation errors (position, velocity and attitude) and the most significant inertial sensor errors (accelerometer/gyro biases and scale

factors) [168]. The reference trajectory around which the linearization of the EKF occurs is provided by the local-level strapdown inertial navigation algorithm which is by itself a self-contained navigation solution affected by errors. The errors estimated by the EKF are in turn used to continuously correct this strapdown navigation solution and calibrate on-the-fly the inertial sensor measurements, as depicted in Fig. 6.10.
The inertial data is processed at its original sampling rate (i.e. 400 Hz in the current configuration of the Scan2map), while the GPS data rate is typically set to one second. The results can be stored to a file, displayed in RT (see Fig. 6.12) and transmitted to different clients via socket connection.

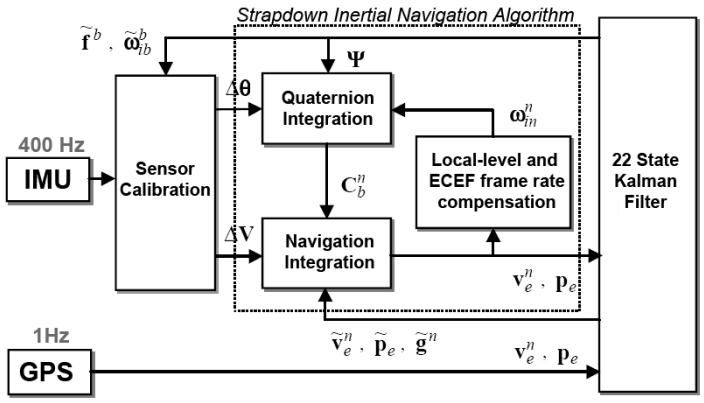

Fig. 6.10: GIINAV GPS/INS integration scheme (adapted after [171]).

6.5.2 IMU Alignment

One of the critical parts of the integration algorithm is related to its initialization, in particular the determination of the initial orientation of the system. IMU alignment in combined GPS/INS systems is less critical than in standalone inertial systems. For the GIINAV navigation module, it is sufficient to know in which quadrant the heading lies, and orientation convergence to a few hundreds of a degree is attained thanks to GPS aiding. For standalone inertial systems, the alignment procedure has to attain this level of accuracy by itself, as no aiding is available to progressively improve this estimation.
Within GIINAV, the operator has the option to select among three coarse alignment modes (see Fig. 6.11):

- **Static alignment**: The initial attitude determination is carried out by gyrocompassing. The IMU deployed in the Scan2map-system has tactical-grade accuracy (gyro-drift of approximately 1 deg/h) and could therefore be used for static alignment by gyrocompassing according to the requirements of a combined GPS/INS system. However, it is very difficult to guarantee static conditions once the system has been installed (suspended on the winch). For this purpose, and for ensuring maximum operation flexibility, the static initialization can be constrained to a very short time provided that an approximate heading is known using some external information.

- **Transfer alignment**: This mode applies if the user has some knowledge about the initial orientation of the system (e.g. heading from an external compass reading).

- **In-flight or dynamic alignment**: The GPS velocity vector is used to approximately align the IMU.

To accommodate to the particular constraints imposed by the Scan2map-system and the coarse alignment procedures described previously, the fine alignment procedure uses a customized version of the large-heading error model proposed in [69] which tolerates well larger initial uncertainties. Hence, it is possible to completely initialize or re-initialize the system in-flight without imposing much restriction on the dynamics (even for a helicopter). The RT navigation performance of GIINAV will be discussed in Chap. 7.1.

Fig. 6.11: GIINAV GUI: Selection of the settings for the IMU initialization.

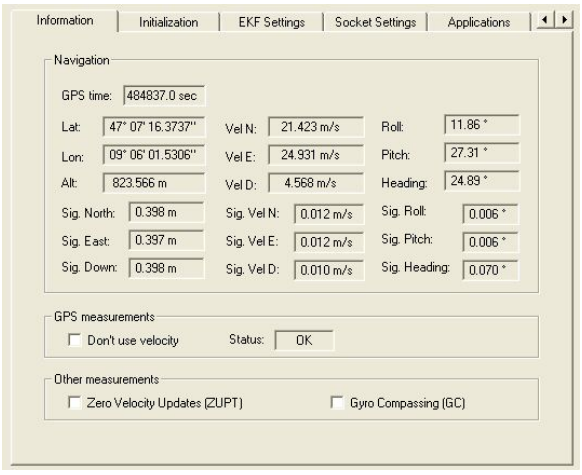

Fig. 6.12: GIINAV GUI: Display of the EKF results in RT.

6.6 RT ALS Georeferencing Engine (LIEOS)

The main role of the georeferencing module is to generate the laser point-cloud while on a flightline. As depicted in Fig. 6.7, the inputs to LIEOS are the LiDAR raw data (time, encoder angle, range and intensity) and the RT trajectory estimate outputted by GIINAV. For the output, LIEOS stores all laser point-cloud coordinates into a file and transmits points related to the swath characteristics (i.e. boarder and nadir points) to the flight-management module HELIPOS for displaying (see Chap. 6.8). If aerial images are taken on a same mission, LIEOS can also compute the exterior orientation (EO) elements and the projection center (PC) for each image event. This data can be logged to a file and transmitted to HELIPOS for display. Although principally designed for in-flight use, the georeferencing engine can also be used for off-line processing [150].

6.6.1 Configuration

The georeferencing algorithms implemented in LIEOS are optimized to allow processing throughput of "tens of thousands" points per second considering that the computational load per laser-return is influenced by several factors:

- Frequency of trajectory output
- Selected output datum/coordinate system
- Choice of the georeferencing/registration algorithm

As the first two factors vary per ALS system or its setup (e.g. scanner rates may vary from 10 to 180 kHz, trajectory rates from 10 to 400 Hz) and from one mapping project to another, all these settings are programmable via configuration files or the LIEOS GUI (see Fig. 6.13): In the processing settings, the user can select between different datums and projections, such as local plane coordinates, geodetic WGS84 coordinates (lat,long), UTM and local national mapping systems (e.g. Swiss national grid). In the algorithm settings, the point-cloud calculation method and the interpolation methods for position and attitude are configurable. The output settings enable to choose among different output formats (ASCII, LAS, TSCAN binary and proprietary binary format) and point selection method (complete line, only nadir point, only border points).

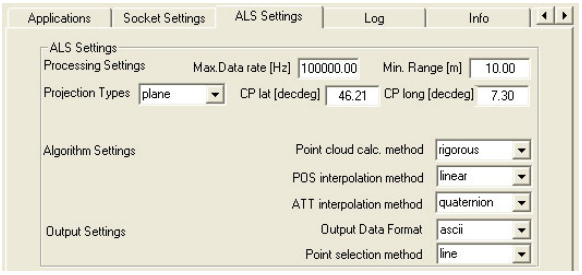

Fig. 6.13: LIEOS GUI: Selection of output datum an format and DG algorithm settings.

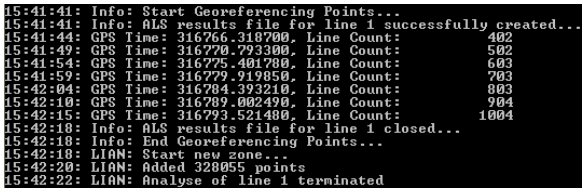

Fig. 6.14: LIEOS DOS-Shell: Display of actual processing status.

6.6.2 Georeferencing Algorithm

The point-cloud calculation method is of great importance for the performance of LIEOS, as the module should handle different laser data rates without loosing its RT georeferencing capability. Besides the implementation, the computation speed largely depends on the available processing power. Another way to influence dynamically the georeferencing speed is to perform either a data thinning (e.g. not all laser measurements are georeferenced in RT) or to adapt the algorithmic efficiency, thus admitting some loss of precision. Hence, to allow a most general use, the data thinning is configurable and three different georeferencing methods are implemented [130]:

- **Coarse**: The coarse option is an approximate method of sub-metric accuracy that is especially advantageous if the point-cloud is requested in the geographical coordinates. It is based on a spherical approximation of the georeferencing equation (Eqn. 2.2.8) expressed in geographical coordinates.
- **Approximate**: Despite its name, the approximate method provides residual distortions at sub-centimeter level (in most flight scenarios) and regardless of the terrain characteristics [80, 153]. Its choice is especially advantageous, if a) the registration is requested in the national coordinates, b) the ratio scanner/trajectory sampling is relatively high [80].
- **Rigorous**: The rigorous method is optimized for speed, but uses no approximations. It performs the calculation of the laser point-cloud coordinates in a Cartesian system (Eqn. 2.2.8) and then applies its rigorous transformation to the specified datum and projection.

The performance of LIEOS, in terms of accuracy and computational speed, will be discussed in detail in Chap. 7.1 and Chap. 7.4.1.

6.7 LiDAR Quality Analysis Module (LIAN)

LIAN represents the core of IQUAL as it performs on one side the in-flight analysis of the georeferenced point-cloud and on the other side the transmission of information about the data coverage and accuracy to the system operator. The LIAN module is in charge of computing these quantities using the raw point-cloud generated by LIEOS. To alleviate the comprehension of the different processes, in the sequel all explications refer to steps indicated by a capital letter in Fig. 6.15 (capital letters marked with * indicate optional steps).

6.7.1 Concept

LIAN is not implemented as standalone application but turns as a separate thread that is entirely managed within the LIEOS module. This ensures a good level of interaction between LIEOS (as data provider) and LIAN (as data analyzer).
If the system-status is online (Fig. 6.15.A), the `LIEOS-thread` is georeferencing the point-cloud. As soon as the system is offline (Fig. 6.15.B), the georeferencing of the point-cloud is stopped and the `LIAN-thread` is started (Fig. 6.15.C). It loads the strip-wise point-cloud file (`ALSfile`) generated in the previous pass into the memory.
At best, the LIAN processing should finish prior to the start of a new flightline, where the processor is charged again by the RT georeferencing. Nevertheless, this is not necessary and LIAN is still allowed to run in the background of LIEOS during the subsequent line. Only if at the end of the next line LIAN has not finished the analysis, a hard termination of the `LIAN-thread` is imposed. To avoid such situations, the LIAN implementation is targeted to be as quick and efficient as possible. For this purpose only the raw point-cloud data of the current flightline is loaded and further processed. All intermediate results are saved to external binary files. The naming of these files enables the unambiguous identification of each data type and

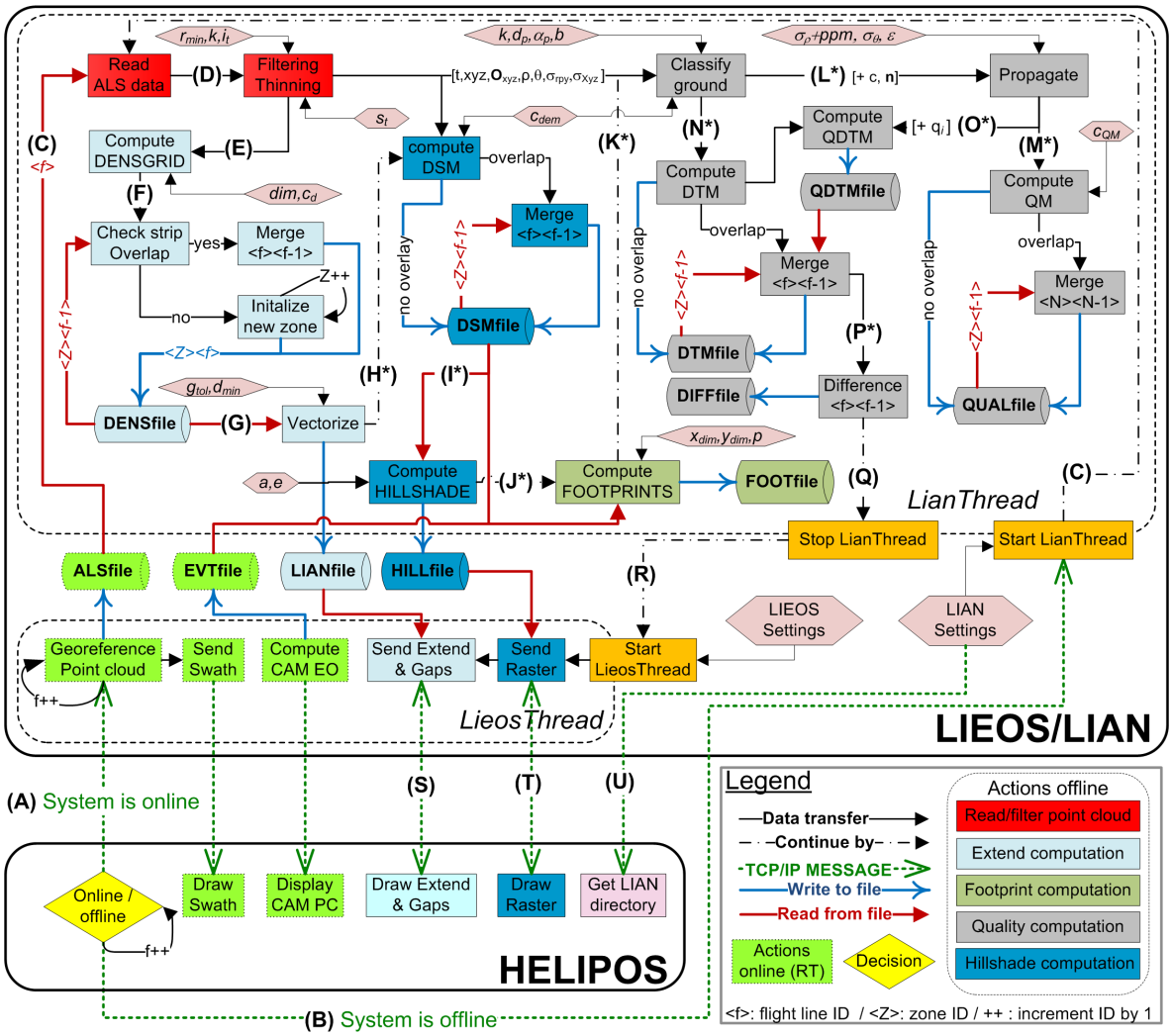

FIG. 6.15: LIAN/LIEOS workflow and communication with HELIPOS module.

its affiliation to a certain flightline $\langle f \rangle$ and flight zone $\langle Z \rangle$. Hence, once the LIAN-processing terminated, all internal memories dedicated to the `LIAN-thread` can be freed without any loss of information.

6.7.2 Configuration

The achievable LIAN performance and accuracy is in direct trade-off with the processing speed. The analyses should accommodate different ALS missions (thus different accuracy and point density requirements) and different scanners. Therefore almost all processing parameters are modifiable by the user either directly using the GUI (FIG. 6.16) or by a configuration file (see e.g. FIG. 6.17). Based on the operator's needs and the available processing power, the analysis can be restricted to a **"basic" in-flight QC**, including extent and gap detection and DSM/hillshade computation or enlarged to **"advanced" in-flight QC**, performing automated DTM generation followed by a full error propagation and quality map production.

Hence, depending on the project requirements and available processing power the algorithm can be parameterized by:

- Density raster resolution (c_d) and point density definition (2D or 3D)
- Minimum required point density (d_{min}) and vector generalization threshold (g_{tol})
- ALS data thinning rate (s_t) and thinning type (point-wise versus line-wise)
- DSM/DTM raster resolution (c_{dem})
- Point quality map resolution (c_{QM})

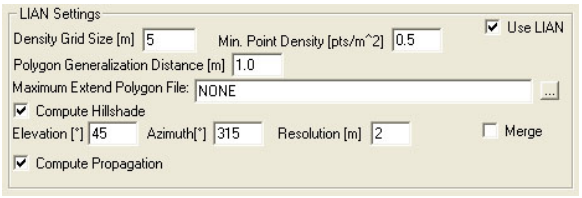

FIG. 6.16: LIAN GUI: Selection of the settings for LIAN processing.

```
; Boresight Accuracy (deg)
sBOREX = 0.005000
sBOREY = 0.005000
sBOREZ = 0.008000

; Lever arm Accuracy (m)
sAX = 0.010000
sAY = 0.010000
sAZ = 0.010000

; Encoder Angle Accuracy (deg)
sEnc = 0.000500

; Ranging Accuracy (m) (-)
sRange = 0.020000
sRange_PPM = 20.000000

; BeamWidth (mrad)
BeamWidth = 3.000000

; Ground Classification Parameters (m) (deg) (m)
sMaxBuildingSize = 20.000000
sPlaneDistance = 0.500000
sPlaneAngle = 20.000000
```

FIG. 6.17: Extract of LIAN configuration file for definitions of calibration and ranging accuracies.

6.7.3 Data Filtering

Prior any further processing by LIAN, the loaded raw point-cloud is passed through a filtering and outliers removal process (FIG. 6.15.D). To avoid incoherent height values, laser measurements with ranges below a certain threshold (typically $r_{min} = 10\,\text{m}$) are removed, as they generally represent non-desired measurements (e.g. scanned parts of carrier, zero-range points) and are of no interest in the further processing. Isolated points that occur below (e.g. due to multi-path) and above ground (e.g. cloud reflections) have also to be removed. Depending on the available computational power and the size of the file the module selects between two methods for point removal:

- ***N*-nearest neighbors search**: For every point his n-neighbors in a given volume are searched. If the number of neighbors is smaller than a given threshold, the point is considered to be isolated and is removed. This method is accurate and reliable but also time-consuming as a kd-tree has to be constructed for the whole dataset prior to the search and every point has to be tested individually.

- **Threshold on height variance**: This method is based on the mean height value ($\bar{Z}$) and the standard deviation (σ_z) of all heights to construct a boolean test:

$$\Delta Z_i = \left| Z_i - \bar{Z} \right| \begin{cases} \text{Leave point } i & \text{if } \Delta Z_i \leq k\sigma_Z \\ \text{Remove point } i, & \text{if } \Delta Z_i > k\sigma_Z \end{cases} \tag{6.7.1}$$

  Where k is the threshold that can be adopted in function of the terrain characteristics. This method is very quick, but may remove possibly correct points when the height difference (thus the variance) in the terrain is important and the threshold is not adapted accordingly.

To speed up the processing further, the raw data can also be thinned by a factor s_t using either point-wise thinning (only every n^{th} point is retained) or line-wise thinning (only every n^{th} scanline is read). The influence of the thinning on the accuracy of the analysis will be discussed in Chap. 7.4.2.

6.7.4 Strip Overlap Control and Zone Handling

Once the thinning process is finished, LIAN computes a density grid for the actual strip (Fig. 6.15.E), where the density raster cell-size (c_d) and the density computation dimension (2D or 3D: see Chap. 5.1.1) can be defined by the user. A crucial step in the whole processing chain is to check whether the strips of the actual and the previous flightline have overlapping parts or not and should be considered as continuous zones or not (Fig. 6.15.F). The main reason for this mechanism is the possibility to detect whether the analysis should be summarized over several strips (thus computationally more demanding) or if the information from the previous strips can be ignored and the analysis can start from scratch.

Testing the Overlap

The control of the overlap is performed by comparing the density grid of the actual strip with the one of the previous strip (if strip exists). An overlap is detected if for at least one pixel coordinate both density rasters have a valid value ($\rho > 0$). Depending on the result, two different actions take place:

1. **Merging of strips to one zone:** If the overlap check is positive, the scanned area is considered as one zone and the density grids of the previous line ($DENS_{f-1}$) and actual line ($DENS_f$) are merged together to construct one unique density grid ($DENS_{f*}$) by summation of the density values for a grid location x, y[1]:

$$DENS_{f*}[x, y] = DENS_{f-1}[x, y] + DENS_f[x, y] \tag{6.7.2}$$

   Hence, in the overlapping part the values of the new density grid $DENS_{f*}$ cummulate the initial point densities. Finally, the merged grid is saved to a binary raster file (`DENSfile`) and serves as foundation for the subsequent analyses.

[1] Valid for all operations merging raster A and B to C: if $A[x, y] = NaN \rightarrow C[x, y] = B[x, y]$, if $B[x, y] = NaN \rightarrow C[x, y] = A[x, y]$, if $A[x, y] = NaN$ and $B[x, y] = NaN \rightarrow C[x, y] = NaN$

2. **Initialization of new zone:** If the algorithm cannot detect an overlap, the two strips are supposed to have no semantic link. Accordingly, a new scanning zone is initialized, by incrementing the zone ID ⟨Z++⟩. No merge is performed, the density file is saved "as is" to a file.

6.7.5 Extent and Gap Detection

Once the density grid is available (either merged or not) the extent and gap detection starts (Fig. 6.15.G). Using the minimum density threshold (d_{min}), the cells in the grid are classified to NoData, Above-threshold and Below-threshold. Subsequently, the extent polygon is extracted using the boundary vectorization algorithm presented as pseudo-code in Alg. 6.1. The algorithm is based on a two-step procedure (see Fig. 6.18): First, starting at the upper left pixel, the algorithm searches for the polygon start node by testing whether a change from NoData to Data-pixel occurs. Second, the pixel transitions are investigated clock-wise from the start node to find a new NoData/Data transition, equivalent to a new node. If the found node is not already used in the polygon, it is a added and serves as new start node for the search of the next node. This procedure is repeated until the initial start node has been reached again.

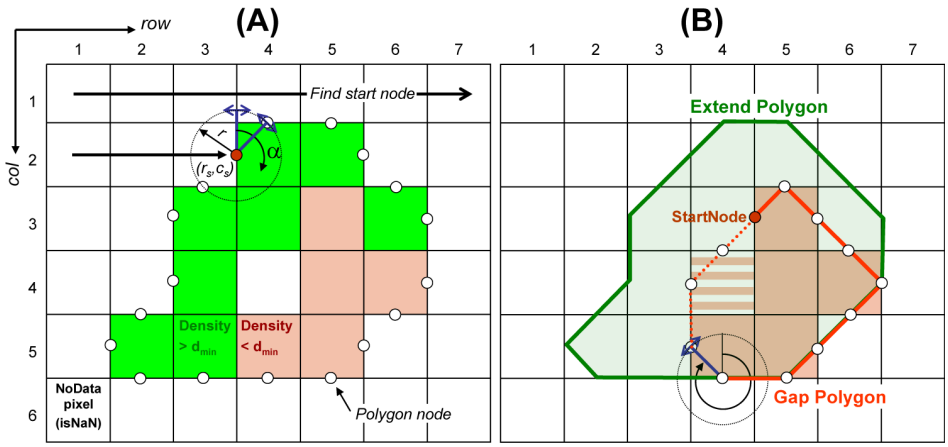

Fig. 6.18: Vectorization of laser data extent and gaps: (A) Density raster classified into NoData(NaN)-pixels and Data-pixels with density above threshold (green) and below (red), (B) Data pixels above threshold were classified to NoData in order to apply vectorization algorithm for the data gap.

LIAN defines gaps as zones within the data extent that either have no data (e.g. not covered by strip, no returns, etc.) or where the point density falls below a certain threshold (see Chap. 5.1.4). According to this definition, once the extent has been detected, all NoData-pixels within the extent are supposed to be gaps and can be classified as pixels of density 0 (see hatched pixel in Fig. 6.18.B), whilst the grid values above d_{min} are classified to NoData. Hence, new Data/NoData-pixel transitions appear that identify the gap borders. Subsequently, the vectorization of the gap zones can continue using the same procedure as for the extent.
The advantage of the proposed vectorization algorithm compared to more sophisticated

Algorithm 6.1 LIAN extent and gap vectorization algorithm

Require: RASTER D of size (row, col)
  for $r = 1 : row$ **do**
    for $c = 1 : col$ **do**
      if $isNaN(D[r, c])$ **and** $isNum(D[r, c + 1])$ **then**
        $r_s = r + 0.5, c_s = r$ {Find Polygon start node}
        $AddtoPolygon(r_s, c_s)$
        goto FINDNEXTNODE
      end if
    end for
  end for
  FINDNEXTNODE
  for $\alpha = 0 : 45 : 360°$ **do**
    $r_l = r_s + \sin(\alpha - \delta\alpha)/\sqrt{2}, c_l = c_s + \cos(\alpha - \delta\alpha)/\sqrt{2}$ {left-hand side pixel address}
    $r_r = r_s + \sin(\alpha + \delta\alpha)/\sqrt{2}, c_r = c_s + \cos(\alpha + \delta\alpha)/\sqrt{2}$ {right-hand side pixel address}
    if $(isNaN(D[r_l, c_l])$ **and** $isNum(D[r_r, c_r]))$ **or** $(isNum(D[r_l, c_l])$ **and** $isNaN(D[r_r, c_r]))$ **then**
      $r_s = (r_l + r_r)/2, c_s = (c_l + c_r)/2$ {newly found node becomes starting point}
      if $IsNotInPolygon(r_s, c_s)$ **then**
        $AddtoPolygon(r_s, c_s)$ {Add node if not already used in polygon}
        goto FINDNEXTNODE
      else
        if $\alpha = 360°$ **then**
          goto POLYGONCLOSED {all nodes were found}
        end if
      end if
    end if
  end for
  POLYGONCLOSED
  $Polygon(r_{1,i}, c_{1,i}) \rightarrow Polygon(X_{1,i}, Y_{1,i})$ {Convert from pixel to map coordinates}

implementations (e.g. [22]) is its computational efficiency and the capacity to produce simple geometries. They can be generalized further by using e.g. the Douglas-Peucker generalization algorithm [27]. Hence, the amount of data that has to be transmitted to HELIPOS by sockets (see Chap. 6.8.2) can be drastically reduced without loss of information. The achievable polygon accuracy in function of the point-cloud accuracy and the cell-size will be discussed in Chap. 7.3.1.

6.7.6 DSM and Hillshade Generation

Optionally LIAN performs a DSM computation using the filtered raw point-cloud (Fig. 6.15.H) as input. To keep the DSM computation as fast as possible, LIAN interpolates the DSM heights from the raw point-cloud using the nearest neighbor search in 2D. The height value of the point closest to the pixel center is directly taken as new elevation value. Subsequently, based on the result of the overlap check, the actual DSM (DSM_f) is either merged with the one from the previous flightline (DSM_{f-1}) or saved "as is" to a binary grid (`DSMfile`). For merging DSM height values at the cell location x, y the following rule is applied:

$$DSM_{f*}[x, y] = \frac{DSM_{f-1}[x, y] + DSM_f[x, y]}{2} \tag{6.7.3}$$

Hence, in the overlapping parts the new DSM heights correspond to the averaged cell values of the initial DSM.
The subsequent hillshade computation (Fig. 6.15.I) is based on the complete DSM (i.e. DSM_{f*} in the case of strip overlap). The computation uses intermediate slope and aspect grids to derive the hillshade (see Chap. 3.4.3). The illumination source (azimuth a and elevation angle e) can be specified by the user. The result is saved as a 1-byte binary grid to a file (`HILLfile`).

6.7.7 Image Footprint Computation

Although not directly related to the point-cloud quality analysis, LIAN also performs an estimation of the image data coverage (Fig. 6.15.J). This is achieved by virtually projecting the image borders (for each image) on the DSM computed in the previous step. The necessary image exterior orientation elements (projection center coordinates and image orientations) are provided by the LIEOS georeferencing engine. The interior orientation parameters, such as CCD size, pixel size and principal point coordinates, are depending on the camera type and are provided by the operator. Using these elements, LIAN intersects the image rays (dotted lines in Fig. 6.19) along the CCD border with the previously computed DSM to reconstruct the 3D image footprint. The final result are 2D footprint polygons and an image coverage map (see Fig. 6.20), where the pixel value corresponds to the number of images in which the pixel location can be seen.

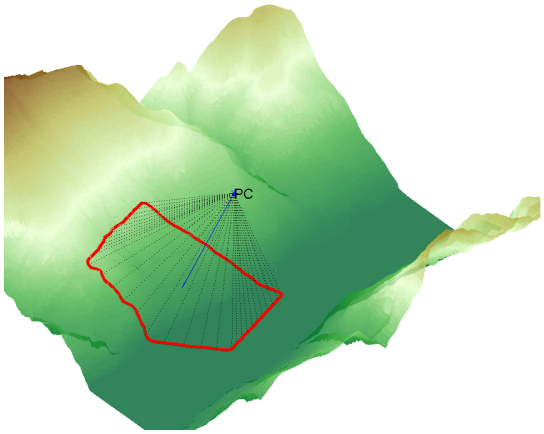

Fig. 6.19: In-flight footprint computation by projection of image borders on DSM.

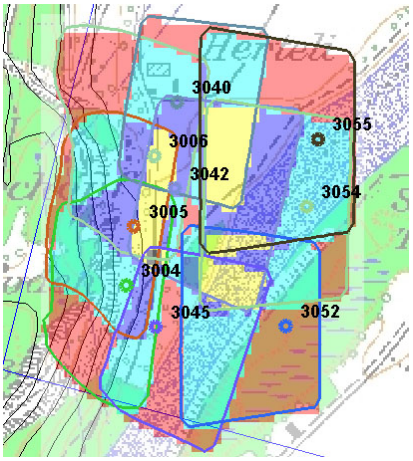

Fig. 6.20: Example for an image coverage map.

6.7.8 Ground Classification

The correct assessment of the scanning geometry requires a foregoing rough ground classification (see Chap. 4.6). Within LIAN, the removal of non-ground points can either be performed by threshold on the curvature value (Eqn. 4.6.2), or by running a ground classification algorithm. For all computations in LIAN the algorithmic efficiency has absolute priority. Hence, to avoid time-consuming surface reconstruction, the classification algorithm implemented in LIAN operates entirely in the point-cloud domain (see Alg. 6.2). It is based

on the point-cloud geometry analysis as presented in Chap. 3.3.3. The key-parameter is the local terrain normal (Eqn. 3.3.4). As a further advantage, these quantity can be directly re-used for the incidence angle estimation necessary for 3D footprint computation.

Adopting the strategy presented by [8], the proposed algorithm first searches for points that serve as first approximation of the ground. These initial points are defined as lowest points within a given cell (see Fig. 6.21), where the cell-size is governed by the maximum building-size parameter b. These points are subsequently used as query points to search for other points belonging to the ground until all points are classified. Similarly to the point-cloud segmentation technique proposed in [175], this is achieved by a region-growing approach that compares the estimated local terrain normals and the orthogonal distance of the points to the tangent plane at the query point. Let us consider a point $\mathbf{p}_q \in \mathbb{R}_3$ identified as ground point. The query point $\mathbf{p}_j$ can also be classified as ground if the following criteria are met (see Fig. 6.22):

$$\mathbf{p_j} \in \text{ground} \Leftrightarrow \begin{cases} \alpha_{\mathrm{j}}^{\mathrm{q}} \leq \alpha_p \\ d_{\mathrm{j}}^{\mathrm{q}} \leq d_p \end{cases} \tag{6.7.4}$$

where α_p (usually around 20°) is the threshold for the directional difference of the normal and d_p (usually around 0.5 m) is the threshold on the orthogonal distance to the tangent plane at point $\mathbf{p}_q$. The orthogonal distance d_j^q from point $\mathbf{p}_j$ to the tangent plane ($\perp \mathbf{n}_q$) at point $\mathbf{p}_q$ is computed by

$$d_j^q = \left\| \mathbf{r}_j^q \cdot \mathbf{n}_q \right\|, \text{where } \mathbf{r}_j^q = \mathbf{p}_q - \mathbf{p}_j \tag{6.7.5}$$

The angular difference α_j^q in direction of the normal $\mathbf{n}_j$ and $\mathbf{n}_q$ is computed by

$$\alpha_j^q = \operatorname{acos}\left(\frac{\mathbf{n}_j \bullet \mathbf{n}_q}{\|\mathbf{n}_j\| \, \|\mathbf{n}_q\|} \right) \tag{6.7.6}$$

The general performance of the proposed ground classification algorithm in comparison to other implementations in commercial software packages will be discussed in Chap. 7.3.3.

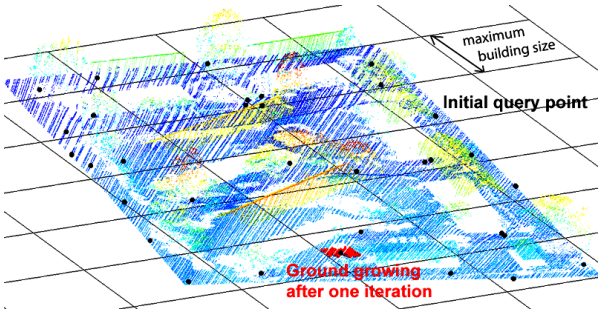

Fig. 6.21: Initial start points (black dots) and found ground points (red dots) after one iteration.

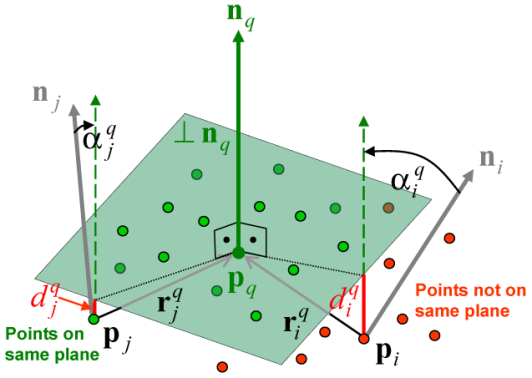

Fig. 6.22: Comparison of tangent plane distance and normal direction for two points.

Algorithm 6.2 LIAN ground classification algorithm

Require: Point-cloud dataset $\mathbf{P}$ with n points, Classification parameters k, b, α_p, d_p
  for $i = 1 : n$ **do**
    $C_{xyz_i} = ComputeCovariance(\mathbf{p}_i, k)$
    $\mathbf{n}_i = ExtractLocalNormal(C_{xyz_i})$ {compute local normal for every point}
  end for
  $\mathbf{P}_{qp} = GetLowestPointsWithinpixel(\mathbf{P}, b)$ {Find set of initial query points}
  while 1 **do**
    if $\mathbf{P}_{qp} = [\,]$ **then**
      break {All query-points were used, classification is over}
    end if
    $\mathbf{p}_q = P_{qp}[1]$ {define actual query-point}
    $\mathbf{P}_{n_{qp}} = GetNeighborPoints(\mathbf{p}_q, k)$
    for $j = 1 : k$ **do**
      if $isNotWithin(\mathbf{P}_{n_{qp}}[j], \mathbf{P}_{qp})$ **then**
        $\mathbf{p}_j = \mathbf{P}_{n_{qp}}[j]$ {Point not now used as query-point so perform test}
        if $PointOnSamePlane(\mathbf{p}_q, \mathbf{p}_i, \alpha_p, d_p)$ **then**
          $\mathbf{p}_j \rightarrow$ ground point
          $AddToQueryPoints(\mathbf{p}_j)$ {Add newly found point as query-point}
        end if
      end if
    end for
  end while

6.7.9 Error Propagation

The computational workflow for error propagation and scanning geometry analysis implemented in LIAN follows the one presented in Fig. 4.7. The only difference is that the pre-filtering based on the local curvature can be replaced by the ground classification procedure presented in the previous section. All the needed quantities to perform a full error propagation and scan geometry analysis are provided by the system:

- The navigation accuracies ($\sigma_{xyz}, \sigma_{rpy}$) and the laser origin coordinates are interpolated in LIEOS.
- The raw laser measurements (range ρ and encoder angle θ) are directly transmitted from the laser.
- The local terrain normals ($\mathbf{n}$), needed for the incidence angle computation and the point class attribute c used for pre-filtering are computed in the ground classification step (see previous section) and passed to the propagation engine.
- The flight-invariant parameters, such as the calibration accuracies ($\sigma_{bore}, \sigma_{leverarm}$), range-finder accuracy ($\sigma_\rho + ppm$), encoder angle accuracy (σ_θ) and beam divergence (ϵ) are inputted by the system operator using the configuration files (see Fig. 6.17).

For non-ground points (i.e. vegetation) the analysis of the scanning geometry makes no sense. Appropriately, only the points belonging to the ground are inputted into the propagation engine (Fig. 6.15.L). The direct output of the propagation engine are point-wise accuracy

estimates for the navigational part ($\sigma_{xy}^{nav}, \sigma_z^{nav}$), the dilution of precision due to the scanning geometry ($\sigma_{xy}^{geom}, \sigma_z^{geom}$) and the global quality indicator (q_i). Depending on the desired quality argument, LIAN directly generates a point quality map (QM_f) by linearly interpolating the point-wise quality metrics in a regular raster (Fig. 6.15.M). This raster map is either saved "as is" or, in the case of strip overlap, merged with the quality map of the previous flightline (QM_{f-1}) according to the following rule:

$$QM_{f*}[x,y] = \begin{cases} QM_f[x,y] & \text{if } QM_f[x,y] \leq QM_{f-1}[x,y] \\ QM_{f-1}[x,y] & \text{if } QM_f[x,y] > QM_{f-1}[x,y] \end{cases} \tag{6.7.7}$$

Accordingly, within a strip overlap, it is always the strip offering the better point quality (thus smaller value) that is retained.

6.7.10 DTM Generation

If required by the operator, the classified point-cloud can be used to generate a DTM (Fig. 6.15.N). The cell-size c_{DEM} is definable by the user. If the point-wise quality indicators are available, LIAN can also compute a DTM quality map (Fig. 6.15.O), using the approach presented in Chap. 5.3.3. If an overlap is detected, the actual and previous DTM are merged. If no DTM quality map is available, Eqn. 6.7.3 is applied (averaging of height values in strip overlap), otherwise the height values in the overlapping parts are constructed as a weighted average (see Fig. 6.23):

$$DTM_{f*}[x,y] = \frac{w_1 \cdot DTM_f[x,y] + w_2 \cdot DTM_{f-1}[x,y]}{w_1 + w_2} \tag{6.7.8}$$

The respective weights w_1 and w_2 are computed as the inverse of the squared DTM reliability index (r_z) values of the respective DTM quality maps. Applying the laws of error propagation, the values of the merged DTM quality map ($QDTM_{f*}$) for a given location x, y can be computed using the following formula:

$$QDTM_{f*}[x,y] = \sqrt{\left(\frac{1}{QDTM_{f-1}[x,y]^2} + \frac{1}{QDTM_f[x,y]^2}\right)^{-1}} \tag{6.7.9}$$

Strip Difference Map

If a strip overlap occurs, LIAN offers the possibility to directly compute strip difference maps (Fig. 6.15.P) that can be displayed in HELIPOS. As discussed in Chap. 5.2, these strip difference maps are a good indicator to estimate the internal data accuracy. Theoretically the strip differences could be evaluated using DSM's. However, such difference maps often suffer of systematic blunders near building edges or areas with vegetation (see e.g. Fig. 5.4) that may blur the real discrepancies. Hence, within LIAN, the strip difference grid $DIFF_{f,f-1}$ is computed using the DTM's of the adjacent strips:

$$DIFF_{f,f-1}[x,y] = DTM_f[x,y] - DTM_{f-1}[x,y] \tag{6.7.10}$$

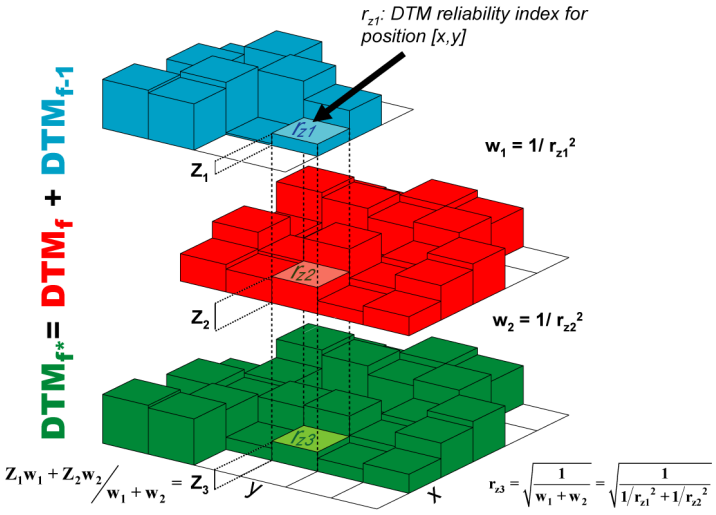

FIG. 6.23: Example for DTM grid merge weighted by DTM reliability index.

6.8 Flight Management and Monitoring Module (HELIPOS)

6.8.1 Concept

The control module HELIPOS acts as GUI between the operator and the previously described modules. It has two major functions:

- To provide standard Flight Management System (FMS) functionalities such as flight-plan handling and pilot guidance.
- To control the system settings and to monitor the data quality and coverage.

The required input data for guidance and system controlling is provided by the previously described modules. FIG. 6.24 depicts the most important visualization and controlling features available to the operator:

(A) **Status log**: All important status messages from the data loggers (GPS/IMU/LiDAR) are gathered and listed in this window.

(B) **GPS/INS info**: The current position, speed, heading and GPS quality indicators (e.g. DOP, number of visible satellites, GSPQUAL quality flag) can be displayed. When GIINAV is running, the integrated trajectory (including RT attitude) can be presented instead.

(C) **Scanner info**: The measured distance by the laser and the swath coverage (in percent) is displayed. This improves the navigation for flightlines where a constant height over the topography is required.

(D) **Online/offline button**: Control button to switch between online and offline mode.

(E) **Flight-plan management toolbox**: Different flight-plans and flightlines can be loaded and activated. The line attributes (such as height, heading or sensor head attitude) can be displayed for each line.

(F) **Layer control**: GIS-like control for displaying or deactivating different data layers on the base map.

(G) **Tracking short-cuts**: buttons to load the flight-plan, activate the cross-track indicator (J) and enable/disable tracking

(H) **Quality map short-cuts**: Buttons for loading and displaying strip-wise results from LIAN.

(I) **Display window**: Map window for the layer-wise display of raster and vector data.

(J) **Cross-track indicator tool**: Indication of perpendicular distance of carrier to active flightline.

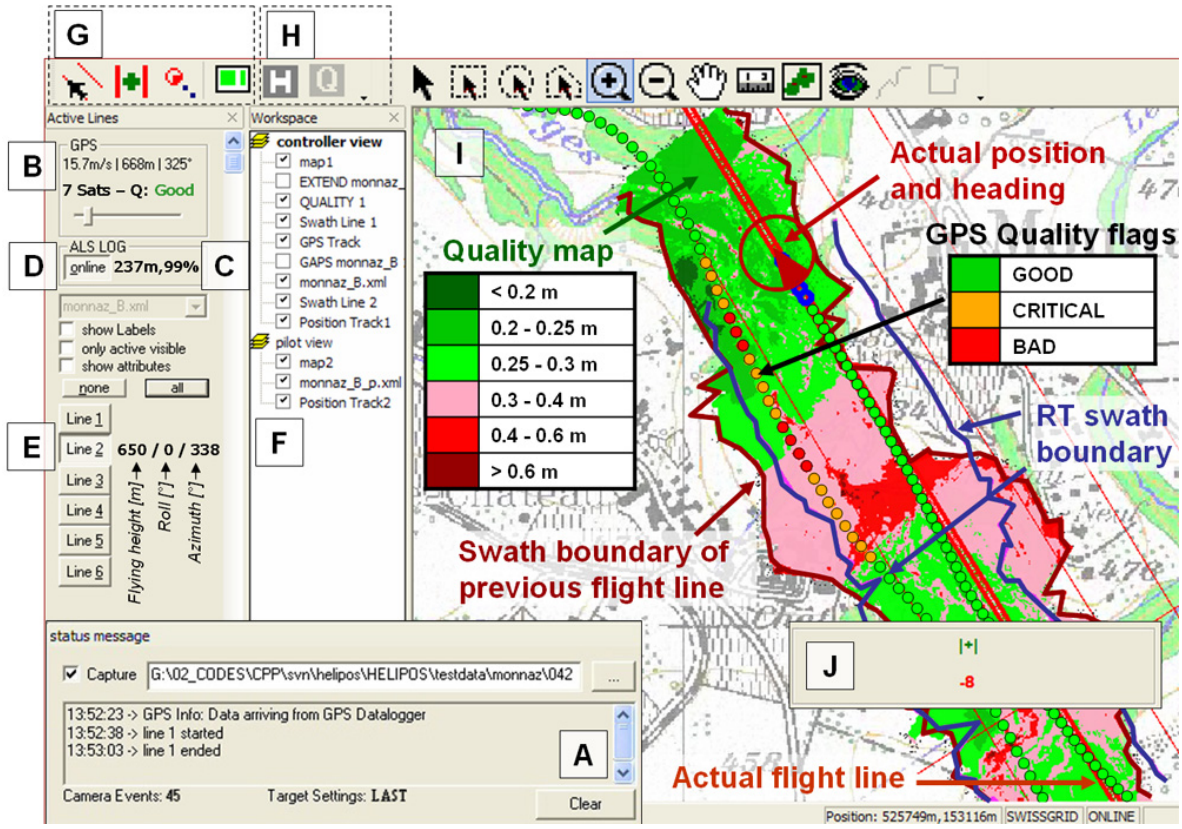

FIG. 6.24: HELIPOS GUI

For the purpose of pilot guidance and system control, HELIPOS offers two different views within the same instance (see FIG. 6.25):

- The **controller view**, where all available information can be displayed (i.e. flightlines, map data, RT position, RT swath, data extent and gaps).

- The **pilot view**, where only the map data, the current flightline, position, heading and the line alignment tool are displayed.

Both views run within the same application and are cross-linked. This enables the operator to rapidly control the pilot's display by changing e.g. the view extent (zoom, pan) or by highlighting or deactivating different layers. The display of these different views can be separated on two monitors. Practically, this is realized by connecting an extended monitor to the controller laptop using the VGA output. The external monitor can be smaller, e.g. in the case of the Scan2map-system a standard 8 inch TFT-screen is used (see FIG. 6.25).

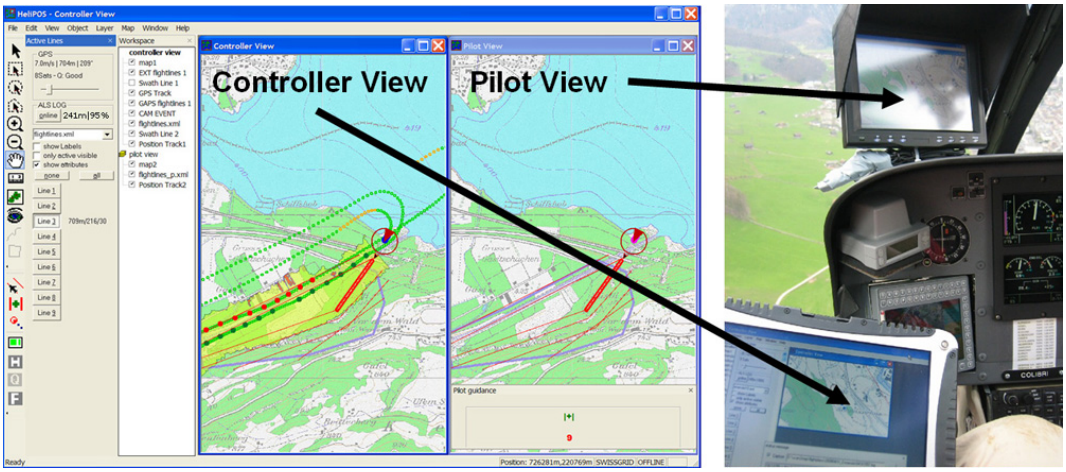

FIG. 6.25: Intercommunicating windows for controller and pilot view within HELIPOS (left) and standard setup using extended screen within helicopter (right).

6.8.2 Communication with other Modules

HELIPOS communicates with the other modules by socket messages. The ports of the data servers from which the messages are received can be configured in the port-settings window (see FIG. 6.26). Based on the latency of the information that is received, the system distinguishes between RT communication (messages within a flightline) and delayed communication (information available after the flightline).

RT Communication

All primary data loggers act as server and deliver uni-directional RT information to HELIPOS (as a client): GPSQUAL (embedded in the GPS datalogger) sends 1 Hz GPS position and a quality flag (i.e. good, critical, bad) for each epoch. The ALS data logger provides direct information about the scan range and the percentage of the covered swath at 1 Hz. GIINAV transmits attitude and integrated position information at 1 Hz and LIEOS delivers swath border coordinates (1 Hz) and image EO (at event rate). HELIPOS also acquires status messages from all data loggers, as they evolve.

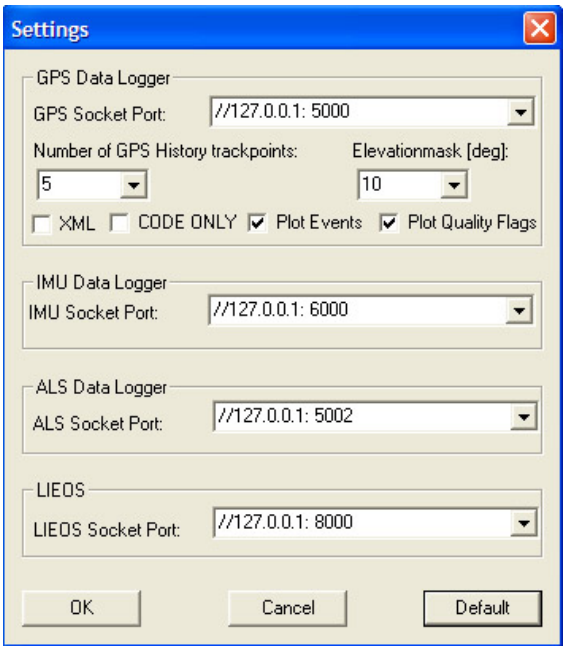

FIG. 6.26: HELIPOS port settings

LIAN_HELIPOS_BOUNDARY				
Fields		Type	Value	Description
MsgID		U1	0x06	Message ID
MsgLen		U2	6 + *n**16	Message length in bytes
MsgDat	Sub-fields			Message contents.
	PolygonType	U1		Polygon type ID (extend,gap)
	CoordSyst	U1		Coordinate system/projection ID
	NPoints	I4	*n*	Number of Points in Polygon
	Point1.X	I4		X Coordinate of first Point
	Point1.Y	I4		Y Coordinate of first Point
	:			
	Point_n.X	I4		X Coordinate of last Point
	Point_n.Y	I4		Y Coordinate of last Point
MsgEnd		1	0x23 ('#')	Message delimiter code.

FIG. 6.27: Definition of vector message to send extent and gap polygons from LIAN to HELIPOS.

Delayed Communication

The results provided by LIAN are only available once a strip is computed and its analysis is finished. As shown in FIG. 6.15, LIEOS is in charge of sending the outcome of LIAN to HELIPOS. Depending on the data type (vector or raster) and the size, three options are implemented:

(A) **Vector data send**: The vectorized extent and gap polygons are read from the `LIANfile` by the `LIEOS-thread` and sent polygon by polygon as socket messages to HELIPOS (FIG. 6.15.S). To prevent a surcharge of the HELIPOS display, the sending of the next polygon is initiated only once HELIPOS acknowledges the correct reception and the drawing of the former polygon. FIG. 6.27 shows the protocol of such message: The message ID identifies the data type to expect. The `PolygonType`-field describes the nature of polygon (either extent or gap). This information allows HELIPOS to draw the polygons into the appropriate layer. The `CoordSyst`-field defines the datum of the points coordinates. This information indicates whether the received coordinates have to be reprojected before displaying. The last field in the header (`NPoints`-field) indicates the number of node points to expect. Every socket message is ended with a message delimiter code (`MsgEnd`-field). This enables to check the correct decoding of the message at reception and to acknowledge a decoding failure if necessary.

(B) **Raster data send**: Raster data is less suitable to be sent by sockets, as the amount of data to transmit is usually considerably larger than for vector data. LIEOS possesses a mechanism to send raster data package-wise through the Ethernet (FIG. 6.15.T). FIG. 6.28 explains this procedure based on a hillshade grid (coded as 1 byte): The message starts with a raster header, where the geo-location of the raster

($X_{UL}, Y_{UL}, x_{dim}, y_{dim}$,cell-size) and the number of bytes (called base) used to store a single pixel value are defined. The last field of the header indicates the number of raster data blocks to come. The header is sent as a standalone message prior to the raster data blocks. FIG. 6.28 shows the construction of such a data block for the first raster row, where until pixel 4 only NoData-pixels occur. The architecture of a data block is such that the first field indicates the 1D start-pixel address, the second the number of values to come followed by the values themselves. The latter are coded with the data-length as indicated in the header (base). The first data block is sent after the correct decoding of the header is acknowledged. Afterwards, the other data blocks are sent using the same send-reception-acknowledgment procedure and the raster is reconstructed piece-wise in HELIPOS.

(C) **File reference**: To limit the communication load, the previously described procedure for rasters is only applied for data that has to be quickly available and that can be coded with a reduced data-length. E.g. hillshade grids are bounded between 0 and 255 and can be coded as 1 byte. However, most of the time the operator does not need to visualize the raster results immediately. In addition, many of the grids generated by LIAN (i.e. DSM, DTM) have non-integer pixel values which requires coding as doubles (8 bytes). Sending doubles-length data packages would certainly saturate the communication link and endanger the important RT messages. The file reference procedure avoids such congestion. This procedure passes the information on the current LIAN working directory to HELIPOS once the `LIAN-thread` has started (see FIG. 6.15.U). After each strip, HELIPOS checks automatically the availability of the LIAN result files in this directory and activates the quality map loading buttons (FIG. 6.24.H) as soon as the grids are available. By pressing these buttons, the data is directly read from the files and displayed in the appropriate layers.

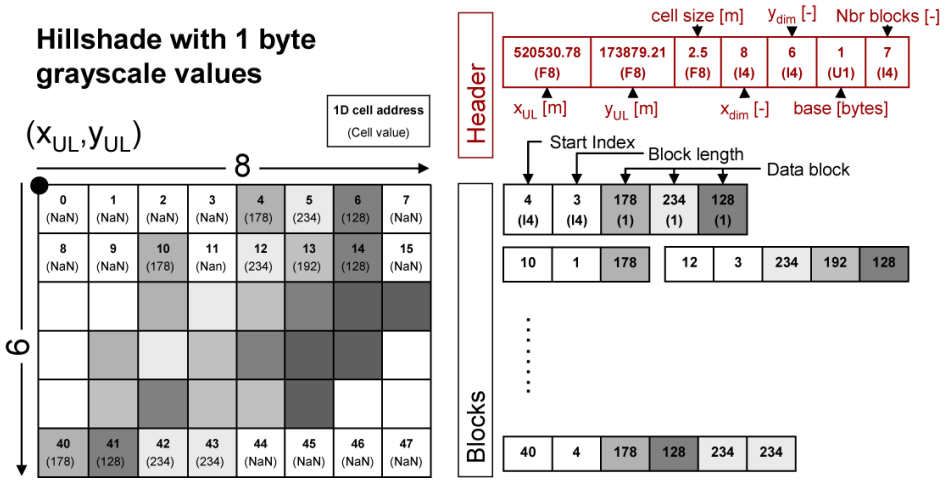

FIG. 6.28: Message structure to send binary rasters through socket to HELIPOS.

6.8.3 Pilot Guidance

An important task of HELIPOS is to guide the pilot over a previously established flight-plan (see CHAP. 6.2) using the available navigation data. In commercial ALS systems the pilot

guidance is optimized for small-scale/large-area projects carried out with airplanes. There, the graphical display is often equipped with an artificial horizon to control the banking and an "ILS[2]-like" screen indicating the horizontal and vertical deviations from the actual flightline (e.g. [66, 74, 168]). Such functionality is quite useful for long-range ALS missions with long parallel flightlines with constant speed and altitude. Scan2map missions are essentially flown with helicopters in geographically demanding terrain and low height over ground. Thus, the flight-plans are more complex, i.e. having short non-parallel flightlines with changing altitudes and changing obliquities. Especially in the alpine environment, helicopter pilots cannot exclusively focus on the flight-plan as they have to continuously monitor the surroundings to detect endangering objects (such as high hanging wires and cables). In this context, ILS-like guidance is not optimal, because it requires too much attention of the pilot. To accommodate these particular conditions, HELIPOS adopts a solution where the planimetric and altimetric navigation are split into two segments:

- **Planimetric navigation**: The planimetric navigation is fully under the pilots responsibility. The display on the pilot screen (Fig. 6.25) shows the base map, the active flightline, the actual and past positions and heading (deduced from GPS velocity vector). Additionally, the cross-track indicator (Fig. 6.24.J) monitors the projected perpendicular 2D-displacement from the actual flightline.

- **Altimetric navigation**: The GPS/INS-info section (Fig. 6.24.B) displays the absolute height. This information can be used for flightlines with constant elevation. The scanner-info section (Fig. 6.24.C) displays the actual laser range (thus height over ground). This is of particular interest, if the flight-planning requires a constant altitude above ground (often the case for corridor mapping). To prevent a visual overflow in the pilot screen, this information is only displayed in the controller screen. Eventual vertical corrections are communicated to the pilot using the voice channel.

Although the operator can define the appropriate map extract for the pilot manually (by using the pan and/or zoom functions), HELIPOS also features an automated pan algorithm, that moves the visible map extract in function of the actual GPS position and the projected flight direction.

6.8.4 In-Flight Quality Data Display

The main advantage of HELIPOS compared to commercial FMS are its versatile possibilities for displaying quality-relevant data in RT or on operators demand. These are:

- **RT swath lines** are displayed as colored polygons in separate layers for each flightline (see Fig. 6.24 and Fig. 6.29.A): This visualization permits following in RT the data coverage of the laser and to anticipate corrections to further lines if necessary. Superimposing the swath border of two adjacent lines allows immediate detection of insufficient strip overlaps.

[2]Instrument Landing System

- **RT GPS quality flags** are displayed to the operator by color-coding each GPS position with the quality flag provided by GPSQUAL (see Fig. 6.24). The color-coded GPS positions (*red* → *bad*, *orange* → *critical*, *green* → *good*) immediately highlight parts of a flight where the resolution of the ambiguities in the PP may be difficult. Based on this information, the operator can react in consequence and repeat parts of the flight.

- **Extent and gap polygon display**: Fig. 6.29.A shows the display of the computed extent (yellow) and the data gaps (red) as semi-transparent polygons. Extent and gaps are displayed in different layers and can be visualized independently. The gap polygons depict areas where the density requirements are not fulfilled. Together with the map information beneath, the operator can decide whether the indicated gap is problematic, thus requiring re-acquisition of this area, or is of minor importance. E.g. in Fig. 6.29.A the two major gaps are within the river, thus re-acquisition is not required.

- **DSM/DTM hillshade display**: HELIPOS can display strip-wise DSM hillshade images (see Fig. 6.29.B). The visualization has no direct quality-relevant information. However, the correct scan of the ground relief can be seen immediately and enables to monitor if certain features (such as buildings, bridges, etc.) are covered with sufficient points to be modeled correctly.
  The display of the DTM hillshade (Fig. 6.29.D) indicates the quality of the automated ground classification. This information can be used to verify if, for example, the ground penetration of the scanner in forested areas is sufficient. Optionally, also the DTM quality map can be displayed. This provides direct information on the reliability of the DTM heights.

- **Image footprints display**: If images are taken, their trigger positions (computed by LIEOS) can be mapped in RT in the controller view (see red dots in Fig. 6.29.C). Once the flightline is finished, LIAN performs the footprint computation for every individual image and processes them to one coverage raster. This raster can be displayed in HELIPOS. If the images are further used for orthophoto production or stereo-restitution, this plot provides immediate information if certain areas are not sufficiently covered by image data.

- **Strip height difference map**: As soon as a strip overlap between two consecutive flightlines occurs, LIAN can compute a strip difference map by subtracting the corresponding DTM's. This map provides useful information about the internal accuracy and can also highlight eventual problems in the ground classification. (Fig. 6.29.E) depicts such situation where in the flat parts the height differences are below 20 cm, whereas in the sloped parts, mainly due to "rough" DTM modeling large discrepancies occur.

- **Point-cloud quality map**: If the full error propagation is enabled, HELIPOS can load and display the strip-wise generated quality maps (see e.g. Fig. 6.29.F and Fig. 6.24). The quality map allows identifying scanned regions, where the point-cloud accuracy does not meet the mission requirements, directly in-flight. The color-coding of the quality map (idem for all other quality rasters) is programmable and can be adapted using a legend editor.

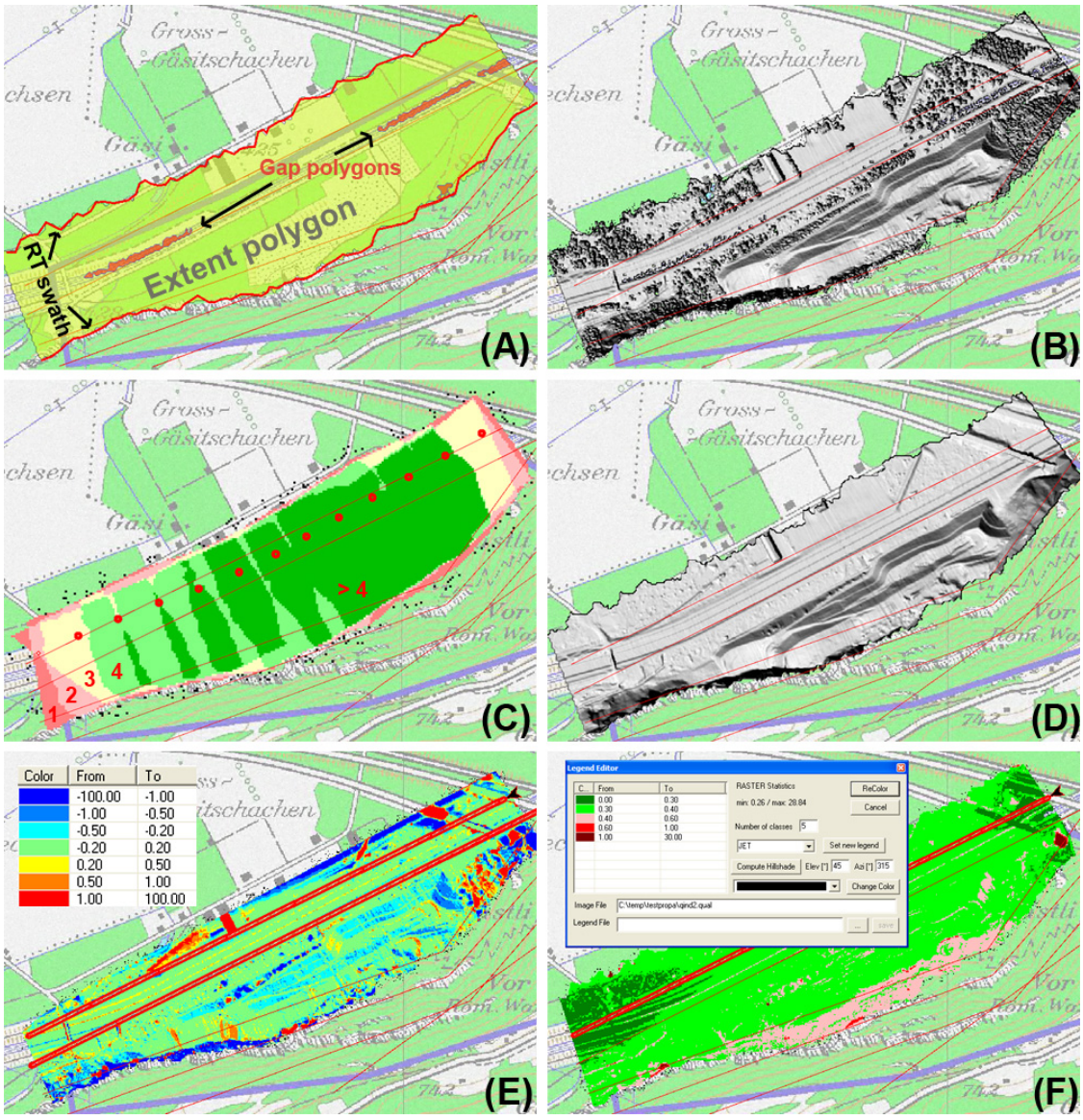

FIG. 6.29: Display options in HELIPOS: (A) Semi-transparent display of extent (yellow) and gap (red) polygons, (B) Hillshaded DSM computed in-flight, (C) Image PC positions (red dots) and footprint map color-coded after image coverage, (D) Hillshaded DTM computed in-flight, (E) Strip difference map, (F) Point quality map.

Chapter 7

Results and Performance Analysis

This chapter is dedicated to the analysis of the performance of IQUAL. The accuracies of the different quantities computed in-flight, such as RT trajectory, point-cloud, data extent and gap vectors and quality indicators, are assessed by comparisons with the post-processed solution. To cope with the time-constraints imposed by in-flight processing, a special attention is drawn to the adopted strategies to increase the computational speed.

7.1 RT Trajectory and Point-cloud Accuracy

This section assesses the performance of the RT GPS/INS integration engine (GIINAV) and the RT georeferencing engine (LIEOS). Special attention is payed on assessing the influence of the GPS positioning mode (Single Point Positioning versus RTK) on the quality of the integrated navigation solution and on the point-cloud accuracy.
For all flights evaluated in this section, appropriate GPS reference stations close to the survey area were installed (baseline length $< 10\,\text{km}$, $\Delta H < 300\,\text{m}$). The time of flight was selected considering the GPS constellation (PDOP < 3.5). Hence, the post-processed GPS/INS trajectory (computed with WayPoint GrafNav for CP-DGPS computation and Applanix PosProc for GPS/INS Integration) and the resulting point-cloud were of excellent quality ($\sigma_{xyz} < 5\,cm, \sigma_{attitude} < 0.01°$) and served as reference for the test-cases presented hereafter.

7.1.1 Single Point Positioning (SPP)

Integrated Trajectory

FIG. 7.1 shows the difference in trajectory estimation (position, attitude and velocity) between the integrated RT solution using SPP (computed by GIINAV) and the post-processed results based on CP-DGPS for a flight conducted in April 2009 near Mollis (Canton Glarus, Switzerland). The red lines in the upper left sub-plot depict when the system was on a flightline. The differences in attitude (roll/pitch/yaw: RMS $< 0.05°$) correspond to what can be expected by the filtered solution using SPP GPS aiding and are primarily driven by the accuracy grade of the IMU (in this case: tactical-grade IMU). The differences in absolute position are more

important (RMS planimetry $> 2\,\text{m}$, RMS altimetry $> 1.5\,\text{m}$) and typical for the SPP mode (see Chap. 2.4.3). The plot also highlights that the SPP solutions are biased and not randomly distributed around zero. The differences rather follow a trend (e.g. North component), reflecting the changes in satellite geometry. The correspondence for the integrated velocities is much better due to the influence of the IMU data [130].

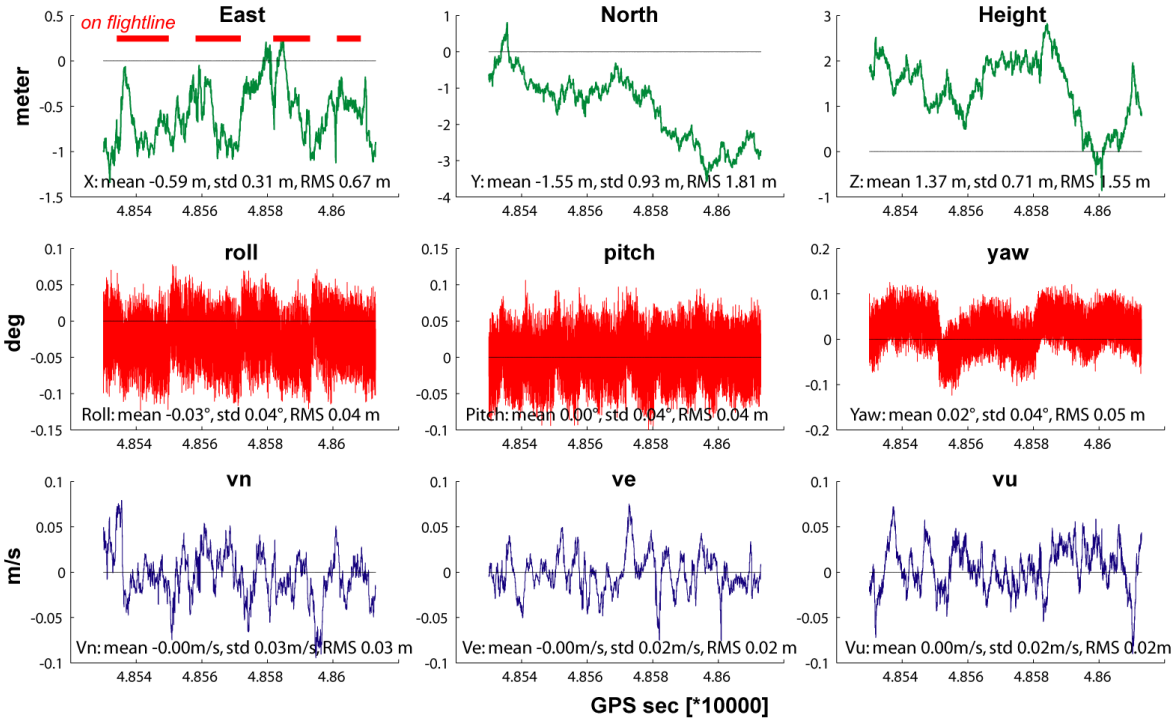

Fig. 7.1: Comparison of trajectory computed in RT (using SPP) and in PP (using CP-DGPS) for Mollis dataset (dataset length $\approx 15\,\text{min}$)

RT Point-cloud Accuracy

The histograms in Fig. 7.2 depict the distribution of the differences between the point-cloud computed in RT and the one computed in PP. For this flight, the height over ground was approximately 250 m. An angular uncertainty of 0.05° at a range of 250 m yields a positioning uncertainty of approximately 0.2 m in the laser point coordinate. Thus, the angular discrepancies had a minor impact on the final georeferencing quality. As errors in position propagate directly to the georeferenced point, the East and North differences are similar ($RMS_E \approx 0.9\,\text{m}$, $RMS_N \approx 1.2\,\text{m}$) to those of the trajectory (see Fig. 7.1). The RMS of the height differences as well corresponds to the point-positioning accuracy in the vertical channel.
Analog to the carrier positions, the histograms also reveal biases in point coordinates (approximately 1 m in each direction). The biases are much larger than the variances, reflecting that the relative accuracy is normally much better than the absolute accuracy. The influence of the relative and absolute RT point-cloud accuracy on the validity of the LIAN results will be discussed in Chap. 7.3.1.

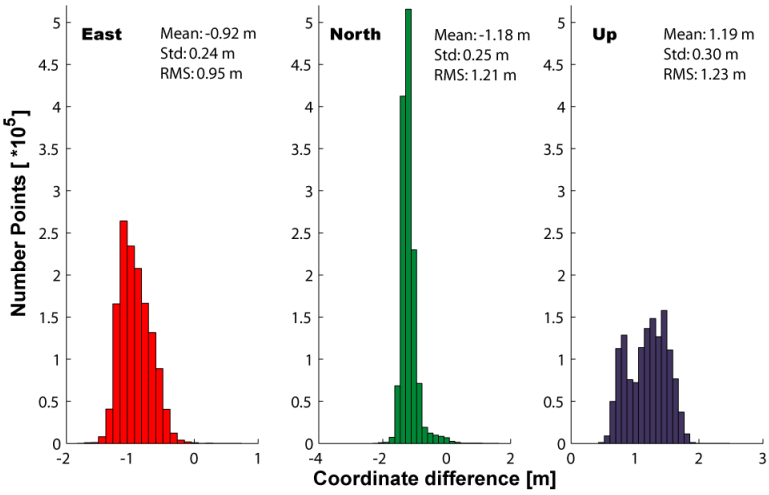

FIG. 7.2: Histograms of difference in point-cloud coordinates computed in RT and in PP (based on 1.4 million points) for Mollis dataset.

Summary of SPP Performance

TAB. 7.1 summarizes the RT positioning accuracy for the aforementioned test flight and for another flight conducted near Lausanne (detailed plots in Appendix C). TAB. 7.2 recapitulates the resulting point-cloud accuracies. For each flight the mean differences and the standard deviation along the three axes are provided. The last column presents the RMS of the 3D differences. The presented flights are representative for typical Scan2map-missions and allow benchmarking the achievable accuracies using SPP. Both datasets deliver 3D positioning accuracies between 2 to 4 m. This order of magnitude is also valid for the point-cloud accuracy, as the contribution of the attitude uncertainties ($\approx 0.05°$) on the point-cloud accuracy remains below meter-level for ranges shorter than 1000 m.
Overall, for short to mid-range scanning missions, the achievable absolute 3D accuracy for a RT point-cloud using SPP is settled between 2 to 5 m. Considering that the typical length of a flightline in a Scan2map-missions is around 2 to 5 min, the relative accuracy within a flightline is normally much better (meter to sub-meter level).

	Mean difference [m]			Standard deviation[m]			RMS [m]
Flight	X	Y	Z	X	Y	Z	$\lvert XYZ \rvert$
Mollis	-0.59	-1.55	1.37	0.31	0.93	0.71	2.47
Lausanne	-1.29	-1.02	2.89	0.59	0.83	1.79	3.72

TAB. 7.1: Summary of accuracies of integrated position estimates for flights with SPP.

	Mean differences [m]			Standard deviation [m]			RMS [m]
Flight	X	Y	Z	X	Y	Z	$\lvert XYZ \rvert$
Mollis	-0.92	-1.18	1.19	0.24	0.25	0.30	2.0
Lausanne	0.95	0.81	-2.07	0.93	1.02	2.31	3.6

TAB. 7.2: Summary of point-cloud differences (RT versus PP) for both flights.

7.1.2 RTK

RTK requires a communication link for RT transmission of the GPS measurements or its corrections from the reference to the rover receiver. This section presents the results of three test flights using either Radio or GPRS for the RTK communication link.

Radio Communication

A test flight using RTK with a radio communication link (emitting power: 2 W) was conducted in June 2008 near Sion (Switzerland). On board of the helicopter two GPS receivers (rovers) were connected through a splitter to the same antenna. One receiver (JAVAD Legacy) was configured in SPP mode while the other (TOPCON Hiper Pro) received the RTK corrections. The raw observations of both receivers were also stored for carrier-phase post-processing. To improve signal reception, a semi-rigid radio antenna was directly mounted on the mapping sensor head pointing downwards.

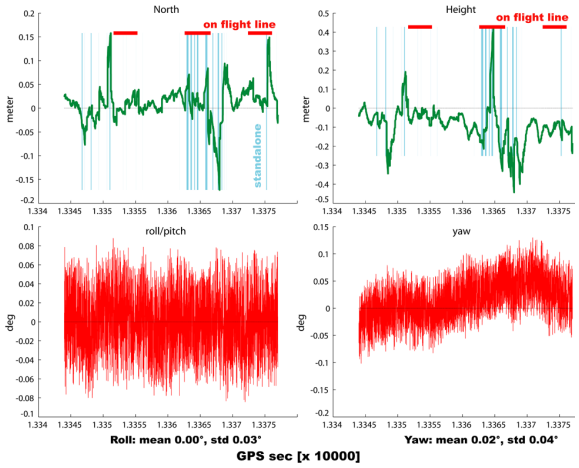

FIG. 7.3: Comparison of trajectory computed in RT (using RTK-Radio) and in PP (using CP-DGPS) for Sion 08 dataset.

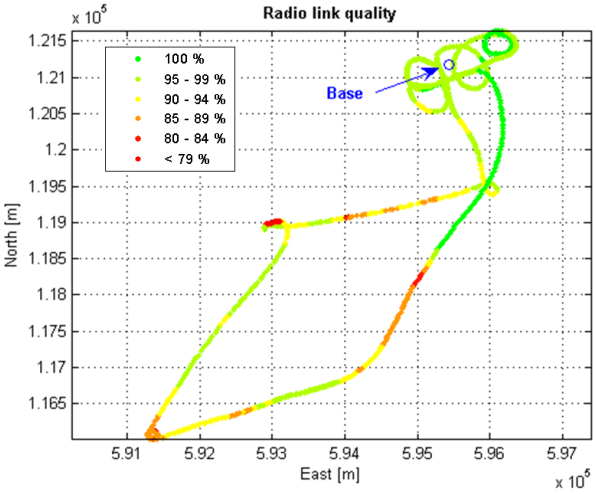

FIG. 7.4: Distance between base receiver and rover and influence on radio link quality (expressed in %) for Sion 08 dataset.

The two upper plots of FIG. 7.3 depict the differences in integrated position solutions between the RT solution (with RTK Radio link, GPS/INS integration with GIINAV) and the trajectory obtained in PP. As the differences in the East and North components (expressed in a local mapping frame) are similar, only the North component is shown in the plot. The horizontal red bars in the upper-left sub-plot indicate periods when the system was on a flightline, thus marking intervals with increased accuracy requirements. The blue vertical lines indicate periods where only a standalone GPS solution could be provided.
In the case of fixed RTK positions, the obtained differences are mostly below 10 cm in the altimetric and planimetric channel, respectively. Nevertheless, the effect of standalone solutions is demonstrated through sudden accuracy losses in the integrated navigation solution (blue vertical bars in upper plots of FIG. 7.3). This is either caused by the reduced quality or

total loss of the radio signal for some parts of the flight. The accuracy of the attitude is not better than for SPP (RMS $< 0.05°$). This can be explained by the fact that the estimation of the attitude is principally depending on the accuracy of the GPS velocity, less influenced by the used GPS positioning mode.
A good quality of the communication link is the prerequisite for the successful application of RTK via radio for ALS. The signal strength and the baseline length have both strong impact on the link quality [165]. Fig. 7.4 depicts the evolution of the radio link quality (expressed in %) for the given test flight. The quality predominantly decreases during transfer periods (thus increased velocity) and in turns where, due to the banking angle, the receiver antenna is no longer oriented vertically. This effect could probably be reduced by employing dedicated airborne radio antennas mounted on the helicopter fuselage.

GPRS Communication

Another mission was flown in April 2009 near Chur (Switzerland). This time, the RTK satellite corrections were obtained from the swipos-NAV service of the Swiss Federal Office of Topography (Swisstopo). This service provides nation-wide corrections from the Automated GNSS Network (AGNES). The correction was sent to the RTK rover receiver (JAVAD Alpha-G2T) via Internet using the NTRIP protocol [47] and GPRS communication. The second receiver (JAVAD Legacy) connected to the same antenna was configured in SPP mode. The virtual reference station (VRS) technique was employed (see Chap. 2.4.4).

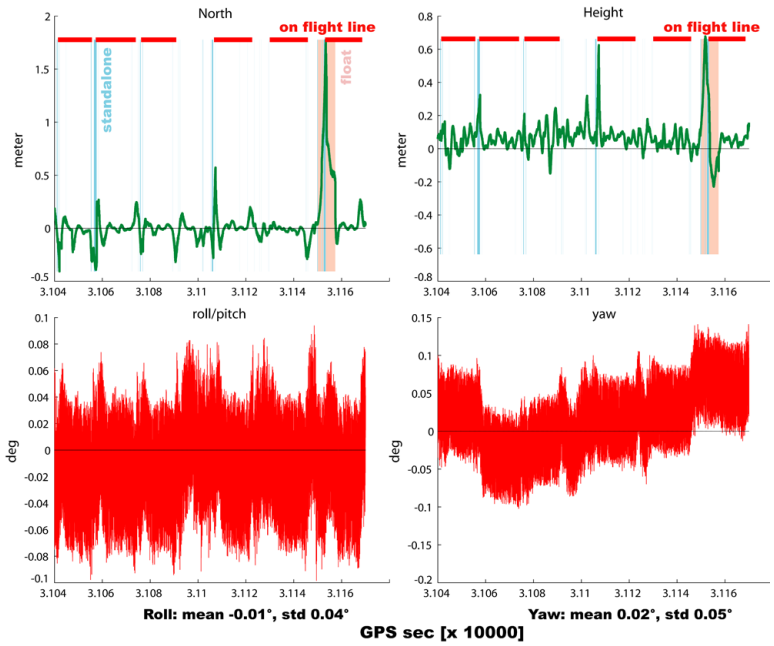

Fig. 7.5: Comparison of trajectory computed in RT (RTK-GPRS) and in PP (using CP-DGPS) for Chur dataset.

Fig. 7.5 displays the difference between the PP solution and the RT solution using GPRS communication link. As in the radio example, the obtained differences for the fixed RTK

positions are generally below 10 cm. The impact of float (red areas) and standalone (blue areas) solutions on the integrated position accuracy is apparent. These situations essentially occur during the transition phases of the flight where the GPS signal reception is affected either by obstructions due to the environment (high mountains) or by the helicopter itself (large banking angle). It should be noticed that even in the PP-step, the ambiguities could not be fixed for a portion of the flight (the large red interval on the right-hand part of the plots). This fact highlights the importance of monitoring the RTK ambiguity status within the flight, as it identifies immediately potential problems in solving the ambiguities in PP.

7.1.3 Summary of RTK Performance

To test the accuracy limitations of the RTK approach, another flight using the swipos-NAV/GPRS service was conducted in July 2009 near Sion. This flight took place under ideal conditions regarding the GPS constellation ($PDOP < 2$) and the RTK infrastructure.

Achievable RT Positioning Accuracy with RTK-GPS/INS

The upper plot of Fig. 7.6 depicts the coordinate differences (RTK minus PP) for non-integrated GPS positions for the Sion 09 dataset. During 98.1% of the flight the ambiguities could be fixed, resulting in generally very small differences (< 0.05 m). Nevertheless, the plot depicts that some epochs are affected by larger discrepancies ($|\Delta E_{max}| = 0.4$ m, $|\Delta N_{max}| = 1.6$ m, $|\Delta U_{max}| = 0.8$ m). However, these sudden "jumps" are not problematic as they occur during sharp turns where the laser data is not used. Additionally, such short positioning quality degradations (< 2 sec) are generally filtered out by the GPS/INS integration process. This is confirmed by the lower plot of Fig. 7.6 presenting the differences for the integrated positions (RTK/GIINAV - PP/PosProc). Here, the outliers have disappeared ($|\Delta E_{max}| = 0.1$ m, $|\Delta N_{max}| = 0.1$ m, $|\Delta U_{max}| = 0.15$ m) and the 3D RMS is below 0.05 m.

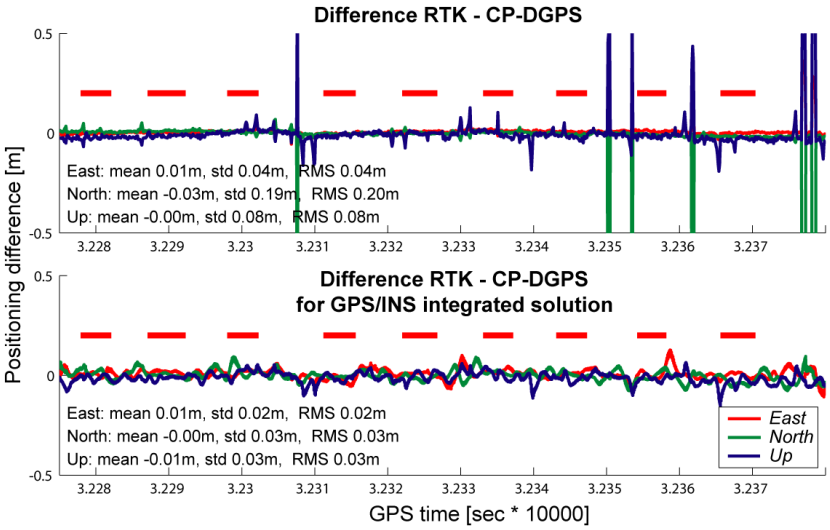

Fig. 7.6: Comparison of differences for non-integrated RTK-GPS positions (upper plot) and RTK-GPS/INS integrated positions (lower plot) for Sion 09 dataset.

			Mean difference			Standard deviation			RMS
GPS mode	Solution type	Epochs [%]	X [m]	Y [m]	Z [m]	X [m]	Y [m]	Z [m]	XYZ [m]
RTK Radio (Sion 08)	Standalone	15.7	0.01	0.03	-0.10	0.06	0.11	0.17	0.23
	Float	0.0	-	-	-	-	-	-	-
	Fixed	84.3	0.01	0.02	-0.08	0.03	0.05	0.08	0.13
	All	100.0	0.01	0.02	-0.09	0.04	0.06	0.10	0.15
	On flightline	**41.7**	**0.02**	**0.03**	**-0.07**	**0.03**	**0.07**	**0.10**	**0.15**
RTK GPRS (Chur)	Standalone	5.2	0.08	0.07	0.17	0.53	0.22	0.16	0.62
	Float	4.8	0.58	0.08	0.08	0.33	0.25	0.29	0.78
	Fixed	90.1	-0.01	-0.01	0.06	0.08	0.05	0.06	0.13
	All	100.0	0.03	0.00	0.07	0.20	0.09	0.10	0.25
	On flightline	**71.5**	**0.03**	**-0.01**	**0.05**	**0.20**	**0.07**	**0.08**	**0.23**
RTK GPRS (Sion 09)	Standalone	1.9	0.00	-0.01	-0.05	0.02	0.06	0.03	0.09
	Float	0.0	-	-	-	-	-	-	-
	Fixed	98.1	0.00	0.00	-0.02	0.03	0.03	0.03	0.05
	All	100.0	0.00	0.00	-0.02	0.03	0.03	0.03	0.06
	On flightline	**20.4**	**0.01**	**0.00**	**-0.01**	**0.01**	**0.02**	**0.02**	**0.04**

TAB. 7.3: Summary of GPS/INS integrated position accuracies for flights using RTK.

TAB. 7.3 summarizes the difference in RT positioning accuracy for the three discussed test flights using RTK. For each flight, the percentage obtained for each GPS solution type (fixed, float, standalone) is indicated as well as the percentage of observations occurring during a flightline. Compared to the SPP results (TAB. 7.1), the overall accuracy is improved by a factor of nearly 20. The results also indicate that the proportion of fixed and float solutions is higher for GPRS than for Radio (94.9% and 98.1% versus 84.3%), highlighting the good availability of the mobile network in the flown regions.
For the Sion 08 dataset, besides the bias in the height channel (ΔZ = -0.1 m: most probably originating from an error in the reference station height coordinates), all mean differences are below 0.05 m when the ambiguities could be fixed on-the-fly. This indicates that RTK by Radio communication can provide very good results, when some precautions to sustain good communication link quality are taken (i.e. sufficient emitting power, rigid antenna type).
The two flights using RTK-GPRS are representative for the bandwidth of achievable accuracies with this technology. The Chur dataset was affected by several phases having float or standalone solutions, pulling down the overall 3D accuracy to approximately 20 cm. For the Sion 09 dataset, the rate of fixed solutions is much higher (98.1%), resulting in an overall 3D positioning accuracy of 0.05 m. This probably represents the upper accuracy limit for RT GPS/INS positions using RTK technology.

Achievable RT Point-cloud Accuracy with RTK-GPS/INS

FIG. 7.7 plots the histograms of the point-cloud differences for the Sion 09 flight. Unlike the point-cloud computed for the Chur dataset, the differences are nearly unbiased and are of the same order of magnitude for all axes. TAB. 7.4 regroups the point-cloud differences for the three presented RTK flights. For the Chur and Sion 08 dataset (see histograms in

Appendix C) the 3D RMS is about 0.15 m, whereas for the Sion 09 dataset, 3D sub-decimeter point-cloud accuracy was achieved, delineating the optimal achievable accuracy for in-flight point-cloud generation.

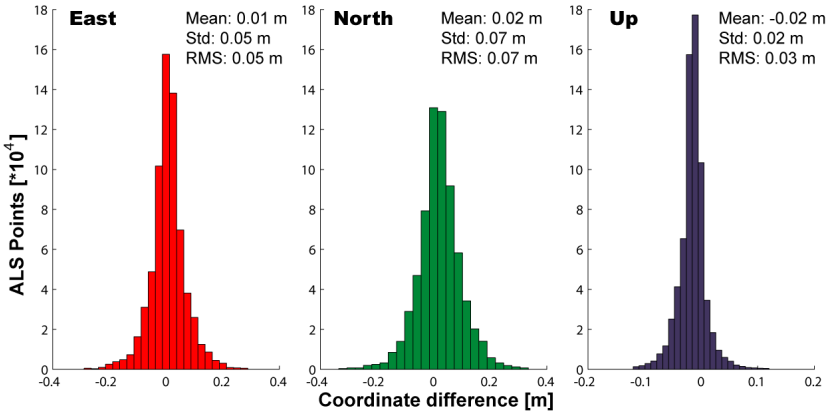

FIG. 7.7: Histograms of coordinate differences for point-cloud computed in RT for Sion 09 dataset.

	Mean differences [m]			Standard deviation [m]			RMS [m]
GPS mode	X	Y	Z	X	Y	Z	XYZ
RTK-Radio (Sion 08)	0.04	0.01	-0.1	0.06	0.07	0.03	0.15
RTK-GPRS (Chur)	0.05	0.04	0.02	0.11	0.08	0.08	0.17
RTK-GPRS (Sion 09)	0.01	0.02	-0.02	0.05	0.07	0.03	0.09

TAB. 7.4: Summary of point-cloud differences (RT versus PP) for flights with RTK.

For a whole spread of applications, sub-decimeter point-cloud accuracy is largely sufficient. This indicates clearly the large potential for RTK in the context of ALS, enabling the generation of point-clouds directly in-flight for projects where a short hand-over time is more important than a marginal accuracy gain that could be achieved by post-processing the data. Furthermore, RTK technology provides the best possible RT control of the quality of the GPS phase data (see also CHAP. 2.4.4).

7.2 Trajectory Quality Analyses (GPSQUAL)

When RTK is not available, GPSQUAL is a crucial component of the overall in-flight ALS data quality analysis. Its role is to predict the likelihood to fix the ambiguities in the PP step. This section evaluates the pertinence of the quality flags issued in-flight. The flags are compared to the ambiguity status issued by GrafNav, i.e. the industry-standard software for GNSS PP.

7.2.1 Application Example

FIG. 7.8 shows the quality flags ($green \rightarrow good, orange \rightarrow critical, red \rightarrow bad$) that were computed in-flight for a Scan2map-mission near Erstfeld (Switzerland) where only SPP was

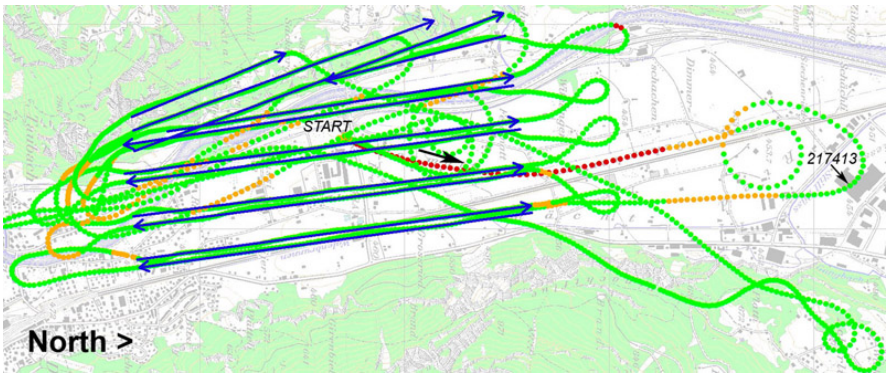

FIG. 7.8: GPS quality flags recorded for flight near Erstfeld (Switzerland).

available. The flight was carried out within a challenging alpine environment where high mountains in east, south and west caused strong obstructions. The reception of the GPS signal was particularly difficult immediately after takeoff. This is well represented by the quality flags provided by GPSQUAL that indicate poor quality (red dots) at the beginning of the flight (see FIG. 7.8). For the rest of the flight, the GPS quality was mainly labeled good with some intermittent critical phases.
FIG. 7.9 compares the recorded quality flags with the post-processed ambiguity status issued by GrafNav. This status has three levels:

1. Float solution → red
2. Ambiguity fixed in one processing direction (forward or backward) → blue
3. Ambiguity fixed in both processing directions → green

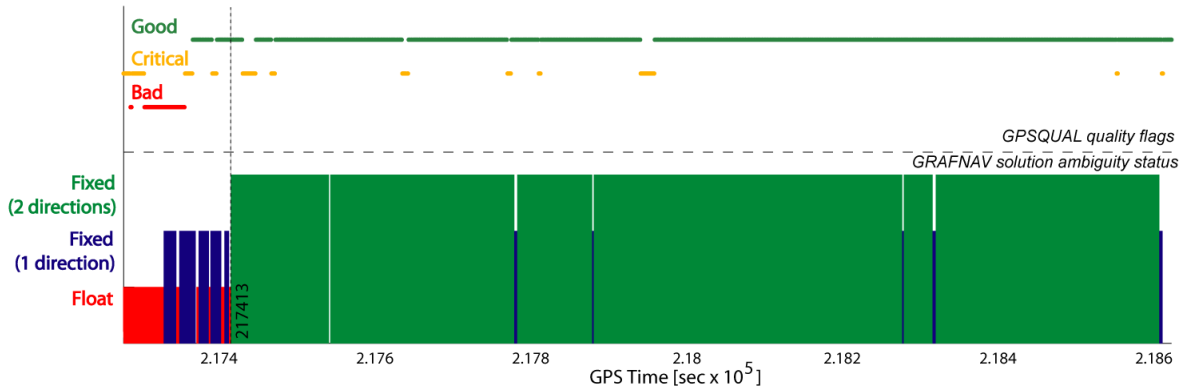

FIG. 7.9: Comparison of GPSQUAL quality flags with ambiguity status for post-processed solution.

The plot illustrates the high congruence between the epochs labeled bad (red) by GPSQUAL and the float PP solution. In the starting period, characterized by alternate good (green) and critical (yellow) solution, the PP algorithm manages to fix the ambiguities only partially and only in one direction. Only after $t_{GPS} = 217413$ sec the ambiguities are predominately fixed in both directions. Nevertheless, in this phase several short intermittent critical periods occur in sharp turns (see FIG. 7.8). They do not stringently overlap with phases where the ambiguity

fix was possible only in one direction. However, periods with one-directional ambiguity fix (blue bars) remain sporadic and are very short (max. 3 sec). They do not have a negative impact on the accuracy of the integrated GPS/INS solution. For such short time intervals the loss of GPS accuracy can be mitigated by the inertial data.

7.2.2 General Validity of Quality Flags

Comparisons between the RT quality flags and the post-processed ambiguity status were carried out for several flights [165]. These evaluations have shown that in most cases intervals labeled "critical" by GPSQUAL are not problematic as long as they remain intermittent with good data and do not exceed a certain duration (< 10 seconds). However, already epochs of 3 to 5 sec duration labeled "bad" are significant as they lead in almost every case to situations where the ambiguities cannot be fixed in the PP step. If this occurs on a flightline, the operator should consider to re-fly the concerned portion in order to prevent situations where the post-processed GPS position will be affected by unacceptable quality degradation.

7.3 ALS Point-cloud Quality Analysis (LIAN)

This section focuses on the evaluation of the quality indicators computed by LIAN. In contrary to the previously assessed modules, these indicators are not computed in RT but their computation is delayed strip-wise as processing starts after each flightline completion.

7.3.1 Data Extent and Gap Polygons

As explained in Chap. 6.7.5, the vectorization of the data extent and gap polygons implemented in LIAN is based on the density grid. Hence, the accuracy of the resulting polygons is depending on two factors: The accuracy of the point-cloud used to derive the density grid and the cell-size c of the grid.
Tab. 7.5 compares the outcome of the LIAN data extent and gap detection algorithm based on a 2D density grid derived from a point-cloud based on SPP positioning ($RMS_{xy} = 1.5$ m) and RTK positioning ($RMS_{xy} = 0.1$ m), respectively. The results based on the post-processed point-cloud were used as reference. To assess the impact of the spatial resolution, the analysis was also performed using two different density grid cell-sizes (2 m and 5 m). The point density threshold was set to a minimum of 1 point/m^2. The results presented in Tab. 7.5 reveal that the accuracy of the 2D boundaries is primarily governed by the resolution of the used density grid. In the SPP-mode for example, the 2D RMS error on the borders is about 0.9 m (for c=2 m) and 2.3 m (for $c = 5$ m), respectively. Logically, increasing the cell-size has the trade-off of loss of resolution (thus accuracy) but also the benefit to reduce the computation-time. Fig. 7.10 visually compares the gap and extent borders detected by LIAN (using a density grid with c=5 m), either based on SPP (red lines) or RTK (blue lines). The borders derived from the post-processed data (green lines), serve as reference. The figure reveals that the location and geometry of the borders is properly recovered for both RT positioning modes. It can be concluded that for the purpose of in-flight extent and gap detection, the point-cloud accuracy achieved by SPP (around 2 to 4 m) and a 5 m density grid is largely sufficient. Additionally,

as the relative accuracy of the laser point-cloud is less affected by the absolute positioning error, the geometrical integrity of the detected borders can be guaranteed.

	Difference to reference data						
	Point-cloud	Density grid with $c = 2$ m			Density grid with $c = 5$ m		
		Polyline[a]		Area[b]	Polyline[a]		Area[c]
	RMS_{xy} [m]	RMS_{xy} [m]	$\lvert max_{\Delta XY} \rvert$ [m]	$\lvert \Delta Area \rvert$ [%]	RMS_{xy} [m]	$\lvert max_{\Delta XY} \rvert$ [m]	$\lvert \Delta Area \rvert$ [%]
SPP	1.5	0.9	3.1	5.5	2.3	7.3	7.1
RTK	0.1	0.4	2.2	3.2	1.4	5.1	4.8

[a]2D differences measured perpendicular to reference line
[b]Mean surface difference computed for 22 gap polygons
[c]Mean surface difference computed for 15 gap polygons

TAB. 7.5: Comparison of extent and gap lines derived from a flightline using a density grid with 2 m and 5 m cell-size (LIAN settings: $\rho_{min} = 1 point/m^2$, minimum gap surface = $250\,m^2$).

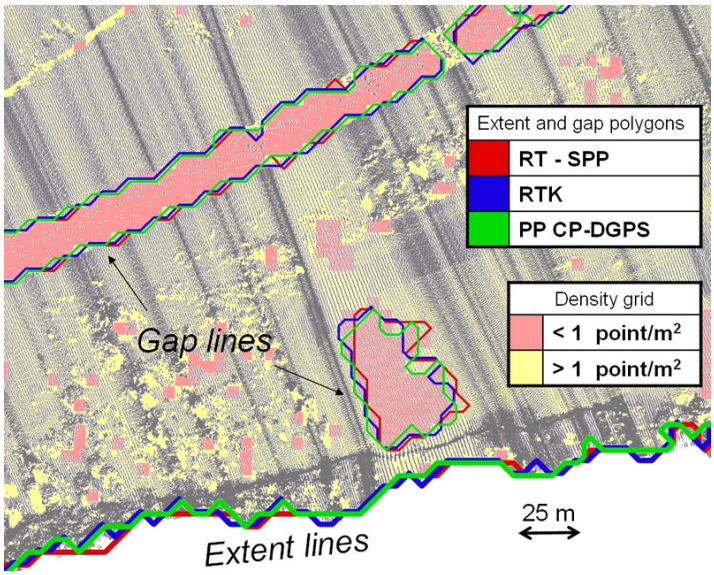

FIG. 7.10: Extent and gap lines ($\rho_{min} = 1\,point/m^2$,, minimum gap surface = $250\,m^2$) computed for flightline using the CP-DGPS, RTK and SPP navigation solution. The displayed density raster (c = 5 m) and the overlaid point-cloud correspond to the CP-DGPS solution.

7.3.2 Point-cloud Quality Map

Besides the scanning geometry, the point-cloud quality map issued by LIAN should reflect the impact of the navigation accuracy on the final point accuracy. To test the adequacy of the inherent model this section presents an evaluation based on data discrepancies between two adjacent strips (called strip 1 and 2 hereafter) computed based on two different scenarios:

(A) Both strips benefit from good GPS data: The ambiguities can be fixed in the forward and backward processing.

(B) Critical GPS data is emulated for strip 2: The resolution of the ambiguities in PP is partially impossible.

FIG. 7.11 depicts the general layout of this evaluation. The green line indicates the smoothed navigation RMS error in height of the "original" data (scenario A), whereas the blue line represents the z position RMS of the data used for scenario B. This dataset was generated by artificially degrading the original GPS dataset during strip 2 by partial masking of satellite signals. The original dataset was acquired using the Scan2map-system. The system and flight characteristics are summarized in TAB. 7.6.

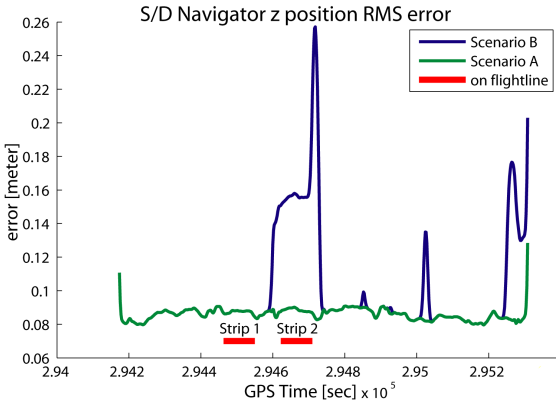

FIG. 7.11: Comparison of the smoothed navigation Z RMS error for both scenarios.

System Calibration parameters	
Boresight	$\sigma_{e_x} = \sigma_{e_y} = 0.002°, \sigma_{e_z} = 0.007°$
Leverarm	$\sigma_{a_x} = \sigma_{a_y} = \sigma_{a_z} = 0.01\,m$
Intrinsic ALS parameters	
Range-finder	$\sigma_\rho = 0.02 + 20\,ppm$
Encoder angle	$\sigma_\theta = 0.005°$
Beam divergence	$\epsilon = 3\,mrad$
Flight parameters	
Mean point density	$d \approx 6\,points/m^2$
Av. height over ground	$h = 250\,m$

TAB. 7.6: Flight parameters and a-priori system and calibration accuracies.

Comparison of Quality Maps

FIG. 7.12 shows the quality flags (as dots) computed by GPSQUAL and the quality maps computed by LIAN for strip 2 in both scenarios. For scenario A, the GPS quality flags remain good (green colored) throughout strip 2, whereas in scenario B the predicted GPS positioning quality oscillates between critical and bad (orange and red colored). As the quality map is based upon a full error propagation using the RT GPS quality flags to scale the position variances, the quality maps reflect the difference in GPS positioning quality (scenario A: $\overline{q}_i = 0.32\,\text{m}$, scenario B: $\overline{q}_i = 0.4\,\text{m}$). The quality maps also demonstrate the spatial non-homogeneity in point accuracy, entailed by the impact of the scanning geometry and the varying laser range. For instance, points scanned at the outer borders of the swath have a reduced accuracy, explainable by the unfavorable incidence angle as compared to points acquired in the middle/nadir of the strip, where the laser range is shorter and almost perpendicular to the terrain.

Evaluation of Strip Differences

For both scenarios height difference grids were computed in the overlapping parts of strip 1 (used as reference strip) and 2 (see FIG. 7.13). Additionally, 3D strip differences were computed using the ICP-algorithm. This provided global 3D-translation parameters between the two

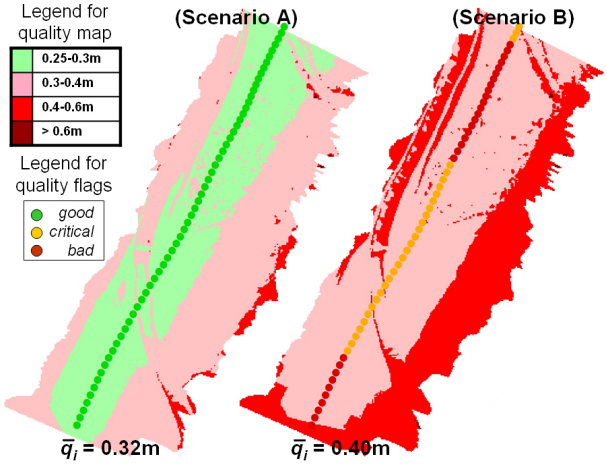

FIG. 7.12: RT GPS quality flags (dots) and q-indicator quality maps computed for strip 2 for both scenarios.

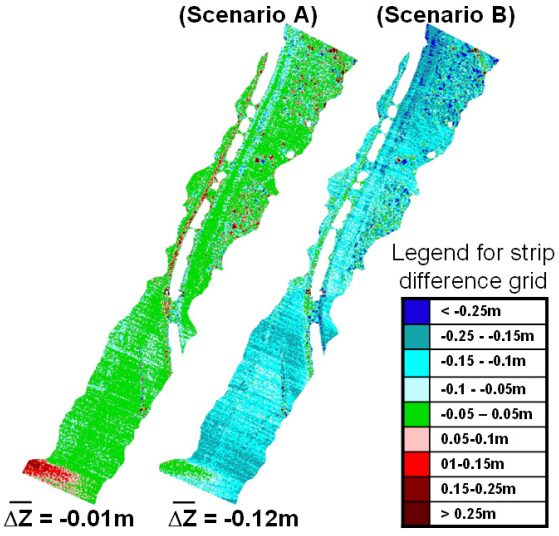

FIG. 7.13: Height difference grids computed for the overlapping parts of strip 1 and 2 for both scenarios.

adjacent strips. TAB. 7.7 shows a summary of the results, where the XYZ-differences computed by ICP and the Z differences (ΔZ) computed by the difference grids can be compared to the mean quality map values ($\overline{q}_i$) predicted during the flight (see FIG. 7.12).
The values for the norm ($|XYZ|$) of the 3D-displacement (computed by ICP) and the mean quality indicator do not correspond completely, but the order of magnitude is similar. The difference can be explained by the contribution of the footprint size to the computation of q_i: For an average flying height of 250 m and beam divergence of 3 mrad, the resulting footprint on the ground is larger than 60 cm, thus significantly contributing to the q_i-value. This reduced spatial resolution is partially recovered by the high point density ($6\,points/m^2$). One can also say that there is a difference of concept: The q_i-value represents the 3D accuracy for a individual laser point, whereas the ICP recovers the differences of two datasets considering a model match, comparing several hundreds of points at once. Obviously, if the mean point density is high, mapping the q_i-value furnishes a rather too pessimistic estimation of the 3D accuracy of the complete height model.

Scenario	Strip difference on point-cloud computed in PP					RT quality map
	ICP				Grid	
	ΔX [m]	ΔY [m]	ΔZ [m]	$\lvert\Delta XYZ\rvert$ [m]	$\overline{\Delta Z}$ [m]	$\overline{q}_i$ [m]
A	0.08	0.05	-0.01	0.09	-0.01	0.32
B	0.12	0.18	-0.11	0.24	-0.12	0.40

TAB. 7.7: 3D strip differences (strip 2 - strip 1) computed by ICP, height differences computed by difference grid and mean RT quality indicator for strip 2.

7.3.3 Ground Classification and DTM Generation

The accuracy evaluations for point-clouds generated in-flight using RTK have pointed out that sub-decimeter accuracy is within reach. However, whether the DTM generated in-flight can reach similar accuracy levels not only depends on the accuracy of the initial point-cloud, but also on the achieved ground point density (thus ground penetration rate) as well as on the correctness of the automated ground filtering (see CHAP. 5.3.1). This section assesses the quality of the ground classification algorithm implemented in LIAN. For this purpose a DTM automatically generated by LIAN is compared with a DTM computed with a reference ground classification algorithm (in this case: Terrasolid TerraScan [8]).

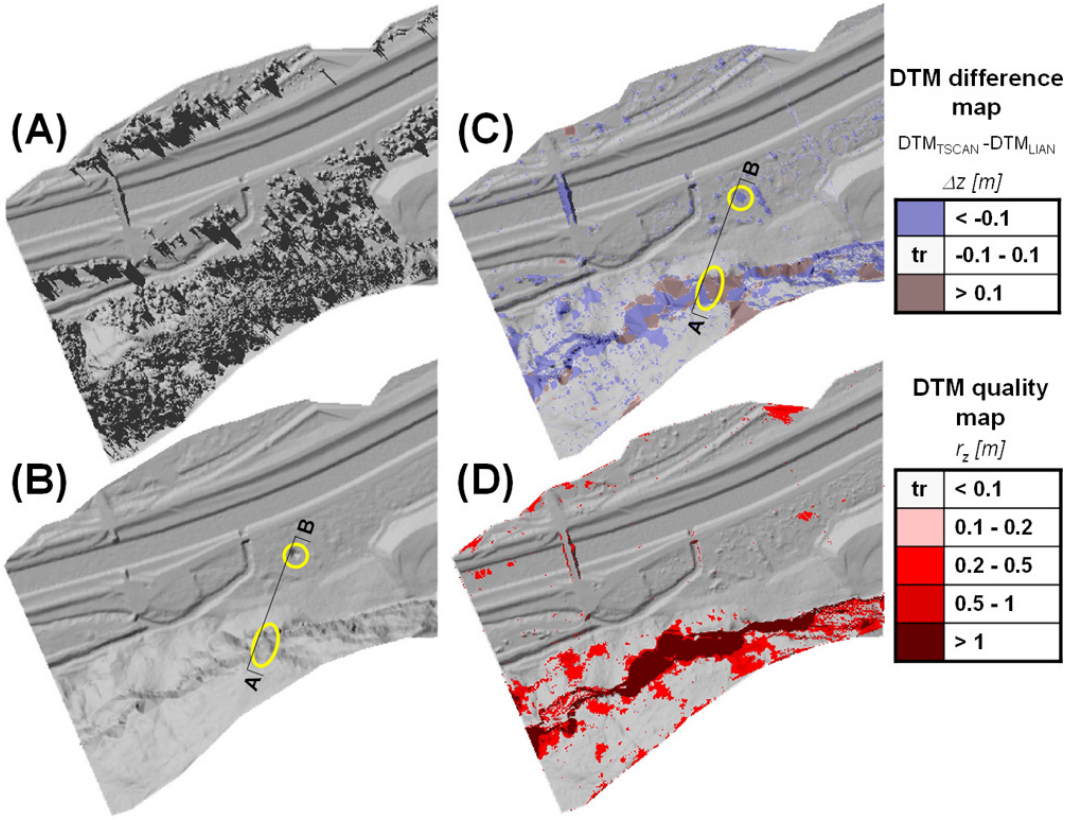

FIG. 7.14: Comparison of ground classification algorithms: (A) Original DSM, (B) 1 m DTM_{tscan}, (C) 1 m DTM_{lian} overlaid with DTM difference map, (D) DTM_{lian} overlaid with DTM quality map. The letters AB refer to the profiles depicted in FIG. 7.15.

Test Setup and Classification Performance

To assess the quality of the ground classification implemented in LIAN, a dataset with challenging topography was selected (see FIG. 7.14.A), that includes strongly sloped parts and varying land cover. FIG. 7.14.B depicts the DTM generated by TerraScan (called DTM_{tscan} hereafter). FIG. 7.14.C and FIG. 7.14.D show the DTM generated by LIAN (DTM_{lian}). Both DTM's were generated automatically applying the default settings of the respective classification algorithms (no tuning of parameters for result improvement). FIG. 7.14.C also plots the

DTM difference grid ($DTM_{tscan} - DTM_{lian}$). The associated color-coding depicts that the height differences occur essentially in the strongly sloped part, whereas in the flatter parts the differences are below 10 cm.
FIG. 7.15 plots the cross-sections $\overline{AB}$ across the classified point-cloud by LIAN (A) and TerraScan (B). These profiles allow identifying differences in the classification performance: In the strongly sloped part, the TerraScan classification outperforms LIAN as it recovers more ground portions within the escarpment. Due to the strong slope in this area ($> 80°$), varying classification results provoke large differences in surface construction (see white dotted lines). This can provoke height discrepancies reaching several meters. In the less inclined parts, both algorithms perform almost equally as they separate correctly the vegetation cover from the bare earth. However, the TerraScan algorithm tends to include isolated low points to the DTM, that are e.g. caused by laser multi-path (see yellow circle). In TerraScan the selection of the initial ground points is exclusively based on the search of lowest points within a certain area [8]. This assumption may lead to "spikes" or "peaks" in the DTM causing large local height errors [128]. The LIAN algorithm is not affected by this problem, because the terrain is builded up applying a region-growing process (see CHAP. 6.7.8). There, the initially selected ground point is only maintained when the search around this point is successful (i.e. delivers new ground points). This is typically not the case for isolated low points.

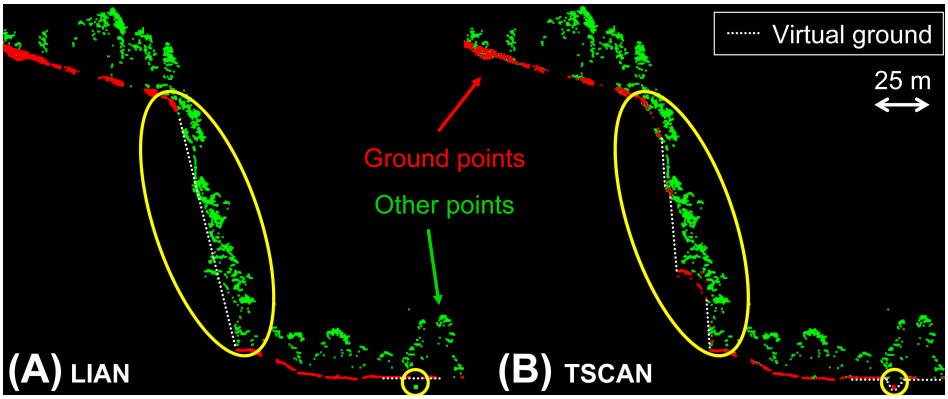

FIG. 7.15: Profiles across point-clouds classified by: (A) LIAN algorithm, (B) TerraScan algorithm.

Use of DTM Quality Map

Without visual inspection and correction a DTM generated by automated ground classification cannot be considered as error-free. The automated DTM quality assessment (see CHAP. 5.3.3) is implemented in LIAN and allows identifying regions within a DTM that may suffer of degraded accuracy. FIG. 7.14.D shows the DTM quality map computed by LIAN for the aforeshown example. Areas with an estimated height reliability index $r_z < 0.1$ m are transparent, whereas areas with poorer reliability are colored according to the legend shown aside. The comparison of FIG. 7.14.C and FIG. 7.14.D reveals that the DTM quality grid reports poor quality exactly in these areas where the DTM difference map reveals the most important discrepancies. Hence, the DTM quality map is an essential component to assess the correctness of a DTM generated automatically in-flight, as it highlights areas where the DTM should not be used without further data inspection. This methodology is also applicable in PP, where

e.g. zones requiring manual classification corrections could be identified automatically, thus drastically reducing the time spent on visual data inspection.

7.4 Computational Performance

To cope with the time-constraints of a RT computational environment, the execution efficiency of the algorithms is crucial. This section investigates the performance (in terms of computation-time) of the critical components of the in-flight quality assessment tool. All performance tests were carried out using a DELL Latitude 820 laptop (Intel(R) DualCore CPU T7600 @ 2.33 GHz, 2 GB RAM).

7.4.1 RT Computations

RT Georeferencing

Within the RT processing chain, the DG of laser data is the computationally most demanding task as it has to handle trajectory data at 400 Hz and laser data at 10 kHz. FIG. 7.16 illustrates the performance of LIEOS for georeferencing one million laser measurements in a local mapping frame. The raw binary data reading and the georeferencing task itself require about 5 sec (corresponds to a processing rate of approx. 200 kHz). For the tested dataset, the computation-time was nearly invariant to the different georeferencing methods (coarse, approximate, rigorous) implemented in LIEOS (see CHAP. 6.6). Simultaneous georeferencing and data logging increases the processing time. If the data is logged to an ASCII file, the computation-time exceeds 20 sec ($\approx$ 50 kHz). However, it the data is stored in some optimized binary format, as typically the case in IQUAL, the slowing-down of the process is moderate, resulting in a processing rate of approx. 150 kHz. This example shows that in the current configuration LIEOS is capable of performing RT DG for scanning rates larger than 100 kHz.

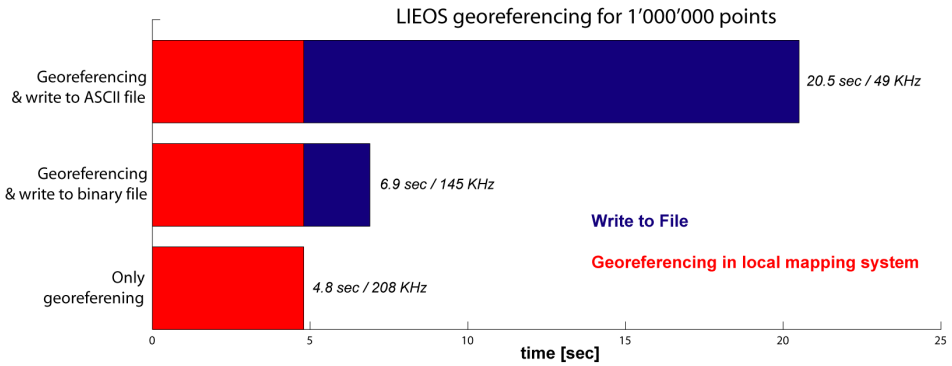

FIG. 7.16: Computation-time for georeferencing 1 mio laser measurements with LIEOS.

RT Data Display

The computation of RT quality indicators used for display HELIPOS (i.e. GPS position and quality flags, swath borders and laser range all at 1 Hz) requires very little computation-time. Within the whole process, the most important latency is introduced by the drawing and rendering of the data on the map (i.e. color-coded dots for GPS positions, polylines for swath, etc.). Although HELIPOS implements an optimized display refreshment algorithm where only the part of the map affected by changes is re-drawn, important time delays due to the graphical refreshment can occur. They can be as long as 1 sec, especially when pan or zoom function are used in parallel, thus requiring an entire screen update. Nevertheless, these latencies are principally hardware-dependent and could be reduced by using e.g. computers with more powerful graphic boards.

7.4.2 Strip-wise Computations

The time-constraints within LIAN are less compelling than those for the aforementioned modules. LIAN starts the computations only once a flightline is completed. Theoretically, LIAN analyses do not stringently have to be finished before the end of the next flightline (see Chap. 6.7.1). However, for the manageability of the flight, it is preferable to provide all quality relevant information as fast as possible.

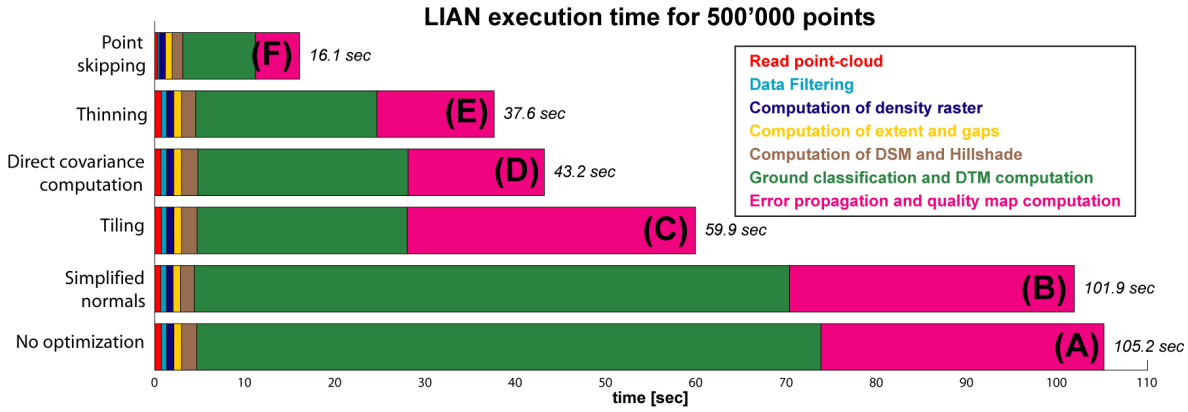

Fig. 7.17: Computation-time for LIAN for point-cloud with 500'000 points.

Fig. 7.17 depicts the computation-time of LIAN for a full quality analysis (using the default LIAN settings) on a point-cloud with 500'000 points for different optimization scenarios. The lowest horizontal bar indicates the needed time when no algorithmic optimizations are performed. The upper bars indicate the processing time for the cumulated optimization steps. For the scenario without code optimization, Fig. 7.17.A illustrates that the "basic" QC steps, such as data reading and filtering, density grid computation, extent and gap detection and DSM computation, require only very little computation-time (ca. 5 sec). The predominant part of the computation-time is used for the "advanced" QC steps, such as ground classification (ca. 65 sec) and error propagation (ca. 35 sec). In the sequel, several strategies to reduce the computational burden of the two latter processing steps are presented.

Aggregated Normal Computation (B)

Both the analysis of the scanning geometry and the ground classification algorithm require the computation of local normals for every point. Within LIAN, this is performed by computing the local covariance matrix for the points within a certain neighborhood N_p of size k and subsequent principal component analysis (PCA) (see Chap. 3.3.3). If the computation is rigorous, the covariance matrix and the PCA have to be performed for every single laser point. However, in cases where the local curvature is low, the change in normal vector orientation for neighboring points remains minimal. Fig. 7.18 illustrates a method taking benefit of this property: If the local curvature Mcc (computed using Eqn. 3.3.7) of a point $\mathbf{p}_i$ is smaller than a certain threshold Mcc_{max}, the computed normal $\mathbf{n}_{p_i}$ can be assigned to the other points that are within a certain distance d_{max} to the original point (see Alg. 7.1). Thus, for all points within the neighborhood $N_p\perp$ no covariance computation is necessary anymore. For the example presented in Fig. 7.17.B the reduction of computation-time is fairly low (time reduction of 3.2 sec or $\approx$ 3%). However, for datasets with smooth topography the time reduction can reach up to 20% of the total processing time.

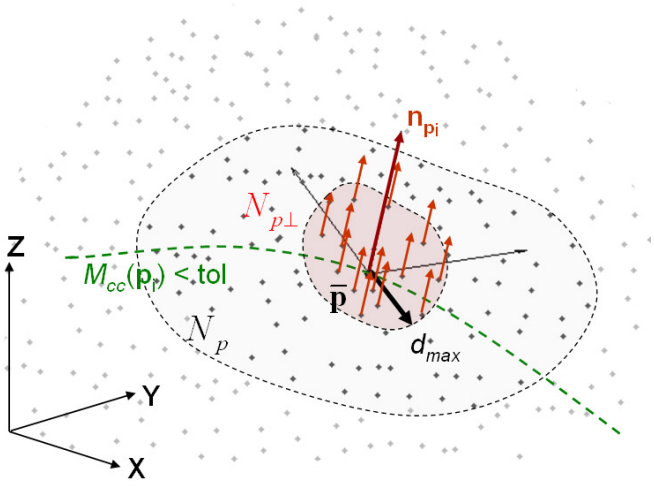

Fig. 7.18: Local normal computation by aggregation.

Data Tiling (C)

Most algorithms used in the ground classification and error propagation step have a non-linear relationship between the size n of the dataset and the computation-time (see e.g. red line in Fig. 7.19). For instance, the construction of a kd-tree for spatial indexing (see Chap. 3.3.1), necessary prior to any data query, has a logarithmic growth in computation-time ($O(n \log n)$). In order to bound the time for spatial indexing and data querying, LIAN implements a dataset tiling procedure, where the point-cloud is subdivided into regular data blocks (typically 50'000 points) based on the timestamp (see Fig. 7.20). To avoid incoherent results at the tile borders, the tiles are defined with a certain overlap (typically 5000 points). Subsequently, the different algorithms (i.e. ground classification) are applied tile-by-tile and the point-cloud is only merged at the end of the process. This procedure allows keeping the

Algorithm 7.1 Fast normal computation by aggregation

Require: Dataset $P_n \in \mathbb{R}_3$, parameters k, Mcc_{max}, d_{max}
  $I_{P_n} = GetAllPointIndexes(P_n)$ {Initially use all points to compute normals}
  while 1 **do**
    if $I_{P_n} = [\,]$ **then**
      break {All normals are computed, processing is over}
    end if
    $i = I_{P_n}[1]$ {Get first index in list of points with no normal assigned until now}
    $I_n = GetNeighborPointIndexes(\mathbf{p}[i], k)$
    $COV_i = ComputeCovarianceMatrix(\mathbf{p}[I_n])$
    $\mathbf{n}_i = ComputeNormal(COV_i)$
    $Mcc_i = ComputeLocalCurvature(COV_i)$
    if $Mcc_i < Mcc_{max}$ **then**
      for $j = 1 : k$ **do**
        if $distance(\mathbf{p}[i], \mathbf{p}[I_n[j]]) < d_{max}$ **then**
          $\mathbf{n}(I_n[j]) = \mathbf{n}_i$ {Assign normal of center point to neighbor}
          $RemoveFromIndexList(I_{P_n}, I_n[j])$ {Remove index to avoid recomputation of normal}
        end if
      end for
    end if
  end while

computation-time linearly proportional to the size of the dataset (see dotted line in Fig. 7.19). The therewith achievable increase in efficiency can also be seen in Fig. 7.17.C, where the computation-time is reduced by more than 40% when implementing the tiling.

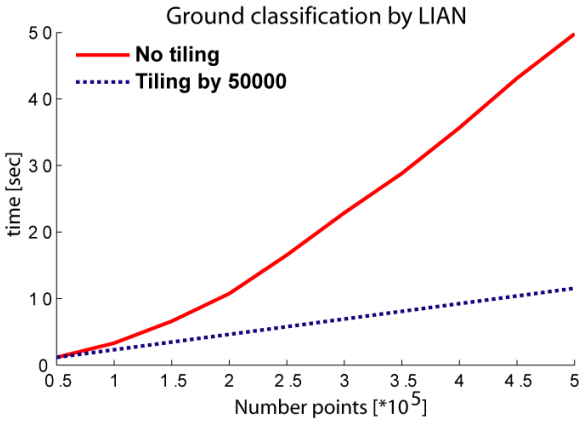

Fig. 7.19: Computation time for ground classification without and with tiling.

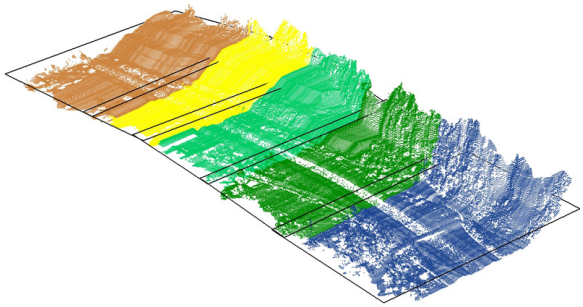

Fig. 7.20: Example of point-cloud tiling by timestamp.

Factorization of Covariance Computation (D)

For the error propagation, LIAN applies Eqn. 4.4.2 to compute the 3×3 covariance matrix for every laser point. Accordingly, for each point a matrix multiplication of complexity $O(2n^2p)$ ($[n \times p] \times [p \times p] \times [p \times n]$, where n=3 and p=14) has to be performed. The construction of the q_i-indicator (see Eqn. 4.6.1) only requires the diagonal elements (variances) of the

covariance matrix. Hence, the off-diagonal elements are of no use and their computation is not necessary. LIAN adopts a strategy to compute directly the diagonal elements. This is achieved by performing a complete factorization and aggregation of repetitive terms for the matrix multiplication. Coding these terms directly (as simple multiplications) for the matrix elements of interest, reduces the computational burden for the covariance matrix estimate by more than 90%. For the total processing chain, this results in further reduction of the computation-time of almost 30% (see FIG. 7.17.D).

Selective Data Thinning (E)

Within LIAN, the individual quality indicators ($\sigma_{xy}^{nav}, \sigma_{z}^{nav}, \sigma_{xy}^{geom}, \sigma_{z}^{geom}, q_i$), computed for every laser point, are used to generate a quality map of a given cell-size (typically 1-2 m). Applying the full error propagation to a dataset with much higher sampling rate than the output quality map is not optimal. Moreover, the point-clouds are often non-homogeneous in point density. FIG. 7.21.A depicts such situation, where due to the changing forward velocity the scan lines are either "stretched apart" or "squeezed together". The selective thinning algorithm implemented in LIAN overcomes this problem by removing points that are within a certain spherical neighborhood of the query point (FIG. 7.21.B). This has several benefits: First, the amount of data that has to be fed into the propagation engine is strongly reduced. Second, the dataset is homogenized and has a sampling rate close to the desired cell-size for the quality map. For the example illustrated in FIG. 7.17.E, the selective thinning reduces the computation-time by more than 5 sec (13% improvement).

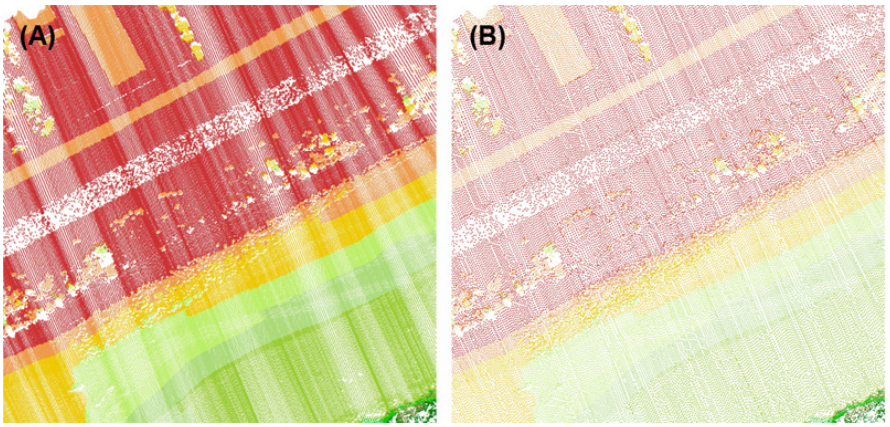

FIG. 7.21: Homogenization of point-cloud density by selective thinning: (A) Original dataset, (B) Thinned dataset (color-coded by elevation).

Data Skipping (F)

For the purpose of in-flight quality assessment, processing the ALS data at the full data rate is not implicitly required. The data skipping can already occur directly in the georeferencing step. However, the performance evaluation presented in CHAP. 7.4.1 has proven that LIEOS can handle the initial data rate of 10 kHz for the Scan2map-system without problem. Thus,

it is advisable to perform the data skipping only when reading the point-cloud data to LIAN. This has the substantial benefit that the point-cloud computed in-flight is complete and could directly be used in the PP-step.
Fig. 7.17.F highlights the reduction in computation-time when reading only every third laser point (skip-factor 3) to LIAN (-21.5 sec or 57% improvement compared to scenario E). Nevertheless, the reduction in computation-time comes together with a loss of spatial data resolution and probably also reduction in the assessment accuracy. Hence, the skipping factor has to be selected appropriatley by maximizing the computational efficiency without substantial loss in the pertinency of the data analysis. If the approximate flying height, carrier speed and PRF of the laser are known the achievable point density can be predicted. Coupling this information with the current LIAN settings (i.e. cell-size of density grid, DSM, DTM and quality map) the optimal skipping value can be determined prior to every mission. For standard Scan2map-missions such skipping factor typically spans between 2 and 4.

Datasets	Grid difference No optimization - cumulated optimizations (B-F)			
	$\overline{\Delta Z}$ [m]	σ_Z [m]	RMS_Z [m]	$\lvert\Delta Z_{max}\rvert$ [m]
Density grid	-0.003	0.16	0.16	1.04
DTM grid	-0.11	0.35	0.37	15.7
Quality grid	0.002	0.09	0.09	9.1

Tab. 7.8: Comparison of LIAN result grid computed by default algorithm (no computation optimization) and using all optimizations (including skip-factor 3).

Tab. 7.8 assesses the compliance of three LIAN result grids (density grid, DTM grid and quality grid) computed once with configuration Fig. 7.17.A (no optimization applied) and once with configuration Fig. 7.17.F (cumulated optimizations). Although the computation-time between the two scenarios is reduced by a factor 6.5 (from 105.2 sec to 16.1 sec), the differences for the density grid and the quality grid are minimal and irrelevant for the purpose of the in-flight quality assessment. As the extent and gap computations are based on the density grid, their validity is not altered by initial point skipping.
The DTM grid is more affected by the quality degradation due to data skipping. As the amount of initial points is drastically reduced, the ground classification in sloped areas becomes problematic. Accordingly, the DTM accuracy principally suffers in those areas. Yet, the computation of the DTM quality map (as shown in Fig. 7.14.D) allows pinpointing such areas.

Chapter 8

Conclusion and Perspectives

This research aimed at developing a methodology to perform in-flight processing and quality assessment of Airborne Laser Scanning (ALS) data. The theoretical concepts have been presented, followed by the description of the implementation in a fully functional software and by performance investigations using emulated and experimental testings. This section first highlights the major contributions of the author. Secondly the performance of the developed system is summarized. Finally, perspectives for future developments and research activities are given.

8.1 Summary of Contributions

The achievement of in-flight ALS data processing and quality assessment capabilities required the development of new methods both on a theoretical/conceptual level and on an algorithmic/engineering level. Accordingly, the main contributions of the author can be divided in these two categories:

Theoretical/conceptual contributions

- The research presented a methodology to perform a full error propagation for ALS data based on a 14 error states model. As a novelty, the functional model is constructed by direct analytical derivation, resulting in highly increased processing speed as compared to numerical derivation by Taylor series expansion.
- A novel approach to assess the impact of the incidence angle and the beamwidth on the total ALS error budget has been introduced. The scanning geometry is assessed quantitatively by estimating the local terrain normal directly from the laser point-cloud by means of principal component analysis of the covariance matrix. This information provides the missing link to the subsequent computation of the 3D footprint.
- This research has introduced the concept of an individual quality indicator for every single laser measurement that reflects not only the georeferencing quality but also the scanning geometry. Its validity has been assessed in simulated and experimental testing. It was shown that such quality indicator can be very valuable within ALS data

processing, e.g. for the generation of quality metadata, for strip adjustment, ground classification and surface modeling.

- Based on the Iterative Closest Point (ICP) algorithm, a methodology to assess the internal ALS data accuracy has been developed. Contrary to strip difference maps reporting only height differences, this method is capable of detecting translational and rotational discrepancies in strip overlaps. In addition, using the ICP stability measure, a concept to perform automated ICP sample area selection has been disclosed.

- An innovative method to perform automated DTM quality assessment has been discussed. The proposed procedure enables the construction of a DTM quality map. This map regroups the main factors influencing DTM quality such as point accuracy and density, terrain slope, ground classification correctness and sampling distance. Additionally, the usability of the DTM quality map to perform weighted grid merging has been demonstrated.

Algorithmic/engineering contributions

- A mission planner module has been developed that allows the computation of virtual scan coverages for given flightline and scanner characteristics based on a coarse DTM. The tool also features a point-cloud accuracy estimation including the scanning geometry and a rigorous spatio-temporal GPS constellation modeling for a planned trajectory.

- The in-flight quality assessment tool IQUAL has been described. A modular design approach has been proposed, that allows scalable distribution of tasks across a network of computers. Specially designed TCP/IP communication protocols, adapted for optimized data exchange between modules in real-time (RT), have been developed.

- As the core of the research, the LiDAR Analysis module (LIAN) was presented. The module incorporates basic QA/QC (Quality Assurance/Quality Control) functionalities, such as density grid computation, automated ALS data extent and gaps detection, DSM hillshade generation and image footprint computation. Advanced in-flight QC includes automated ground classification and DTM generation, computation of strip differences and an error propagation engine, yielding point and surface quality maps.
  An innovative workflow has been designed that handles the import, export and merge of intermediate strip-wise QC results. This allows coping with time-constraints imposed by the in-flight processing.

- The HELIPOS module, responsible for the centralized monitoring and control of all IQUAL functionalities, has been presented. HELIPOS has full Flight Management System (FMS) capabilities and excels with versatile possibilities for displaying quality-relevant data in RT or on operators demand.

- Several strategies to improve the computational efficiency of RT point-cloud processing have been suggested. This includes methods like aggregated normal computation, tiling, covariance factorization and data thinning. Their successful implementation into LIAN has been demonstrated by experimental testings.

8.2 Conclusions

In-flight QA/QC Functionalities. The current industry-standard QA/QC approach for ALS only considers the evaluation of the most important quality parameters (i.e. homogeneity, completeness and accuracy) in post-processing (PP). This research has proposed a tool called IQUAL that achieves ALS data processing and full quality assessment directly during data acquisition. Ordered by their operation mode (latency), the most important functionalities of IQUAL are:

(A) **RT Computations**

- RT GPS quality flags computation
- RT GPS/INS integration
- RT georeferencing and swath display

(B) **Delayed or strip-wise computations**

- Data extent and gap detection
- Image footprint detection
- DSM and hillshade generation
- Automated ground classification
- Full error propagation and point quality map generation
- DTM and DTM quality map generation

Besides the RT GPS/INS integration and the RT swath display, all other functionalities are novelties and do not exist in any commercial FMS suite known to the author.

Integration into the Scan2map-system. The developed in-flight QA/QC tool (IQUAL) has been embedded into the ALS system called Scan2map. The system design was tailored to the needs of challenging close-range ALS missions, characterized by complex flight-plans and changing sensor orientation (nadir, oblique). IQUAL has been successfully tested in many commercial survey missions using the Scan2map-system. The user-friendliness and the ergonomics of the proposed GUI was evaluated and validated. These evaluations have also shown that the provided QC information is necessary to assure data acquisition satisfying the requirements in terms of data coverage, accuracy and homogeneity. By enabling such analysis in-flight, the operator is immediately informed if a part of the mission is affected by unacceptable quality degradation. Adequate countermeasures can be taken immediately during data acquisition (e.g. re-flying a flightline, adopting the sensor orientation).

SPP Operating Mode. The evaluation of several test flights operating in SPP mode have illustrated that the achievable absolute accuracy for a point-cloud generated in-flight is situated at a 2 to 4 m level, whereas the relative accuracy is typically at a sub-meter level. Further evaluations have shown that such accuracy proved to be largely sufficient to control the completeness of the scanning mission in terms of its coverage and density.

Additional experiments have depicted that the adopted strategy to anticipate the final quality of post-processed ALS datasets yields conclusive results. A first evaluation has demonstrated the capacities of GPSQUAL to identify parts of a flight that might be problematic in CP-DGPS. The point quality map generated in-flight was able to predict the quality deterioration of the point-cloud computed in PP.

RTK Operating Mode. Several test flights using RTK have shown that under optimal conditions, point-clouds generated in-flight can reach sub-decimeter accuracy. Additionally, the integrity control of the GPS code and phase measurements is more reliable by solving the ambiguities directly on-the-fly. As all the necessary processing steps needed for producing a final geo-product can be performed in-flight, the delivery of a final mapping product directly after landing becomes possible without substantial loss of accuracy. Hence, the potential benefits using RTK technology for ALS missions are multiple:

- As the whole chain of the data processing can be automated, ALS becomes more economic and faster in production.
- The quality of all data sources can be controlled integrally and directly within the flight.
- The technology is potentially viable for a new type of monitoring missions where short reaction and hand-over time are crucial (i.e. natural hazards, homeland security, etc.).

System Performance. The performance evaluations have shown that LIEOS could perform RT georeferencing for a LiDAR with a PRF up to 100 kHz.
By applying initial data skipping the LIAN performances are scalable. The basic QC operations, such as data extent and gap detection, are very fast (i.e. less than 5 sec for 0.5 million points) and could cope with higher data rates. The advanced QC functionalities, such as ground classification and error propagation require more computation time (i.e. about 25 sec for 0.5 million points). Their applicability may be limited for systems with data rates exceeding 50 kHz.
It is important to mention that the performances of the system are largely depending on the employed processors. The use of more powerful computers (i.e. industrial racks) could certainly reduce the computation time drastically and would render possible the use of full IQUAL functionalities for much higher data rates.

Portability. The necessity of performing QA/QC as early as possible in the processing chain is acknowledged by the ALS community (e.g. [30]). Hence, the availability of a tool such as IQUAL would most certainly represent a substantial economic benefit for all types of ALS systems. Most likely, ALS service providers will expect such functionality for future generations of ALS systems.
Although IQUAL in its current configuration is tightly connected to the hardware devices used in the Scan2map-system, the whole architecture was designed to achieve most optimal portability and scalability. Thus, adopting IQUAL for other commercial-off-the-shelf systems is possible, under the condition that the system providers unfold the necessary information to interface their hardware.

8.3 Perspectives

During this work, several new scientific and engineering challenges have emerged that would make further investigations worthwhile.

Improvement of Point-cloud Post-Processing. Although RT processing was the driving force behind the developments in this research, the majority of the presented tools are as valuable in RT as in PP. The availability of the q-indicator may lead to a paradigm change in point-cloud processing: Today, most point-cloud processing algorithms misleadingly assume a homogeneous point-cloud accuracy. Knowing the variance for each individual point creates new possibilities:

- Automated generation of comprehensive, complete and accurate point-cloud and surface quality metadata.
- Improvement of ground filtering and segmentation algorithms.
- Optimization of DSM/DTM interpolation algorithms.
- Possibility to estimate the height model accuracies without use of external control measurements.
- Improvements in strip adjustment procedures.

This research has already delivered some indicative examples. However, the potential of point-wise variance information to improve processing and QA/QC of ALS data has not nearly been exhausted.

Automated Guidance. In its current design, IQUAL is limited to visually displaying quality relevant information. Based on the provided information, the operator has to decide without assistance by the system what might be his optimal reaction. Further developments should incorporate an anticipation and correction strategy. The software could e.g. predict degrading GPS constellation considering the broadcast ephemeris, a coarse DTM and the flight-plan. Alternatively, an adaptation of the flight-plan may be automatically proposed if e.g. an insufficient strip overlap is detected. In a further step, such system could be adapted to perform automated data acquisition and quality control for mapping missions with unmanned autonomous vehicles (UAV).

Increase of Computational Speed. The current computation-time is the limiting factor for the applicability of the in-flight QA/QC concepts. Especially the point-cloud data querying and derivation of variance information (i.e. data classification, error propagation) requires high computing power. Graphics Processing Units (GPUs) inside graphics cards might be a solution as they have tremendous parallel processing capabilities. For example [40] demonstrates that parallel processing using a standard graphic card accelerates the k-nearest neighbor search (one of the most frequent operations in LIAN) up to a factor of 120. Adapting the software to parallel processing would open the field to in-flight data analysis for ALS data originating from systems with much higher PRF or even recording the full-waveform signal.

Bibliography

[1] F. Ackermann. **Experimental Test on Fast Ambiguity Solution for Airborne Kinematic GPS Positioning**. In *ISPRS congress B6, Vienna*, pages 1–6, 1996.

[2] F. Ackermann. **Airborne laser scanning – present status and future expectations**. *ISPRS Journal of Photogrammetry and Remote Sensing*, 54:64–67, 1999.

[3] O.A. Al-Bayari, N.N. Al-Hanbali, M. Barbarella, and A. Nashwan. **QUALITY ASSESSMENT OF DTM AND ORTHOPHOTO GENERATED BY AIRBORNE LASER SCANNING SYSTEM USING AUTOMATED DIGITAL PHOTOGRAMMETRY**. In *ISPRS Commission III, PCV Symposium 2002*, volume IAPRS, Vol. XXXIV, part 3A/B, ISSN 1682-1750, Graz, Austria, 2002.

[4] A. Alharthy, J. Bethel, and E.M. Mikhail. **Analysis and Accuracy Assessment of Airborne Laserscanning System**. In *XXth ISPRS Congress*, pages 144–149, Istanbul, Turkey, 2004.

[5] R. Artuso, S. Bovet, and A. Streilein. **Practical Methods for the Verification of Countrywide Terrain and Surface Models**. In *Int. Archives of Photogrammetry and Remote Sensing*, volume XXXIV of *part 3/WG13*, page 1419, 2003.

[6] S. Arya and D.M. Mount. **Approximate Nearest Neighbor Queries in Fixed Dimensions**. In *Proceedings of the 4th Annual ACM Symposium on Discrete Algorithms,*, pages 271–280, January 1993.

[7] ASPRS. **ASPRS LIDAR GUIDELINES: Horizontal Accuracy Reporting**. Technical report, ASPRS, 2005.

[8] P. Axelsson. **Processing of laser scanner data – Algorithms and applications**. *ISPRS Journal of Photogrammetry and Remote Sensing*, 54:138–147, 1999.

[9] K.-H. Bae, D. Belton, and D. Lichti. **A framework for position uncertainty of unorganised three-dimensional point clouds from near-monostatic laser scanners using covariance analysis**. In *Proceedings of the ISPRS Workshop "Laser scanning 2005"*, volume XXXVI, Enschede, the Netherlands, 2005.

[10] K.-H. Bae and D. Lichti. **Automated Registration of Unorganised Point Clouds from Terrestrial Laser Scanners**. In *XXth ISPRS Congress*, volume XXXV-B5, Istanbul, 2004.

[11] K.-H. Bae and D. Lichti. **Edge and Tree Detection from Three-dimensional Unorganised Point Clouds from Terrestrial Laser Scanners**. In *12th Australian Remote Sensing and Photogrammetry Conference*, Fremantle, Australia, 2004.

[12] D. Belton and D. Lichti. **Classification and feature Extraction of 3D Point Clouds from Terrestrial Laser Scanners**. In *Spatial Sciences Institute Biennial Conference*, pages 39–48, Melbourne, Australia, 2005.

[13] J.L. Bentley. **Multidimensional Binary Search Trees Used for Associative Searching**. *Communications of the ACM*, 18:209–517, 1975.

[14] T. Beran. **High-accuracy point positioning with low-cost GPS receivers: How good can It get?** In *GNSS 2005*, pages 1524–1534, Long-Beach, CA, 2005.

[15] P.J. Besl and H.D. McKay. **A method for registration of 3-D shapes**. *IEEE Transactions on Pattern Analysis and Machine Intelligence*, 14(2):239–256, 1992.

[16] F. Bretar, M. Pierrot-Deseilligny, and M. Roux. **Solving the strip adjustment problem of 3D airborne lidar data**. In *Proceeding of Geoscience and Remote Sensing Symposium, 2004. IGARSS '04*, volume 7, pages 4734–4737, September 2004.

[17] S. Buckley, J. Vallet, A. Braathen, and W. Wheeler. **Oblique helicopter-based laser scanning for digital terrain modelling and visualisation of geological outcrops**. *International Archives of the Photogrammetry, Remote Sensing and Spatial Information Sciences, 37(B4)*, pages 493–498, 2008.

[18] H. Burman. ***Calibration and orientation of airborne Image and laser scanner data using GPS and INS***. PhD thesis, Royal Institute of Technology, 2000.

[19] S. Calinon and A. Billard. **Teaching a Humanoid Robot to Recognize and Reproduce Social Cues**. In *Proc. IEEE Intl Symposium on Robot and Human Interactive Communication*, pages 346–351, September 2006.

[20] T. Cary. **Lidar Market: Status and Growth Trends**. Technical report, Cary and Associates, Cary and Associates 540 Saint Andrews Drive Longmont, CO 80501-9500 USA, January 2009.

[21] Y. Chen and G. Medoni. **Object modelling by registration of multiple range images**. *Image and Vision Computing*, 10:145–155, 1992.

[22] A.K. Chhabra and I.T. Phillips. **The Second International Graphics Recognition Contest Raster to Vector Conversion: A Report**. *Graphics Recognition Algorithms and Systems*, 1389:390–410, 1998.

[23] I. Colomina, M. Giménez, J.J. Rosales, M. Wis, A. Gómez, and P. Miguelsanz. **Redundant IMUs for Precise Trajectory Determination**. In *Proceedings of the XXth ISPRS Congress, Istanbul, Turkey, Working Group I/5*, 2004.

[24] N. Csanyi and C. Toth. **Improvement of LiDAR Data Accuracy Using LiDAR-Specific Ground Targets**. *Photogrammetric Engineering and Remote Sensing*, 73:385–396, 2007.

[25] Y. Devouassoux and A. Pritchett. **Application of Kalman Filtering to Pilot Detection of Failures**. *IEEE*, 2001.

[26] W.D. Ding, J.L. Wang, P. Mumford, Y. Li, and Rizos C. **TIME SYNCHRONIZATION DESIGN FOR INTEGRATED POSITIONING AND GEOREFERENCING SYSTEMS**. In *Proceedings of SSC 2005 Spatial Intelligence, Innovation and Praxis: The national biennial Conference of the Spatial Sciences Institute, September, 2005. Melbourne*, 2005.

[27] David H. Douglas and Thomas K. Peucker. **Algorithms for the reduction of the number of points required to represent a digitized line or its caricature**. *Canadian Cartographer*, 10(2):112–122, 1973.

[28] G. Droj. **IMPROVING THE ACCURACY OF DIGITAL TERRAIN MODELS**. *STUDIA UNIV. BABES-BOLYAI, INFORMATICA*, LIII(1):65–82, 2008.

[29] M. Elmqvist. **Ground surface estimation from airborne laser scanner data using active shape models**. *International Archives of Photogrammetry Remote Sensing and Spatial Information Sciences 34 (Part 3A)*, pages 114–118, 2002.

[30] B. Emison. **Top 10 LiDAR Data Issues – A QA/QC Primer**. In *The International LiDAR09 Mapping Forum, New Orleans, USA. January 26-28*, 2009. PPT presentation.

[31] ESRI. **ArcGIS 9.2 Desktop Help: How Hillshade works**, 2008. on website: http://webhelp.esri.com/arcgisdesktop/9.2/index.cfm?TopicName=Howe

[32] J. E. Estes and J. Hemphill. ***Introduction to Photo Interpretation and Photogrammetry***, volume 1. The International Center for Remote Sensing Education (ICRSEd), 2001.

[33] H. Fan. ***Theoretical Geodesy***. Royal Institute of Technology (KTH), Department of Geodesy and Photogrammetry, Stockholm, Sweden, 2000.

[34] E. Favey. ***Investigation and Improvement of Airborne Laser Scanning Technique for Monitoring Surface Elevation Changes of Glaciers***. PhD thesis, SWISS FEDERAL INSTITUTE OF TECHNOLOGY ZURICH (ETHZ), 2001.

[35] S. Filin. **Analysis and Implementation of a laser strip adjustment model**. *International Archives of Photogrammetry and Remote Sensing*, 34:65–70, 2003.

[36] S. Filin. **Recovery of Systematic Biases in Laser Altimetry Data Using Natural Surfaces**. *Photogrammetric Engineering and Remote Sensing*, 69(11):1235–1242, 2003.

[37] S. Filin and G. Vosselman. **Adjustment of Airborne Laser Altimetry Strips**. In *International Archives of Photogrammetry and Remote Sensing, XXXV, B3, Istanbul, Turkey*, volume 34, pages 285–289, 2004.

[38] M. Flood. **ASPRS Guidelines: Vertical Accuracy Reporting for Lidar Data**. Technical report, ASPRS, 2004.

[39] P. Friess. **Toward a rigorous methodology for airborne laser mapping**. In *EuroCOW*, page 7, Castelldefels, Spain, 2006. on CDROM.

[40] V. Garcia, E. Debreuve, and M. Barlaud. **Fast k nearest neighbor search using gpu**. In *In CVPR Workshop on Computer Vision on GPU, Anchorage, Alaska, USA*, 2008.

[41] N. Gelfand, L. Ikemoto, S. Rusinkiewicz, and M. Levoy. **Geometrically Stable Sampling for the ICP Algorithm**. In *Proceedings of the Fourth International Conference on 3-D Digital Imaging and Modeling (3DIM03)*, 2003.

[42] G.P. Gerdan. **A Comparison of Four Methods of Weighting Double-Difference Pseudorange Measurements**. *Australian surveyor*, 40:60–66, 1995.

[43] C.L. Glennie. **Rigourous 3D Error Analysis of Kinematic Scanning LIDAR Systems**. *Journal of Applied Geodesy*, 1:147–157, 2007.

[44] S. Godha and M.E. Cannon. **GPS/MEMS INS Integrated System for Navigation in Urban Areas**. *GPS Solutions*, 11(3):193–203, 2007.

[45] R.L. Greenspan. **Inertial Navigation Technology from 1970-1995**. *Journal of The Institute of Navigation*, 42:165–186, Spring 1995.

[46] A. Grimm. **New Products and Services from IGI**. In *Proceedings of Photogrammetric Week '07, Stuttgart, Germany*, 2007.

[47] S. Grünig and U. Wild. **Swipos über Internet. Neue Entwicklungen bei der Echtzeit-Positionierung**. *Geomatik Schweiz*, 3:121–124, 2005.

[48] S. Guerrier. **Integration of Skew-Redundant MEMS-IMU with GPS for Improved Navigation Performance**. Master's thesis, EPFL, 2008.

[49] A.F. Habib and R.W.T. Cheng. **Surface Matching Strategy for Quality Control of LIDAR Data**. *Innovations in 3D Geo Information Systems*, pages 67–83, 2006.

[50] H. Hartinger and F.K. Brunner. **Attainable Accuracy of GPS Measurements in Engineering Surveying**. In *Proceedings of FIG XXI International Conference, 21-25 July, Brighton, U.K.*, pages 18–31, 1998.

[51] M.E. Hodgson and P. Brenahan. **Accuracy of Airborne Lidar-Derived Elevation: Empirical Assessment and Error Budget**. *Photogrammetric Engineering & Remote Sensing*, 70:331–339, 2004.

[52] B. Hoefle and N. Pfeifer. **Correction of laser scanning intensity data: Data and model-driven approaches**. *ISPRS Journal of Photogrammetry & Remote Sensing*, 62:415–433, 2007.

[53] B. Hofmann-Wellenhof, K. Legat, and M. Wieser. ***Navigation – Principles of Positioning and Guidance***. Springer Verlag Wien, 1 edition, 2003.

[54] C. Hug, A. Ullrich, and Grimm. Litemapper-5600: a waveform-digitizing lidar terrain and vegetation mapping system. *International Archives of Photogrammetry, Remote Sensing and Spatial Information Sciences*, 36:24–29, 2004.

[55] E. J. Huising and L. M. Pereira Gomes. **Errors and accuracy estimates of laser data acquired by various laser scanning systems for topographic applications**. *ISPRS Journal of Photogrammetry and Remote Sensing*, 53(5):245–261, 1998.

[56] H. Hyyppä, X. Yu, H. Kaartinen, S. Kaasalainen, E. Honkavaara, and P. Rönnholm. **FACTORS AFFECTING THE QUALITY OF DTM GENERATION IN FORESTED AREAS**. In *ISPRS WG III/3, III/4, V/3 Workshop "Laser scanning 2005", Enschede, the Netherlands, September 12-14*, 2005.

[57] D. Ineichen, E. Brockmann, and S. Schaer. **Enhancing the Swiss Permanent GPS Network (AGNES) for GLONASS**. In *Subcommission for the European Reference Frame (EUREF), London, UK*, 2007.

[58] H. Ingensand. **METROLOGICAL ASPECTS IN TERRESTRIAL LASER-SCANNING TECHNOLOGY**. In *3rd IAG / 12th FIG Symposium, Baden, May 22-24, 2006*, 2006.

[59] D. Issler. **European avalanche test sites. Overview and analysis in view of coordinated experiments**. Technical report, Mitteilungen Nr.59, SLF Davos, 1999.

[60] B. Jutzi and U. Stilla. **Range determination with waveform recording laser systems using a Wiener Filter**. *ISPRS Journal of Photogrammetry and Remote Sensing*, 61(2):95–107, 2006.

[61] H. Kager and K. Kraus. **Height discrepancies between overlapping laser scanner strips - simultaneous fitting of aerial laser scanner strips**. In *Fifth Conference on Optical 3-D Measurement Techniques, Vienna, Austria*, 2001.

[62] E.D. Kaplan. ***Understanding GPS: Principles and Applications***. Artech House, 2006.

[63] W. Karel and K. Kraus. **Quality parameters of digital terrain model**. In *EuroSDR: Seminar on Automated Quality Control of Digital Terrain Models*, 2005.

[64] W. Karel, N. Pfeifer, and C. Briese. **DTM QUALITY ASSESSMENT**. In *ISPRS Technical Commission II Symposium, 2006, Vienna*, 12-14.July 2006.

[65] R. Katzenbeisser. **About the Calibration of Lidar Sensors**. In *ISPRS Workshop 3-D Reconstruction from Airborne Laser-Scanner and InSAR data*, Dresden, 2003.

[66] G. Kemper and F. Pinicka. **AeroTopoL: A system for planning, navigation and managing of aerial photo campaigns or scanning operations**. Technical report, GGS Büro fr Geotechnik, Geoinformatik, Service, 2003.

[67] J. Kilian, N. Haala, and M. Englich. **Capture and evaluation of airborne laser scanner data**. *International Archives of Photogrammetry and Remote Sensing 31 (Part B3)*, pages 383–388, 1996.

[68] M.A. King. **The GPS Contribution to the Error Budget of Surface Elevations Derived From Airborne LIDAR**. *IEEE TRANSACTIONS ON GEOSCIENCE AND REMOTE SENSING*, 47(3), March 2009.

[69] X. Kong, E.M. Nebot, and H. Durrant-Whyte. **Development of a non-linear psi-angle model for large misalignment errors and its application in INS alignment and calibration**. In *Proceedings of the IEEE International Conference on Robotics & Automation*, pages 1430–1435, 1999.

[70] W. Kornus and A. Ruiz. **Strip adjustment of LiDAR data**. *International Archives of Photogrammetry and Remote Sensing*, 34:47–50, 2003.

[71] K. Kraus and N. Pfeifer. **Derivation of difgital terrain models in wooded areas with airborne laser scanner data**. *ISPRS Journal for Photogrammetry and Remote Sensing*, 53:193–203, 1998.

[72] K. Kraus and N. Pfeiffer. **Advanced DTM generation from LIDAR data**. *International Archives of the Photogrammetry, Remote Sensing and Spatial Information Sciences 34 (Part 3/w4)*, pages 23–30, 2001.

[73] K. Kraus, C. Ressl, and A. Roncat. **Least squares matching for airborne laser scanner data**. In *International Symposium Turkish-German Joint Geodetic Days, Berlin, March 29-31*, 2006.

[74] J. Kremer. **CCNS and AEROcontrol: Products for Efficient Photogrammetric Data Collection**. In *in Proceedings of Photogrammetric Week 2001, Stuttgart*, 2001.

[75] KTI. **The innovation promotion agency CTI**. on website: http://www.bbt.admin.ch/kti/index.html?lang=en. last visited: 22.10.2009.

[76] A. Kukko, S. Kaasalainen, and P. Litkey. **Effect of incidence angle on laser scanner intensity and surface data**. *Applied Optics*, 47:986–992, March 2008.

[77] K. Lambers, H. Eisenbeiss, M. Sauerbier, D. Kupferschmidt, T. Gaisecke, S. Sotoodeh, and T. Hanusch. **Combining photogrammetry and laser scanning for the recording and modelling of the Late Intermediate Period site of Pinchango Alto, Palpa, Peru**. *Journal of Archaeological Science*, 34:1702–1712, 2007.

[78] S. Landtwing. **Airborne Laser Scanning: Genauigkeitsinformationen fuer den Auswertungsprozess**. Master's thesis, Swiss Federal Institute of Technology, Zürich (ETHZ), 2005.

[79] R.B. Langley. **GPS Receiver System Noise**. *GPS World*, 8(8):40–45, 1997.

[80] K. Legat. **Approximate direct georeferencing in national coordinates**. *ISPRS Journal of Photogrammetry Engineering & Remote Sensing*, 60:239–255, 2006.

[81] K. Legat, J. Skaloud, and P. Schaer. **Real-time processing of GPS/INS data for on-the-fly quality control in airborne mobile mapping**. In *European Navigation Congress ENC-GNNS*, Manchester, 2006.

[82] LEICA. **Product Description Leica FCMS Release 3.1**. Technical report, Leica GeoSystems, 2009.

[83] M. Lemmens. **Product Survey: Airborne Lidar Sensors**. *GIM International: The Global Magazine for Geomatics*, 23(2):16–19, February 2009.

[84] D. Lichti and S.J. Gordon. **Error Propagation in Directly Georeferenced Terrestrial Laser Scanner Point Clouds for Cultural Heritage Recording**. In FIG, editor, *FIG Working Week*, Athens, Greece, 2004.

[85] D. Lichti and J. Skaloud. **Chapter 3: Registration and Calibration**. *In Airborne and terrestrial laser scanning, G. Vosselman and H.-G. Maas (Eds.)*, 2009. Expected publication Date December 2009.

[86] D.D. Lichti. **Error modelling, calibration and analysis of an AMCW terrestrial laser scanner system**. *International Journal of Photogrammetry and Remote Sensing*, 61:307–324, 2007.

[87] N. Lima, J. Casaca, and M. J. Henriques. **Accuracy of Displacement Monitoring at Large Dams with GPS**. *International Association of Geodesy Symposia*, 131:239–243, 2006.

[88] G. Lindstroem and G. Gasparini. **The Galileo satellite system and its security implications. EU-ISS Occasional Paper 44**. Technical Report 44, Europeean Union for Security Studies, March 2003.

[89] X. Liu, Z. Zhang, J. Peterson, and S. Chandra. **The effect of LiDAR data density on DEM Accuracy**. In *MODSIM07 International Congress on Modelling and Simulation*, December 2007.

[90] J. Luethy. ***Entwicklung eines Qualitätsmodells für die Generierung von Digitalen Geländemodellen aus Airborne Laser Scanning***. PhD thesis, Swiss Federal Institute of Technology, Zürich (ETHZ), 2007.

[91] J. Luethy and R. Stengele. **3D MAPPING OF SWITZERLAND CHALLENGES AND EXPERIENCES**. In *ISPRS WG III/3, III/4, V/3 Workshop "Laser scanning 2005", Enschede, the Netherlands, September 12-14, 2005*, 2005.

[92] F. Luy. **Cartographie aéroportée de haute précision**. *Flash EPFL*, 7:3, 2009.

[93] H.-G. Maas. **Least-squares matching with airborne laserscanning data in a TIN structure**. *The International Archives of the Photogrammetry, Remote Sensing and Spatial Information Science, Amsterdam, The Netherlands,*, XXXIII:548–555, 2000.

[94] H.-G. Maas. **Planimetric and height accuracy of airborne laserscanner data – User requirements and system performance**. In *Proceedings 49. Photogrammetric Week (Ed. D. Fritsch)*, pages 117–125, 2003.

[95] S.M. Magrabi and P.W. Gibbens. **Decentralised Fault Detection and Diagnosis in Navigation Systems for Unmanned Aerial Vehicles**. *IEEE 2000 PLANS*, pages 363–370, 2000.

[96] C. Mallet and F. Bretar. **Full-Waveform Topographic Lidar: State-of-the-Art**. *ISPRS Journal of Photogrammetry and Remote Sensing*, 64(1):pp. 1–16, 2009.

[97] M. Matton and R. Cools. **A comparison of different k-nearest neighbour algorithms with performance results on speech data**. Technical report, Department of Computer Science, Katholieke Universiteit, January 2004.

[98] R. Mehra, C. Rago, and S. Seereeram. **Autonomous Failure Detection, Identification and Fault-Tolerant Estimation with Aerospace Applications**. *IEEE*, 1998.

[99] X. Meng, L Wang, J.L. Silvan-Cardenas, and N. Currit. **A multi-directional ground filtering algorithm for airborne LIDAR**. *ISPRS Journal of Photogrammetry and Remote Sensing*, 64(1):117 – 124, 2009.

[100] K. Morin. ***Calibration of Airborne Laser Scanners***. PhD thesis, University of Calgary, 2002.

[101] K. Morin and N. El-Sheimy. **Post-mission adjustment of airborne laser scanning data**. In *FIG XXII International Congress*, volume CD-ROM, page 12, Washington DC, USA, 2002.

[102] D.M. Mount. ***ANN Programming Manual***. Department of Computer Science and Institute for Advanced Computer Studies University of Maryland, College Park, Maryland., 1.1.1 edition, 2006.

[103] M.R. Napolitano, D.A. Windon, J.L. Casanova, M. Innocenti, and G. Silvestri. **Kalman Filters and Neural-Network Schemes for Sensor Validation in Flight Control Systems**. *IEEE TRANSACTIONS ON CONTROL SYSTEMS TECHNOLOGY*, (5), 1998.

[104] U.S Department of Defense. **GLOBAL POSITIONING SYSTEM POSITIONING SERVICE PERFORMANCE STANDARD**, 2008.

[105] Optech. **ALTM 30/70/100 User Manual**. Technical report, 2004.

[106] Optech. **Gemini ALTM Airborne Laser Terrain Mapper**, 2008.

[107] R. Passini and K. Jacobsen. **Filtering of digital elevation models**. In *Proceedings of the ASPRS Annual Convention, Washington DC*, 2002.

[108] M. Pauly, M. Gross, and L.P. Kobbelt. **Efficient simplification of point-sampled surfaces**. In *Proceedings of the conference on Visualization '02, Boston, Massachusetts*, 2002.

[109] O. Perrin, M. Scaramuzza, Th. Buchanan, S. Soley, P.-Y. Gilliron, and A. Waegli. **Challenging EGNOS in the Swiss Alps**. In *Proceedings of the European Navigation Conference ENC-GNSS 2003, Graz, Austria*, 2003.

[110] O. Perrin, M. Scaramuzza, M. Schwendener, and J. Bredemeyer. **EGNOS test flights within Switzerland**. In *Proceedings of the European Navigation Conference (ENC) in Manchester , 7.-10. May*, 2006.

[111] N. Pfeifer and C. Briese. **GEOMETRICAL ASPECTS OF AIRBORNE LASER SCANNING AND TERRESTRIAL LASER SCANNING**. In *Proceedings of the ISPRS Workshop on Laser Scanning 2007 and SilviLaser 2007*, September 2007.

[112] T. Produit. **Recover ALS Strip differences by ICP**. Technical report, Geomatic Engineering Laboratory (TOPO), Swiss Federal Insitute of Technology Lausanne (EPFL), 2009.

[113] P. A. Psimoulis, V. A. Kontogianni, A. Nickitopoulou, S.I. Pytharouli, P. Triantafyllidis, and S.C. Stiros. **Estimating the Optimum Duration of GPS Static Observations for Short Baseline Length Determination in Greece**. In *FIG Working Week 2004, Athens, Greece, May 22-27*, 2004.

[114] U. Pyysalo. ***Generation of elevation models in wooded areas from a three dimensional point cloud measured by laser scanning***. PhD thesis, Helsinki University of Technology, 2000.

[115] J. Reitberger, O. Krzystek, and U. Stilla. **Analysis of full wavefrom LIDAR data for the classification of deciduous and coniferous trees**. *International Journal of Remote Sensing*, 29:1407–1431, 2007.

[116] C. Ressl, H. Kager, and G. Mandlburger. **QUALITY CHECKING OF ALS PROJECTS USING STATISTICS OF STRIP DIFFERENCES**. In *Proceedings of the XXI ISPRS Congress, Beijing, China*, 2008.

[117] C. Ressl, G. Mandlburger, and N. Pfeifer. **INVESTIGATING ADJUSTMENT OF AIRBORNE LASER SCANNING STRIPS WITHOUT USAGE OF GNSS/IMU TRAJECTORY DATA**. In *Proceedings of Laser scanning 2009, IAPRS, Paris, France, September 1-2, 2009*, 2009.

[118] G. Retscher. **Accuracy Performance of Virtual Reference Station (VRS) Networks**. *Journal of Global Positioning Systems*, 1:40–47, 2002.

[119] Riegl. **LMS-Q240, www.riegl.co.at**, 2004.

[120] Riegl. **LMS-Q240(i), www.riegl.co.at**, 2006.

[121] Riegl. **Airborne Laser Scanner RIEGL VQ-480: Preliminary Datasheet**. Technical report, Riegl Laser Measurement System GmbH, 2009.

[122] Riegl. ***RiACQUIRE Software Description & User's Instructions***, 2009.

[123] C. Rodarmel, A. Samberg, H. Theiss, and T. Johansen. **A review of the asprs guidelines for the reporting of horizontal and vertical accuracies in lidar data**. *Revue française de photogrammétrie et de télédétection*, 182:34–39, 2006.

[124] R. B. Roth and J. Thompson. **PRACTICAL APPLICATION OF MULTIPLE PULSE IN AIR (MPIA) LIDAR IN LARGE-AREA SURVEYS**. In *Proceedings of the XXI ISPRS Congress, Beijing, China*, 2008.

[125] M. Rutzinger, B. Hoefle, and N. Pfeifer. **Detection of high urban vegetation with airborne laser scanning data**. In *ForestSAT07, Montpellier (France)*, May 2007.

[126] C. Satirapod and P. Homniam. **GPS Precise Point Positioning Software for Ground Control Point Establishment in Remote Sensing Applications**. *Journal of Surveying Engineering (ASCE)*, 132(1):11–14, 2006.

[127] P. Schaer. ***MissionPlanner: Software for flight planification for Scan2map-system***. Swiss Federal Institute of Technology, Lausanne, 2008.

[128] P. Schaer, J. Skaloud, S. Landtwing, and K. Legat. **Accuracy Estimation for Laser Point Cloud including Scanning Geometry**. In *5th International Symposium on Mobile Mapping Technology (MMT2007)*, Padua, Italy, 2007.

[129] P. Schaer, J. Skaloud, Y. Stebler, P. Tomé, and R. Stengele. **Airborne LiDAR: In-Flight Accuracy Estimation**. *GPS World*, 20(8):37–41, August 2009.

[130] P. Schaer, J. Skaloud, and P. Tomé. **Towards In-Flight Quality Assessment of Airborne Laser Scanning**. In *Proceedings of the XXI ISPRS Congress, Beijing, China*, 2008.

[131] P. Schaer and Y. Stebler. **In-flight Accuracy Estimation for Airborne Lidar Data**. In *Proceedings of the ION GNSS 2009, Savannah, Georgia, USA*, 2009.

[132] T. Schenk. **Modeling and Analyzing Systematic Errors in Airborne Laser Scanners**. Technical report, Technical Notes in Photogrammetry No. 19, Department of Civil and Environmental Engineering and Geodetic Science, The Ohio State University, Columbus, OH, USA,, 2001.

[133] T. Schenk, S. Seo, and B. Csatho. **ACCURACY STUDY OF AIRBORNE LASER SCANNING DATA WITH PHOTOGRAMMETRY**. *International Archives of Photogrammetry and Remote Sensing*, XXXIV-3/W4 Annapolis, MD, 22-24 Oct. 2001:113–118.

[134] K.P. Schwarz and N. El-Sheimy. **Mobile Mapping Systems - State of The Art And Future Trends**. *International Archives of Photogrammetry, Remote Sensing and Spatial Information Sciences*, 35, Part B:10, 2004.

[135] G. Seeber. ***Satellite Geodesy***. Walter de Gruyter, Berlin, 1993.

[136] L. Shan and C.K. Toth. ***TOPOGRAPHIC LASER RANGING AND SCANNING – Principles and Processing***. CRC Press, 2008.

[137] S. Shan, M. Bevis, M. Kendrick, G. L. Mader, D. Raleigh, K. Hudnut, M. Sartori, and D. Phillips. **Kinematic GPS solutions for aircraft trajectories: Identifying and minimizing systematic height errors associated with atmospheric propagation delays**. *Geophys. Res. Lett*, 34(23), 2007.

[138] C.E. Shannon. **Communication in the presence of noise**. *Proc. Institute of Radio Engineers*, 37:10–21, 1949.

[139] X. Shen and Y. Gao. **Kinematic Processing Analysis of Carrier Phase based Precise Point Positioning**. In *Proceedings of FIG XXII International Congress, Washington DC, USA*, 2002.

[140] M. R. Sitar. **ALTM Orion**. *Professional SURVEYOR Magazine: Aerial Mapping Supplement*, 29:2 –5, 2009.

[141] G. Sithole. **Filtering of laser altimetry data using a slope adaptive filter**. *International Archives of Photogrammetry and Remote Sensing.*, 34:203–210, 2001.

[142] G. Sithole and G. Vosselman. **Experimental comparison of filter algorithms for bare earth extraction from airborne laser scanning point clouds**. *ISPRS Journal of Photogrammetry and Remote Sensing*, 59:85–101, 2004.

[143] J. Skaloud. **Strapdown INS Orientation Accuracy with GPS Aiding**. Master's thesis, University of Calgary, 1995.

[144] J. Skaloud. ***Optimizing Georeferencing of Airborne Survey Systems by INS/DGPS***. PhD thesis, University of Calgary, 1999.

[145] J. Skaloud. **Problems in Direct-Georeferencing by INS/DGPS in the Airborne Environment**. In *Workshop on 'Direct versus indirect methods of sensor orientation',Commission III, WG III/1, Barcelona, Spain*, 1999.

[146] J. Skaloud. **Direct Georeferencing in Aerial Photogrammetric Mapping**. *Photogrammetric Engineering & Remote Sensing*, pages 207–210, 2002.

[147] J. Skaloud. ***Manual for ALS DataLogger***. Swiss Federal Institute of Technology, Lausanne, 2005.

[148] J. Skaloud. **Reliability in direct georeferencing: an overview of the current approaches and possibilites**. In *Proc. EuroCOW 2006*, Castelldefels, Spain, 2006.

[149] J. Skaloud. **Reliability of Direct Georeferencing Phase 1: An Overview of the Current Approaches and Possibilities**. In *Checking and Improving of Digital Terrain Models / Reliability of Direct Georeferencing.* EuroSDR Official Publication 51, 2007.

[150] J. Skaloud. ***LIEOS: LiDAR Exterior Orientation Software***. Swiss Federal Institute of Technology, 2009. http://topo.epfl.ch/research/techtransfer.

[151] J. Skaloud. ***RFLOWS: Manual for RT simulation server***. EPFL-TOPO, 2009.

[152] J. Skaloud, H. Gontran, and B. Merminod. **GSM-distributed RTK for precise analysis of speed skiing**. In *8th European Navigation Conference GNSS 2004*, Rotterdam, 2004.

[153] J. Skaloud and K. Legat. **Theory and reality of direct georeferencing in national coordinates**. *Journal of Photogrammetry & Remote Sensing*, 63:272–282, 2008.

[154] J. Skaloud and D. Lichti. **Rigorous approach to bore-sight self calibration in airborne laser scanning**. *ISPRS Journal of Photogrammetry and Remote Sensing*, 61(1):47–59, 2006.

[155] J. Skaloud and P. Schaer. **Towards A More Rigorous Boresight Calibration**. In *ISPRS International Workshop on Theory Technology and Realities of Inertial/GPS/Sensor Orientation*, Castelldefels, Spain, 2003.

[156] J. Skaloud and P. Schaer. **Towards Automated LiDAR Boresight Self-calibration**. In *5th International Symposium on Mobile Mapping Technology (MMT2007)*, Padua, Italy, 2007.

[157] J. Skaloud, P. Schaer, Y. Stebler, and P. Tomé. **Real-time Registration of Airborne Laser Data with Sub-Decimeter Accuracy**. Submitted for ISPRS Journal of Photogrammetry and Remote Sensing in August 2009, 2009.

[158] J. Skaloud and J. Vallet. **High Accuracy Handheld Mapping System for Fast Helicopter Deployment**. In *Joint International Symposium on Geospatial Theory, Processing and Applications, ISPRS Comm. IV*, Ottawa, Canada, 2002.

[159] J. Skaloud, J. Vallet, K. Keller, G. Veyssiere, and O. Koelbl. **HELIMAP: Rapid Large Scale Mapping Using Handheld LiDAR/CCD/GPS/INS Sensors on Helicopters**. In *ION GNSS 2005*, Long Beach, CA, USA, 2005.

[160] J. Skaloud and P. Viret. **GPS/INS Integration: From Modern Methods of Data Acquisition to New Applications**. *European Journal of Navigation*, (November):60–64, 2004.

[161] A. Soininen. **Ground Classification**, 2005. Presentation available on the web site of TerraSolid Inc., Finland.

[162] A. Soininen and H. Burman. **TerraMatch for MicroStation**, 2005.

[163] A. Solimeno. ***Low-Cost INS/GPS Data Fusion with Extended Kalman Filter for Airborne Applications***. PhD thesis, Instituto Superior Tecnico, Universidade Tecnica de Lisboa, 2007.

[164] S. Soudarissanane, R. Lindenbergh, M. Menenti, and P. Teunissen. **INCIDENCE ANGLE INFLUENCE ON THE QUALITY OF TERRESTRIAL LASER SCANNING POINTS**. In *ISPRS Workshop Laserscanning'09, September 1 − 2, 2009, Paris, France*, 2009.

[165] Y. Stebler. **GPS/INS Integrity in Airborne Mapping**. Master's thesis, Swiss Federal Institute of Technology, Lausanne (EPFL), 2008.

[166] C.C.J.M. Tiberius. ***Recursive data processing for kinematic GPS surveying***. Nederlandse Commissie Voor Geodesie, 1998.

[167] D.H. Titterton and J.L. Weston. ***Strapdown Inertial Navigation Technology***, volume 207. Peter Peregrinus Ltd, 2 edition, 1997.

[168] P. Tomé. ***Integration of Inertial and Satellite Navigation Systems for Aircraft Attitude Determination***. PhD thesis, University of Porto, Portugal, 2002.

[169] P. Tomé. **LIAISON: D066 MEMS Module (HMEMS) Interface Control Document (ICD)**. Technical report, EPFL-TOPO, 2007. Document not available to public.

[170] P. Tomé. ***Manual GPS DataLogger for Scan2map-system***. EPFL-TOPO, 2007.

[171] P. Tomé, T. Cunha, S. Cunha, and L. Bastos. **Position+Attitude from GPS+INS for RTK Airborne Sensoring**. In *Proceeding of ION 55th Annual Meeting, 28-30 June 1999, Cambridge, MA 339*, pages 339–346, 1999.

[172] P. Tomé, T. Cunha, S. Cunha, and L. Bastos. **Evaluation of a DGPS/IMU Integrated Navigation System**. In *ION GPS*, pages 2233–2242, Salt Lake City, UT, 2000.

[173] TopoSys. **FALCON LIDAR SENSOR SYSTEM**. Technical report, TopoSys Geographische Systemdaten GmbH, 2004.

[174] C. Toth, S. W. Shin, D. A. Grejner-Brzezinska, and J. H. Kwon. **On accurate time synchronization of multi-sensor mobile mapping systems**. *Journal of Applied Geodesy*, 2(3):159–166, 2008.

[175] D. Tovari and N. Pfeifer. **SEGMENTATION BASED ROBUST INTERPOLATION: A NEW APPROACH TO LASER DATA FILTERING**. In *IAPRS XXXVI, 3/W19, Enschede, The Netherlands*, 2005.

[176] R.V. Ussyshkin and B. Smith. **PERFORMANCE ANALYSIS OF ALTM 3100EA: INSTRUMENT SPECIFICATIONS AND ACCURACY OF LIDAR DATA**. *The International Archives of the Photogrammetry, Remote Sensing and Spatial Information Sciences*, 34:Part XXX, 2006.

[177] J. Vallet. ***Saisie de la couverture neigeuse de sites avalancheux par des techniques aéroportées***. PhD thesis, Swiss Federal Institute of Technology, Lausanne (EPFL), 2002. Thse EPFL N 2610.

[178] J. Vallet. **GPS-IMU and Lidar integration to aerial photogrammetry: Development and practical experiences with Helimap System**. In *Voträge Dreiländertagung 27. Wissenschaftlich-Technische Jahrestagung der DGPF, 19-21 June 2007, Muttenz*, 2007.

[179] J. Vallet and J. Skaloud. **Development and Experiences with A Fully-Digital Handheld Mapping System Operated From A Helicopter**. In *The International Archives of the Photogrammetry, Remote Sensing and Spatial Information Sciences*, volume XXXV, pages Part B, Commission 5, Istanbul, 2004.

[180] F. Van Diggelen and A. Brown. **Mathematical aspects of GPS RAIM**. In *IEEE Position Location and Navigation Symposium*, pages 733–738, Las Vegas, NV, USA, 1994.

[181] C.R. Vaughn, W. Bufton, B. Krabill, and Rabine D.L. **Georeferencing of Airborne Laser Altimeter Measurements**. *International journal of remote sensing*, 17:2185–2200, 1996.

[182] TU Vienna. **Website Christian Doppler Laboratory, TU Vienna**. http://www.ipf.tuwien.ac.at/cd-labor/26.0.html, 2009.

[183] P. Viret. **Development of a Miniaturized Inertial Data Logger**. Master's thesis, Swiss Federal Institute of Technology, Lausanne, 2003.

[184] G. Vosselman. **On estimation of planimetric offsets in laser altimetry data**. *International Archives of Photogrammetry and Remote Sensing*, 34:375–380, 2002.

[185] G. Vosselman and H.-G. Maas. **Adjustment and Filtering of Raw Laser Altimetry Data**. In *OEEPE Workshop on Airborne Laserscanning and Interferometric SAR for Detailed Digital Elevation Models*, volume 40, pages 62–72, Stockholm, Sweden, 2001. OEEPE Publication.

[186] A. Vydhyanathan. **EFFECT OF ATMOSPHERIC PARTICULATES ON AIRBORNE LASER SCANNING FOR TERRAIN-REFERENCED NAVIGATION**. Master's thesis, the Russ College of Engineering and Technology of Ohio University, 2006.

[187] A. Waegli. **Analyse de données dynamiques pour l'aviation civile dans le cadre du projet EGNOS**. Master's thesis, EPFL, 2003.

[188] A. Waegli. ***Trajectory Determination and Analysis in Sports by Satellite and Inertial Navigation***. PhD thesis, Thesis 4288, EPFL, 2009.

[189] A. Waegli, S. Guerrier, and J. Skaloud. **Redundant MEMS-IMU integrated with GPS for Performance Assessment in Sports**. In *Proceedings of the IEEE/ION PLANS 2008, Monterey, CA, USA*, 2008.

[190] T. Warriner and G. Mandlburger. **Generating a New High Resolution DTM Product from various Data Sources**. In *Proceedings of Photogrammetric Week 05, Stuttgart, Germany*, 2005.

[191] A. Wehr and U. Lohr. **Airborne laser scanning–an introduction and overview**. *ISPRS Journal of Photogrammetry and Remote Sensing*, 54(2-3):68–82, 1999.

[192] J.D Weiss and D.S. Kee. **A Direct Performance Comparison Between Loosely Coupled and Tightly Coupled GPS/INS Integration Techniques**. In *Proceedings of the 51st Annual Meeting of the Institute of Navigation June 5 - 7, 1995, Colorado Springs, CO*, pages 537 – 544, 1995.

[193] J. Whitacre. **Independent Geo-Spatial Quality Review, Is It Really Worth the Extra Money?** on website: http://lidarcomm.com/id2.html, September 2007. last visited: 10.9.2009.

[194] J. Wu, H. Ma, and Q. Li. **LEAST SQUARES MATCHING WITH AIRBORNE LIDAR DATA FOR STRIP ADJUSTMENT**. In *The International Archives of the Photogrammetry, Remote Sensing and Spatial Information Sciences*, volume XXXVII, Part B3b, 2008.

[195] G. Xu. ***GPS: Theory, Algorithms and Applications***. Springer Verlag, Berlin, 2nd edition, 2007.

[196] Y. Yokoo and T. Ooishi. **QUALITY CONTROL METHOD FOR FILTERING IN AERIAL LIDAR SURVEY**. In *The International Archives of the Photogrammetry, Remote Sensing and Spatial Information Sciences. Vol. XXXVII. Part B1. Beijing 2008*, 2008.

[197] K. Zhang and D. Whitmann. **Comparison of three algorithms for filtering airborne LIDAR data**. *Photogrammetric Engineering & Remote Sensing*, 73:313–324, 2005.

Appendix A

Derivation of Sub-matrices

The ALS observation equation for an arbitrary laser point $\mathbf{x}_p$ expressed in an arbitrary mapping frame m can be written as:

$$\mathbf{x}_p^m = \begin{bmatrix} X \\ Y \\ Z \end{bmatrix}^{\mathrm{m}} + \mathbf{R}_{\mathbf{b}}^{\mathbf{m}}(r,p,y) \left[\mathbf{R}_{\mathbf{s}}^{\mathbf{b}}(e_x,e_y,e_z)\rho \begin{pmatrix} \sin\theta \\ 0 \\ \cos\theta \end{pmatrix} + \begin{bmatrix} a_x \\ a_y \\ a_z \end{bmatrix}^{\mathrm{b}} \right] \tag{A.1}$$

where

$\mathbf{R}_{\mathbf{b}}^{\mathbf{m}}(r,p,y)$	is the attitude matrix from the IMU body frame to the mapping frame parametrized by roll, pitch and yaw.
$\mathbf{R}_{\mathbf{s}}^{\mathbf{b}}(e_x,e_y,e_z)$	is the boresight matrix describing the angular offsets between the body frame and ALS frame
ρ,θ	are the range and encoder angle measurements, respectively, of the laser scanner
$[a_x,a_y,a_z]_T$	is the leverarm from the IMU center to the GPS antenna expressed in the b-frame

For the purpose of the error analysis, 14 error states are retained:

- 3 positioning errors: $\sigma_X, \sigma_Y, \sigma_Z$
- 3 attitude errors: $\sigma_r, \sigma_p, \sigma_y$
- 3 leverarm calibration errors: $\sigma_{a_x}, \sigma_{a_y}, \sigma_{a_z}$
- 3 boresight calibration errors: $\sigma_{e_x}, \sigma_{e_y}, \sigma_{e_z}$
- 2 internal laser range-finder errors: $\sigma_\rho, \sigma_\theta$

Accordingly, the functional model can be written as

$$\underset{3\times14}{\mathbf{F}} = [\mathbf{F}_{pos}|\mathbf{F}_{att}|\mathbf{F}_{leverarm}|\mathbf{F}_{boresight}|\mathbf{F}_{range}|\mathbf{F}_{encoder}] \tag{A.2}$$

For simplification of the calculations the m-frame is defined as local tangent plane, with East, North and Up component.

Auxiliary Expressions

Computations in the s-frame

Computation of position vector $\mathbf{x}^s$ in the scanner frame

$$\mathbf{x}^s = \begin{bmatrix} \rho\sin(\theta) \\ 0 \\ \rho\cos(\theta) \end{bmatrix} \tag{A.3}$$

Computations in b-frame

Assuming a mounting matrix ($\mathbf{T}_s^b = \mathbf{I}_3$), and small angular displacements ($< 1^\circ$), the boresight matrix $\mathbf{R}_s^b$ can be modeled by a skew-symmetric matrix with the remaining misalignments in roll(e_x), pitch(e_y) and yaw(e_z):

$$\mathbf{R}_s^b = \begin{bmatrix} 1 & -e_z & e_y \\ e_z & 1 & -e_x \\ -e_y & e_x & 1 \end{bmatrix} \tag{A.4}$$

Using Eqn. A.3 and Eqn. A.4 the position vector $\mathbf{x}^b$ in the body-frame can be expressed such as:

$$\mathbf{x}^b = \begin{bmatrix} a_x \\ a_y \\ a_z \end{bmatrix}^{\mathrm{b}} + \mathbf{R}_s^b\mathbf{x}^s = \begin{bmatrix} a_x + \rho\sin(\theta) + e_y\rho\cos(\theta) \\ a_y + e_z\rho\sin(\theta) - e_x\rho\cos(\theta) \\ a_z - e_y\rho\sin(\theta) + \rho\cos(\theta) \end{bmatrix} \tag{A.5}$$

Re-arranging the elements of a 3D vector in a 3D matrix such as $\mathbf{X}^b* = [\mathbf{x}^b\times]$ leads to

$$\mathbf{X}^b = \begin{bmatrix} 0 & -x_3^b & x_2^b \\ x_3^b & 0 & -x_1^b \\ -x_2^b & x_1^b & 0 \end{bmatrix} \tag{A.6}$$

Computations in the l-frame (NED)

The rotation matrix from the b-frame to the l-frame is the transpose of $\mathbf{R}_l^b$ (see Eqn. 2.2.4):

$$\mathbf{R}_b^l = \begin{bmatrix} \cos(p)\cos(y) & \sin(r)\sin(p)\cos(y) - \cos(r)\sin(y) & \cos(r)\sin(p)\cos(y) + \sin(r)\sin(y) \\ \cos(p)\sin(y) & \sin(r)\sin(p)\sin(y) + \cos(r)\cos(y) & \cos(r)\sin(p)\sin(y) - \sin(r)\cos(y) \\ -\sin(p) & \sin(r)\cos(p) & \cos(r)\cos(p) \end{bmatrix} \tag{A.7}$$

The position vector $\mathbf{x}^l$ in the local-level (ned) (mapping) frame can be expressed as:

$$\mathbf{x}^l = \mathbf{R}_b^l\mathbf{x}^b \tag{A.8}$$

By re-arranging the elements of a 3D vector in a 3D matrix such as: $\mathbf{X}^l* = [\mathbf{x}^l\times]$

$$\mathbf{X}^l = \begin{bmatrix} 0 & -x_3^l & x_2^l \\ x_3^l & 0 & -x_1^l \\ -x_2^l & x_1^l & 0 \end{bmatrix} \tag{A.9}$$

Computations in the m-frame

Approximating the mapping frame by the ENU frame, the rotation matrix to pass from the b-frame to the m-frame is given by

$$\mathbf{R}_b^m = \mathbf{T}_{NED}^{ENU}\mathbf{R}_b^l \tag{A.10}$$

where $\mathbf{T}_{NED}^{ENU}$ is the rotation matrix to express the coordinates in the local tangent plane frame:

$$\mathbf{T}_{NED}^{ENU} = \begin{bmatrix} 0 & 1 & 0 \\ 1 & 0 & 0 \\ 0 & 0 & -1 \end{bmatrix} \tag{A.11}$$

The rotation matrix relating the s-frame to the m-frame is given by

$$\mathbf{R}_s^m = \mathbf{R}_b^m\mathbf{R}_s^b \tag{A.12}$$

Euler Angle Derivatives

The transformation matrix to express the angular rate vector such as $\partial\mathbf{R}_l^b = \mathbf{R}_l^b\mathbf{\Psi}_{bl}^l$ can be written as:

$$\mathbf{\Psi}_{bl}^l = \begin{bmatrix} -\cos(p)\cos(y) & \sin(y) & 0 \\ -\cos(p)\sin(y) & -\cos(y) & 0 \\ sin(p) & 0 & -1 \end{bmatrix} \tag{A.13}$$

The angular rate vector to express the derivatives of the boresight angles ($\partial\mathbf{R}_s^b = \mathbf{R}_s^b\mathbf{\Psi}_{bs}^s$) takes the following form:

$$\mathbf{\Psi}_{bs}^s = \begin{bmatrix} -\cos(\beta_2)\cos(\beta_3) & \sin(\beta_3) & 0 \\ -\cos(\beta_2)\sin(\beta_3) & -\cos(\beta_3) & 0 \\ sin(\beta_2) & 0 & -1 \end{bmatrix} \tag{A.14}$$

where the boresight angles $\beta_1, \beta_2, \beta_3$ can be extracted from $\mathbf{R}_s^b$:

$$\begin{aligned} \beta_1 &= \text{atan2}\left(\frac{\mathbf{R}_s^b[3,2]}{\mathbf{R}_s^b[3,3]}\right) = \text{atan2}(e_x) \\ \beta_2 &= \text{atan2}\left(\frac{-\mathbf{R}_s^b[3,1]}{\sqrt{\mathbf{R}_s^b[1,1]^2 + \mathbf{R}_s^b[2,1]^2}}\right) = \text{atan2}\left(\frac{-e_y}{\sqrt{1+e_x^2}}\right) \\ \beta_3 &= \text{atan2}\left(\frac{\mathbf{R}_s^b[2,1]}{\mathbf{R}_s^b[1,1]}\right) = \text{atan2}(e_z) \end{aligned} \tag{A.15}$$

Partial derivatives

Using the auxiliary expressions introduced before, the functional model $\mathbf{F}$ can be expressed as the partial derivatives with respect to the different error sources.

Position uncertainties

$$\underset{3\times3}{\mathbf{F}_{pos}} = \begin{bmatrix} \frac{\partial \mathbf{x}_p}{\partial X} & \frac{\partial \mathbf{x}_p}{\partial Y} & \frac{\partial \mathbf{x}_p}{\partial Z} \end{bmatrix} = \begin{bmatrix} 1 & 0 & 0 \\ 0 & 1 & 0 \\ 0 & 0 & 1 \end{bmatrix} \tag{A.16}$$

Attitude uncertainties

$$\underset{3\times3}{\mathbf{F}_{att}} = \begin{bmatrix} \frac{\partial \mathbf{x}_p}{\partial r} & \frac{\partial \mathbf{x}_p}{\partial p} & \frac{\partial \mathbf{x}_p}{\partial y} \end{bmatrix} = \mathbf{T}_{NED}^{ENU} \mathbf{X}^l \mathbf{\Psi}_{bl}^l \tag{A.17}$$

$$\begin{aligned}
\mathbf{F}_{att}[1,1] =& -(\sin(p)(a_x + \rho\sin(\theta)) - \sin(r)\cos(p)a_y - \cos(r)\cos(p)(a_z + \rho\cos(\theta)))\cos(p)\cos(y) + \\
& (\cos(p)\cos(y)(a_x + \rho\sin(\theta)) + (\sin(r)\sin(p)\cos(y) - \cos(r)\sin(y))a_y + (\cos(r)\sin(p)\cos(y) + \sin(r)\sin(y))(a_z + \rho\cos(\theta)))\sin(p) \\
\mathbf{F}_{att}[1,2] =& (\sin(p)(a_x + \rho\sin(\theta)) - \sin(r)\cos(p)a_y - \cos(r)\cos(p)(a_z + \rho\cos(\theta)))\sin(y) \\
\mathbf{F}_{att}[1,3] =& -\cos(p)\cos(y)(a_x + \rho\sin(\theta)) - (\sin(r)\sin(p)\cos(y) - \cos(r)\sin(y))a_y - (\cos(r)\sin(p)\cos(y) + \sin(r)\sin(y))(a_z + \rho\cos(\theta)) \\
\mathbf{F}_{att}[2,1] =& -(-\sin(p)(a_x + \rho\sin(\theta)) + \sin(r)\cos(p)a_y + \cos(r)\cos(p)(a_z + \rho\cos(\theta)))\cos(p)\sin(y) + \\
& (-\cos(p)\sin(y)(a_x + \rho\sin(\theta)) - (\sin(r)\sin(p)\sin(y) + \cos(r)\cos(y))a_y - (\cos(r)\sin(p)\sin(y) - \sin(r)\cos(y))(a_z + \rho\cos(\theta)))\sin(p) \\
\mathbf{F}_{att}[2,2] =& -(-\sin(p)(a_x + \rho\sin(\theta)) + \sin(r)\cos(p)a_y + \cos(r)\cos(p)(a_z + \rho\cos(\theta)))\cos(y) \\
\mathbf{F}_{att}[2,3] =& \cos(p)\sin(y)(a_x + \rho\sin(\theta)) + (\sin(r)\sin(p)\sin(y) + \cos(r)\cos(y))a_y + (\cos(r)\sin(p)\sin(y) - \sin(r)\cos(y))(a_z + \rho\cos(\theta)) \\
\mathbf{F}_{att}[3,1] =& -(-\cos(p)\sin(y)(a_x + \rho\sin(\theta)) - (\sin(r)\sin(p)\sin(y) + \cos(r)\cos(y))a_y - (\cos(r)\sin(p)\sin(y) - \sin(r)\cos(y))(a_z + \rho\cos(\theta)))\cos(p)\cos(y) - \\
& (\cos(p)\cos(y)(a_x + \rho\sin(\theta)) + (\sin(r)\sin(p)\cos(y) - \cos(r)\sin(y))a_y + (\cos(r)\sin(p)\cos(y) + \sin(r)\sin(y))(a_z + \rho\cos(\theta)))\cos(p)\sin(y) \\
\mathbf{F}_{att}[3,2] =& (-\cos(p)\sin(y)(a_x + \rho\sin(\theta)) - (\sin(r)\sin(p)\sin(y) + \cos(r)\cos(y))a_y - (\cos(r)\sin(p)\sin(y) - \sin(r)\cos(y))(a_z + \rho\cos(\theta)))\sin(y) - \\
& (\cos(p)\cos(y)(a_x + \rho\sin(\theta)) + (\sin(r)\sin(p)\cos(y) - \cos(r)\sin(y))a_y + (\cos(r)\sin(p)\cos(y) + \sin(r)\sin(y))(a_z + \rho\cos(\theta)))\cos(y) \\
\mathbf{F}_{att}[3,3] =& 0
\end{aligned}$$

Leverarm uncertainties

$$\underset{3\times3}{\mathbf{F}_{leverarm}} = \begin{bmatrix} \frac{\partial \mathbf{x}_p}{\partial a_x} & \frac{\partial \mathbf{x}_p}{\partial a_y} & \frac{\partial \mathbf{x}_p}{\partial a_z} \end{bmatrix} = \mathbf{R}_b^m = \begin{bmatrix} \cos(p)\sin(y) & \sin(r)\sin(p)\sin(y) + \cos(r)\cos(y) & \cos(r)\sin(p)\sin(y) - \sin(r)\cos(y) \\ \cos(p)\cos(y) & \sin(r)\sin(p)\cos(y) - \cos(r)\sin(y) & \cos(r)\sin(p)\cos(y) + \sin(r)\sin(y) \\ \sin(p) & -\sin(r)\cos(p) & -\cos(r)\cos(p) \end{bmatrix} \tag{A.18}$$

Boresight uncertainties

$$\underset{3\times3}{\mathbf{F}_{bore}} = \begin{bmatrix} \frac{\partial \mathbf{x}}{\partial e_x} & \frac{\partial \mathbf{x}}{\partial e_y} & \frac{\partial \mathbf{x}}{\partial e_z} \end{bmatrix} = \mathbf{R}_b^m \mathbf{X}^b \mathbf{\Psi}_{bs}^s \tag{A.19}$$

$$\begin{aligned}
\mathbf{F}_{bore}[1,1] =& -((\sin(r)\sin(p)\sin(y)+\cos(r)\cos(y))(a_z - e_y\rho\sin(\theta)+\rho\cos(\theta)) + (\cos(r)\sin(p)\sin(y)-\sin(r)\cos(y))(-a_y - e_z\rho\sin(\theta)+e_x\rho\cos(\theta)))\cos(\beta_2)\cos(\beta_3)- \\
& (\cos(p)\sin(y)(-a_z + e_y\rho\sin(\theta)-\rho\cos(\theta)) + (\cos(r)\sin(p)\sin(y)-\sin(r)\cos(y))(a_x+\rho\sin(\theta)+e_y\rho\cos(\theta)))\cos(\beta_2)\sin(\beta_3)+ \\
& (\cos(p)\sin(y)(a_y + e_z\rho\sin(\theta)-e_x\rho\cos(\theta)) + (\sin(r)\sin(p)\sin(y)+\cos(r)\cos(y))(-a_x-\rho\sin(\theta)-e_y\rho\cos(\theta)))\sin(\beta_2) \\
\mathbf{F}_{bore}[1,2] =& ((\sin(r)\sin(p)\sin(y)+\cos(r)\cos(y))(a_z - e_y\rho\sin(\theta)+\rho\cos(\theta)) + (\cos(r)\sin(p)\sin(y)-\sin(r)\cos(y))(-a_y - e_z\rho\sin(\theta)+e_x\rho\cos(\theta)))\sin(\beta_3)- \\
& (\cos(p)\sin(y)(-a_z + e_y\rho\sin(\theta)-\rho\cos(\theta)) + (\cos(r)\sin(p)\sin(y)-\sin(r)\cos(y))(a_x+\rho\sin(\theta)+e_y\rho\cos(\theta)))\cos(\beta_3) \\
\mathbf{F}_{bore}[1,3] =& -\cos(p)\sin(y)(a_y + e_z\rho\sin(\theta)-e_x\rho\cos(\theta)) - (\sin(r)\sin(p)\sin(y)+\cos(r)\cos(y))(-a_x-\rho\sin(\theta)-e_y\rho\cos(\theta)) \\
\mathbf{F}_{bore}[2,1] =& -((\sin(r)\sin(p)\cos(y)-\cos(r)\sin(y))(a_z - e_y\rho\sin(\theta)+\rho\cos(\theta)) + (\cos(r)\sin(p)\cos(y)+\sin(r)\sin(y))(-a_y - e_z\rho\sin(\theta)+e_x\rho\cos(\theta)))\cos(\beta_2)\cos(\beta_3)- \\
& (\cos(p)\cos(y)(-a_z + e_y\rho\sin(\theta)-\rho\cos(\theta)) + (\cos(r)\sin(p)\cos(y)+\sin(r)\sin(y))(a_x+\rho\sin(\theta)+e_y\rho\cos(\theta)))\cos(\beta_2)\sin(\beta_3)+ \\
& (\cos(p)\cos(y)(a_y + e_z\rho\sin(\theta)-e_x\rho\cos(\theta)) + (\sin(r)\sin(p)\cos(y)-\cos(r)\sin(y))(-a_x-\rho\sin(\theta)-e_y\rho\cos(\theta)))\sin(\beta_2) \\
\mathbf{F}_{bore}[2,2] =& ((\sin(r)\sin(p)\cos(y)-\cos(r)\sin(y))(a_z - e_y\rho\sin(\theta)+\rho\cos(\theta)) + (\cos(r)\sin(p)\cos(y)+\sin(r)\sin(y))(-a_y - e_z\rho\sin(\theta)+e_x\rho\cos(\theta)))\sin(\beta_3)- \\
& (\cos(p)\cos(y)(-a_z + e_y\rho\sin(\theta)-\rho\cos(\theta)) + (\cos(r)\sin(p)\cos(y)+\sin(r)\sin(y))(a_x+\rho\sin(\theta)+e_y\rho\cos(\theta)))\cos(\beta_3) \\
\mathbf{F}_{bore}[2,3] =& -\cos(p)\cos(y)(a_y + e_z\rho\sin(\theta)-e_x\rho\cos(\theta)) - (\sin(r)\sin(p)\cos(y)-\cos(r)\sin(y))(-a_x-\rho\sin(\theta)-e_y\rho\cos(\theta)) \\
\mathbf{F}_{bore}[3,1] =& -(-\sin(r)\cos(p)(a_z - e_y\rho\sin(\theta)+\rho\cos(\theta)) - \cos(r)\cos(p)(-a_y - e_z\rho\sin(\theta)+e_x\rho\cos(\theta)))\cos(\beta_2)\cos(\beta_3)- \\
& (\sin(p)(-a_z + e_y\rho\sin(\theta)-\rho\cos(\theta)) - \cos(r)\cos(p)(a_x+\rho\sin(\theta)+e_y\rho\cos(\theta)))\cos(\beta_2)\sin(\beta_3)+ \\
& (\sin(p)(a_y + e_z\rho\sin(\theta)-e_x\rho\cos(\theta)) - \sin(r)\cos(p)(-a_x-\rho\sin(\theta)-e_y\rho\cos(\theta)))\sin(\beta_2) \\
\mathbf{F}_{bore}[3,2] =& (-\sin(r)\cos(p)(a_z - e_y\rho\sin(\theta)+\rho\cos(\theta)) - \cos(r)\cos(p)(-a_y - e_z\rho\sin(\theta)+e_x\rho\cos(\theta)))\sin(\beta_3)- \\
& (\sin(p)(-a_z + e_y\rho\sin(\theta)-\rho\cos(\theta)) - \cos(r)\cos(p)(a_x+\rho\sin(\theta)+e_y\rho\cos(\theta)))\cos(\beta_3) \\
\mathbf{F}_{bore}[3,3] =& -\sin(p)(a_y + e_z\rho\sin(\theta)-e_x\rho\cos(\theta)) + \sin(r)\cos(p)(-a_x-\rho\sin(\theta)-e_y\rho\cos(\theta))
\end{aligned}$$

Laser range uncertainties

$$\underset{3\times1}{\mathbf{F}_{range}} = \begin{bmatrix} \frac{\partial \mathbf{x_P}}{\partial \rho} \end{bmatrix} = \mathbf{R}_s^m \begin{bmatrix} \sin\theta \\ 0 \\ \cos\theta \end{bmatrix} \tag{A.20}$$

$$\begin{aligned}
\mathbf{F}_{range}[1] =& (\cos(p)\sin(y)+(\sin(r)\sin(p)\sin(y)+\cos(r)\cos(y))e_z - (\cos(r)\sin(p)\sin(y)-\sin(r)\cos(y))e_y)\sin(\theta)+ \\
& (\cos(p)\sin(y)e_y - (\sin(r)\sin(p)\sin(y)+\cos(r)\cos(y))e_x + \cos(r)\sin(p)\sin(y)-\sin(r)\cos(y))\cos(\theta) \\
\mathbf{F}_{range}[2] =& (\cos(p)\cos(y)+(\sin(r)\sin(p)\cos(y)-\cos(r)\sin(y))e_z - (\cos(r)\sin(p)\cos(y)+\sin(r)\sin(y))e_y)\sin(\theta)+ \\
& (\cos(p)\cos(y)e_y - (\sin(r)\sin(p)\cos(y)-\cos(r)\sin(y))e_x + \cos(r)\sin(p)\cos(y)+\sin(r)\sin(y))\cos(\theta) \\
\mathbf{F}_{range}[3] =& (\sin(p)-\sin(r)\cos(p)e_z + \cos(r)\cos(p)e_y)\sin(\theta) + (\sin(p)e_y + \sin(r)\cos(p)e_x - \cos(r)\cos(p))\cos(\theta)
\end{aligned}$$

Encoder angle uncertainties

$$\underset{3\times1}{\mathbf{F}_{enc}} = \left[\frac{\partial \mathbf{x_p}}{\partial \theta}\right] = \mathbf{R}_s^m \begin{bmatrix} \cos\theta \\ 0 \\ -\sin\theta \end{bmatrix} \rho \tag{A.21}$$

$$\begin{aligned}
\mathbf{F}_{enc}[1] = \rho((&\cos(p)\sin(y) + (\sin(r)\sin(p)\sin(y) + \cos(r)\cos(y))e_z - (\cos(r)\sin(p)\sin(y) - \sin(r)\cos(y))e_y)\cos(\theta) - \\
&(\cos(p)\sin(y)e_y - (\sin(r)\sin(p)\sin(y) + \cos(r)\cos(y))e_x + \cos(r)\sin(p)\sin(y) - \sin(r)\cos(y))\sin(\theta)) \\
\mathbf{F}_{enc}[2] = \rho((&\cos(p)\cos(y) + (\sin(r)\sin(p)\cos(y) - \cos(r)\sin(y))e_z - (\cos(r)\sin(p)\cos(y) + \sin(r)\sin(y))e_y)\cos(\theta) - \\
&(\cos(p)\cos(y)e_y - (\sin(r)\sin(p)\cos(y) - \cos(r)\sin(y))e_x + \cos(r)\sin(p)\cos(y) + \sin(r)\sin(y))\sin(\theta)) \\
\mathbf{F}_{enc}[3] = \rho((&\sin(p) - \sin(r)\cos(p)e_z + \cos(r)\cos(p)e_y)\cos(\theta) - (\sin(p)e_y + \sin(r)\cos(p)e_x - \cos(r)\cos(p))\sin(\theta))
\end{aligned}$$

Appendix B

Computation of 3D Laser Footprint

A point $\mathbf{x}$ on the cone with origin $\mathbf{O}$ must satisfy the condition:

$$[\mathbf{x}-\mathbf{O}]^{\mathrm{T}}\mathbf{M}\,[\mathbf{x}-\mathbf{O}]=0,\ \text{where}\ \mathbf{M}=\mathbf{l}^{\mathrm{T}}\cdot\mathbf{l}-\cos\left(\epsilon/2\right)^{2}\cdot\mathbf{I}_{3\times3} \tag{B.1}$$

A point $\mathbf{x}$ lying on the local tangent plane is defined by

$$\mathbf{x}=x_0+x_1\mathbf{d}_1+x_2\mathbf{d}_2 \tag{B.2}$$

Combining Eqn. B.2 with Eqn. B.1 results in a quadratic equation:

$$c_1x_1^2+2c_2x_1x_2+c_3x_2^2+2c_4x_1+2c_5x_2+c_6=0 \tag{B.3}$$

where $c_1=\mathbf{d}_1^T\mathbf{M}\mathbf{d}_1, c_2=\mathbf{d}_1^T\mathbf{M}\mathbf{d}_2, c_3=\mathbf{d}_2^T\mathbf{M}\mathbf{d}_2$
$c_4=\mathbf{l}^T\mathbf{M}\mathbf{d}_1, c_5=\mathbf{l}^T\mathbf{M}\mathbf{d}_2, c_6=\mathbf{l}^T\mathbf{M}\mathbf{l}$

Eqn. B.3 can be re-written in a homogeneous matrix form:

$$\mathbf{X}^{\mathrm{T}}\mathbf{C}\mathbf{X}=0,\ \text{where}\ \mathbf{C}=\begin{bmatrix}c_1 & c_2 & c_4\\ c_2 & c_3 & c_5\\ c_4 & c_5 & c_6\end{bmatrix}=\begin{bmatrix}\mathbf{C}_R & \mathbf{C}_t\\ {\scriptstyle[2\times2]} & {\scriptstyle[1\times2]}\\ \mathbf{C}_t{}^{\mathrm{T}} & \mathbf{C}_\delta\\ {\scriptstyle[2\times1]} & {\scriptstyle[1\times1]}\end{bmatrix} \tag{B.4}$$

where $\mathbf{C}$ is the conic matrix. The canonical form of the conic $\mathbf{C}_c$ can be defined by transforming the matrix $\mathbf{C}$ through a rotation $\mathbf{R}_{[2\times2]}$ and a translation $\mathbf{t}$:

$$\mathbf{C}_c=\begin{bmatrix}C_{c1} & 0 & 0\\ 0 & C_{c2} & 0\\ 0 & 0 & C_{c3}\end{bmatrix}=\mathbf{H}^{\mathrm{T}}\mathbf{C}\mathbf{H},\ \text{with}\ \mathbf{H}=\begin{pmatrix}\mathbf{R} & \mathbf{t}\\ {\scriptstyle[2\times2]} & {\scriptstyle[1\times2]}\\ \begin{bmatrix}0 & 0\end{bmatrix} & 0\end{pmatrix} \tag{B.5}$$

$\mathbf{C}_c$ defines the canonical conic such as

$$C_{c1}x_{c1}^2+C_{c2}x_{c2}^2+C_{c3}=0 \tag{B.6}$$

This can be re-written in the well-known equation for a 2D ellipse

$$\frac{x_{c1}^2}{a^2}+\frac{x_{c2}^2}{b^2}=1,\ \text{with}\ a=\sqrt{-c_{c3}/c_{c1}}, b=\sqrt{-c_{c3}/c_{c2}} \tag{B.7}$$

The parameter b represents the semi-minor axis and a the semi-major axis of the ellipse. The corresponding 2D vectors can be written such as

$$\mathbf{a}^{2D} = a\mathbf{e}_x, \mathbf{b}^{2D} = b\mathbf{e}_y \tag{B.8}$$

where $\mathbf{e}_x$ and $\mathbf{e}_y$ are the unity vectors in x and y-direction, respectively. It can be shown that the main axis of the 3D ellipse must coincide with the projection of the laser beam $\mathbf{l}$ on the plane, expressed as $\mathbf{l}_\angle$ (see FIG. B.1). If the local plane is parameterized by vectors $\mathbf{d}_1$ and $\mathbf{d}_2$ forming an orthogonal base with the normal $\mathbf{n}$, the projection $\mathbf{l}_\angle$ of the laser direction $\mathbf{l}$ on the plane can be computed by

$$\mathbf{l}_\angle = \mathbf{d}_1 (\mathbf{l} \bullet \mathbf{d}_1) + \mathbf{d}_2 (\mathbf{l} \bullet \mathbf{d}_2) \tag{B.9}$$

Using this information, the axis of rotation $\boldsymbol{\omega}$ and the rotation angle θ between $\mathbf{a}^{2D}$ and $\mathbf{a}^{3D}$ can be computed:

$$\boldsymbol{\omega} = \begin{pmatrix} \omega_x \\ \omega_y \\ \omega_z \end{pmatrix} = \mathbf{a}^{2D} \times \mathbf{l}_\angle, \theta = \operatorname{acos}\left(\frac{\mathbf{a}^{2D} \bullet \mathbf{l}_\angle}{|\mathbf{a}^{2D}|\,|\mathbf{l}_\angle|} \right) \tag{B.10}$$

The transition from 2D to 3D is performed with Rodrigues' rotation formula expressing a rotation by an angle θ around a fixed axis ω:

$$\mathbf{R}_{2D}^{3D} = \mathbf{I} + \tilde{\boldsymbol{\omega}} \sin\theta + \tilde{\boldsymbol{\omega}}^2 (1 - \cos\theta), \tilde{\boldsymbol{\omega}} = \begin{pmatrix} 0 & -\omega_z & \omega_y \\ \omega_z & 0 & -\omega_z \\ \omega_y & \omega_z & 0 \end{pmatrix} \tag{B.11}$$

Finally the 3D semi-minor and semi-major axis can be computed:

$$\mathbf{a}^{3D} = \mathbf{R}_{2D}^{3D} \cdot \mathbf{a}^{2D}, \mathbf{b}^{3D} = b \left(\frac{\mathbf{a}^{3D}}{|\mathbf{a}^{3D}|} \times \mathbf{n} \right) \tag{B.12}$$

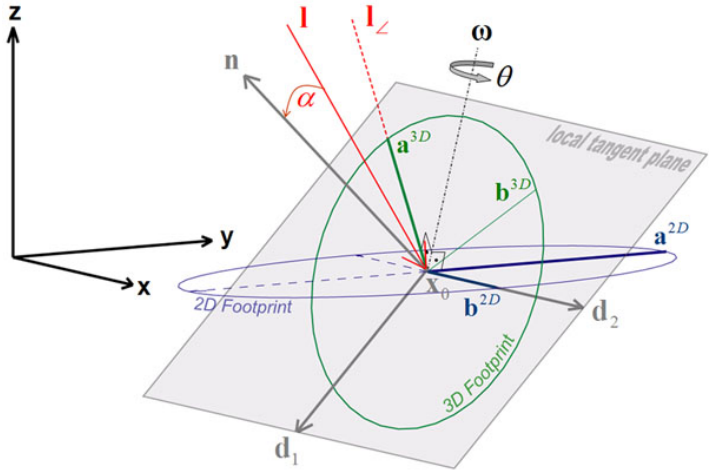

FIG. B.1: Computation of 2D footprint by intersection of laser cone with local tangent plane and subsequent re-projection into 3D.

Appendix C

Comparison RT - PP

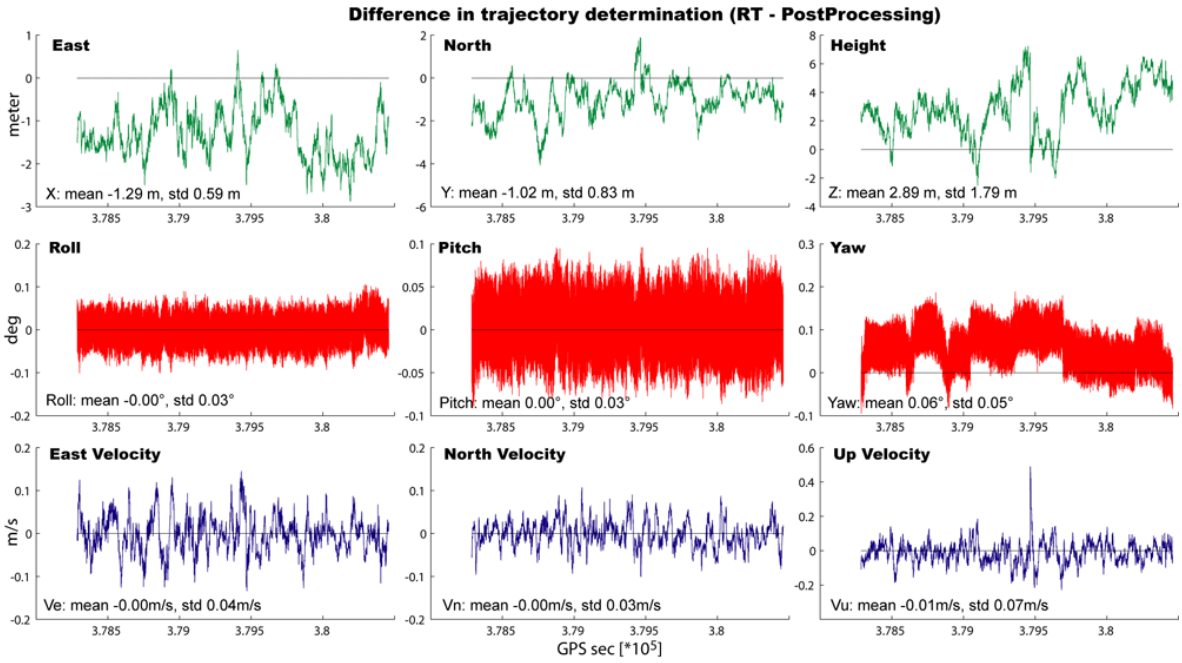

FIG. C.1: Comparison of trajectory computed in RT (using SPP) and in PP (using CP-DGPS) for Lausanne dataset.

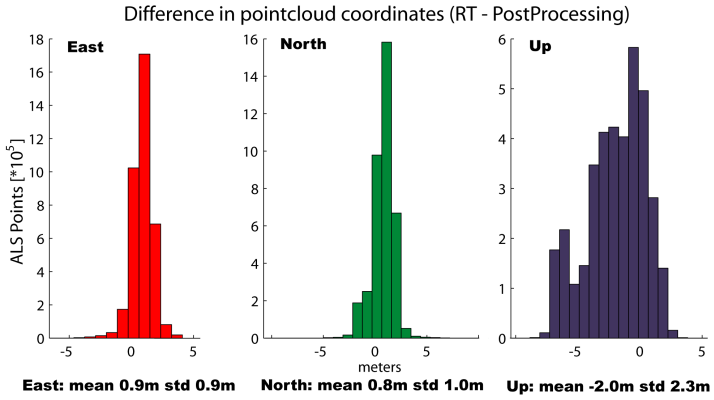

FIG. C.2: Histogram of coordinate differences (SPP -PP) for Lausanne dataset.

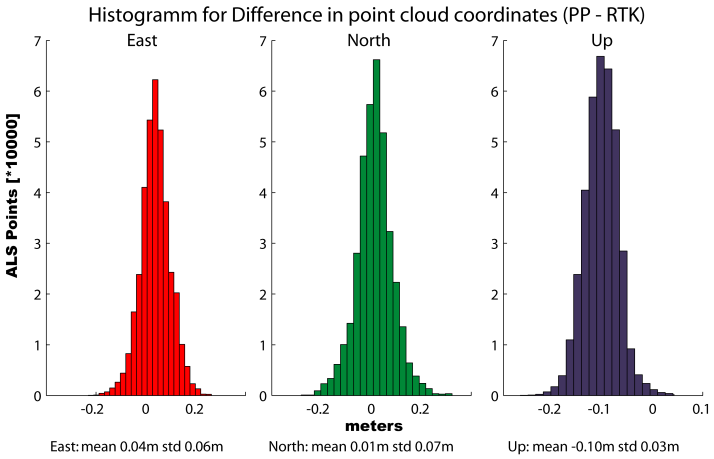

FIG. C.3: Histogram of coordinate differences (RTK-Radio - PP) for Sion 08 dataset.

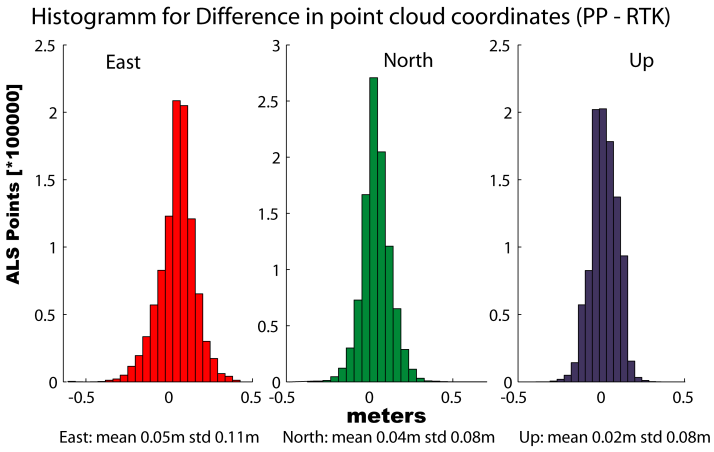

FIG. C.4: Histogram of coordinate differences (RTK-GPRS -PP) for Chur dataset.